FACULTAD DE FISICA
Departamento de Física de Partículas

Quasi-Free Scattering of Light Neutron-Deficient Nuclei

Memoria presentada por:

Juan Manuel Boillos Betete
como disertación para optar al
Grado de Doctor
en Ciencias Físicas
Santiago de Compostela, Abril 2019

USC
UNIVERSIDADE
DE SANTIAGO
DE COMPOSTELA

Quasi-Free Scattering of Neutron Deficient Exotic Nuclei

fue realizada por **D. JUAN MANUEL BOILLOS BETETE** Declara que:

1. La tesis abarca los resultados de elaboración propia de su propio trabajo,
2. de lo contrario, la tesis hace refrencia a las colaboraciones que tuvo en este trabajo.
3. La tesis es la versión definitiva presentada para la defensa y coincide con la versión en formato electrónico.
4. Confirma que la tesis no incurre en ningún tipo de plagio de otros autores ni de ningún otro trabajo presentado por el autor para la obtención de otros títulos

Santiago de Compostela,
25 de abril de 2019

Juan Manuel Boillos Betete
Departamento de Física de Partículas

USC
UNIVERSIDADE
DE SANTIAGO
DE COMPOSTELA

Dña. Dolores Cortina, PROFESORA DEL DEPARTAMENTO DE FISICA DE PARTICULAS DE LA UNIVERSIDAD DE SANTIAGO DE COMPOSTELA,

CERTIFICA:

que la memoria titulada:

Quasi-Free Scattering of Neutron Deficient Exotic Nuclei

fue realizada por **D. JUAN MANUEL BOILLOS BETETE** en el Departamento de Física de Partículas de la Universidad de Santiago de Compostela bajo su dirección, y constituye el trabajo de **tesis** que presenta para optar al grado de **Doctor en Ciencias Físicas.**

Santiago de Compostela,
1 de Julio de 2018

Dolores Cortina Gil
Departamento de Física de Partículas

USC
UNIVERSIDADE
DE SANTIAGO
DE COMPOSTELA

Acknowledgements

First of all, I wish to thank, first and foremost, my supervisorDolores Cortina Gil, who guided, supported, and motived me for this four years. She also gave me the chance to discover the amazing world of experimental nuclear physics. Without her assistance, valuable comments, and suggestions, this work could not become a reality.

I am also indebted to all colleagues belonging to the Experimental Group of Nuclei and Particles (GENP) of University of Santi- ago de Compostela, specially prof. José Benlliure Anaya, Jośe Luís Rodríguez Sanchéz and Pablo Cabanelas Eiras to afford useful discussions and provide guidance in nuclear reactions and programming tasks.

During the last year, discussions with Theoretical Sevilla's group, Antonio Moro and Marío Gómez Ramos, were deeply useful and enjoyable. I really appreciate it and I want to express my gratitude for it.

I do not forget GSI and TU-Darmsdadt collaborators, in particularly Matthias Höll, Leyla Atar, Paloma Fernández Díaz, Felix Wammers, Dominic Rossi, Marcel Heine, Ana Henriques, and professor Thommas Aumann; to help and reply me so many times. Specially thanks Ralf Plag for his huge effort developing code and responding my silly questions.

Finalmente quiero agradecer la disposiciń y paciencia de aquellas personas más cercanas: mis padres, José María y María Begoña; mi novia Sisi (gracias de corazón), mis amigos Víctor, Julio, Adrián, José Luís, OGEL; mi hermano Pablo, y un largo ectétera. Gran parte de tesis es vuestra por hacerme levantarme tras caer.

This work was partially supported by the Spanish "Ministerio de Economía y Competitividad", under the grant BES-2014-069385.

USC
UNIVERSIDADE
DE SANTIAGO
DE COMPOSTELA

Because atomic behaviour is so unlike ordinary experience, it is very difficult to get used to, and it appears peculiar and mysterious to everyone - both to the novice and to the experienced physicist.

Richard P. Feymann

USC
UNIVERSIDADE
DE SANTIAGO
DE COMPOSTELA

Contents

Introduction

The origin of nuclear physics is intimately related to the discovery of the atomic nucleus produced by a nuclear reaction over a century ago. Early experiments with scattering of *alpha particles* developed by Geiger and Marsden in 1909, and, subsequently by Rutherford in 1911, shed some light on the atom picture. The most relevant facts were that positive charges and most of the mass were concentrated at the centre of the atom (nucleus). Further studies by Geiger and Marsden, in 1913, could even estimate roughly the nuclear radius (less of $10^{-14}m$). For over ten years, a wrong idea of the nucleus composition remained, due to "transmutation" experiments performed by Rutherford in 1919 and the following explanation of β-decay in which those electrons are emitted from nucleus. It was not until 1932 when Chadwick (also Curie and Joliot) established a proof of the existence of a massive particle (at least similar to proton) named as *neutron*. At his point, the nuclear structure was clear, neutrons and protons (as nucleons) composed the nucleus.

Following, lots of discoveries such as β-decay explained by the Fermi theory (1934), the nuclear strong force interpreted through meson exchange by Yukawa in 1935 or the group of theories and experiments of fusion (Gamow, von Weizsäcker, Bethe) and fission (Strassman, Meitner, Frisch) including the Manhattan project (developed by Oppenheimer in 1942) ended with nuclear shell model (Mayer, Haxel, Jensen, [1, 2]) which brought a breakthrough in the nuclear field. Experiments performed during the next years and theoretical models focused their efforts on understanding nuclear and nucleon structure. The interpretation of unusual phenomenons, like stellar nucleosynthesis (Burgide, Fowler, Hoyle in 1957), neutron star, nuclear superconductivity (Bohr Mottelson in 1958) or the composition of nucleon within quark model development, symbolise the most relevant discoveries in this period.

During the last third of the past century, and especially, in the eighties and nineties, numerous large collaborative experiments took place over the world; Fermilab, Berkeley, Argonne, RIKEN, GANIL, GSI, ISOLDE, CERN. These large infrastructures also brought a relevant development in interdisciplinary fields.

The new century started with several discoveries and scientific evidences: neutrino oscillations, superheavy elements close to the "stability island" [1], hypernucleus [2], amongst others, that were only possible thanks to the continuous upgrade of experiments in research centres. That is the case of GSI Helmholzzentrum für Schwerionenforschung which is going to turn into the international accelerator facility FAIR (Facility for Antiproton and Ion Research).

The use of X-rays for medical purposes is a reality since the end of 19th century and it was extended with the application of γ radiation (Mendelssohn in 1936) and, later, proton and hadron beams. Treatment of cancer tissues and therapy achieved with proton/hadron beams was also introduced in nuclear physics laboratories (in 1954 at Berkeley laboratory) and is an example of the relevance of these activities in the nuclear field. In addition, the development of medical imaging has also experimented a great development, starting with the first PET-scan (Positron-emission tomography) at Brookhaven.

It is clear that nuclear physics needed of many different experimental and theoretical inputs to construct the picture of the nucleus as it is today. Experimentally the determination of the energy spectra of the low-lying states, spins, magnetic moments, observation of polarisation effects of nucleons in nuclear collisions and, also, the internal momentum determination of nucleons in nuclei amongst others, were very important. It was also necessary to combine different approaches such as decay studies or the use of nuclear reactions to shape not only dynamical aspects but also single particle information on nuclei.

The use of direct reactions, proceeding in one (few) steps and in a short time ($\sim 10^{-22}$s) is proved to be a very useful spectroscopic tool. They allowed together with decay spectroscopy studies to establish the solid bases of the shell model of nuclei. We will restrict the discussion to direct reactions at relativistic energy conditions, as this is the case addressed in this work. First experiments of (p,2p) on stable nuclei were undertaken in the 50's in Berkeley [3, 4], and involved the detection of strongly correlated proton pairs that reflected the momentum distribution of the protons in the nucleus. High energy beams, that cover between 100-1500 AMeV [3], allowed to neglect the role of spectator nucleons simplifying the reaction mechanism. The reaction occurs in regimen of quasi-free, just considering the interaction between two nucleons projectile-target.

[1] The zone where nuclei with so-called magic numbers of protons and neutrons become long-lived.

[2] A hypernucleus is a kind of nucleus where, at least one of nucleons is an hyperion -baryon that carry the strangeness quantum number.

[3] The associated wavelength of incoming nucleus is comparable to internuclear distances

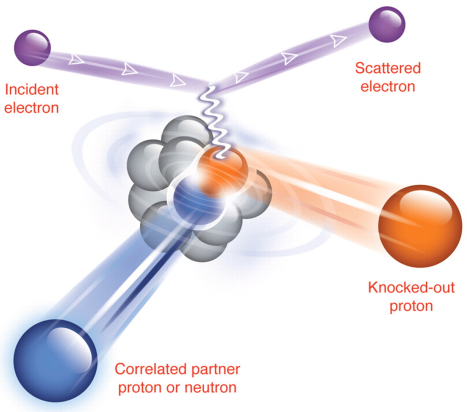

Figure 1: Illustration of the 12C(e,e'pN) reaction taken from [5]. A virtual photon is exchanged between incident electron and the nucleon. In the final state, the scattered electron is detected along with the two nucleons that are ejected from the nucleus. The local density for pairs is approximately five times larger than the typical nuclear density ($0.16 fm^{-3}$).

The measured separation energy distribution showed structures that were related to the binding energies of the various nuclear shells from which the protons were ejected [6, 7]. These studies only covered light nuclei (Ca) being the poor energy resolution achievable in these experiments the limiting factor [3, 4]. The alternative was the use of high energy electrons. Nuclear transparency of the electrons was considered as an advantage. The distortion of the associated momentum distributions was expected to be much smaller and offered the possibility of studying inner shells. Very successful experiments of (e,e'p) reactions were carried out in different facilities (Figure 2.18), for nuclei ranging from ^{2}H to ^{209}Bi.

Profiting from the higher experimental resolution transitions to many states in the resulting nucleus could be separated and the corresponding momentum distributions accurately measured [8]. The interpretation of this data yield to a significant reduction of the spectroscopic strength with an average quenching of 60-70[9].

The advent of fast radioactive beams produced by projectile fragmentation and in-flight identification approach, were an important milestones in the systematic study of unstable nuclei. Nucleon-knockout in inverse kinematics on light targets was extensively used to obtain single-particle properties on unstable nuclei [10].

The compiled results shown a compatible "quenching" (measured in form or reduction factor R_S), for small isospin asymmetry, but also a very strong dependence for very isospin asymmetric nuclei. These correlation effects seemed to be enhanced for removal of strongly-bound nucleons (in the neutron-deficient region) and decreased for less bound ones (in the opposite region in [11] and references therein). This dependence was not observed in reduction factors extracted in transfer reactions [12].

Our collaboration proposed the use of Quasi-Free Scattering (QFS) reactions in inverse kinematics [13],which is capable to explore a deeper region of the projectile wave function, as an alternative to knockout experiments. The method was validated with stable ^{12}C beams [14] and later extended to unstable species as neutron-rich oxygen isotopes [15, 16]. In these cases, the strong isospin dependence of R_s for the case of very asymmetric nuclei was not observed either.
On the other hand combined results from exclusive and inclusive experiments (e,e'p) at higher energy and large momentum transfer, Thomas Jefferson National Accelerator Fa-

cility Jefferson-Lab (Virginia, USA) brought also very nice results in recent years. The analysis [5] in the momentum space determine the presence of $20-25\%$ of nucleons with momenta above the Fermi momentum. They were identified to be dominated by NN in short correlated pairs (NN-SRC). It was also found that neutron-proton pairs were far more common than proton-proton or neutron-neutron , pointing to the contribution of the tensor part of the NN interaction at short distances.

One effect of the np-SRC dominance would be that in neutron-rich nuclei a larger fraction of protons will be in a SRC pair. This has important implications in fundamental questions such as nuclear symmetry energy or neutron stars composition, that should be explored in close future in high-energy radioactive beam facilities [17].

In this work, we have made use of direct reactions in inverse kinematics such as QFS with the goal of gaining information on the single-particle structure of neutron deficient oxygen and nitrogen. We have also explored the reactions mechanism involved. The analysis of other fragmentation channels leading to lighter isotopes has been addressed with the spirit of contributing to better definition of transport codes or hadron therapy treatments.

This dissertation is structured as follows. Chapter 1 summarises the information related to the R^3B-LAND experimental set-up (Reactions with Relativistic Radioactive Beams [18]) used. The S393 experiment performed in 2010 brought lots of Ph.D. dissertations in the last years [19, 20, 21, 22, 23, 24, 25, 26, 27, 28, 29, 30, 31, 32]. The results presented in this work focus on oxygen isotopic chain and neutron-deficient nitrogen isotopes. These data expand on and complement the aforementioned publications.

Chapter 2 explains in detail the analysis procedure used to extract all needed observables, i.e. cross section, gamma decay spectra and fragment momentum distributions.

Chapter 3 and 4 bring the experimental results of proton- and neutron-removal and QFS reactions which were induced by neutron-deficient and rich unstable beams. Special attention has been paid to the comprehension and control of the reaction mechanism used in each case. A detail comparison of the results obtained together with previously published data [16, 15, 14] is included in the manuscript. The results are compared with realistic model calculations performed by Sevilla Reaction's group, based on a Continuum Discretised Couple Channel (CDCC) approach ([33, 34]).

At this point, we have extended the analysis to the study of several fragmentation channels induced by the same nuclei and they can be found in chapter 5. Some of them are particularly interesting since involve reactions that could play a role in the development of proton-therapy [35] and PET imagining. They could also be of interest to complete data bases that are needed for physical simulations in hadrontherapy [36] and space shielding [37] fields.

The dissertation finalises with conclusions extracted from this 4-years work.

Chapter 1

The S393 Experiment

This chapter summarises the S393 experiment, performed at GSI in 2010. It includes a brief description of detectors employed and their calibrations. Some information about the data acquisition system and trigger patterns is also provided.

1.1 General Overview

The GSI [1], Helmholzzentrum für Schwerionenforschung, is a heavy-ion-beam facility located in Darmstadt, Germany. A schematic view of this facility is depicted in Figure 1.1.

A primary beam of $^{40}Ar^{+11}$ was produced in the ion source, accelerated in the UNILAC (UNIversal Linear ACcelerator) and, subsequently, injected in the SchwerIonenSynchrotron, SIS-18[2] in which it was accelerated again up to approximately 500 A MeV.

The SIS is connected to a high resolution forward spectrometer [38] called FRagment Separator (FRS) (see Figure 1.2 for details). It is composed of four stages, each of them made up of a 30 degrees dipole magnet (drawn in green colour) to deflect the ions, five quadrupole magnets to focus the beam and two sextupole magnets to correct for second-order aberrations.

At the entrance of the FRS there was a production target of beryllium (4.011 g/cm^2). The primary beam impinged on this Beryllium target and produced *via* nuclear fragmentation a wide range of secondary beams. The FRS separates these nuclei depending on their mass-to-charge ratio (A/Q). When a particle with Q charge and A mass travels through the magnetic fields of FRS it suffers the Lorentz force, $F_L = qv \times B$, and bends its trajectory according to:

$$B\rho = \frac{p}{Q} \propto \frac{A}{Z} \cdot \beta\gamma \tag{1.1}$$

[1] http://gsi.de/portrait/index.html

[2] The 18 in the name depicts the maximum magnetic rigidity, $B\rho = 18\ Tm$

where $B\rho$ is the magnetic rigidity of FRS, p is the momentum of the particle, the charge Q refers to Z number in absence of charge states - ions are fully stripped, $\beta = v/c$ is the velocity v of the particle in units of the speed of light, and $\gamma = 1/\sqrt{1-\beta^2}$ is the Lorentz factor.

Equation 1.1, means that for a certain magnetic field (FRS rigidity) only ions with a specific A/Z can follow the trajectory determined by the beam line. The FRS momentum acceptance ($\Delta p/p = 2\%$) leads to the fact, that beam traversing the set-up could be indeed composed by different nuclides.

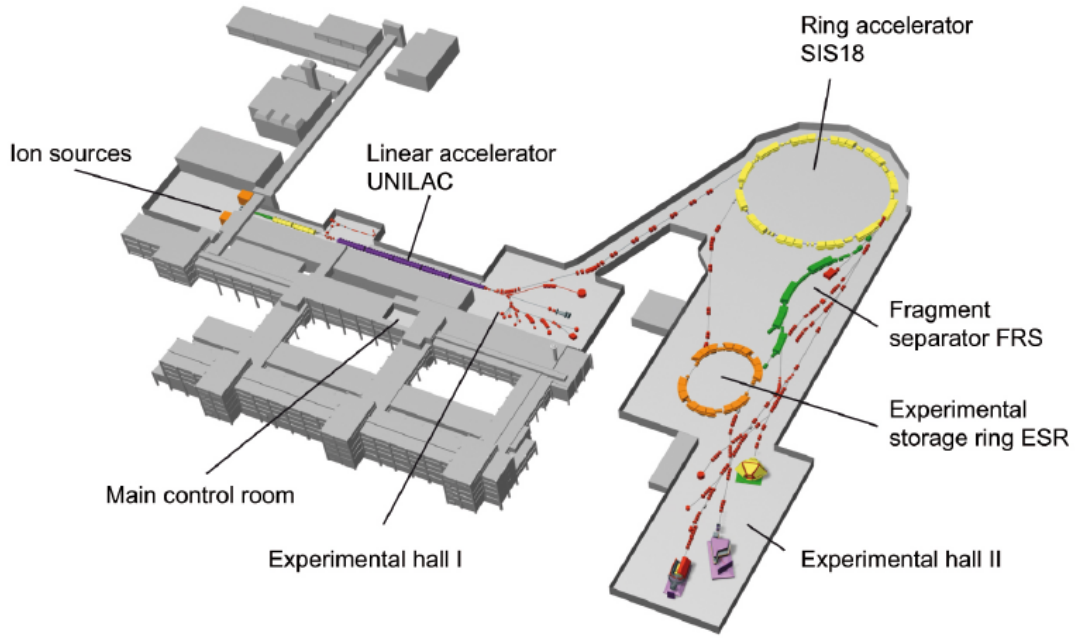

Figure 1.1: Schematic view of GSI facility as it was in 2010. Ions of $^{40}Ar^{+11}$ were produced in the *Ion sources* (left superior corner), accelerated in the *UNILAC* up to an energy of 11.4 *A*MeV and injected in the *SIS-18* (yellow ring, right top corner). There, they were accelerated up to 490 *A*MeV and transported to the entrance of the *FRS*. Numerous secondary beams were obtained *via* fragmentation reactions in a Beryllium target, selected by the *FRS* - according to their A/Z ratio - and transported downwards to the *experimental hall II*, in particular to Cave C where the R^{3}B-LAND experimental set-up was located. Picture taken from [39].

For S393 experiment, six different values of magnetic rigidity, $B\rho$, were selected permitting A/Z variation from $\approx$ 1.5 to 3.0. This large A/Z variation allows for instance the study of the complete oxygen isotopic chain covering from neutron deficient (^{13}O) up to neutron rich nuclei (^{24}O).

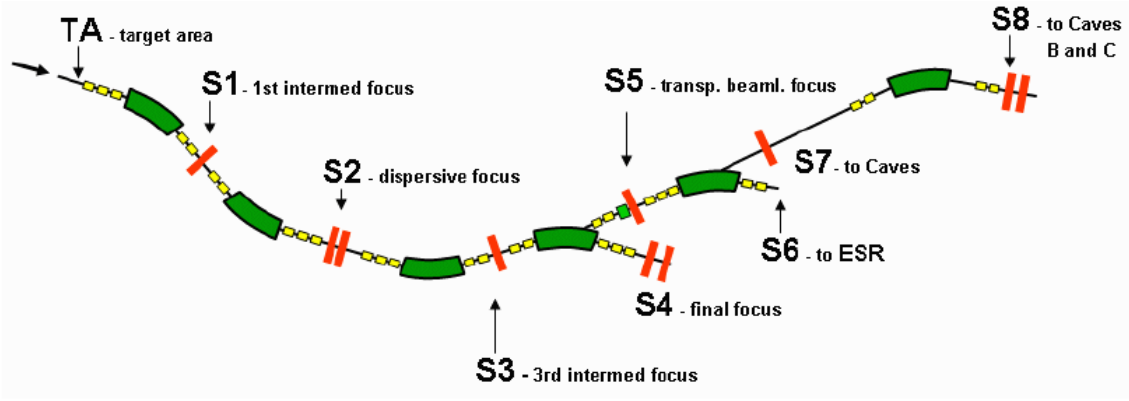

Figure 1.2: Schematic view of FRS and the transmission line to Cave C. The beam coming from the SIS-18 arrives to the entrance of the FRS where a production target of beryllium was placed (TA). Several nuclei were produced *via* fragmentation reactions, selected by the different FRS sections (S1,S2,S3,S4) and transported to Cave C. Two scintillators (S2 and S8) were used to determine the velocity of the isotopes. Picture Taken form [39].

To evaluate the ion velocities, FRS was equipped with two in-beam scintillator paddles (3mm of thickness) which provide time-of-flight measurements in an event-by-event basis. The first scintillator detector was located at the middle focus (S2) and the second was placed behind the FRS (S8), both depicted in Figure 1.2.

The fragment selection was achieved in two stages. The former involves the first two dipole magnets (drawn in green colour in Figure 1.2). Only fragments with an appropriate combination of mass, charge and velocity are transmitted. At the intermediate focal plane, a degrader (wedge-shaped material) was inserted. This material induces a ΔE and slow down the beam being the energy loss induced proportional to Z^2 according to the Bethe-Bloch formula.

In the second step, formed by the other two dipoles, S2 and S8, fragments were selected according to their A/Z ratio by their velocities, which are determined by time-of-flight measurements.

The cocktail beam can be isotopically identify in flight, i.e. mass, atomic number and velocity are determined.

The R^{3}B -LAND Set-up

The R^{3}B-LAND set-up, located in Cave C (belonging to Experimental Hall II in Figure 1.1), allows to study nuclear reactions induced by relativistic radioactive beams in inverse and complete kinematics.

It was design in the early 1990s and known as ALADIN-LAND - triggered by the construction of the LAND detector (Large Area Neutron Detector), and used in combination with the ALADIN magnet (A LArge DIpole magNet) [13]. This set-up was regularly upgraded and it has been the seed for the R^{3}B experiment [18] at the FAIR facility (Facility

Antiproton Ion Research, [39]).

The cocktail beam left the FRS, travelled around 55m and reached Cave C, where was located the S393 experiment depicted an schematic apparatus configuration in Figure 1.3.

Firstly, we find several detectors belonging to the **projectile area**. We calculate the velocity of our projectiles (secondary beams) *via* time-of-flight measurements from time difference signals recorded in S2, S8 and the first scintillator, POS, in Cave C (POsition-sensitive Scintillator). The Bρ values of the FRS allowed us to determine the projectile A/Z.

An active collimator, ROLU, consisting on four movable plastic scintillators, was used to centre the beam. Before ROLU, for tracking and energy loss measurements a position sensitive silicon detector, PSP (Position-sensitive Si-Pin diodes), was inserted.

Then, the cocktail beam entered in the **target area**, which included a reaction target chamber within a target wheel that can host several targets, and eight stripped silicon plane detectors (DSSSDs) in a box-configuration. The target chamber was surrounded by a 4π calorimeter named Crystal Ball (CB). It is a 4π array of 162 thallium-doped sodium iodide - NaI(Tl)- crystals (see [22] and references therein), that serves for the identification of γ-rays coming from de-excitation of outgoing fragments, and fast light particles emitted in the nuclear reaction.

After interacting of secondary beams with the target, the outgoing particles travelled in forward direction, were deflected by the ALADIN magnet and they reached the **Fragment Area**.

According to their masses and charges, the trajectories of these outgoing products were bent and focused on to different branches. Whereas neutrons, were not deflected and detected by LAND, located at zero degrees respect to the beam line - neutron arm; heavy fragments (with Z >3) and protons from nuclear reactions were tracked into their respectively arms. Fragment arm was composed by two fibre detectors (GFIs, Gross Fibre detektors) and a time-of-flight wall (TFW); and the proton arm used two drift chambers (PDCs) and a time-of-flight wall (PTW) allowing to obtain 2-D position, energy losses and time-of-flight measurements for these particles.

1.2 From Raw Data to Calibrated Events

Once a particle passes through any detector and leaves energy in it, the energy is transformed into electrical signals.

The Data Acquisition System, DAQ, converts the analogue electrical signals from detectors into digital values which are stored in list-mode data files, called LMDs.

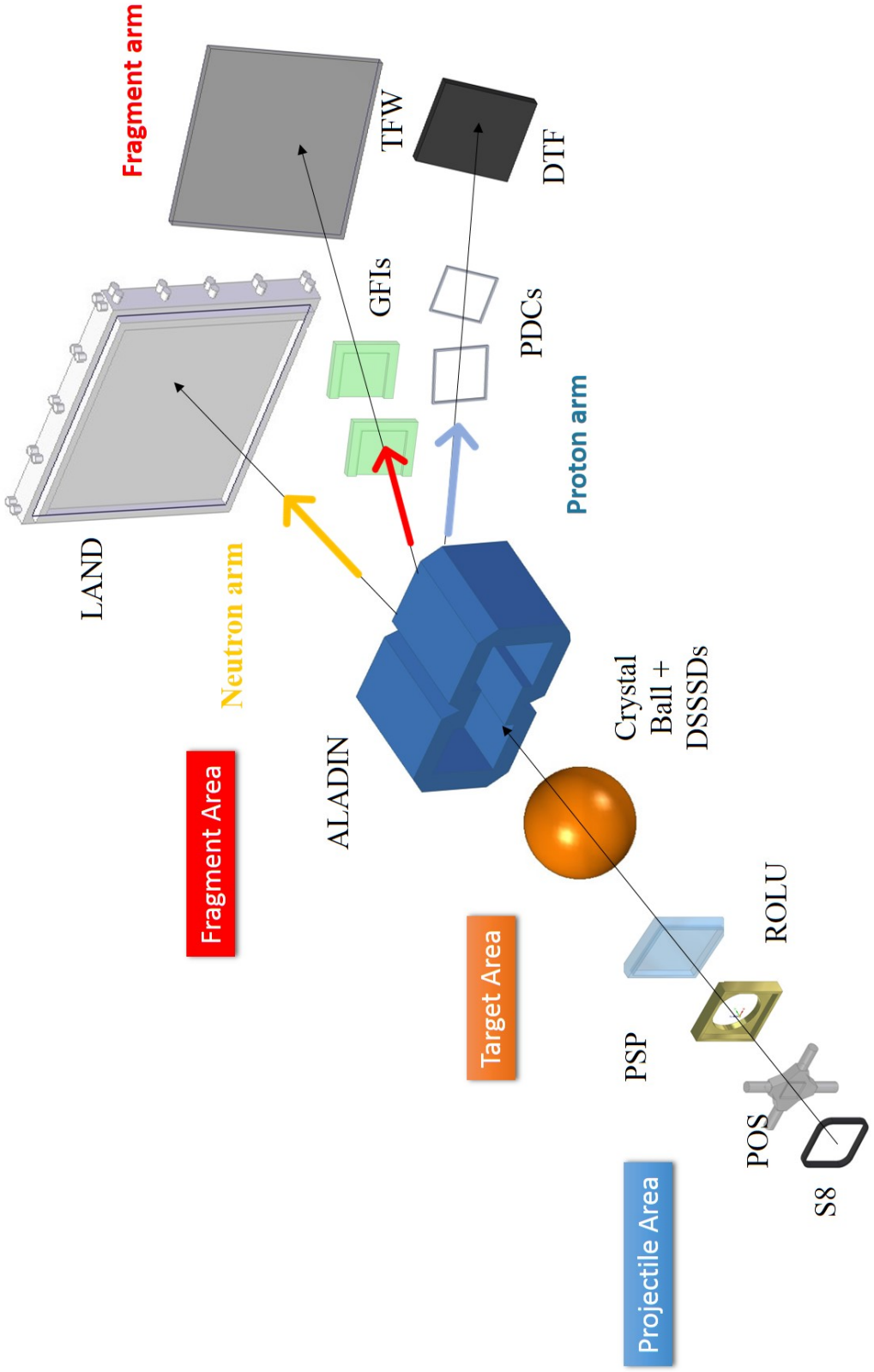

Figure 1.3: Schematic draft of R^{3}B-LAND set-up as used for S393 experiment.

The DAQ is compound by hardware digitization modules (MBS, Multi-Branch System [40]), software controls and sequences of the read-out for these modules, allowing to store data event-by-event (complementary information is found in [19, 28, 41] and references therein). At the occurrence of an accepted trigger, the characteristics of the signals, i.e. amplitudes, number of events, times, etcetera; are digitized.

The information contained in the LMD files can be extracted using the software package *land02*,[19, 42]. This program converts the LMD files into *rootfiles* - known as *unpacking process*. In addition, *land02* contains calibrations routines for any detector that will be presented in detail in the next section.

1.2.1 Trigger Patterns

Due to the existence of many subsystems into the set-up with different associated dead times, data reduction is critical. Therefore, before digitization process, the DAQ needs to distinguish events of interest from the rest. The decision to store information about a particular event is taken by the trigger logics. They are signals stemming and created from one, or usually multiple individual detectors. The experimentalist chooses and constructs these triggers to select the possible reaction channel of interest. These triggers, corresponding to a certain channel, are identified by different trigger bits (Tbit) and its corresponding trigger patterns ($Tpat = 2^{Tbit-1}$) and are shown in Table 1.1.

The S393 experiment used 16 different triggers. The first eight "on-spill" triggers are used for analysis purpose (*Tbit* from 1 to 8). Whereas, the rest of the triggers, (9 - 15) are the "off-spill" and they are used for calibration purposes. We summarize the "on-spill" triggers used in this analysis.

- The first trigger minimum bias also known as **good beam** (Tpat=1) stands for events with a potentially good incoming ion and it requires the spill-on logical signal from the accelerator plus a signal from POS in anti-coincidence with ROLU (which acts a Veto detector).

- **Fragment trigger** (Tpat=2) requires the good beam trigger plus a hit into the fragment wall i.e. a signal stems either from un-reacted beam or from 'not too violent' reaction allowing to be registered. Data recorded under this particular trigger are downscaled by numerical factors.

- **Reaction trigger** (Tpat=8) points to the existence of nucleon removal nuclear reactions. It requires in addition to good beam, high energy signals - nucleons - in the Crystal Ball plus another into TFW. Unlike events recorded under *Fragment trigger*, the *reaction trigger events* are not downscaled.

- **Neutron trigger** (Tpat=128) is used to select neutron hits in LAND detector in coincidence with a fragment signal in TFW. These neutrons come in many cases from fragment de-excitations (evaporation processes).

- In order to study weakly and unbound nuclei in the neutron deficient part, we use **proton trigger** (Tpat=16). It requires the presence of a proton event, i.e. a forward proton hit in the DTF, in coincidence with a fragment signal in TFW.

Several "off-spill" triggers were also used in the calibration phase. For example, cosmic muons were used for the Crystal Ball and LAND calibrations (*Tbit* numbers 9 and 10 respectively). On the other hand, TCAL and CLOCK triggers are used by the calibration routines. CLOCK trigger is sent regularly in absence of beam and used to determine the pedestal[3] of the charge-to digital-converter (QDC[4]) channels by sampling the data coming from them without physics data. TCAL trigger is sent to the time calibration modules which choose a random time period, sends this time duration to the DAQ to be stored into the LMDs and fixed gates of this duration to every time-to-digital converters (TDCs). The information gained can be used as cross check of the real duration and improve the TDC data calibration.

Figure 1.4 shows an sketch of *land02* software and its different data levels including the reconstruction algorithms - routines - used to determine each calibration parameter. A briefly explanation of each data level is detailed below:

1 RAW: Data are stored as collected by the DAQ provided in units of channels, (12bit,0-4095), for typical ADC- QDC-, TDC systems. The information is ordered by detector, module and channel.

2 TCAL: This is the first step for time and energy calibrations. A slope and an offsetin time signals are obtained by fitting and they are applied to the timing channels whose units are now in ns. For energy signals, the pedestal are subtracted. The routines used are: *clock* and *tcal*.

3 SYNC: This is the second step for time and energy calibration. Some detectors are composed by different detection channels[5]. To treat the detector as a single unit, each detection channel needs to be synchronized with the others. In addition, energies are converted to MeV by applying gain match factors - *Phase1* and *cosmic1* are the routines used to synchronize the signals.

4 DHIT: At this level, we obtain energy loss, position and time values in detector-specific coordinates describing the particle interactions with the material.

[3]small quantity of charge without physical information
[4]At RAW level, since data is provided in units of channels being one of these QDC
[5]For instance, in the case of time-of-flight walls (LAND, TFW, DTF) the channels from each paddle

5 HIT: The unpacked *rootfiles* of this level contain data in laboratory coordinates, positions are given in cm, time in ns and energy in MeV.

6 TRACK: This final level provides the particle identification, i.e. the atomic number (Z), mass-over-charge (A/Z), and velocities of ions are calculated and store in the *rootfiles*.

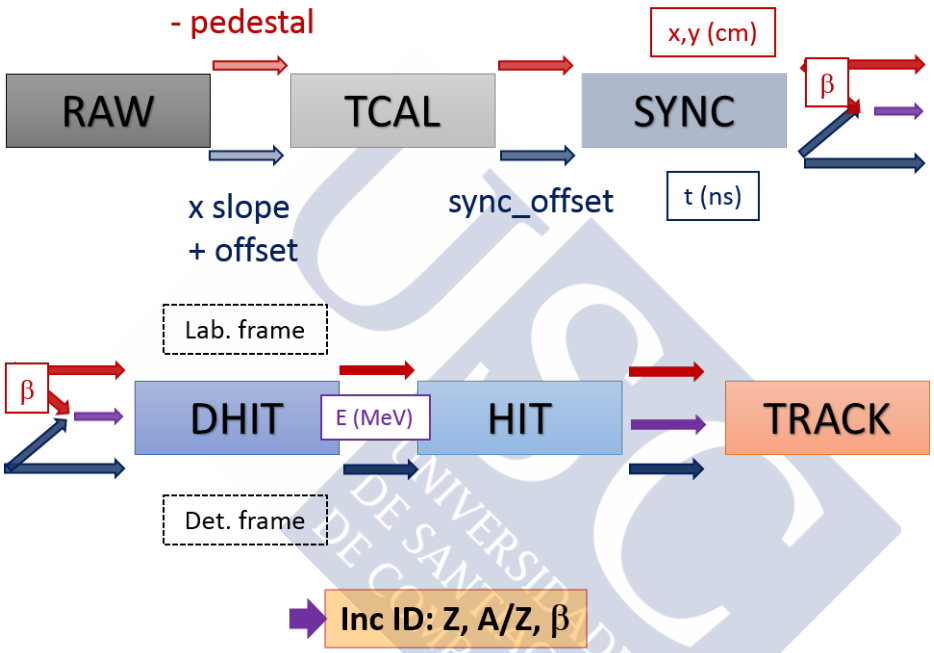

Figure 1.4: The sketch shows the different calibration data levels, starting with RAW level until full identification. Small solid boxes refer to the physical parameters in certain level, whereas the dash-lines boxes are linked with relative coordinate systems, i.e. detector or laboratory frame. At the end of the calibration process - TRACK - , full identification of incoming channel (i.e. Z, A, and velocity) is achieved.

Despite calibrations included in *land02* framework, several cases require additional manual corrections. For example, sometimes the detector information suffers variations along the time. To correct these fluctuations *land02* uses a time variable function, `LT_RANGE` which allows to specify different parameters for different ranges of the data set.

1.3 Incoming Beam Channel

We briefly describe the main characteristics of the detectors used for identifying isotopically the secondary beams and the procedures followed to get it.

Trigger			Signal(s)								
Tbit	Tpat ($=2^{Tbit-1}$)	Description	POS ! ROLU	S8	CB sum	CB OR	Pixel	LAND	Fragment wall	Proton wall	Spill on
1	1	**Minimum bias** (Good beam GB)	✖								✖
2	2	**Fragment** (GB+fragment at the TFW)	✖						✖		✖
3	4	**FRS S8** (plastic scintillator hit)	✖	✖							✖
4	8	**Reaction** (Crystal Ball energy Threshold)	✖		✖				✖		✖
5	16	**Proton** (hit it the DTF)	✖						✖	✖	✖
6	32	**GB-Pile-up** (identification of pile-up)	✖								✖
7	64	**Pixel** (hit in the pixel detector)	✖				✖	+			✖
8	128	**Neutron** (hit in LAND)	✖					✖	✖		✖

Table 1.1: On-spill trigger patterns used during the experiment. Names of the triggers are shown on the left side, while the detectors participating in the trigger generation are marked by crosses on the right area.

1.3.1 Detectors Description

The incoming detectors - located between the entrance of the Cave C and the target area - serve to determine event-by-event the initial state of a nuclear reaction. The cocktail beam provided by FRS needs to be identified in charge and mass. Therefore, the four momentum vector $P_\mu = (E/c, \vec{p})$ should be evaluated for each projectile. Signals of scintillators S8 and POS, Si-pin diode PSP and two Double-side Silicon Strip Detectors (DSSSDs) are used to complete this task.

1. S8 is a paddle like plastic-scintillator detector with dimensions 20.0 x 8.0 x 0.1 cm^3. The time signals are provided by two photo-multipliers placed at both horizontal edges of the paddle.

2. POS, POsition-sensitive Scintillator, (shown in Figure 1.3) is a scintillator of 5x5x0.02 cm^3 that serves as main trigger and time reference. When the incoming beam passes

through the plastic, it produces light which is read-out by four photo-multipliers (held in the edges of the plastic) delivering time and energy signals.

3. ROLU, in German, Rechts-Oben-Lincks-Unten (right-up-left-down). It consists in four movable plastic-scintillators and defines the beam size, acting as veto for any particle hitting these scintillators.

4. PSP, is a Position-sensitive Silicon Pin diode with square shape and an active area of 4.5 x 4.5 cm^2. This detector provides position information (x,y), *via* four-corner anodes (Q_i) read-out in one face (Q) and energy loss ΔE, measured in the cathode. The energy loss measurement is used for the Z-identification through the Bethe-Bloch formula:

$$\frac{dE}{dx} = \frac{4\pi Z^2}{m_e c^2 \beta^2} \frac{N_A Z \rho}{M_u} \left(\frac{e^2}{4\pi\epsilon_0} \right) \cdot \left[ln \frac{2 m_e v^2}{I} - ln\left(1 - \frac{v^2}{c^2}\right) - \frac{v^2}{c^2} \right] \tag{1.2}$$

where E is the energy of the particle, x the distance travelled by the particle, m_e the electron mass at rest, c speed of light in vacuum, v the velocity of the particle, N_A Avogadro's number, e electron charge, ϵ_0 vacuum permittivity, $\beta = v/c$, and I, Z, A, M_u, ρ are the mean excitation potential, atomic number, mass number, molar mass and density of the target respectively. The energy resolution achieved with PSP is around 1%. The position information is obtained by a pixel mask, which in S393 experiment unfortunately did not work properly.

The incoming identification was achieved combining signals from S8 and POS, and PSP. The former detectors provide time-of-flight measurements which are related to isotope mass-to-charge ratio (A/Z), and the energy loss in PSP is linked with the ion charge.

To ensure a clean incoming isotopes selection we added a redundant ion charge identification by using the response of the second striped silicon detector, i.e. energy losses in DSSSD2, the closest to the target (explained in section 1.4).

1.3.2 Projectile Identification

The following steps serve to calibrate in-beam detectors: S8,PSP and POS to accomplish the *Identification Plot* depicted in Figure 1.8.

Incoming Energy Losses Calibration

The charge identification is obtained directly from energy loss measurements in the cathode of the PSP detector. The Bethe-Bloch formulae, Equation 1.2, relates ion-energy losses in a material with its charge. Using a simplification of the energy loss formula, and discarding all correction terms.

$$Z_{proj} \sim \beta_{proj} \sqrt{\Delta E_{proj}} \tag{1.3}$$

where Z_{proj} and β_{proj} are the projectile charge and velocity[6] respectively.
The calibration parameters are obtained using a setting that favours the magnetic selection, $B\rho$, of ions with $A/Z = 2$[7].

Figure 1.5 shows non calibrated energy losses recorded under the *fragment trigger* condition for $A/Z = 2$. Since ^{8}Be is a very weakly bound nucleus[8] the PSP cathode does not record $Z = 4$ signals. Thus, the existence of a *hole* around 600 channel in the ΔE spectrum provides a cross-check for the final identification.

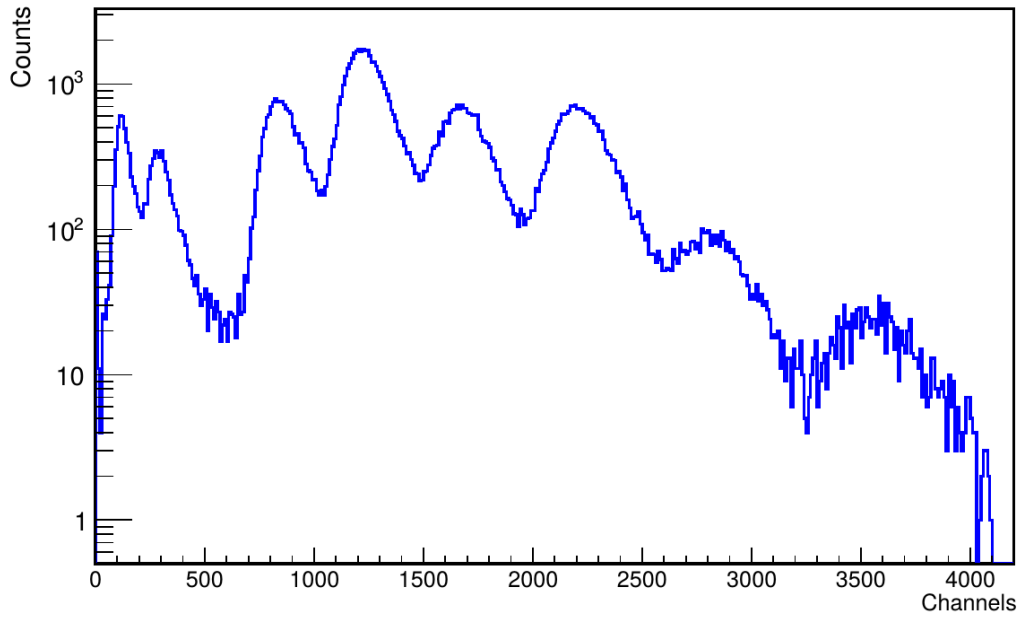

Figure 1.5: Energy losses measured in PSP cathode (un-calibrated channels) are related with the charge of the particles. The *fragment trigger* condition, which requires a good beam plus fragment-signal at the TFW, was selected. The very weakly bound ^{8}Be ($Q_\alpha = 91.84keV$) shown as a hole (∼600 channels) in the energy spectrum that provides an unambiguous normalization for the identification in charge.

To complete the charge identification the peaks depicted in Figure 1.5 are approached to Gaussian distributions. These mean values are used for charge calibrations. The simplified method utilises a linear fit approximation, displayed in Figure 1.6, that restricts the identification range to charges used in the calibration Z=5 − 9; those are, in principle, enough for our analysis.

[6] The natural units, i.e. c=1, $\hbar$ =1 are used
[7] $A/Z = B\rho/\beta\gamma$
[8] $Q_\alpha(^{8}Be) = 91.84keV$

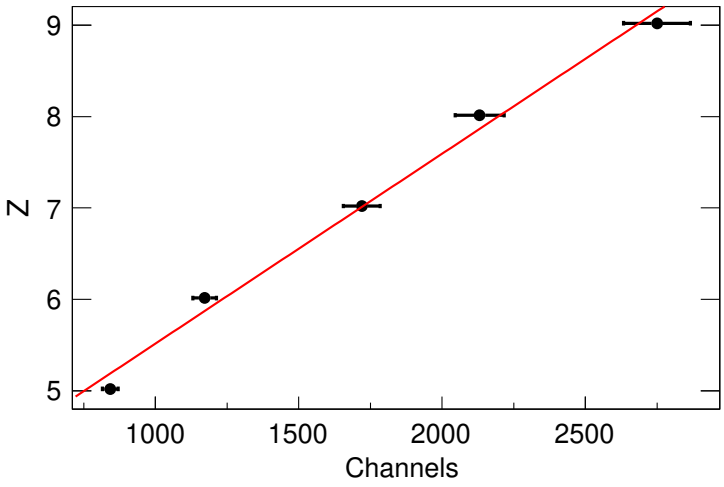

Figure 1.6: Z versus PSP signals (channels) for $A/Z = 2$ run. Signals coming from B, C, N, O and F ions have been used and correspond to the calibration validity range.

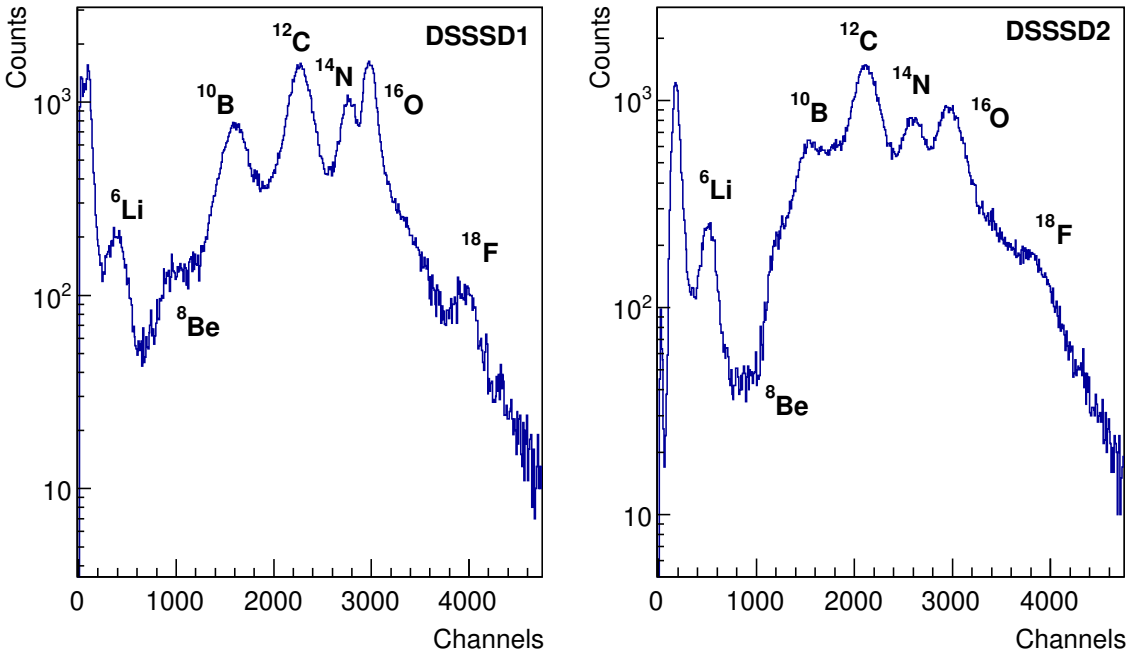

Figure 1.7: Energy loss measured in k-sides of DSSSD1 and DSSSD2 (un-calibrated channels) under the *fragment trigger* condition together with a small window around $A/Z = 2$.

In addition, to perform an accurate projectile identification the redundant energy loss measured in one of the first two in-beam silicon detectors was occasionally used. Figure 1.7 shows ΔE signals in the k-side[9] of first (DSSSD1 - left picture) and second (DSSSD2 - right one) silicon detectors, which have been obtained under a small software gate around $A/Z = 2$ and the *fragment trigger* pattern in order to reduce contamination from neighbouring contributions.

Despite DSSSD1 provides a better resolution (minor straggling and, thus, narrower peaks) than DSSSD2, the second silicon detector is used for being the closest detector to the target, and providing more realistic response.

Incoming Velocity Calibration

In to order to accomplish the mass identification of the incoming ions, their velocity determination is mandatory. For that objective, time-of-flight from time difference signals between S8 and POS detectors are used (time), as well as, the path of the ions S.

$$\beta = \frac{S}{time\cdot} \tag{1.4}$$

The velocity calibration is usually performed using runs with different primary beam energy. However, this procedure could not be applied in this experiment (further details in [27]). Instead, the data set centred around $A/Z = 2$ was used for β calibration. The corrected time difference, δt, between S8 and POS signals is expressed as follow:

$$\delta t = time + time_{offset} \tag{1.5}$$

And combining Equation 1.4 and 1.5 we obtain:

$$\delta t \cdot \beta = time_{offset} \cdot \beta + S \tag{1.6}$$

Plotting $\delta t \cdot \beta$ versus β and reckoning the linear fit parameters we obtain the $time_{offset}$ (slope) and S (offset) ([27]).

With all this information, a complete incoming beam identification is feasible. Figure 1.8 shows an example of projectile identification (Z versus A/Z) of a setting centred at A/Z $\sim$ 2.15, underlying the absence of ^{8}Be ions.

[9]The k-side provides better resolution than the s-side

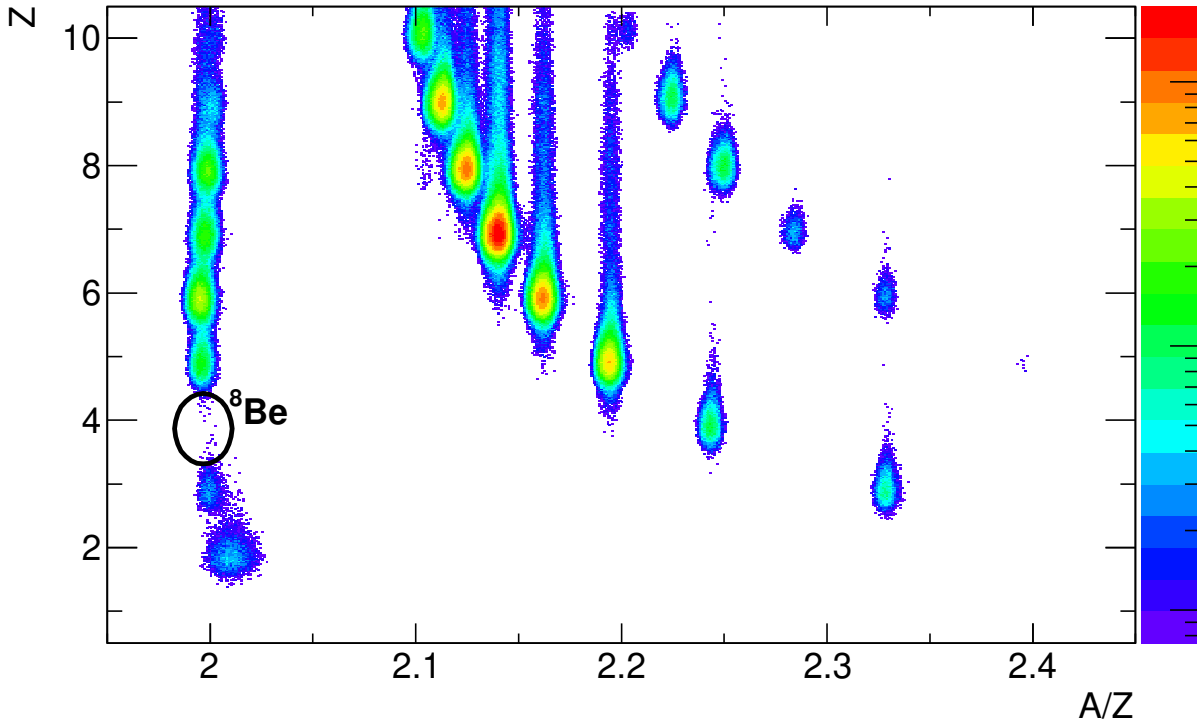

Figure 1.8: 2 dimensional identification plot (Z versus A/Z) of a setting centred at A/Z $\sim$ 2.15. *Fragment trigger* condition is applied. The "unbound" ^{8}Be signal, depicted with a dashed circle, helps us to validate the identification of the rest of nuclei.

1.4 The Reaction Area

The target area is composed by a target wheel, a set of silicon detectors and a multi-array calorimeter. An automatised target wheel allowed for mounting up to 9 different targets of 3 x 3 cm^2. For S393 experiment two materials, polyethylene and carbon with different thickness, were used as main targets. The double-sided silicon strip detectors (DSSSDs) in box-configuration (2 in front, 2 behind and 4 for perpendicular axes) surrounded the target wheel. Both target system and silicon box were inside a reaction vacuum chamber. The 4π spherical calorimeter Crystal Ball (CB) enclosed the reaction chamber.

1.4.1 Target Wheel

As mentioned before, the target wheel could hold up to 9 different targets. In the present work, polyethylene and carbon targets have been used (see Table 1.2). One holder was left empty to allow background measurements.

		Setting1 & 4		Setting 2 & 3	
Target	$\rho(g \cdot cm^{-3})$	w (mm)	$\rho_s(g \cdot cm^{-2})$	w (mm)	$\rho_s(g \cdot cm^{-2})$
$(CH_2)_n$	0.94	0.98	0.92	5	0.46
C	1.87	5	0.94	3	0.52

Table 1.2: Main target characteristics (density, width and superficial density) for different settings.

1.4.2 Double-Sided Silicon Strip Detectors (DSSSDs)

The configuration of DSSSDs used in this experiment is shown on the left side in Figure 1.9. The design is based on detectors developed by the Alpha Magnet Spectrometer, AMS collaboration, which were created for tracking high-energy cosmic rays [43]. Each detector has an area of 7.2 x 4.1 cm^2, and of 300 μm thickness. They have two sides, each one contains strips in perpendicular direction to each other and allow precise position measurements.

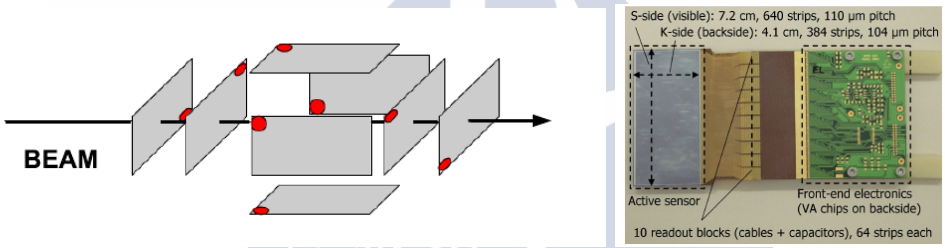

Figure 1.9: Left figure: depicts the silicon detectors configuration in S393 experiment. Red marks show the coordinates origin, i.e. where the first strip is located. Right figure shows a photography of a single silicon strip sensor (taken from [28]). There are 640 vertical (long side) plus 384 horizontal (short side) readout strips. The in total 1024 strips are grouped in 10 (visible) plus 6 (rear side) blocks of 64 read-out lines each, which are capacitive to 10+6 VA-chips with pre-processing on the front-end board.

The long edge side called "S-side", has an implantation pitch of 27.5μm and a read-out pitch of $d_S = 110\mu$m. The number of strips in this side is 2560, being every fourth strip connected to a read-out channel, leaving the rest of the strips floating; as a result we have 640 read-out channels. The charge collection of the floating strips is achieved by capacity coupling of the strips, thus improving the position resolution significantly over the read-out pitch of 110 μm. The other side, "K-" which corresponds to the shortest dimension, 40 mm length; has a read-out pitch of $d_K = 104\mu$m with each of the 384 strips being read-out. The number of strips being read-out in every DSSSD is 1024.

Four detectors were located in the beam direction, whereas the other four were surrounded the target conforming a "silicon box" (see left picture in Figure 1.9).

The first couple of two in-beam detectors (following named DSSSD1 or SST1 and DSSSD2 or SST2) are commonly used for charge identification of incoming ions. The other two in-beam silicons (DSSSD3 or SST3 and DSSSD4 or SST4) were placed at 10 and 13 cm downstream the target wheel and allowed us tracking (angles and positions) the outgoing products. In addition, they could identify in charge the products such as heavy fragments and protons *via* energy loss measurements.

The aim of the four box-detectors was to track (angular measurements) protons and neutrons scattered coming from Quasi-Free Scattering reactions. However, due to internal malfunctions, their signals could not be used in this work.

Calibration of Silicon Detectors

The calibration of the in-beam double-side silicon strip detectors has been meticulously studied in [23, 22, 28].

It consists in, at least four sequential steps which are presented briefly. Despite each side is calibrated separately, the procedure followed is always similar. ADC signals from an individual read-out silicon strip are given by:

$$S_{ADC} = \sigma_{ped} + \sigma_s + \sigma_{va} + S_p \tag{1.7}$$

where, σ_{ped} and σ_s are the pedestal[10] and the strip noise[11], σ_{va} is related with the coherent noise of the VA-chip and S_p is the energy loss measurement in the silicon volume.

The calibration procedure uses a *land02* routine (*clock*) to determine strip pedestal and the strip noise in "off spill" conditions.

We identify several anomalous cases: "dead" strips (provide no signals); "noisy" strips (large sigma σ_s); different gains for each strip (reduced energy resolutions and distorted positions).

The energy measurement should be corrected at least two times due to the fact that calibration procedure is a self-consistent method, which depends on the hit position (this correction is also dependant of the energy). Additionally, the silicon response during whole S393 experiment was assumed stable.

Depending on the charge of the hitting particle (and, also, what side is considered), different number of strips are fired. The size of strip-cluster, called "base-width", which is determined by the range of the overall energy signal, is not greater than 3 strips for a proton events, increasing up to 6 strips for Z=8. Therefore, the total charge deposited in the detector, Q is the cluster sum, combining strips within signals above $3\sigma_s$ and they are stored at SYNC level. Performing the sum over any strip (numbered N_i), in a cluster

[10] A small quantity of charge read by QDC even when no signal is registered.

[11] standard deviation of pedestals.

(from a, first strip, up to b, last strip), the total energy loss can be calculated;

$$E = \sum_{a}^{b} e_i \tag{1.8}$$

The information related to the position is obtained from charged-weighted centre of gravity, CoG:

$$X_{CoG} = \frac{\sum_{i=a}^{b} S_i N_i}{\sum_{i=a}^{b} S_i} \tag{1.9}$$

where both sums cover from the first up to last strip of the cluster, S_i is a signal in individual i-th strip (after pedestal and noise correction) and N_i strip number. Then, the hit position is given by multiplying the CoG for the strip read-out pitch size[12]:

$$X_{S,K} = p_{S,K} \cdot X_{CoG} \tag{1.10}$$

The next step it to correct for the presence of "floating" strips, named because these strips are no read-out, and influence the reconstructed cluster sum. The impact parameter characterises the "inter-strip" position of the hit, as follow:

$$\eta = X_{CoG} - int(X_{CoG}) \quad \text{with} \quad \eta \in [0, 1] \tag{1.11}$$

approximately in the centre of the read-out strip, and $\eta \simeq 1$ is related to the next read-out strip. An "inter-strip", $\eta \simeq 0.5$, corresponds to a intermediate read-out shared by two strips. As it has been mentioned before, the dependence on the position of the hit within the read-out gap can be corrected using the normalised η distribution $f(\eta)$:

$$X_\eta = X_1 + p \int_0^\eta f(\eta) d\eta \tag{1.12}$$

where X_1 is the central strip position in a cluster (the integer part of the CoG) and p is the read-out strip pitch. Due to the charge-dependence in η, this position correction should be applied into the vicinity of interesting charges, in the current analysis Z=8 and, it remains valid up to $\Delta Z = \pm 2$.

A dead strip does either not deliver any signal (after pedestal and noise subtraction) or those signals sent are too low to be detected (below threshold). There is a non zero possibility of obtaining fake reconstructed clusters because of the presence of dead strips into previous position algorithm. To prevent undesired effects, dead strips are identified and removed from the cluster finding algorithm.

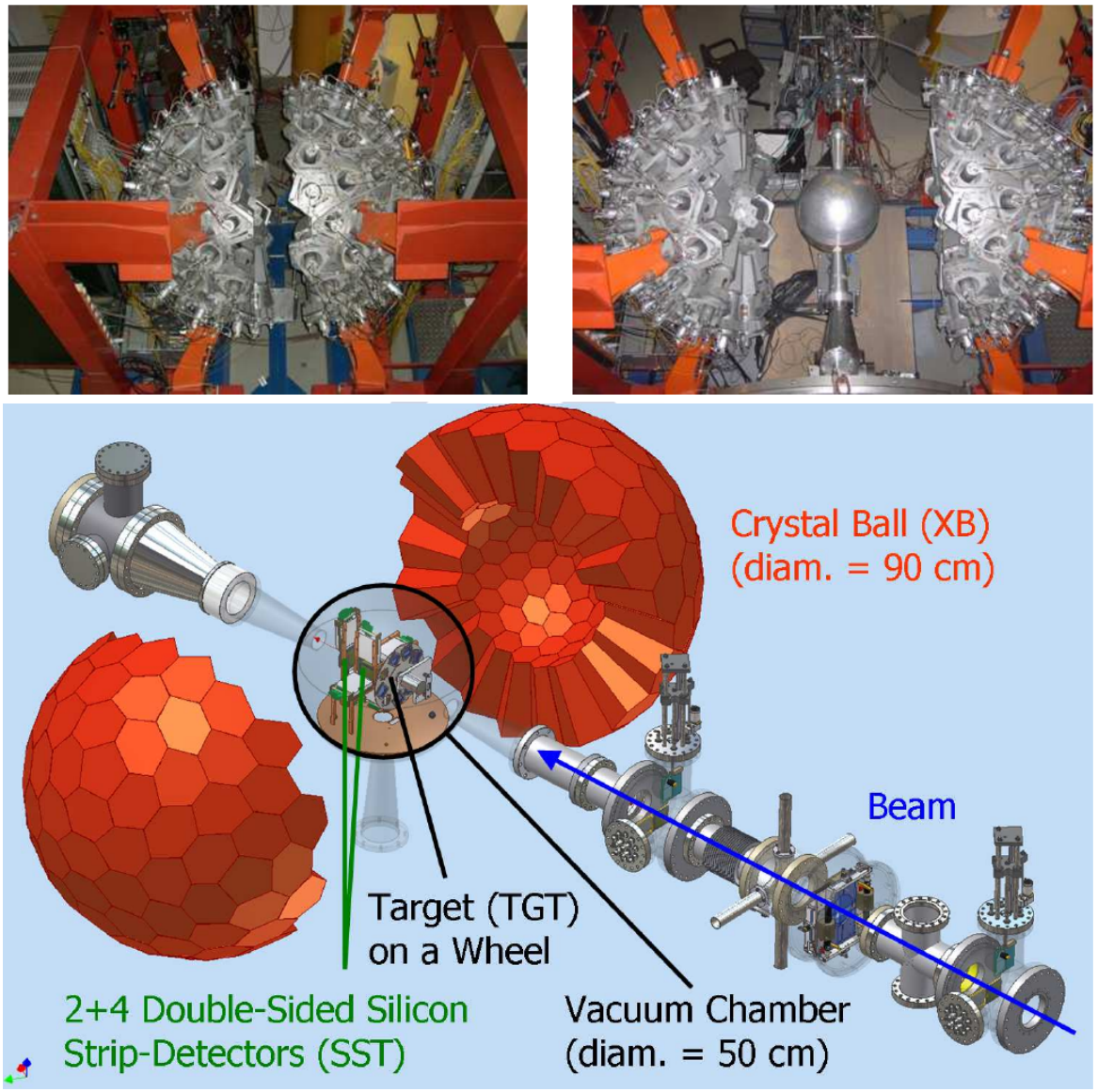

Figure 1.10: Top two photographs of Crystal Ball partly (left image) and fully opened (right one) with the vacuum chamber installed. Bottom: Schematic view of Crystal Ball calorimeter. Beam is entering on the right side, impinging to a target placed onto target wheel (TGT). Neutrons, protons and γ-rays produced by the nuclear reactions in the target and the de-excitation of outgoing fragments respectively can be measured by the calorimeter. Photographs and sketch of the Crystal Ball calorimeter are taken from [22].

1.4.3 Crystal Ball (CB)

Crystal Ball is a 4π calorimeter used for the detection of γ-rays emitted by the fragment de-excitation. It can also detect light scattered particles - protons and neutrons resulting after reactions in the target (see Figure 1.10).

The detector is compound of 162 thallium-doped sodium iodide crystal [44] which surround the target chamber. Each crystal has a length of 20 cm, they are wrapped by an aluminium skin of 600μm. In S393 experiment, only 159 crystals were used. This configuration allowed to free the space necessary for the beam pipe.

To reach the maximum angular coverage, crystals have four different shapes, i.e. regular pentagons and three different irregular hexagons, each covering a solid angle of approximately 77 msr (for further information see [22] and references therein). The high granularity of the calorimeter allows the determination of outgoing angles and the application of the Doppler correction for the γ-rays.

The scintillation light produced by the interaction of γ-rays or light charged particles with NaI(Tl) is converted to electric signals by photomultiplier tubes (PMTs). In particular, for S393 experiment, we implemented dedicated electronics in 64 crystals located in the forward hemisphere. This arrangement was based on the splitting of signals to cover adequately the energy range of both high-energy particles (protons and neutrons) and γ-rays.

This ensure an additional read-out branch in front of the last amplification stage of the PMTs obtaining signals 15 times higher than the ones from the normal branch.

The whole detector is mounted on a structure which allows to move the two hemispheres of the detector individually using guides, the two photographs in Figure 1.10.

Crystal Ball (CB) Calibration

The energy calibration of γ-rays and proton read-out was made using different radioactive sources and cosmic muons.

In S393 experiment three γ-sources were used: ^{22}Na, ^{88}Y, and ^{60}Co. The channels of each crystal were related to energy of γ- peaks of Na and Co. While, proton read-out calibrations were performed using cosmic muons. In this analysis previous calibrations have been taken from [22, 27].

1.5 Outgoing Particles Identification

Leaving the target area, the reaction products and the un-reacted beam passed through the dipole magnet ALADIN. The strong magnetic field of ALADIN deflected the charged particles according to their mass-to-charge ratio, and led them into different detection branches.

[12] That is 104 μm for K-side and 110 μm for S-side

The angular acceptance of ALADIN is ±60 mrad and the maximum current undertaken by the magnet is 2500 A. It is worthy to note that a current above 1900 A produces saturation effects which become important and not negligible, being the relation between magnetic field and current not linear.

1.5.1 The Neutron Arm

The Large Area Neutron Detector, LAND [45] was designed to measure neutrons with energies from 100 up to 1000 MeV, with an efficiency above 94% for $E_n \geq 400$ MeV. Neutrons are not affected by the magnetic field of ALADIN and, thus , they flew straight and hit the LAND detector. It served as time-of-flight spectrometer and allowed to determine velocity and positions (in X,Y,Z) of the neutrons.

LAND was placed at 0^0 in-beam direction and, approximately, 13 m behind the target. The detector has 200 paddles organised in 10 planes each one of which is formed by 20 plastic scintillator paddles. The paddles of consecutive layers are perpendicular to each other in order to measure horizontal and vertical hit positions. At the end of each paddle we localised two photomultipliers, used to read-out purposes. Notice, LAND was only marginally employed in this analysis, taking the calibration parameters from [27].

1.5.2 The Fragment Arm

Heavy reaction fragments, with $A/Z > 1.6$, were bent towards *the fragment arm*, which was centred at 16.7^o with respect to the incoming beam axis. This branch consisted of two fibre detectors used for position and energy loss (related to isotopic masses) measurements followed by a plastic time-of-flight wall (TFW) (see red arrow in Figure 1.3).

GFI, Grosse Fibre Detektor

The *Gross Fibre Detektors*, GFIs, provide horizontal position measurement with high accuracy ($\sim$ 1mm) and a geometrical efficiency of 89% for Z$\geq$3. This efficiency becomes significantly lower for lower charges [46].

The GFIs were placed 3 and 5 m behind the centre of the ALADIN. Each GFI consists of 475 vertical 1 mm wide and 50 cm long scintillating fibres that cover an active area of approximately 50 x 50 cm^2. Each fibre has an optical coat to guide the light and to avoid cross talk. Each end of fibre is connected to a photo-cathode in a position sensitive photomultiplier (PSPM) using a mask (further information can be found in [47]). The PSPM is a photo cathode with an area of 64 x 58 cm^2 mesh-type dynode and a rectangular anode grid with 18 and 16 wires in the X and Y direction respectively.

The fibres are organised in a 20 x 25 matrix, showed in the Figure 1.3, (fragment arm). The distances between rows and columns are 2.2 mm and 3 mm respectively.

When a charged particle passes through the active area of a GFI, scintillation light is produced proportional to the energy lost in the detector. This light was guided to the mask producing energy signals in one (or more) of the 475 fibres which are used to reconstruct positions.

Initially, the pedestal signal is subtracted using routines inside *land02* at TCAL of a higher calibration level.

Since the amplitude of the signals depends on their amplification, which is usually different for each case, and, it is position-dependant of the photo-cathodes, it becomes necessary to perform the gain-match for all anode wires previous to reconstruct the position-hit.

The charge distributions in the 18 x 16 anode wires are used to determine the position (u,v) of the light spot on the photo-cathode, with sub-wire resolution. The internal coordinates (u,v) of the GFIs are in turn converted to laboratory coordinates, (x,y). We make use of "sweeping-run"[13] for illuminating the full detector area. Thus, all light spots corresponding to the fibres can be reconstructed accurately. We made use of another *land02* internal routine (*phase1*) to unpack the data at DHIT level.

Once the gain-matching for the clusters is performed, the (x,y) positions are well-defined and they are given in *cm* at HIT level.

TFW, Time-of-Flight Wall

The Time-of-Flight Wall was situated behind the two fibre detectors, and was used to determined the charge *via* energy loss measurements, and to reconstruct the heavy fragment velocity (β) via time-of-flight measurements between PSP/DSSSD3 and TFW. The TFW is made of two crossing (x,y) planes of double-end read-out plastic scintillator paddles. It is formed by 32 scintillator modules-paddles, 18 horizontal and 14 vertical, arranged in two layers perpendicular to in-beam direction. The total size of the TFW is 147 x 189 cm^2 (see Figure 1.3). The paddle thickness is 0.5 cm and the width is 10.4 cm, and, has two photomultipliers on both ends for read-out (further information can be found in [22, 27] and references therein).
The TFW can measure the position of the heavy fragments within 5 cm of resolution, their time, depending on isotopes, with $\sim$ 30 ps; and identify their charge via energy loss measurements.

Plastic Scintillator Detectors Calibration (TFW and DFT)

Heavy fragment and proton arms share similar made-of detectors: their final detectors. The TFW and the DTF respectively are composed of several plastic scintillator

[13] This kind of runs allowed a complete illumination of all the detectors thanks to the field variations of ALADIN magnet

paddles and their calibrations are described together following.

Each plastic scintillator paddle has two photomultiplier tubes read-out on both edges which provides time and amplitude information (see Figure 1.11). Time is measured by time-to-digital converter (TDC) whereas amplitude is given by a charge-to-digital converter (QDC).

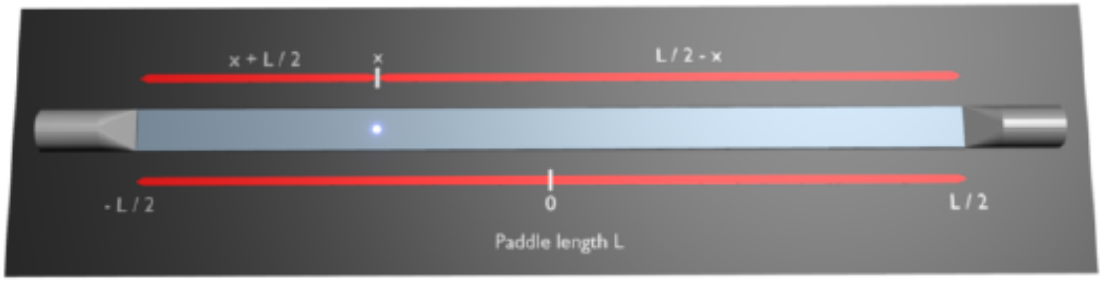

Figure 1.11: Hit of a particle - white dot - in a scintillator paddle. There are two photomultiplier tubes connected at each ends (Picture taken from [21]).

The measured time and energy in the left (t_L, e_L) and in the right (t_R, e_R) sides can be expressed as follow:

$$t_L = t_0 + \frac{1}{v_{light}}\left(\frac{L}{2} + x\right) \tag{1.13}$$

$$t_R = t_0 + \frac{1}{v_{light}}\left(\frac{L}{2} - x\right) \tag{1.14}$$

$$e_L = E\left[-\left(\frac{\frac{L}{2} + x}{\lambda}\right)\right] \tag{1.15}$$

$$e_R = E \cdot exp\left[-\left(\frac{\frac{L}{2} - x}{\lambda}\right)\right] \tag{1.16}$$

where t_0 is the interaction time, v_{light} is the effective light velocity in the scintillator, L is the total paddle length and x is the hit- position. Moreover, E is proportional to the deposited energy at the interaction point x, and λ is the light attenuation length characteristic of the scintillator material. The time and the amplitude, E energy loss, of the interaction are expressed using both measurements:

$$t_0 = \frac{t_L + t_R}{2} - \frac{L}{2v_{light}} \tag{1.17}$$

$$E = \sqrt{e_L e_R} \cdot exp\left[\frac{L}{2\lambda}\right] \tag{1.18}$$

Therefore, ideally, the interaction position x can be calculated:

$$x = v_{light}\left(\frac{t_1 - t_2}{2}\right) \tag{1.19}$$

$$x = \lambda\left(\frac{\ln e_R + \ln e_L}{2}\right) \tag{1.20}$$

Considering the analogue-digitization process, the cable lengths, signals losses, and processing times, a realistic time measurement in ns ($t_{L,R_{cal}}$) can be displayed as:

$$t_{L_{cal}} = t_L \cdot \alpha_{t_L} + t_{diff} + t_{sync} + t_{L_{cal}} \tag{1.21}$$

$$t_{R_{cal}} = t_R \cdot \alpha_{t_R} - t_{diff} + t_{sync} + t_{R_{cal}} \tag{1.22}$$

$$\tag{1.23}$$

where $t_{L,R}$ are related to the raw time in channels; $\alpha_{t_{L,R}}$ are the time-calibration slope constants due to time-to-digital conversion whereas $t_{L,R_{cal}}$ are the offsets; t_{diff} is the time offset to synchronise the two photomultipliers of the each paddle and t_{sync} is the time-synchronisation offset for all the paddle in the same detector. Otherwise, for energies measured, the calibrated amplitudes $e_{L,R_{cal}}$ in MeV as expressed as:

$$e_{L_{cal}} = (e_L - e_{L_p}) \cdot \alpha_{e_L} \cdot \frac{e_{sync}}{e_{diff}} \tag{1.24}$$

$$e_{R_{cal}} = (e_R - e_{R_p}) \cdot \alpha_{e_R} \cdot e_{sync} \cdot e_{diff} \tag{1.25}$$

where $e_{L,R}$ represent the raw amplitudes in channel units; e_{L,R_p} are their pedestal; $\alpha_{e_{L,R}}$ are factors converting channels into energy units; and e_{diff} and e_{sync} are the analogous to t_{diff} and t_{sync}, for enough signals.

1.5.3 The Proton Arm

Finally, the experiment includes a branch focussed on detecting protons. The proton arm was located at approximately 31^0 with respect to centre of ALADIN allowing the light particle detection with a magnetic rigidity of $A/Z = 1.008$, lower than heavy fragments (see light-blue arrow in Figure 1.3).

Protons traversed two Particle Drift Chambers (PDCs), used for tracking calculations and they were registered in a time-of-flight wall (DFT, from German *Dicke ToFwand*), which determines their velocities and works for triggering purposes.

PDCs, Proton Drift Chambers

The PDCs are located at 2.5 and 3.5 m behind centre of ALADIN, see in Figure 1.3. Each detector consisted of two orthogonal planes of gas filled[14] wires covering an active

[14] 20/80 CO_2/Ar mixture

area of 100 x 80 cm ^{2}. Each individual cell has a diameter $\sim$16 mm and is read-out *via* one sense wire in its centre. In the widest direction, X-axis, there were 144 sense wires, while in the perpendicular direction, Y-axis, 112 wires. In total, one PDC detector had 256 read-out channels.

When a charged particle, for instance a proton, passes through a PDC, within each plane it causes ionisation avalanches towards the closest sense wires. From the measured time, over threshold on each of the two wires, the exact positions of the proton track between is reconstructed. A spatial resolution of 200 μm can be achieved for protons.

Monte Carlo simulations are used to estimate the intrinsic resolution of the straggling, $\Delta p/p \sim 3\ x\, 10^{-3}$ [21].

DFT

Behind the PDC, protons were registered in a large area plastic scintillator wall used also as trigger (see Figure 1.3). The proton ToF wall was placed at 8 m behind ALADIN centre (10.5 m with respect to reaction target), and it consists of 6 vertical paddles (20x120x1.5 cm^3) and 3 horizontal paddles (10.4x140x0.5 cm^3) which are separated around 44 cm. All paddles have photomultipliers on both sides - read-out. The detection principles are the same as for other detectors based on scintillators paddles.

Chapter 2

Analysis Techniques and Physical Observables

This chapter compiles the techniques and procedures used to extract physical information from the data, as well as the formalism applied to construct our physical observables.

We start showing the identification of particles involved in the reactions, i.e. projectiles and outgoing products.

Incident projectiles are selected from the cocktail secondary beam applying charge (Z) and mass (A) software gates.

The identification of the outgoing particles is carried out via a *tracker routine*. This program calculates the trajectory for a given outgoing charge selection from the measured positions and $B\rho$ values of the ALADIN magnet. In some cases, these fragments can de-excite emitting protons or neutrons. The proton velocities and trajectories can be also evaluated using detectors located in the proton arm. At the same time, neutron energies can be determine in LAND.

In addition, light particles coming from the nuclear reaction, such as neutrons protons and, as well as γ-rays emitted by projectiles; could be detected by the 4-π the Crystal Ball calorimeter.

Next, we describe the formalism to evaluate different reaction cross sections for polyethylene, carbon and proton targets. Evaluations of the relative detection efficiencies for several different conditions have been performed and they are included *via* correction factors.

Nucleon (proton and neutron) removal - (p,X) - , and Quasi-Free Scattering (QFS) - both (p,2p) and (p,pn) channels - reactions are studied in detailed and their corresponding fragment momentum distributions are derived.

2.1 Incoming Projectiles Selection.

The charge, (Z), and the mass-over-charge ratio, (A/Z), measurements are used to identify and select the projectile of interest from the secondary cocktail beam that leaves the FRS. We combine the information from different in-beam detectors. PSP cathode signals provide energy losses, which are proportional to the charge; and time of flights, evaluated between S8 and POS scintillators, are related to A/Z. Since we work with high energy beams, differential energy losses per thickness dE/dx though PSP can be assumed to be constant.
Figure 2.1 shows 2-dimensional identification histograms where charge versus mass- over-charge ratio is depicted. Four different $B\rho$ selections of the FRS (named settings and summarise in Table 2.1) have been considered, covering completely the oxygen chain.

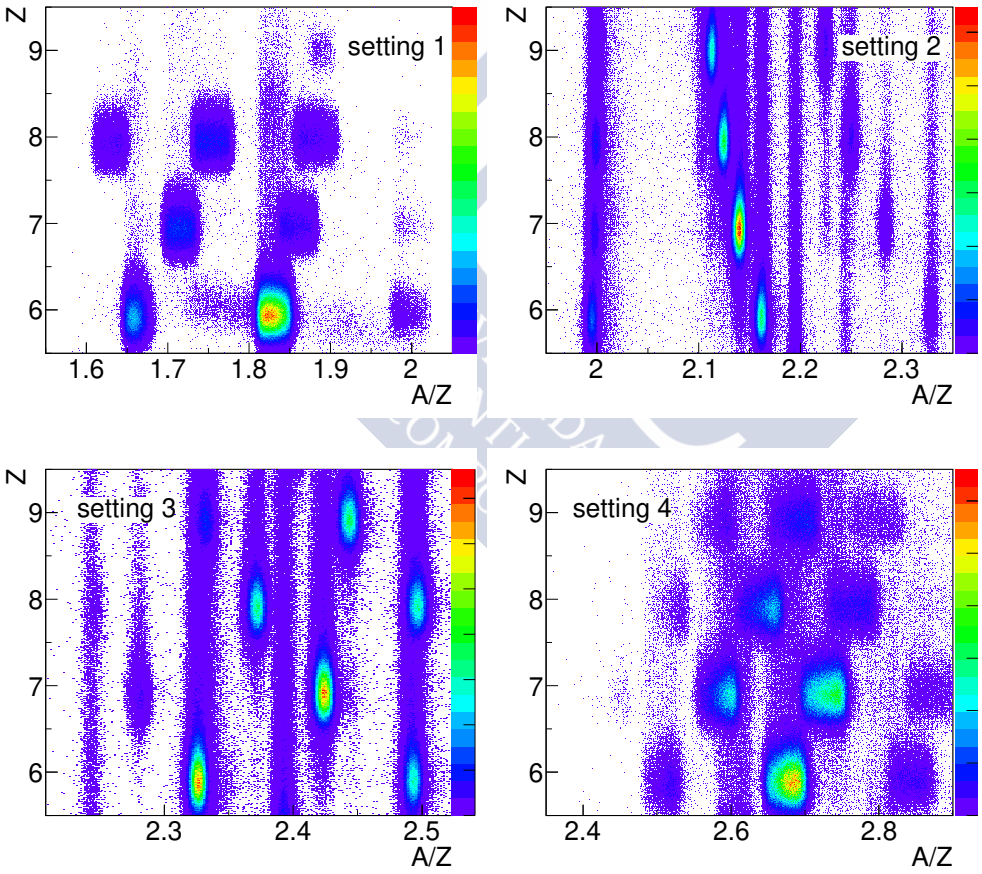

Figure 2.1: 2-Dimensional incoming identification plots are displayed for four $B\rho$ configurations, settings 1, 2, 3, 4 which are centred in ^{14}O,^{17}O,^{19}O,^{22}O, respectively (see Table 2.1). The fragment trigger condition and zoom-in are applied showing the region of interest.

These configurations (settings) were respectively centred in ^{14}O,^{17}O,^{19}O,^{21}O.

setting	centred at	$B\rho$ (Tm)	C thickness (mm)	CH_2 thickness (mm)
1	^{14}O	5.2813	5	9.81
2	^{17}O	6.9105	3	5
3	^{19}O	8.123	3	5
4	^{22}O	9.0502	5	9

Table 2.1: Main setting characteristics used in the current analysis.

Charges are accurately calculated with a resolution of $\Delta Z/Z \sim 0.01$ [48]. A/Z values present lower resolution $\frac{\Delta(A/Z)}{A/Z}$, particularly for setting 1 and 2 and they oscillate around the expected value for each case producing ovoid-shapes instead of perfect dots. Since we deal with relatively light species, the limited A/Z resolution does not have a critical effect on the incoming projectile selection.

Figure 2.2 depicts the Z and A/Z projections (left and right histograms) corresponding to settings centred in ^{17}O (setting 2). We have performed a Gaussian fit for each incoming charge and calculated the associated mean and sigma values. In order to achieve a clear A/Z selection, we have applied the obtained charge conditions to extract the mass-over-charge parameters.

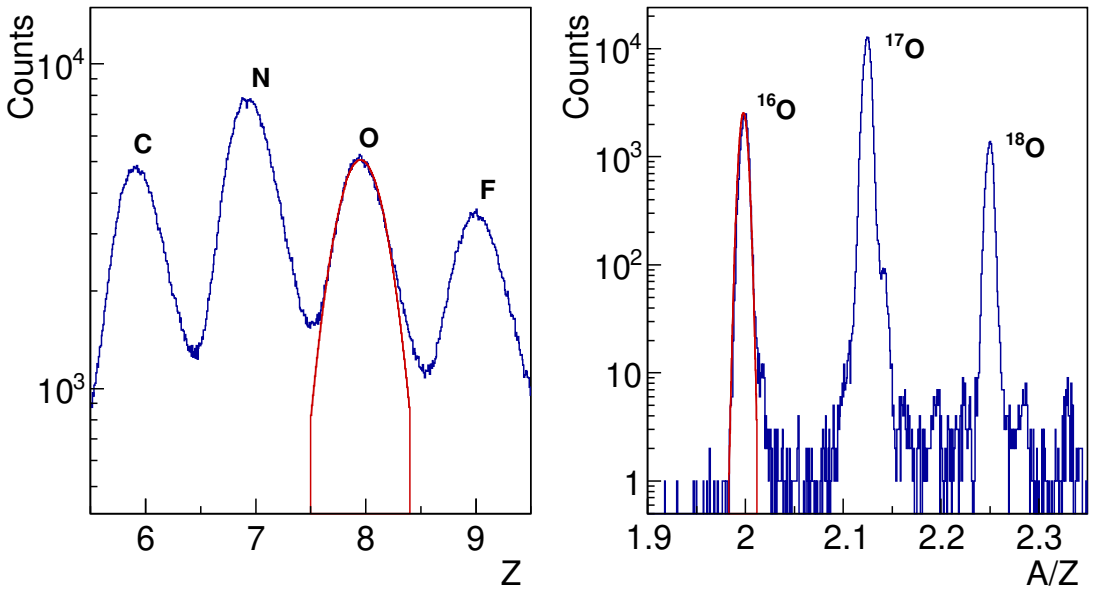

Figure 2.2: Example of a projectile selection in a setting centred on ^{17}O. The left histogram depicts a Z projection and the right one shows a A/Z projection for oxygen isotopes, where a condition in charge is applied, under the *fragment trigger*. The Gaussian fit (red lines) is used to obtain parameters serving to define conditions applied to achieve a proper incoming selection.

Usually, a signification of 2 σ around the mean value generates clean projectile selection. However, to prevent neighbouring contamination from closer isotopes we have performed systematic variation in the Z and A/Z software gates to determine the optimum selection.

Additionally, the fragment trigger pattern condition is applied[1], together with an extra condition in the energy loss signals measured in one side of the second silicon detector[2] to have a redundant charge determination. These conditions ensure that contamination from neighbouring isotopes are reduced to minimum.

Notice that all calibrations have been done for charge Z=8, which remains stable up to 2 unit variations in Z. For that reason we could extend the analyse to nitrogen projectiles with the same calibration parameters.

2.2 Outgoing Fragments Selection.

Once projectile selection is achieved, we proceed with the isotopic identification of the outgoing fragments. We follow a step process that determine in first place the outgoing charge, and then, the isotopic mass of the fragments for each previous charge selection *via* a tracking procedure.

2.2.1 Outgoing Fragment Charge Identification

The first selection for outgoing fragments corresponds to charge, determined *via* energy loss measurements in both silicon and TFW detectors. The in-beam silicon detector located immediately after the target (DSSSD3) and, more precisely, its k-side, which provides the most accurate response, is chosen.

Figure 2.3 displays ΔE measurements recorded in TFW versus DSSSD3 for a selection of ^{16}O projectiles. *Fragment trigger* was used to determine un-reacted beam contributions (left histogram) whereas *reaction trigger* was applied to measure ΔE in removal channels (right one). Diagonals in these plots correspond to those fragments that have same charges in silicon and in TFW detectors, whereas particles with lower charges in TFW than in silicon left appear in the vertical lines.

2.2.2 Outgoing Fragment Mass Identification

Once achieved the charge identification of the fragments, we combine - for a fixed outgoing charge - the position information of particles recorded in silicon, GFI and TFW

[1] All events have reached the final TFW detector and, thus, the relative efficiency between detectors is cancelled.

[2] The k-side of the closest detector - DSSSD2 - to the target was used to impose the extra-charge condition.

detectors to determine the associated trajectory and assign the corresponding momentum.

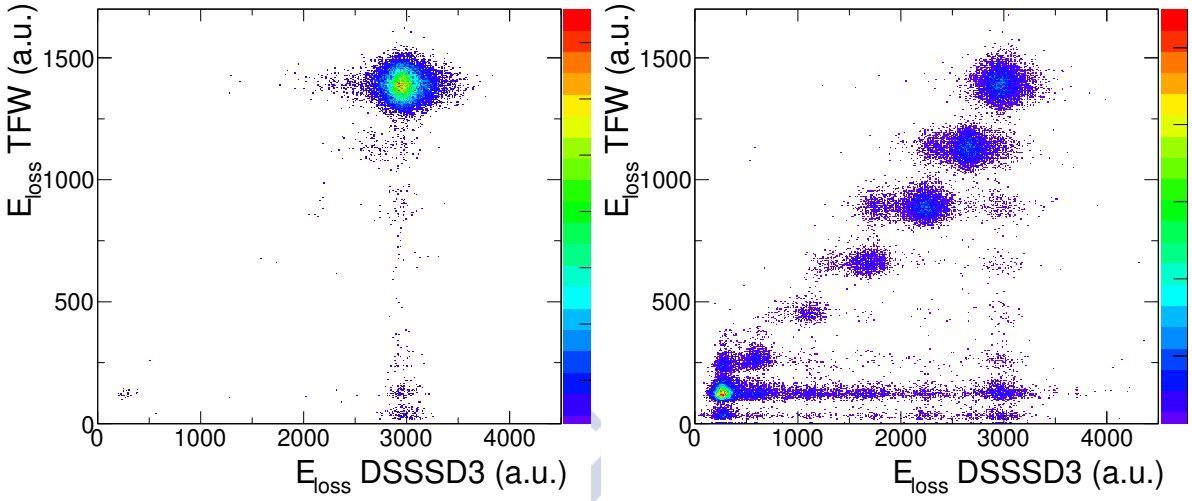

Figure 2.3: Energy loss measurements in the k-side of DSSSD3 versus energy losses in TFW for a ^{16}O projectile selection. Axes are in arbitrary units, and charges range from 2 to 8. For left picture the *fragment trigger* is applied - main contribution comes from un-reacted beam, whereas for the right one the *reaction trigger* is used to determine reaction fragments - removal channels.

The tracker routine calculates all feasible trajectories of the fragments from target to the end of the path - TFW for heavy fragments or PDC for protons. It uses an iterative process based on Runge-Kutta minimisation method that assigns momentum and mass for any fragment with a given Z [23, 24, 42].

The mass-over-charge ratio is determined using the equation 2.1.

$$B\rho = \frac{A}{Z}\frac{m_0 c}{e}\beta\gamma \tag{2.1}$$

The tracking procedure uses an initial mass (m_0) and the projectile velocity to reconstruct a trial trajectory. Initial masses are taken from data evaluation tables [49], whereas velocities β are evaluated between S8 and DSSSD3 using time of flight measurements.

In addition, the tracker takes the position measurements recorded in the in-beam silicon and TFW detectors. Signal hits from GFIs can be used to verify this step.

The initial mass is modified until we get a particle trajectory matching with the silicon position measurements, and the projectile velocity, β, is corrected with the outgoing fragment time of flight coming from ToF Walls. The process continues until user reaches the desired level of accuracy.

The un-reacted beam, depicted in Figure 2.5 (left) for ^{16} O projectiles, is employed to detect those events that have survived after collision with the target. This value amounts for ∼95% of the total incoming nuclei. The large value shows that the associated reaction probability is low, as it corresponds to thin targets and very energetic beams ($\beta \sim 0.75$), and allows to use the un-reacted events as the total number of incoming projectiles. We can determine the total incoming particles more accurately considering the contribution of all reacted fragments that were tracked together with un-reacted beam events. The result increases of roughly 3% more events.

The relative difference between all fragments tracked (included un-reacted beam) and just for un-reacted ^{16} O projectiles is:

$$\frac{n(allfrag) - n(unreacted)}{n(allfrag)} \cdot 100 = (2.81 \pm 0.09)\% \tag{2.2}$$

This procedure presents a clear benefit since it involves final trajectory detectors for counting both incoming and outgoing events, and, thus geometrical and intrinsic detector efficiencies are cancelled, reducing systematic uncertainties in the cross section calculation.

Complementary, Figure 2.4 displays horizontal GFI position measurements for a ^{16}O projectile selection on a polyethylene target. These pictures confirm the correct calibration of the tracker routine.

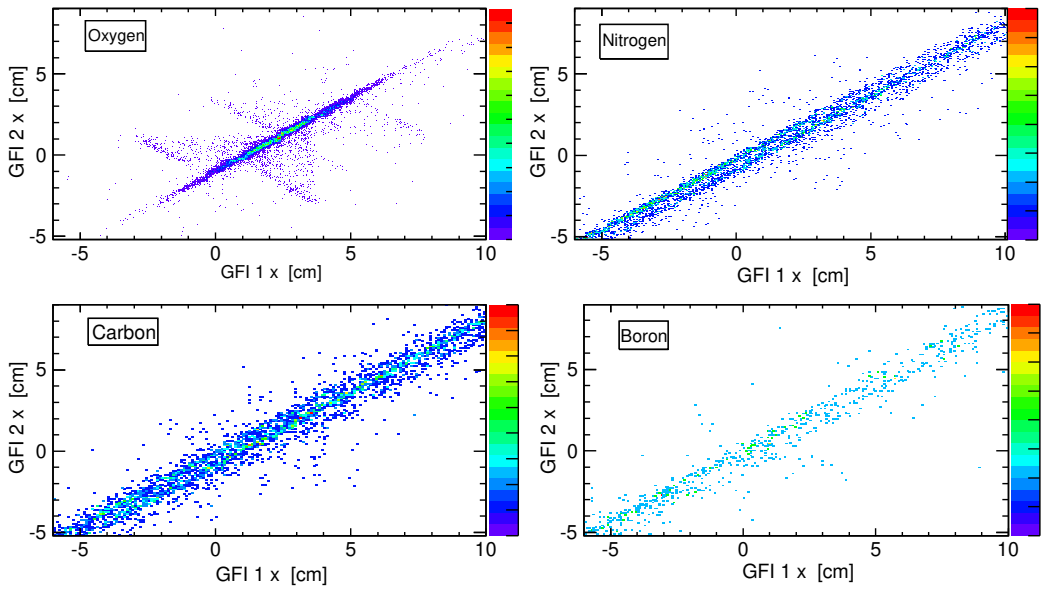

Figure 2.4: Horizontal position measurements (x versus y axes) in one of GFIs versus another for a ^{16} O projectile selection and for different outgoing charges: oxygen, nitrogen, carbon and boron isotopes.

2.2.3 Fragment-Mass Cut

The physical observables can be constructed once the isotopic identification of the recoil fragments is performed. We follow with ^{16}O projectiles on a polyethylene target as example of isotopic identification depicted in Figure 2.5. We observe on its left side, a 2-D fragment identification under *fragment trigger* condition, and on the right side the 2-D histogram is obtained under *reaction trigger* pattern and corresponded to all fragments produced in the reaction.

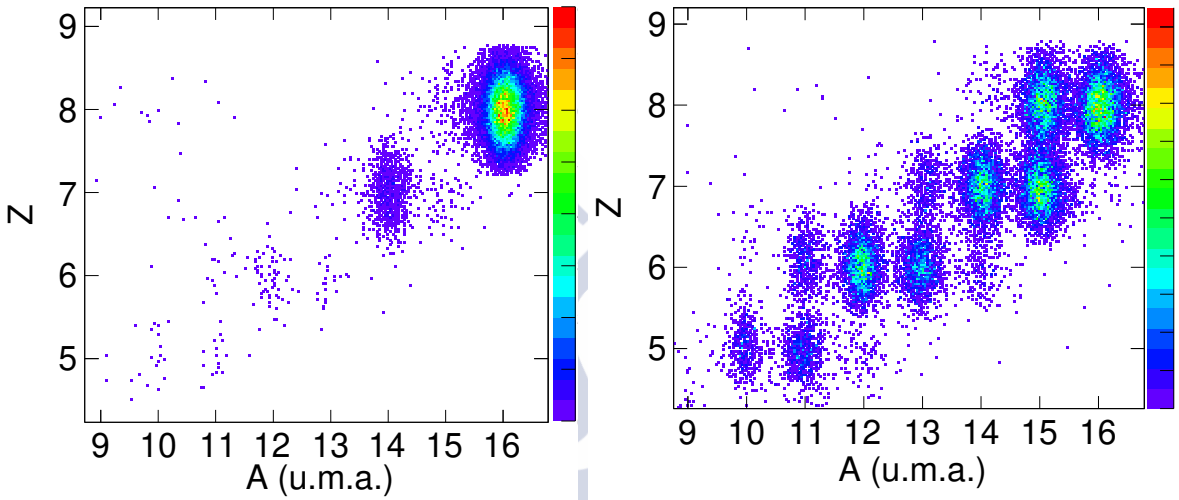

Figure 2.5: 2-Dimensional outgoing identification plots for ^{16}O projectiles over CH_2. For the left picture the *fragment trigger* pattern is applied while for right one the *reaction trigger* condition is considered.

Fixing the outgoing charges, we project in A obtaining several 1-D histograms shown in Figure 2.6. We display for each element (from top to bottom O,N,C and B) a multi-Gaussian fit on the mass histogram. Parameters obtained from the fitting allow us to determine definitely in A and Z the outgoing fragments reaching the TFW. This information is used to estimate events in the cross section calculations and also to impose conditions for its momentum distributions.

Detector Alignment, Angular Resolution

The tracker routine relies strongly on position measurements. Therefore, it is important to ensure that all detectors used[3] to determine trajectories are correctly aligned. For that purpose, we depict angular differences between incoming and outgoing angles for X and Y axes (in Z direction the corrections are negligible), calculated with positions from in-beam silicon detectors as follows: $\Delta\theta^j = \theta^j_{inc} - \theta^j_{out}$ where $j = x, y$.

[3]We have used in-beam silicon detectors.

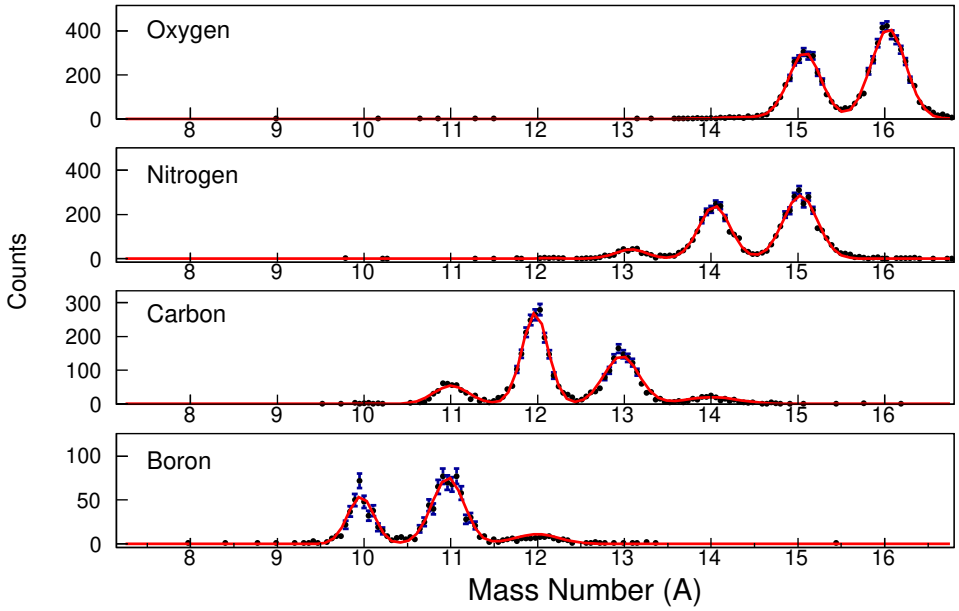

Figure 2.6: Example of the outgoing mass identification for an incoming selection of ^{16}O nuclei impinging on a polyethylene target. Mass distributions are plotted under *reaction trigger* conditions for a different outgoing charges (oxygen, nitrogen, carbon and boron). For each charge, multi-Gaussian fits (red lines) are performed for the most relevant mass peaks.

Despite we did not aligned in this work the silicon detectors, a comparison of the previous alignments performed by other collaborators [27, 29] has been investigated. The angular differences are calculated for all configurations of interest.

In this work we only display two examples of $\Delta\theta^j$.The first example corresponds for an empty run centred in ^{19}O projectiles, depicted in Figure 2.7. The second illustration shows in Figure 2.8 corresponds to an un-reacted beam centred in ^{14}O projectiles impinging on a carbon (first row) and a polyethylene targets (second row). As one expect, the angular differences evaluated in presence of matter (target runs) are wider than those acquired with an empty run due to straggling processes.

The results of these comparisons allowed to conclude that the method described in [27] achieve slightly better alignment, i.e. smaller residues; than the proposed in [29]. Thus, we adopted the former parameters for the silicon alignment calibration in our analysis.

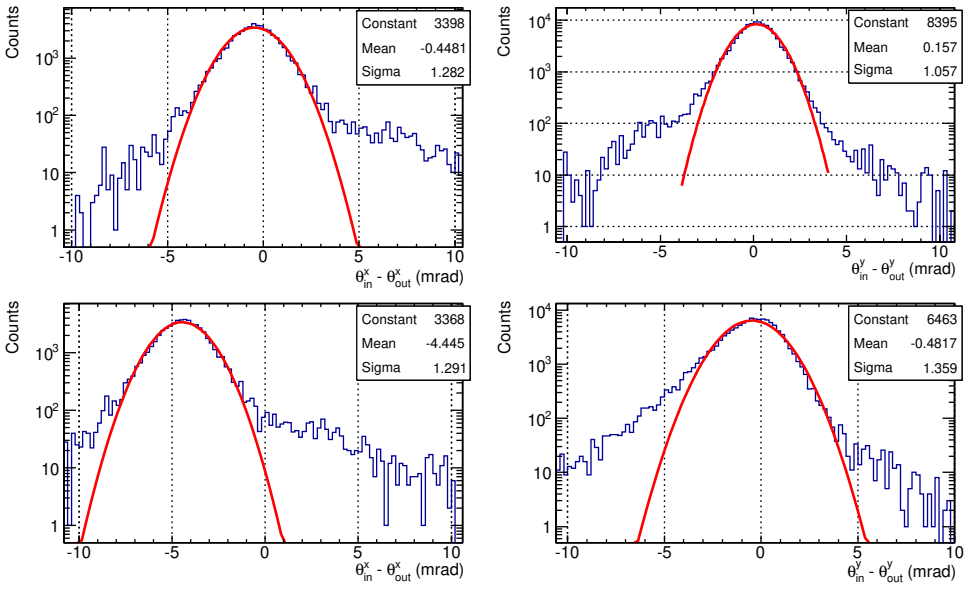

Figure 2.7: Angular differences between incoming and outgoing angles for x and y axes (first and second columns) for an empty run. We check different positions and alignments, from [29] in the first row and from [27] in the second row.

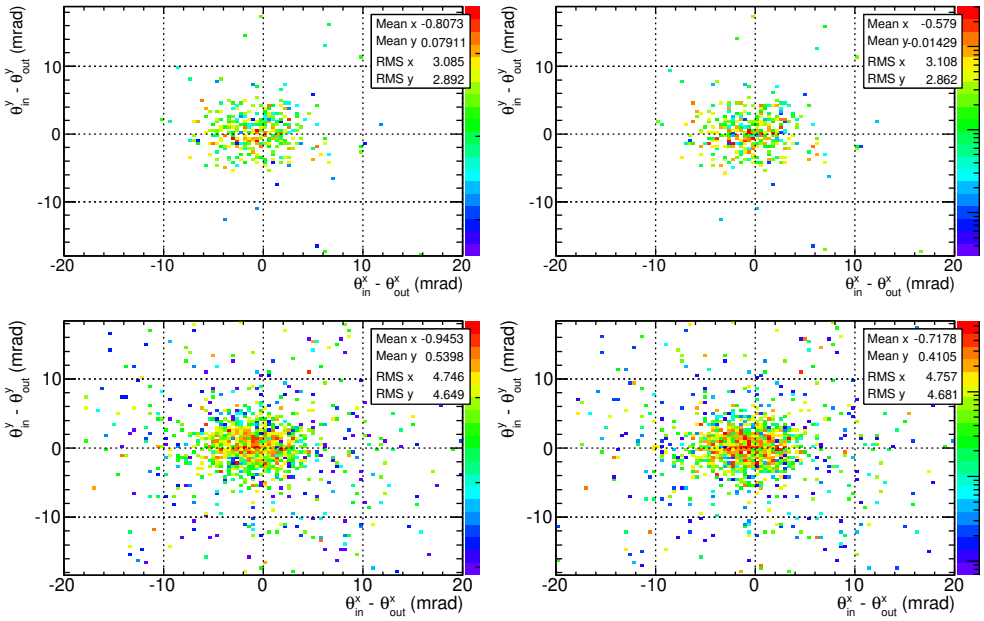

Figure 2.8: Cross check of the alignment parameters where histograms depicted show the angular differences between incoming and outgoing angles for the x and y axes ($\theta^{x/y}_{in}$-$\theta^{x/y}_{out}$). Unreacted beam of ^{14}O projectiles impinging on a carbon (first row) and polyethylene (second row) targets are used. Alignment calibrations taken from [29] are used in the first column, and those calculated in [27] are considered in the second column.

2.3 Identification of Light Particles and γ-rays

2.3.1 The Target Area Detectors

When a primary projectile impinged on the target, heavy fragments were emitted in the forward direction. Light residues, like a proton or a neutron or even photons from de-excitation of residual nuclei, could be characterised by detectors which surrounded the target (a silicon box and the Crystal Ball calorimeter).

The silicon box, designed to detect and measure both energy loss and positions of high energy light particles (see section 1.4.2); did not performed perfectly during this experiment, being not possible to estimate an angular correlation between the two outgoing nucleons (two protons in (p,2p) or a proton and a neutron in (p,pn) reactions), neither disentangle between protons and neutrons.

Instead, we used the Crystal Ball Calorimeter, which has significantly lower angular resolution. In particular, position information was provided by the centre of the fired crystals with the highest energy signal. This detector is also used as γ-ray spectrometer with a moderate energy resolution $\frac{\Delta E}{E} \sim 10\%$ [22].

Crystal Ball Calorimeter

The Crystal Ball calorimeter, which surrounded the R3B target, was used to measure the de-excitation γ-rays. The implementation of double electronic[4] channels in the forward sector increased the performance of CB, enlarging the dynamical range and allowed to measure and identify light particles coming from QFS. In both cases, the recorded signal usually involved several crystals, being necessary to determine and classify these clusters to recover the total deposited energy.

We define a proton/neutron cluster as a high-energy event recorded in the forward crystals (the sole part of the detector able to do it).

A γ-ray cluster corresponds to events with lower energies compared to proton ones, and involved all crystals in CB[5].

The frequency (or energy) of any emitted particle by a relativistic nucleus (i.e. our fragment moving in the beam direction), changes as a function of the polar angle emission. The measurement of the scattering polar angle is thus necessary, and it is determined by the relative position between the emitted nucleus (the source, which is identified in this case with the target position) and the centre of the cluster (the observer, related to the geometrical centre of crystal with the highest energy detected and the outgoing projectile direction). This shift in energy is known as the *Doppler Effect*. It affects the γ-ray emissions and, thus, the cluster energy of this γ-ray must be corrected according with the

[4]The crystals equipped with double electronic channels cover solely from $8 - 23^o$ degrees in polar angles.

[5]CB has 162 crystals three of them were removed for the installation of in-beam vacuum chamber pipe, thus 159 crystals were used.

expression in the rest frame:

$$E_{cm} = E_{lab} \cdot \gamma(1 - \beta \cdot cos(\theta_{lab})) \tag{2.3}$$

where E_{cm} is the corrected energy, E_{lab} is the energy in the laboratory framework, γ is the Lorentz constant, β is the projectile velocity in units of c and θ_{lab} is the laboratory detection angle, previously referred as scattering polar angle.

The maximum energy of an event can spread to the neighbouring crystals, therefore to recover the total energy it is necessary to implement an *addback algorithm* that identifies what crystal is fired and creates lists of events (hits) according to their energy.

The starting point of the used addback algorithm is the determination of the central cluster, that corresponds to the one with the largest energy deposited compared to the neighbouring crystals. This first energy determination allows to discriminate between γ-rays or light particles (protons or neutrons). Once the central cluster crystal is identified, any energy collected above a threshold in the nearest neighbours is added to the cluster. The γ-rays threshold is determined by the limit of QDC range in the low energy read-out. If the collected energy is less than 20 MeV the event is considered as a photon hit. Otherwise, if the energy measured by a crystal is in overflow (over 100 MeV) and as well as in the proton QDC read-out the energy measured is larger than 20 MeV the hit is considered a proton event. As a result, we assign each event to two different lists, one for proton/neutron clusters and another for gamma clusters (Doppler shift corrected).

As previously mentioned, the angle of the nucleon emerging from the reaction is determined using the central angle of the crystal with highest energy. To reproduce a realistic angular distribution, these angles are randomised within the solid angle of the corresponding crystal, taking into account the non-uniform crystal shape by the use of a randomization algorithm [22]. These angles recreate the angular distributions between two outgoing light particles in the QFS cases.

The different addback algorithms used are explained below. We have chosen a (p,2p) QFS as a example ($^{15}O(p,2p)^{14}N$), where the excited levels and the γ-rays considered are depicted in Figure 2.9. Finally, the spectra obtained with different addback routines are displayed in Figure 2.10.

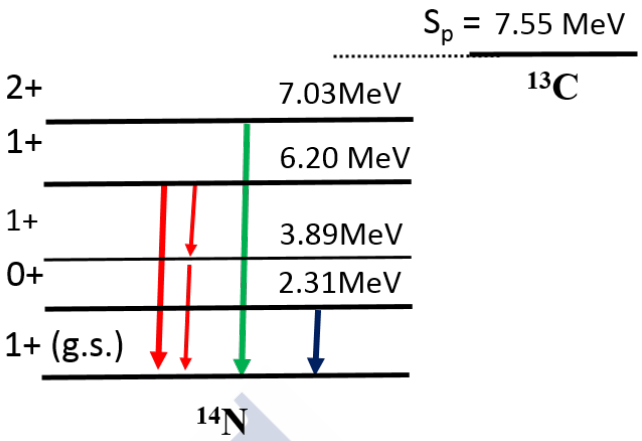

Figure 2.9: Main γ-rays of ^{14}N de-excitation after $^{15}O(p,2p)^{14}N$ reaction using the available data from [50].

a) An extended addback algorithm is appropriate to study the nucleus decay and to make coincidences (γ-rays with fragments). This algorithm seeks the crystal with the maximum energy registered, creates gamma and proton lists, and finally adds the neighbour's energies into the appropriate list. The sum continues until the software cannot find any more neighbours with lower energy. Therefore, the cluster energy is defined as the sum of energies of the main crystal and their neighbours. Thresholds are used to distinguish proton signals and high-energy gamma.

b) A first and second order neighbouring addback is used for studies involving a cascade decay. The routine searches and adds the energy to the gamma or proton lists until a list of first and second neighbouring crystals are completed.

c) A first order neighbouring addback is used to detect only one γ-ray. The main difference with the previous procedure is that only the closest neighbours of the main crystal, which has the highest energy, are considered

d) A first order neighbouring addback with a slight modification of the previous routine. Some conditions are changed for taking into account the identification of no-proton signals as γ-hits.

Notice that the efficiency of the addback algorithms can be different. In particular, first neighbours addback presents less events than other algorithms.

In this analysis we have chosen "a first and second order neighbouring addback" (i.e. b) picture in Figure 2.10) since it optimises the case of nucleus with de-excitation via γ-ray cascades.

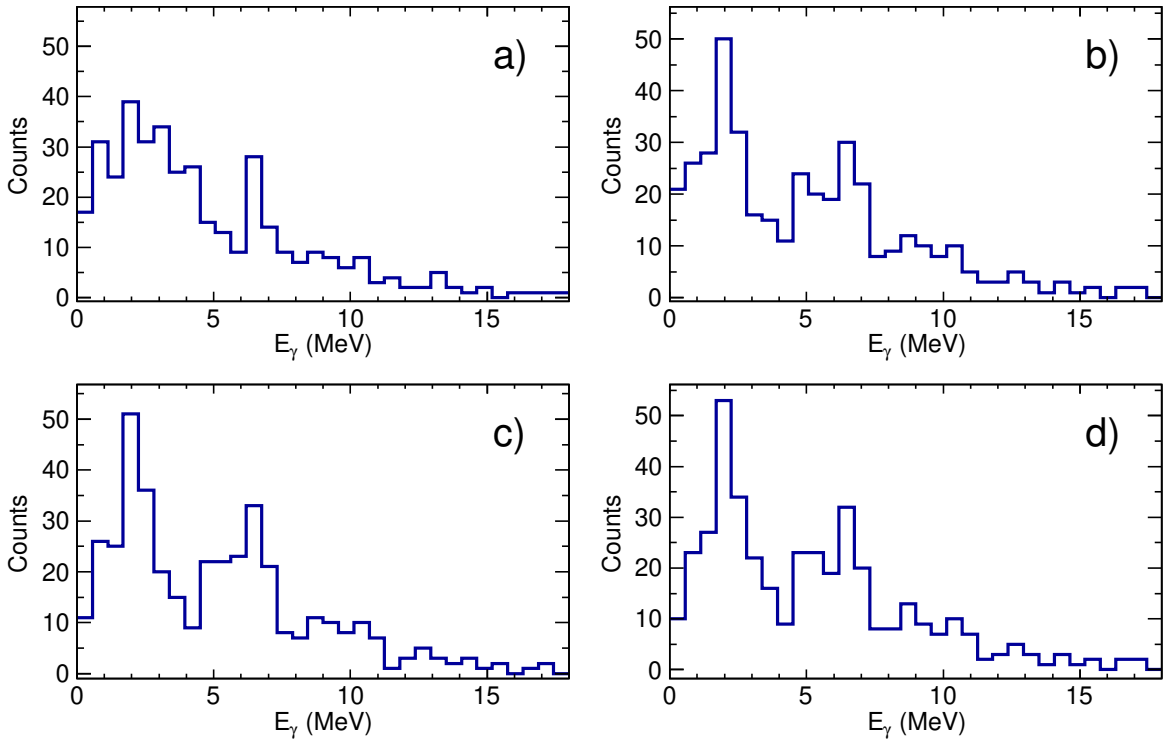

Figure 2.10: γ-ray spectra for different addback algorithms: a) Extended addback, b) First and second neighbouring addback, c) First neighbouring addback, and d) First neighbouring addback variation. The b) addback routine has been chosen in this work.

2.4 Identification of the Reaction Channels

A nuclear reactions is a process in which two nuclei interact to produce one (or more) different nuclear species.

A proper isotopic identification of projectiles and fragments allows to extract information about the nuclear processes occurring and to compare with theoretical models. Physical observables and deductions inferred with them, can be altered if the reaction channel is not precise selected.

In this dissertation, we focus on rather direct reactions where one (or few) nucleon is removed out from the projectile (and/or a target). Depending on the detection or not, and conditions applied in the outgoing light particles identification, we distinguish in this work the follow reactions:

1. Single-nucleon removal channels, where incoming projectiles and outgoing particles are observed under the *reaction trigger* pattern.

2. Quasi-Free Scattering (QFS) reactions, which imply a determination of the reaction channel together with the detection of two angle-correlated high energy signals recorded in CB and can be interpreted as two knocked-out nucleons.

2.4.1 Single Nucleon Removal Reactions

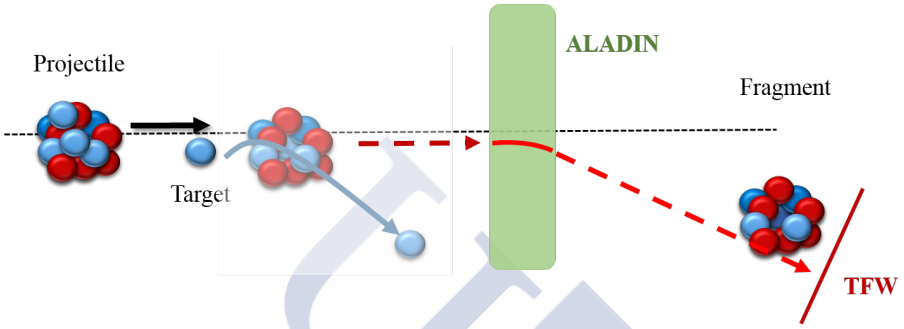

Figure 2.11: A conceptual view for a single-nucleon removal reaction performed in inverse kinematics. A heavy projectile impinges on a light target (carbon or polyethylene). The recoil heavy nucleus is detected by in-beam silicons and detectors of the fragment arm, and arrives to TFW.

In this work, we show one-single proton or neutron removal ($^{A}X(,)^{A-1}Y$) (see Figure 2.11 and the histogram on the left in Figure 2.5) and, also other fragmentation channels ($^{A}X(,)^{A-f}Z$) where several nucleons (even clusters) (right histogram in Figure 2.5) are knocked-out at the same time (see Chapter 5).

The former reactions, which involve the removal of a single nucleon, are useful tool to extract information about single-particle structure. There are numerous examples of experiments that made use of this technique to demonstrate the existence of structures,vanishing or creation of new magic numbers, etcetera [3, 4, 11, 51, 52, 53, 54].

The fragmentation reactions have been studied using light projectiles (^{12}C, ^{14}N, $^{13-16,20,22}$O) and could be of interest in space shielding and in hadrontherapy [55, 56, 57, 58, 59, 37], either to improve the prediction capabilities of transport codes [60].

From the practical point of view, fragments are studied under the *reaction trigger* condition that applies a threshold of 0.1 MeV in CB signals before unpacking data. In fact, this trigger condition is understood as an indication that a reaction has occurred in the target, and provides a clean identification of neutron and proton breakup channels. That is not possible to achieve with the *fragment trigger* condition where the un-reacted beam contributions are so intense that hide the identification of neighbour channels.

Another advantage of the *reaction trigger* is that data obtained are not downscaled; whereas statistics under the *fragment trigger* pattern are compromised since unpacked

data are highly compressed with large downscaled factors in all studied settings. For instance, for the very light outgoing nuclei we observe just a few events while *reaction trigger* pattern includes hundreds of it.

2.4.2 Quasi-Free Scattering: (p,2p) and (p,pn) Reactions

Quasi-Free Scattering, (QFS), on a proton target was performed in inverse kinematics where one nucleon is knocked-out of the target nucleus as the schematic Figure 2.12 displays.

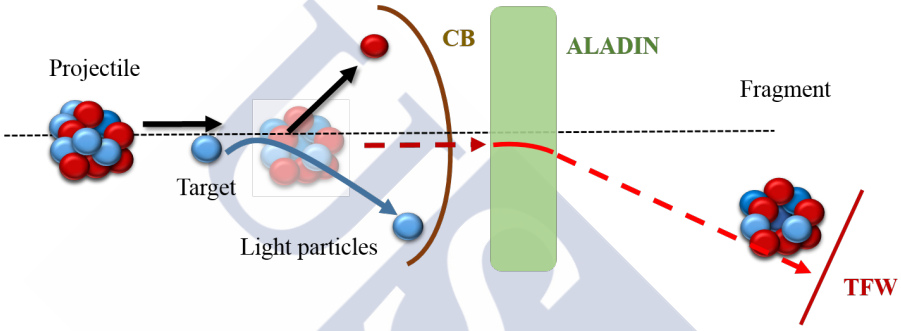

Figure 2.12: A conceptual view of a QFS in inverse kinematics. A heavy projectile impinges on a light target (carbon or polyethylene). The nucleons knocked out are registered by CB. The heavy fragment travels through ALADIN, is also registered by several detectors and reach the final one, TFW)

Several experiments covering wide range of stable nuclei and light nuclei [15, 16, 23, 61, 62, 63, 64] using this reaction channel have been already addressed by R^{3}B collaboration [18]. The notation we will use is ${}^{A}X(p,pN)^{A-1}Y$ where N is a nucleon (neutron or proton) and X, Y are the incoming (projectile) and the outgoing (fragments) nuclei. For (p,pn) reactions it takes the form ${}^{A}_{Z}X(p,pn)^{A-1}_{Z}X$, the charge is conserved; whereas in (p,2p) ones, the nuclear specie is exchanged decreasing a unit its charge ${}^{A}_{Z}X(p,2p)^{A-1}_{Z-1}Y$.

Quasi-Free (p,pN) (N=proton or neutron) reactions are most restrictive than removal ones. We assure that a QFS event has happened in our experimental device when we register the simultaneous detection of the projectile together with two angle-correlated outgoing nucleons in CB calorimeter - one coming from the projectile and another from the target- in coincidence with the final ejectil (registered in in-beam silicons and detectors of the fragment arm - GFIs and TFW) (see the conceptual picture in Figure 2.12).

In order to obtain physical observables of these reactions, fragment hits are registered by silicons DSSSD3 and DSSSD4 and TFW detector under *reaction trigger* condition. To detect the footprints from two outgoing nucleons in CB we impose the condition of two

high energy signals within a relative angle minor than 90 deg [6]. Figure 2.13 depicts on its right side an example of fragment identification under QFS conditions for a ^{16}O projectile selection on a polyethylene target.

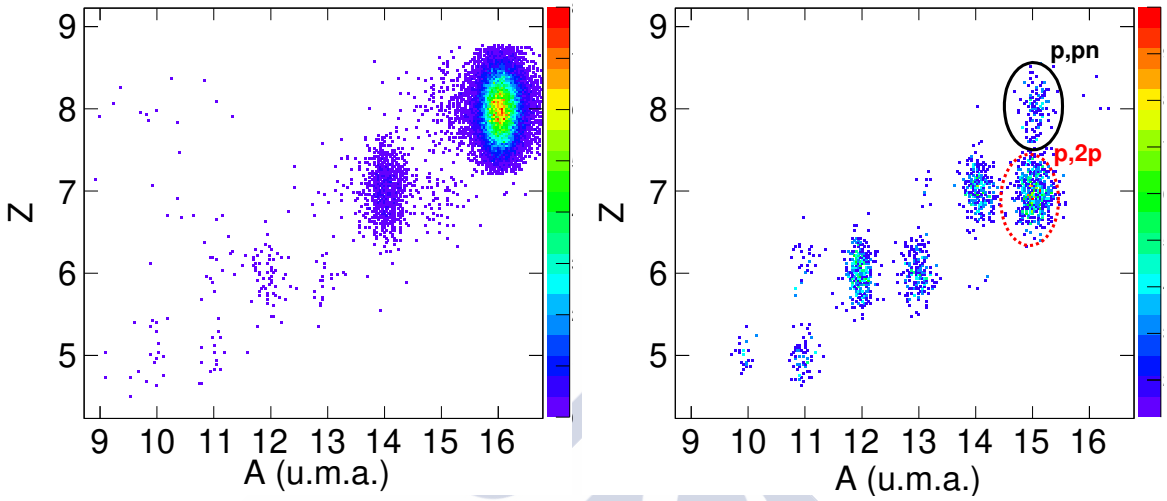

Figure 2.13: 2-Dimensional outgoing fragment identification plots for a ^{16}O projectile on a polyethylene target. Left picture is obtained under *fragment trigger* whereas the right one fulfils QFS conditions: *reaction trigger* pattern plus two angle-correlated high energy signals detected in forward crystal of CB. QFS (p,2p) and (p,pn) channels are highlighted with black solid and red dashed ellipses.

The kinematics of an inverse Quasi-Free Scattering event is depicted in Figure 2.14, where a heavy projectile impinges on a light target (carbon or polyethylene).

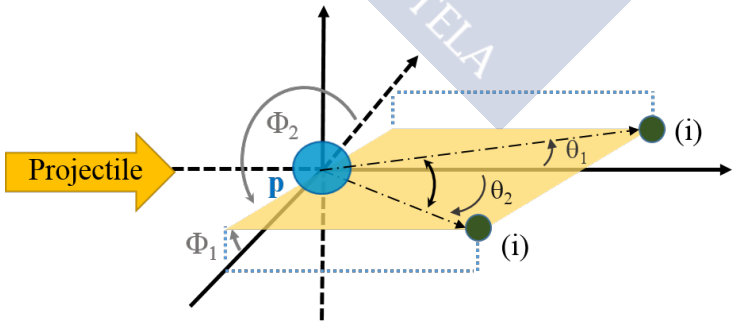

Figure 2.14: In plane a Quasi-Free Scattering event displayed in the laboratory framework. The opening angle is depicted into the plane formed by two outgoing nucleons, (i) (it can be proton or neutron) and its value is the sum of $\theta_1 + \theta_2$.

[6] Kinematic calculations of non relativistic protons determine an opening angle of 90^o, smaller angles arise when we consider a proton with $\beta \sim 0.8$ obtaining a 82^o in this case.

The knocked-out nucleons are, approximately, in the same plane forming θ_1 and θ_2 polar angles respect to the beam line (in the laboratory system). The azimuthal angles Φ_1 and Φ_2 are defined on the plane perpendicular to the beam line. The relative polar angle between the two outgoing protons $(\theta_1 + \theta_2)$, known as *opening angle*, provides a signature of the strong angular dependence of the two scattered particles under this process. The kinematics of QFSs can be computed. Figure 2.15 displays azimuthal and polar angles for the case of ^{16}O(p,2p)^{15}N [23, 65].

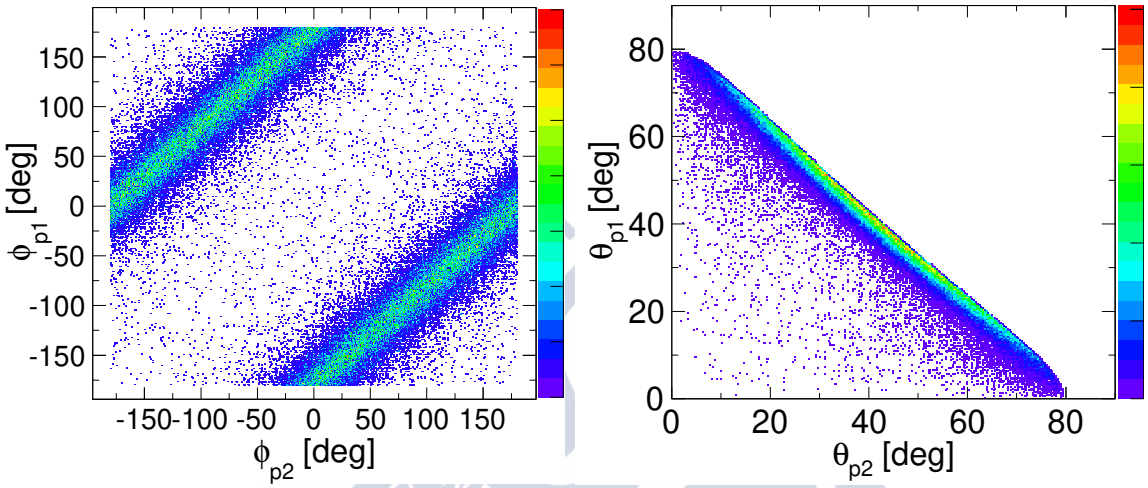

Figure 2.15: Azimuthal angles (ϕ_1, ϕ_2) on the left side, and polar angles (θ_1, θ_2) on the right, formed between the two outgoing protons from a kinematic simulation of (p,2p) QFS, i.e. ^{16}O(p,2p)^{15}N.

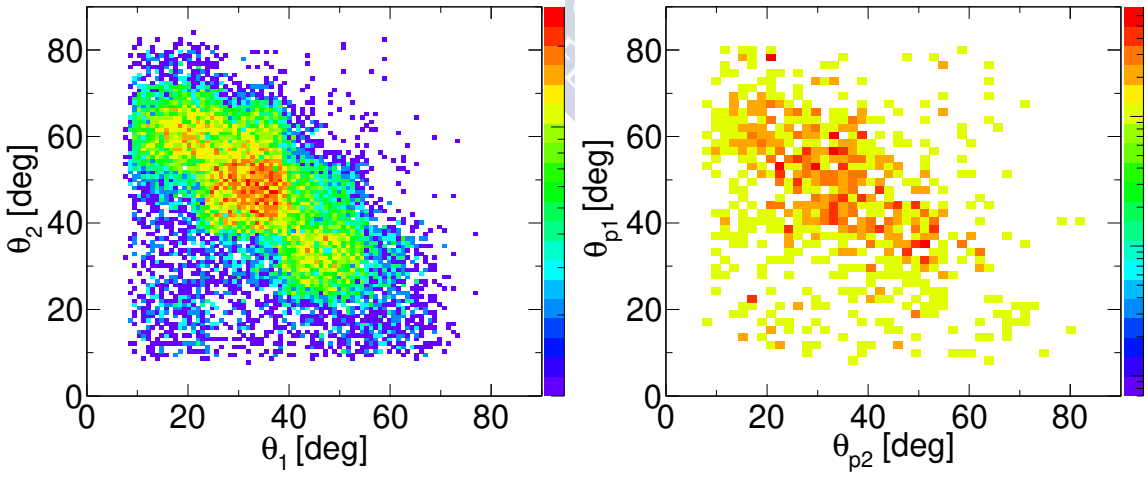

Figure 2.16: Simulated (left) and experimental (right) opening angle distributions formed by two knocked-out protons from a (p,2p) QFS, ^{16}O(p,2p)^{15}N.

This calculation uses as input the experiment conditions (E_{beam}, beam spot, momentum widths). A Monte Carlo simulation, running in R^{3}BRoot framework-GEANT4 and taking the previous kinematics distribution as input, is used to evaluate the detection efficiency of (p,2p) events. Figure 2.16 shows simulated and experimental opening angle for ^{16}O(p,2p)^{15}N, where we observe that he maximum of the *opening angle* ($\theta_1 + \theta_2$)falls around 80^o degrees.

Following the same idea, the (p,pn) channels are also computed. Different input parameters have been used in order to reproduce the physics of the reaction. Finally, we have adopted nucleon-nucleon parametrisations provided by Nijmegen website [66] according to PWD (Plane Wave Approximation) [67]. We notice that the correct description of the reaction kinematics is very important to correctly determine the light particles detection efficiency.

2.5 Reaction Cross Sections

Reaction cross sections are crucial physical observables that can provide information about structure, size and matter properties of a nucleus.

A cross section for a given reaction is defined as the interaction probability per fluency of particles[7], or, in nuclear physics terms the effective area for collision between a projectile and a target. They are given in barn (in nuclear field) $1mbarn = 10^{-3}barn = 10^{-31}m^2$, and mathematically expressed as:

$$\sigma_\tau = \frac{Out_\tau}{Inc_\tau} \cdot \frac{1}{T_\tau} \tag{2.4}$$

where Out_τ is the number of outgoing fragments, Inc_τ is the number of the projectiles (incoming nuclei) impinging on the target, and T_τ is the number of scattering centres per unit area of the given target τ which is expressed as follow:

$$T_\tau = s_\tau \cdot \frac{1}{m_\tau} = \rho_\tau d_\tau \cdot \frac{1}{m_\tau} \tag{2.5}$$

and $s_\tau = \rho_\tau d_\tau$ is the area density of the target with the volume density ρ_τ, and the thickness d_τ; $m_\tau = A_\tau$ / N_A is the mass of a single scattering centre expressed via the molar mass of the target, A_τ, and the Avogadro number, N_A.

2.5.1 Background Subtraction

One goal of this work is to reckon cross sections on a proton target. In absence of a pure hydrogen target, a combination of carbon and polyethylene targets allowed us to obtain these cross section values.

[7] number of particles per area

The following expression shows how the number of reactions for a H_2 target has been estimated, R_{H_2}.

$$R_{H_2} = R_{CH_2T} - \frac{Inc_{CH_2T}}{Inc_{CT}} \cdot \frac{T_{CH_2T}}{T_{CT}} \cdot R_{CT} - \frac{M(Inc)}{M(ET)} \cdot \left(1 - \frac{T_{CH_2T}}{T_{CT}}\right) \cdot \frac{Inc_{CH_2T}}{Inc_{ET}} \cdot R_{ET} \quad (2.6)$$

The amount of reactions, R_{H_2}, induced by the hydrogen component of the CH_2 target can be calculated from the subtraction of the corresponding number of carbon-induced reactions, R_{CT} - the second term, and all corrected by the empty target contributions, R_{ET} - the third term. Since not all settings have empty target measurement we have used values from other settings and correct them by a scale factor (weighted with the nuclear masses of projectiles of the studied reaction in the current setting, $M(Inc)$; and in the empty run, $M(ET)$).

The "raw" cross section on a proton target, is obtained as follow:

$$\sigma_H^{raw} = \frac{1}{2} \cdot \frac{R_{H_2}}{Inc_{CH_2T} \cdot N_t(CH_2)} \quad (2.7)$$

And finally, we can include all the correction factors (CF) which will be described below:

$$\sigma_H = \frac{\sigma_H^{raw}}{CF} \quad (2.8)$$

2.5.2 Correction Factors

Different factors are introduced in order to correct the "raw" cross sections in order to taken into account physical processes that affect and modify our measurements.

Secondary Reaction Probabilities

Once the reaction fragments are produced, included the un-reacted beam; they have a non negligible probability to react with materials located in the beam line. The probability of secondary reactions, SRP, should be estimated for any recoil nucleus. We have used the transport code MOCADI [68] that reports on the survival probabilities of the particles of interest, using cross sections provided by the EPAX parametrizations [69].

In general terms, secondary reaction probability varies with the mass and charge of fragments. In this experiment, we are considering fragments that span from oxygen (Z=8) to beryllium (Z=4) and the corresponding corrections account from 3.6 to 7.8 % respectively with relative associated errors of 5%.

Geometrical Acceptance

The geometrical acceptance factor, GAF takes into consideration the detection efficiency reduction due to the finite size of the detectors in our set-up.

To evaluate this effect, a dedicated simulation in the R^3B framework (based on GEANT4 code [70, 71]) was performed. Realistic physical parameters and electromagnetic physical libraries are included to estimate the normalised percentage of detected products.

The simulation recreates the complete S393 experimental set-up and allows us to calculate the rate of particles which are produced at the middle of the target, fly through ALADIN and finally reach the TFW. The momentum of each fragment (energy and direction) and the beam spot (the physical size of the projectile before impinging on the target) are used as inputs. Part of these input parameters are evaluated using the in-beam silicon positions (DSSSD3 and DSSSD4) and the energy loss measurements in both TFW and DSSSD3 detectors.

The GAF isvery close to 1 for one nucleon removal reactions, i.e. almost all fragments are detected; while for reactions that involve a large number of nucleons removed (more than 6 nucleons), this factor can decrease to rates below 50%. Full tables can be found in Appendix D (5.4.3).

The associated systematic errors are presented in Table 2.2. These uncertainties fluctuate from 2.5%, when set-up acceptance is large (about $98-100\%$), to 20% for those cases with very small experimental acceptance (less than 39%).

Acceptance range (%)	$\Delta GAF(\%)$
100-98	2.5
98-90	5
89-75	7.5
74-60	10
59-40	15
< 39	20

Table 2.2: Systematic errors considered for the Geometrical Acceptance Factors.

Relative Trigger Efficiency

The relative trigger efficiency (RTE) is defined as the ratio of the number of events of a given fragment measured in a detector (TFW in our case) under *reaction* and *fragment trigger* conditions.

Since the triggers used to estimate events of the projectile and fragments are different, to calculate an accurate survival fragment probability for a given reaction it is necessary to correct it by the *relative trigger efficiency* (RTE). The RTE was already evaluated for carbon and boron isotopes in one-proton-x-neutron removal (1pXn) channels in another work related to the same experiment S393 in [61]. In this case, authors achieved a global fit of the data sampled and obtained a relative mean efficiency of $85.3\% \pm 2.5$ for all channels in this study. We could corroborate this result, applying similar conditions.

However, we have chosen to perform a more detailed study since RTE is sensitive to the projectile mass-to-ratio, A/Z_p, and to the charge shift, $\Delta Z = Z_{proj} - Z_{frag}$.

The prior article, [61], all analysed fragments had ΔZ=1 with respect to the projectile charge (i.e. carbon projectiles leading to boron fragments). In the current work, we had larger charge variations, ΔZ=1-4, leading to relatively light fragments such as beryllium isotopes. For these cases, moderate fluctuations have been observed in the RTE values. The efficiencies can reach 100% for three or more removed proton channels. For that reason, we summarise in Table 2.3 the average value for neutron-deficient ($A/Z < 2$) and neutron-rich projectiles ($A/Z > 2$) where we also split between carbon and polyethylene targets for the different reactions.

Reaction type	RTE $(\%)_{A/Z<2}$	RTE $(\%)^{C}_{A/Z>2}$	RTE $(\%)^{CH_2}_{A/Z>2}$
0p x-n-removal	81.3 ± 1.5	83.0 ± 6.2	84.2 ± 3.8
1p, x-n-removal	80.7 ± 4.0	89.6 ± 6.7	85.5 ± 3.4
2p, x-n-removal	83.0 ± 13.8	87 ± 4.9	87 ± 4.9
3p, x-n-removal	100 ± 5	100 ± 5	100 ± 5

Table 2.3: Relative trigger efficiencies (RTE) for several removal reactions (reaction type) expressed as function of the number and nature of the nucleon removed. We also distinguish between neutron-deficient ($A/Z < 2$), and neutron rich projectiles ($A/Z > 2$) on a carbon and on a polyethylene targets. Errors are purely statistics, taking into account standard deviations around the RTE mean value.

CB Detection Efficiencies for Light Outgoing Particles

We have focused on estimating the CB efficiency evaluation for the detection of high-energy events corresponding to nucleons (protons or neutrons) emitted in QFS.

The simulation of the two energetic nucleons (QFS events) is performed in the R^3BRoot framework within Liège intranuclear-cascade model (INCL [72]). Input data for this simulation comes from a kinematic generator code originally written by L.Chulkov and V. Panin [23]. This generator uses also as input the beam spot dimension, measured for each projectile just before impinging on the target; its energy, estimated by the ATIMA code [73] at the middle of the target; the associated atomic and mass numbers; and the width of the momentum distributions for the each fragment, which are calculated using Goldhaber model (see Equation 2.9) and compared with the experimental values (being in very good agreement).

$$\sigma^2 = \sigma_0^2 \frac{A_f \cdot A_i}{(A_f + A_i)} \tag{2.9}$$

where $A_{f,i}$ are the masses of the fragment and removed nucleon (proton or neutron) and the σ_0 is a constant related to the nucleon separation energy $\sigma_0 = \sqrt{2 \cdot S_i}$. Further details

can be found in dissertations [23, 32].

The detection efficiency for the (p,2p) channel is relatively easy to simulate. The angular distribution of the two outgoing nucleons is rather isotropic, whereas the angular distribution of a proton and a neutron following a (p,pn) reaction exhibit an important anisotropy [74].

These different scenarios are used to evaluate the detection efficiencies of (p,2p) and (p,pn) reactions. For the (p,2p) case, isotropic distributions of the two outgoing protons are included automatically in our simulations. While for a (p,pn) channel, anisotropic distributions, which are obtained from nucleon-nucleon distributions according to PWD (Plane Wave Approximation), and available in the Nijmegen website [66], are used. Moreover the parametrization of these distributions, (see Figure 2.17) offers us the possibility to reproduce for a wide energy range a realistic response of the angle formed by a neutron and a proton. This method was also implemented in [67].

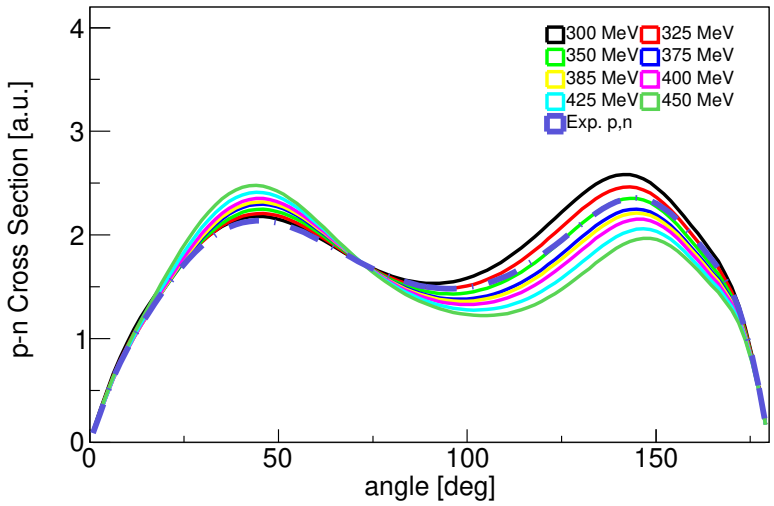

Figure 2.17: Proton-neutron parametrised cross section as a function of the scattered angle for several energies. Data are taken form the Nijmegen website [66].

Tables 2.4 and 2.5 summarise all detection efficiencies of (p,2p) and (p,pn) channels for oxygen and nitrogen projectiles. We have also studied the simultaneously detection of two nucleon in CB without angular conditions. These simulations will be used in section 4.4 to evaluate cross sections associated to other channels associated to absorption processes (for QFS channels are explained deeply in section 4.4). For these cases, the efficiency results are shown with under-script "iso" and (pn) or (pp) for the absorption processes.

Proj	E(AMeV)	$Eff(p,2p)_{iso}$ (%)	$Eff(p,pn)_{ani}$ (%)	$Eff(2p)_{iso}$ (%)	$Eff(pn)_{iso}$ (%)
^{13}O	397	55.6	15.45	62.1	21.4
^{14}O	349	54.7	14.7	60.9	20.9
^{15}O	308	53.5	13.7	60.7	20.5
^{16}O	450	62.2	17.1	72.4	20.1
^{17}O	406	58.1	16.6	67.8	19.8
^{18}O	369	55.2	16.1	62.4	18.8
^{19}O	442	61.1	16.1	65.4	19.9
^{20}O	406	60.2	16.4	63.2	19.8
^{21}O	448	57.2	15.7	66.1	20.0
^{22}O	414	55.6	16.0	62.4	19.7

Table 2.4: Detection efficiencies calculated for different reaction channels on a proton target induced by oxygen projectiles. QFS and two high energy signals without angle-correlated conditions are condisired under isotropic ("iso") and anisotropic ("ani") distributions

Proj	E(MeV)	$Eff(p,2p)_{iso}$ (%)	$Eff(p,pn)_{ani}$ (%)	$Eff(2p)_{iso}$ (%)	$Eff(pn)_{iso}$ (%)
^{12}N	370	57.5	15.4	68.2	21.1
^{13}N	323	56.6	14.1	64.9	20.7
^{14}N	450	63.0	16.3	70.5	20.2
^{15}N	401	60.9	15.6	68.8	19.8
^{16}N	471	62.8	16.5	70.8	20.7

Table 2.5: Detection efficiencies calculated for different reaction channels on a proton target induced by nitrogen projectiles.

Finally, we have made a comparison of the QFS efficiencies calculated in this work with the ones evaluated in previous works [15][16], presented in Table 2.6. We have estimated the systematic uncertainties for (p,2p) channel of 6%, and for (p,pn) around 13% of the CB efficiencies. Taking into account the total uncertainties of the QFS efficiencies, our estimated magnitudes overlap with evaluated by other collaborators.

Reaction	CB^1_{EFF} %	CB^2_{EFF} %	CB_{EFF} %
^{14}O (p,2p) ^{13}N	-	54.0	54.7
^{16}O (p,2p) ^{15}N	-	63	62.2
^{17}O (p,2p) ^{16}N	-	60.7	58.1
^{21}O (p,2p) ^{20}N	-	61.0	57.2
^{22}O (p,pn) ^{21}O	14.0	-	16.0
^{22}O (p,2p) ^{21}N	58.0	58.9	55.6

Table 2.6: CB efficiencies for several QFS. Results [1] and [2] are taken from [15, 16] respectively.

Efficiencies for Proton Detection

The response of evaporated protons by excited fragment or projectile during the collision is also investigated in the R^3BRoot framework. These protons are emitted in forward direction and they can be detected into the proton arm.

The momentum of a simulated outgoing proton has been calculated using the energy and positions recorded in the in-beam silicon detectors. The detection efficiency for one evaporated proton event is $\sim$ 62%; and for two proton, a less common process (from neutron-removal reactions induced by ^{13}O nuclei), efficiencies go down to values of $\sim$ 49%. Associated systematic uncertainties for either one or two proton detections are fixed as either 2% or 5%, respectively.

2.6 Momentum Distributions

Momentum distributions after nucleon removal are another useful tools to learn about the internal structure of the projectile nucleus. The comparison of these observables with theoretical calculations is relatively easy and bear to extract information about shell occupancy of the removed nucleon in the original system. The tri-momentum of projectile is expressed in terms of longitudinal ($\vec{P}_{\parallel}$, is parallel to the direction motion), and transverse ($\vec{P}_{\perp}$, perpendicular to the fragment direction) components.

$$\vec{P} = \vec{P}_{\perp} + \vec{P}_{\parallel} \tag{2.10}$$

Whereas the transverse component is an invariant Lorentz[8], the velocity of the longitudinal component needs to be corrected by Lorentz factor. The longitudinal momentum in the laboratory frame is:

$$P_{\parallel} = \sqrt{P^2 - \sqrt{P_x^2 + P_y^2}} \tag{2.11}$$

And using a Lorentz transformation we obtain its expression in the centre of masses:

$$P_{\parallel}^{cm} = \gamma(P_{\parallel} - \beta\sqrt{M_{frag} + P^2}) \tag{2.12}$$

To calculate x- and y-components, angles of incoming projectiles and outgoing fragments are needed. We use the silicon positions in front and behind the target to estimate them as follow:

$$\theta_{inc}^{k} = \arctan\frac{k_2 - k_1}{z_2 - z_1} \qquad \theta_{out}^{k} = \arctan\frac{k_4 - k_3}{z_4 - z_3} \tag{2.13}$$

where k corresponds to x, y coordinates. Therefore, using the angles described above we obtain:

$$P_x = P \cdot \sin(\theta_x^{out} - \theta_x^{inc}) \qquad P_y = P \cdot \sin(\theta_y^{out} - \theta_y^{inc}) \tag{2.14}$$

[8]The tracker routine provides the the absolute value of the fragment momentum

In this work, P_y [9] is used to obtain Root Mean Square (RMS) values and make comparison with theoretical calculations. Since the majority of the reaction of interest have low statistics, the resolution is limited, and we have decided to present RMS and Full Width Half Maximum (FHWM) results obtained from Gaussian fits to characterise the momentum distributions.

The module of the momentum in the laboratory frame is calculated by the tracker routine using the mass of each fragment given by the mass evaluation from [49]

$$|\vec{P}| = \gamma\beta M_{frag} \tag{2.15}$$

2.6.1 Intrinsic Momentum

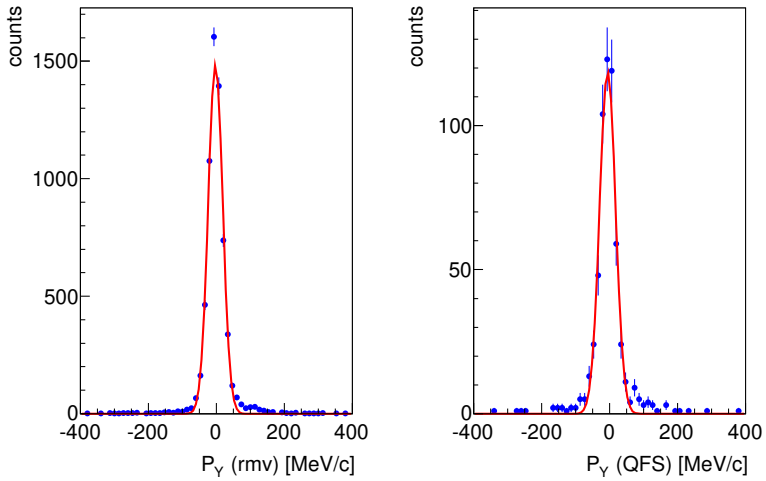

Figure 2.18: P_y distributions of signals from ^{19}O projectiles with no target. Removal and QFS have been considered obtaining RMS^{rmv}_{empty} = 36.5MeV/c, σ^{rmv}_{empty} = 21.3 MeV/c; and RMV^{QFS}_{empty} = 51.0MeV/c, σ^{QFS}_{empty} = 23.5MeV/c.

To correctly evaluate the momentum width[10], we need to remove the intrinsic resolution that limits our detection system. This is presented in the un-reacted beam distribution over an empty target. We did not have empty target runs corresponding to all different secondary projectiles. For that reason, in this analysis we subtract the width of the distribution of ^{19}O projectiles with no target $\sigma_i \equiv \sigma_{empty}(^{19}O)$ from each width fragment distribution. The effect on different projectiles has been scaled as follow:

$$\sigma_{corr} = \sqrt{(\sigma_{frag})^2 + (\frac{M_{inc}}{M_{^{19}O}} \cdot \sigma_i)^2} \tag{2.16}$$

[9] This component has better quality since it has been obtained from more accurate silicon strips
[10] Both results, RMS and FWHM, are validates to compare with theoretical calculations

We remind that the correction, only evaluated for P_y, assumes Gaussian distributions for the momenta which are not always the case (other effects such as straggling effects and/or maybe other reactions can modify the shapes of distributions).

2.6.2 Straggling

It is helpful to verify the consistency and rightness of the determination of the angular straggling caused by the target, by comparing it to simulation, for instance with the ATIMA code [73]. Experimentally, the straggling in the target is calculated by width differences between measurement of widths from the recoil fragment and un-reacted beam (see Figure 2.19).

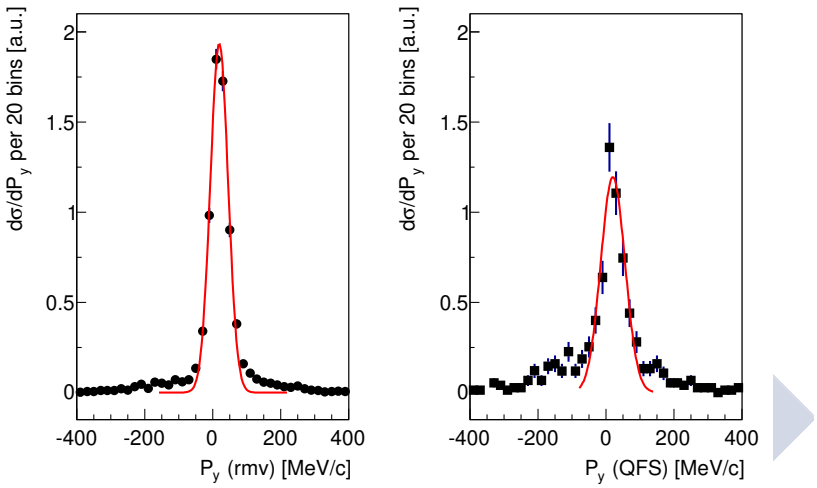

Figure 2.19: P_y distributions of ^{16}O un-reacted contributions ^{16}O on a proton target. Left picture is related to removal channel and the right with QFS conditions being: $RMS^{rmv} = 19.1$ MeV/c, $\sigma^{rmv} = 26.1$ MeV/; ,and $RMV^{QFS} = 20.43$MeV/c, $\sigma^{QFS} = 35.6$MeV/c.

The subtraction of the momentum width, in a first approximation, can be done normalising by nuclear masses of the fragment respect to the projectile. Using the previous example, a (p,2p) reaction induced by ^{16}O projectiles, we have:

$$\sigma^2_{react}\left(^{16}O \rightarrow ^{15}O\right) = \sigma^2_{meas}\left(^{16}O \rightarrow ^{15}O\right) - \left(\frac{M^{15}O}{M^{16}O}\sigma^2_{meas}\left(^{16}O \rightarrow ^{16}O\right)\right)^2 \qquad (2.17)$$

where σ_{react} is the width of the reaction, and σ_{meas} is the width obtained in momentum distributions for ^{15}O and ^{16}O nuclei in the final state.

For instance, for a $\sigma^2_{meas}\left(^{16}O \rightarrow ^{16}O\right)^{rmv} = 26.1$ MeV/c and $\sigma^2_{meas}\left(^{16}O \rightarrow ^{16}O\right)^{QFS} = 35.61$ MeV/c, we find $FWHM_i^{rmv} = 2(\cdot\sqrt{2ln(2)})\sigma_i = 61.5$ MeV/c, and $FWHM_i^{QFS} = 83.8$MeV/c.

Chapter 3

Single-Nucleon Removal Reactions

Single-nucleon removal reactions of exotic projectiles on proton target were performed in inverse kinematics. A single nucleon was removed away from the high-energy projectile ($^{A}_{Z}X$) when it impinged on a light target such as carbon or polyethylene. Measurements on a proton target were obtained combining the polyethylene and the carbon results. The notation to design these reaction channels is $^{A}_{Z}X(p,pX)^{A-1}Y$ with X being a nucleon (proton or neutron), ($^{A}_{Z}X$) the incoming projectile and ^{A-1}Y the outgoing fragment, i.e. in proton removal channels $^{A-1}_{Z-1}Y$, whereas in neutron removal the fragment has the same charge as the projectile, $^{A-1}_{Z}X$.

These results complement previous analysis achieved by R^{3}B collaborators [22, 23, 61] which focus mainly on the proton removal reactions [75].

A precise reaction channel identification has been achieved through a unique identification and selection for projectile and fragment events as explained in sections 2.1 and 2.2. For single-nucleon removal reactions the detection of knocked-out is not explicitly imposed and the heavy outgoing fragment is identified and selected under the *reaction trigger* condition. This particular trigger guarantees that a nuclear reaction has happened in the R^{3}B target, and it avoids the contamination of neighbour isotopes.

Depending on the energy involved into the collision, the recoil fragment could be formed either in its ground state or in excited ones (if they are energetically available). Therefore, we split our discussion differentiating about inclusive and exclusive measurements relying upon the final state selection of outgoing fragments. Whereas an inclusive measurement can be obtained without imposing any conditions in the fragment final state, an exclusive result requires to disentangle all involved final states using in-flight detection of γ-rays from fragment de-excitation. These γ-rays were registered in CB calorimeter and allowed us to estimate the population rates of each excited state.

An example of identification matrix is displayed in Figure 3.1 for fragments coming

from removal reactions induced by ^{14}O projectiles on a polyethylene target at 348 $AMeV$ under two different trigger patterns (fragment and reaction ones). On the left side, the identification matrix (under *fragment trigger* condition) allows indeed to extract information related to the incoming projectile; whereas the right picture displays a matrix (under *reaction trigger* pattern) where all removal channels are shown making a spotlight on the one neutron (black line) and one proton (red dashed line) removal channels.

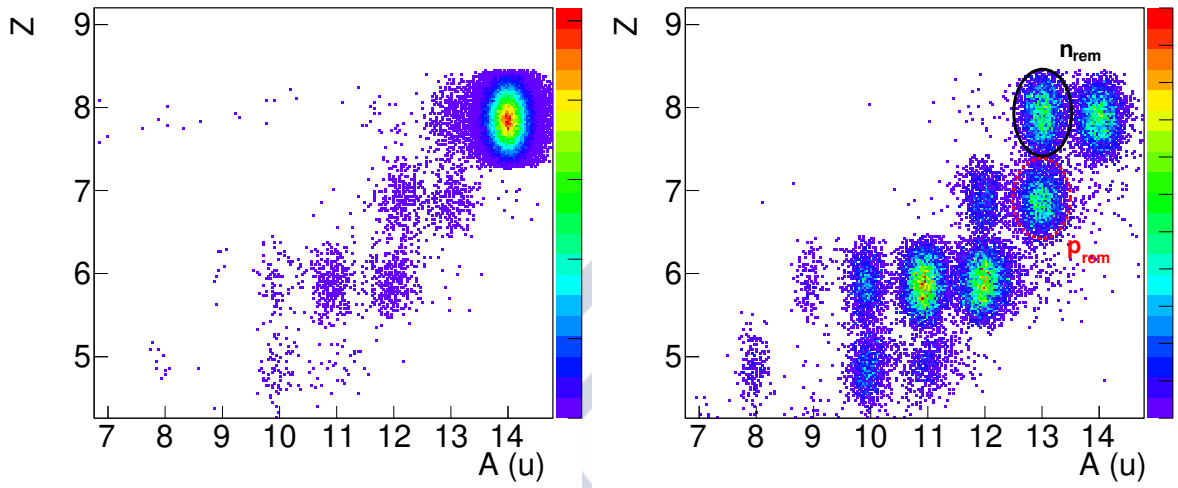

Figure 3.1: Fragment identification matrices (Z versus A) for outgoing fragments reconstructed from ^{14}O projectiles impinging on a polyethylene target. The left picture shows all recoil fragments that reach the final detector under *fragment trigger* pattern and the right one is depicted under *reaction trigger* conditions.

3.1 Cross Sections

We present firstly measurements for polyethylene and carbon targets (τ). Although S393 experiment did not include a pure proton target, measurements on a proton target can be obtained (see section 2.5) from the combination of carbon and polyethylene targets. The following equation gives the uncorrected cross section, σ_τ^{raw}, of a given target τ as:

$$\sigma_\tau^{raw} = \frac{Out_\tau}{Inc_\tau} \cdot \frac{1}{T_\tau \cdot Factors} \tag{3.1}$$

Out_τ and Inc_τ are the number of outgoing fragment and incoming projectiles and T_τ is the number of scattering centres per unit area of the given target τ. This raw cross section must be corrected by several factors which take into account geometrical acceptance, reactions with other detectors in the beam line and efficiencies of the processes (see section

2.5.2 in Chapter 2). The carbon target subtraction provides single nucleon removal cross sections on a proton target which is performed using equations 2.4-2.6.

The evaluation of cross sections is strongly sensitive to the ratio of incoming and outgoing events. Neighbouring contamination coming from close isotopes (both in charge and mass numbers) produce undesired variations in the cross sections. In order to guaranty the reproductivity of these results a systematic study of the measurement stability was performed.

For instance, for a specific removal channel i.e. $^{14}O(p,pX)^{13}N$, we depict in Figure 3.2 uncorrected cross sections (σ_{rmv}^{raw}) versus the size of software gates applied to select both incoming and outgoing nuclei (in arbitrary units). This type of analysis shows a stable region of cross sections where we can select our events of interest and the contributions from others neighbours are disregarded. The existence of a *plateau* (depicted with a red line) is understood as a proof of the stability of our measurements. The final uncorrected cross sections are achieved by reckoning the average value in this region.

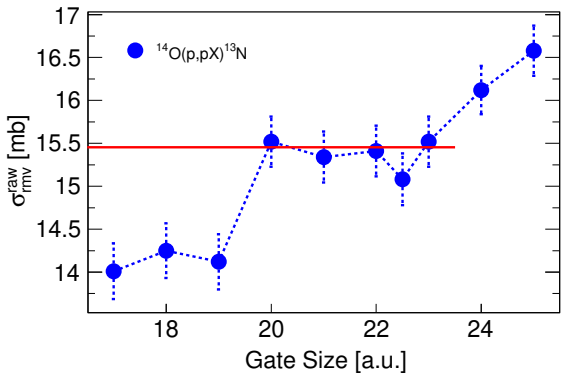

Figure 3.2: Uncorrected cross section, σ_{raw}, for proton removal reactions with ^{14}O projectiles on a calculated proton target versus the software gate (in arbitrary units).

The cross section errors are estimated as:

$$\Delta\sigma^{rmv} = \sqrt{(\Delta\sigma^{sta})^2 + (\Delta\sigma_{rmv}^{sys})^2} \tag{3.2}$$

being the total error the root of the sum of squares of systematic and statistical uncertainties.

On one hand, the statistics uncertainties, $\Delta\sigma^{sta}$, are related to the standard deviation of the Poisson distribution of the total entries, i.e. $\Delta Out_\tau = \sqrt{Out_\tau}$. In addition, standard deviations around the cross section mean, reckoned in the stable region, are included.

On the other hand, the systematic errors for removal channels, $\Delta\sigma_{rmv}^{sys}$, are associated to different correction factors and take different relative values which are explained below:

- The target thickness (ΔT_τ) has an estimated relative error of 2%.
- The error of geometrical acceptance factor, ΔGAF, was already discussed in Table 2.2 (see section 5.4.3). It has different values depending on the value of this correction, and increases significantly for smaller acceptance factors.

- The associated uncertainties of secondary reaction probabilities, ΔSRP, are estimated to be of the order of 5 % of the total factor.
- Uncertainties of *reaction trigger efficiency*, ΔRTE, are obtained quantifying the standard deviation of different RTE values calculated for the same reaction channel (see Table 2.3).

As a result, we have the following expression computing all errors mentioned above:

$$(\Delta\sigma_{sys}^{rmv})^2 = (\Delta T_\tau)^2 + (\Delta GAF)^2 + (\Delta SRP)^2 + (\Delta RTE)^2 \tag{3.3}$$

The majority of results of this work concern to neutron-deficient light nuclei. For these isotopes, the probability to find states de-exciting electromagnetically (*via* γ-ray) is rather low. These nuclei have tiny proton separation energies allowing de-excitation *via* proton emission (see Table 3.1). If we do not apply conditions in the selection of the final state of recoil fragment, our measurements are considered as inclusive. In some cases, the ejectile does not have any bound excited states below the proton emission threshold, and thus the cross section can be also considered directly a exclusive measurement since the fragment final state is unambiguously determined.

A	Isotope	S_n[MeV]	S_p[MeV]	Isotope	S_n[MeV]	S_p[MeV]	Isotope	S_n[MeV]	S_p[MeV]
12	^{12}C	18.7	16.0	^{12}N	15.0	0.6	^{12}O	-	-0.3
13	^{13}C	4.5	17.6	^{13}N	20.1	1.9	^{13}O	16.9	1.5
14	^{14}C	8.2	20.8	^{14}N	10.6	7.6	^{14}O	23.2	4.6
15	^{15}C	1.2	21.1	^{15}N	10.8	10.2	^{15}O	13.2	7.3

Table 3.1: Neutron and proton separation energies for carbon, nitrogen and oxygen nuclei (data are taken from [50]). Full table can be found in Appendix A.

For the rest of cases, the in-flight γ-rays detection by CB is needed to reach this selection.

3.1.1 Inclusive Results

Table 3.2 summarises inclusive cross sections results for single removal reactions of ^{14}O projectiles impinging on different targets, i.e. polyethylene, carbon and proton. Uncertainties are presented separately, and included statistical errors, in parenthesis; and systematic uncertainties coming from measurement process, in square brackets. The stability of cross section has been deeply studied following the explanation provided in Figure 3.2.

Some of the reported sections involve final fragments with excitation energies below (or close) to the lowest of the particle emission thresholds of these fragments (also see the Table A1 [49, 50]). In these cases, their cross sections can be considered as exclusive,

as the example with ^{14}O projectiles shown. To differentiate which measurements are inclusive and exclusive we add superscripts "i" and "e".

Target	$\sigma_{p-rmv}[mb]$	$\sigma_{n-rmv}[mb]$
$(CH_2)_n$	70.21 (1.40) [6.32]	67.23 (1.39) [8.07]
C	39.6 (2.28) [3.56]	36.9 (2.31) [4.43]
H	15.45 (0.32) [1.39]	15.16 (0.33) [1.82]

Table 3.2: Corrected cross section for one-proton and neutron removal channels with ^{14}O projectiles impinging on different targets. Statistical and systematic uncertainties are shown in parenthesis and square brackets respectively.

Figures 3.3 and 3.4 depict single proton and neutron-removal cross sections for oxygen (from neutron drip line, A=13, to A=22) and nitrogen (from A=12 to A=16) projectiles measured in this work (only statistics uncertainties are represented). Dashed lines simply link the experimental points to guide the eye.

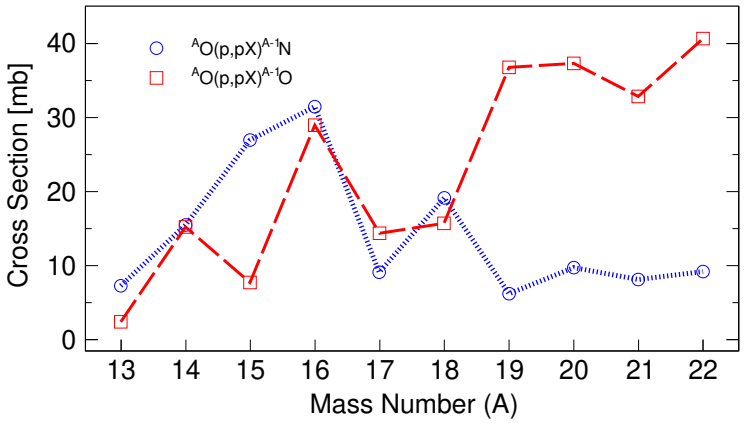

Figure 3.3: Single-proton and neutron removal cross sections for the oxygen chain (covering $A = 13 - 22$). Data includes only statistical errors.

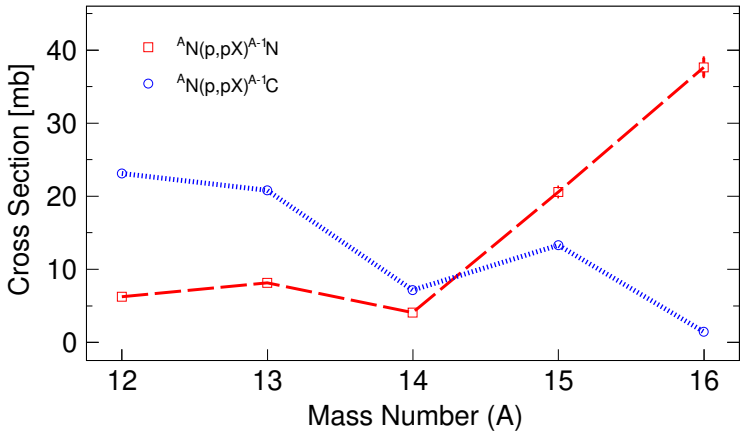

Figure 3.4: Single-neutron removal cross sections for nitrogen isotopes (covering $A = 12 - 16$). Data includes only statistical errors.

At first glance, and for both stable isotopes studied (^{16}O and ^{14}N), the measured cross sections are, as expected, similar for neutron and proton channels. We observe that one-proton removal cross sections induced by neutron-deficient oxygen decrease with the mass number (A). The opposite situation happens with nitrogen projectiles. The explanation will be that this channel transform nitrogen into more stable carbon nuclei and will be commented in detail in the next chapter.

3.1.2 Exclusive Results

We present the results associated to exclusive measurements. They correspond to few cases in which it is feasible to disentangle the final state of the recoil nucleus, i.e. either in its ground or in a γ-bound excited state, using in-flight γ-rays spectroscopy.

Reference Case: ^{16}O(p,pX)^{15}N

We start using as reference case the ^{16}O. It corresponds to a stable nucleus that would allow comparison with data collected in direct kinematics data [8, 76]. Figure 3.6 corresponds to a level sequence of ^{15}N that would help to interpret the reconstructed γ spectrum.

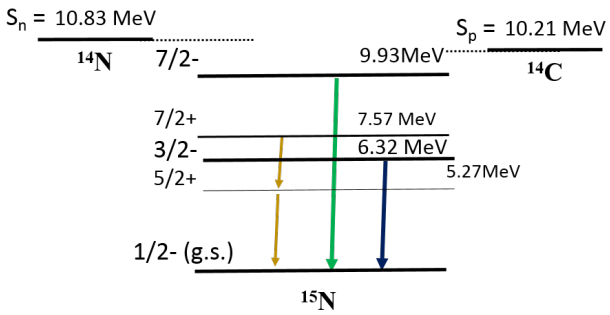

Figure 3.5: Level scheme for ^{15}N using the available data from [50]. Arrows correspond to the most probable transitions in terms of spin and parity rules. In order to reproduce a narrow peak observed around 2.5 MeV an excited state of 7/2+ has been included. However, as Figure 3.6 depicts, we achieve the best fitting considering the green and blue γ-rays, i.e. 7/2- and 3/2- excited states.

The reconstructed γ spectrum of ^{15}N de-excitation after single-proton removal reactions with ^{16}O projectiles is depicted with black dots in Figure 3.6.

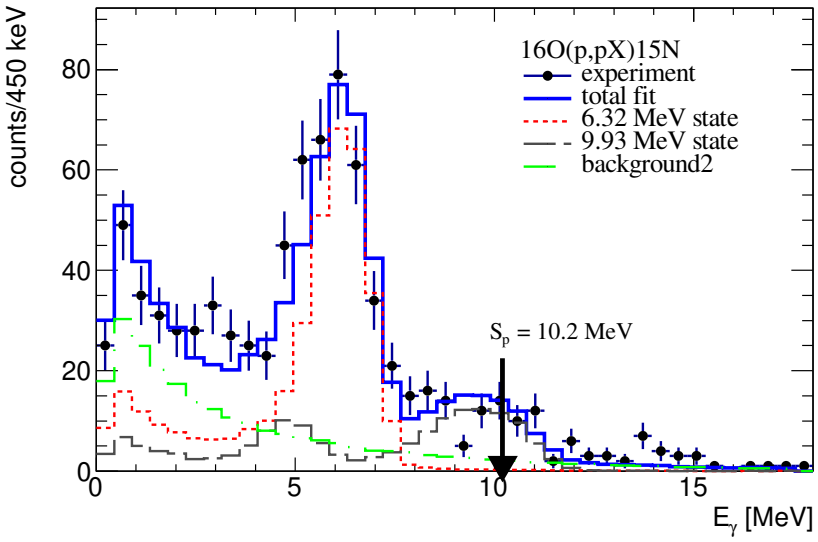

Figure 3.6: Gamma spectrum of ^{15}N fragments de-excitation after one-proton removal reactions induced by ^{16}O. Data are adjusted using simulations of the states previously shown in the level scheme (considering spin and parity rules for the transitions). The fit procedure yields a χ^2_{red}=1.40.

The identification of states involved into the de-excitation process is performed considering only the most probable transitions in terms of spin and parity rules. The main

peak is interpreted as a transition from 3/2- state to ground state with $E_\gamma = 6.32$ MeV. Other peak registered falls around 10 MeV and it is identify with another 3/2- state with $E_\gamma = 9.93$ MeV transition to the ^{15}N ground state.

γ Spectrum Interpretation

In order to obtain the global fit shown in Figure 3.6 (and also Figure 3.7) it is necessary to go through software reconstruction. The procedure adopted has some limitation, we decide to use addback algorithm which recover information of γ-rays as the section 2.3.1 in Chapter 2. Our addback program takes individual low-energy thresholds (around hundreds of keV for each crystal) to reproduce the experimental response of CB detection channels. In addition CB calibrations were performed with natural radioactive sources covering γ energies below 2 MeV, which are far away of the high energy γ-rays detected (around 6-10 MeV). The combination of these effects produces fluctuations in reconstructed events that are particularly relevant for transition energies above 10 MeV. For that reason, excited states above 10 MeV are not properly reconstructed. It should be note that the current addback routine includes the experimental energy resolution of each crystal to reproduce the experimental conditions. The assignment of the relative probabilities for the studied transitions considered is performed with simulations in the R^{3}BRoot framework.

Each experimental γ spectrum was fitted with a simulated response that includes background, f_{bg} , and different states contributions, f_j. We extract in this way information about the populations of the different final states, and thus, we deduce exclusive cross sections.

$$f = \sum_j \alpha_j f_j + \beta_{bg} f_{bg} \tag{3.4}$$

The ground state contribution is achieved using reaction channels without γ rays (anti-coincidence), where additionally a background contribution is included. For the excited states, we have considered the most probable states according to parity conservation rules, obtained from the decay scheme of [50], including γ cascades in some cases.

Populations of excited states are estimated from the ratios between events in each state to the total as follows:

$$P_j = \frac{N_j^{exp}}{N_{total}^{exp}} \tag{3.5}$$

where N_j^{exp} is reckoned normalising the simulated events with the ratio between the integral of the fitted events and the simulated ones.

$$N_j^{exp} = N_j^{sim} \cdot \frac{Int_j^{fit}}{Int_j^{sim}} \tag{3.6}$$

The background events are determined by subtracting the excited state contributions from the total events.

$$N_{bg} = N_{total}^{exp} - \sum_{j} N_{j}^{exp} \tag{3.7}$$

Finally, Table 3.3 exhibits the populations rates of ^{16}O(p,pX)^{15}N reaction for those level aforementioned (see Figure 3.6).

State	$P_{p-rmv}(\%)$
g.s.	31.2 (3.2)
^{1st} at 6.32 MeV	48.1 (2.3)
^{2nd}at 9.93 MeV	20.7 (0.8)

Table 3.3: Populations rates for a single-proton removal channel with ^{16}O projectiles.

The uncertainties associated to population rates are obtained applying the error propagation theory. They include binning variations into the γ spectrum and a 10% coming from the individual thresholds of crystals in the addback algorithm, which are 4%, a bit larger uncertainty than previous works reports [30].
The best results in terms of χ^2 analysis are retained (for Figure 3.6 a χ^2_{red} 1.40 value is achieved[1]).

Experimental Spectra for ^{14}N Fragments

We proceed now to the study of tow reactions ^{15}O(p,pX)^{14}N and ^{15}N(p,pX)^{14}N, that lead to ^{14}N depicted in Figure 3.7

We detect two peaks, one of them falls around 2 MeV and the another is registered between 6 and 7.5 MeV, being wider than the former one. As we mentioned before, spin and parity rules bring information about which states are more probables. Using spectroscopic information of ^{14}N(Figure 3.8) we could associated the first peak to a transition from 0+ state with a $E_{\gamma}^{1st} = 2.31 MeV$ to the ground state. The other one, can be estimated as superposition of two γ-rays with $E_{\gamma}^{2nd} = 6.20 MeV$ and $E_{\gamma}^{3rd} = 7.03 MeV$ from 1+ and 2+ excited states, respectively, that also feed the ground state 1+. Additionally the 1+ excited state located at 6.20 MeV can be de-excited via a γ-ray cascade with a probability of 23.1% respect to the main γ-ray.

[1] $\chi^2_{red} = \chi^2/\nu$

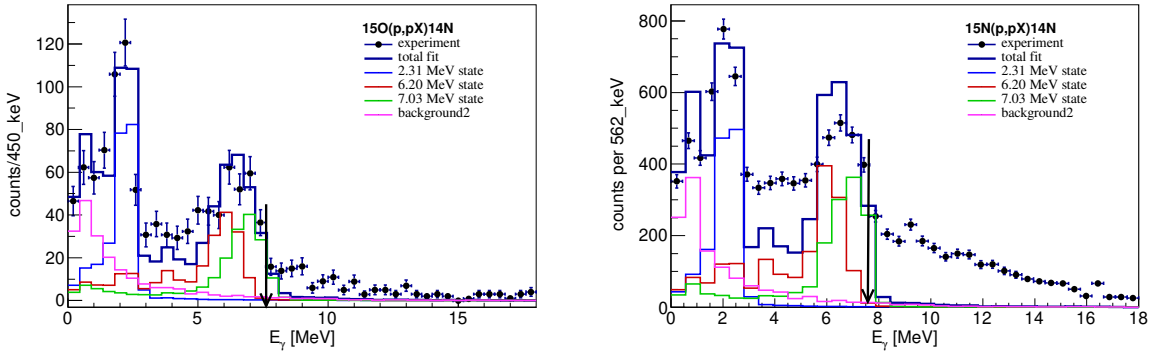

Figure 3.7: Gamma spectrum of ^{14}N fragments under proton removal conditions. The spectrum has been obtained with ^{15}O (left) and ^{15}N (right) projectiles on a proton target. Three excited states have been considered into the simulations and depicted separately (see level scheme of ^{14}N Figure 3.8). The total fit includes the atomic background with the three excited states. To fit spectra an special option which takes into account the integral of function in bin instead of value at bin centre has considered up to proton separation energy, $S_p(^{14}N) = 7.6MeV$, displayed with a vertical black arrow.

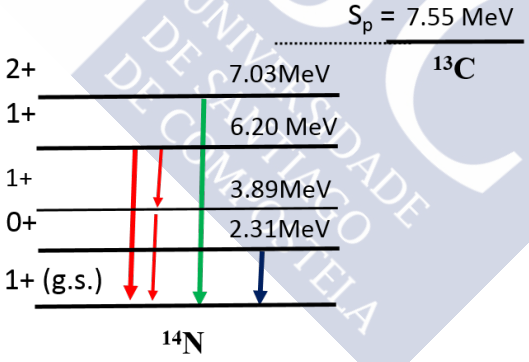

Figure 3.8: Levels observed for ^{14}N gamma spectrum.

It should be noted that the different reactions were registered in separate settings. Even thought we detect different strengths for one-proton and one-neutron removal channels, when we include the associated uncertainties, both populations are in good agreement.

The estimated population rates for 2^{nd} and ^{3rd} excited states are similar in both reaction channels. Differences appear for ground state and 1^{st} state rates, where the background in ^{15}N(p,pX)^{14}N reaction becomes important and it increase the g.s. contribution. The events observed above 8 MeV in the one-neutron spectrum come from an

incomplete carbon subtraction and we are still analysing this effect.

State	$P_{^{15}O(p,pX)^{14}N}(\%)$	$P_{^{15}N(p,pX)^{14}N}(\%)$
g.s.	42.24 (3.22)	48.42 (1.07)
^{1st} at 2.32 MeV	20.70 (1.02)	14.85 (0.61)
^{2nd}at 6.20 MeV	20.13 (0.99)	19.95 (0.82)
^{3rd}at 7.02 MeV	16.93 (0.91)	16.78 (0.69)

Table 3.4: Population rates for ground state and three excited level considered according to 3.8 for ^{14}N fragments. Second and third columns are related to single-proton and neutron removal reactions induced by ^{15}O and ^{15}N on a proton target. Uncertainties in parenthesis are purely statistical ones.

3.1.3 Momentum Distributions

Momentum distributions of the recoil fragments after one step removal reactions at relativistic energies can be interpreted as a footprints of the angular momentum (l-value) of the removed nucleon.

The R^{3}B-LAND set-up give us the possibility to reconstruct tri-momenta associated to the outgoing channel. In addition, parallel ($P\|$) and perpendicular ($P\perp$) components can be extracted. An inspection of momentum distributions, obtained in a complete kinematics experiments, can bring a certain amount of information.

- The centroid position of the transverse components (P_x and P_y) contains information on the energy transferred in the removal reaction. This information will be used to compare with the Quasi-Free Scattering case and explain the differences due to absorptive processes contributiomns.

- The width and in a greater extent the shape of the momentum distributions have been extensively used to gain spectroscopic information of the projectile. We should note that due to the low statistics we had, and also to the fact that the majority of the nucleons involved are in p-orbitals, these observables will be difficult to exploit to pi-down valuable single-particle information. For this reason we will concentrate the discussion on few selected cases.

Figure 3.9 displays both perpendicular components, i.e. P_x and P_y of the transverse momentum distributions of ^{13}N fragments from single-proton removal reactions on a carbon (top) and on a polyethylene targets (bottom) following the procedure described in section 2.6 of Chapter 2.

In this particular setting (neutron-deficient nuclei), reactions on carbon target have significantly less statistics than the ones on polyethylene. This issue affects to the final measurements since the carbon subtraction can produce some artefacts when extracting

the momentum distributions on a proton target. To minimise this effect a investigation varying the binning of the momentum distributions was performed. Thus, the binning chosen is limited by the low events obtained with the carbon target run.

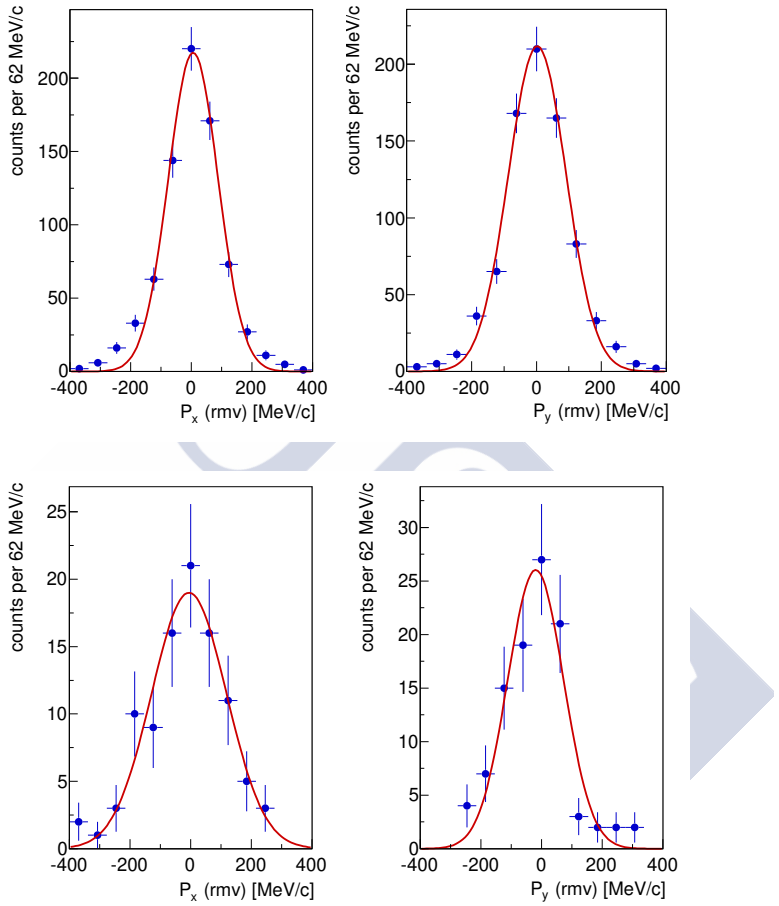

Figure 3.9: Momentum distributions of ^{13}N fragments of the transverse components (P_x and P_x) displayed from removal reactions of ^{14}O projectiles on different targets (polyethylene - first row -, carbon - second row).

Next Figure 3.10 depicts P_x and P_y distributions of ^{13}N fragments after one proton removal reactions for ^{14}O projectiles on a proton target. In this case, the presented momentum distributions are normalised to the single-proton cross section. In these cases we increase the previous binning by a factor of to minimise fluctuations in the (smaller or larger) momentum tails. Finally, we exhibit in Figure 3.11 transverse and longitudinal momentum distributions obtained for the same reaction channels. We can complete the description showing same momentum distributions for ^{13}O fragments produced by single-neutron removal reaction (see Figure 3.12).

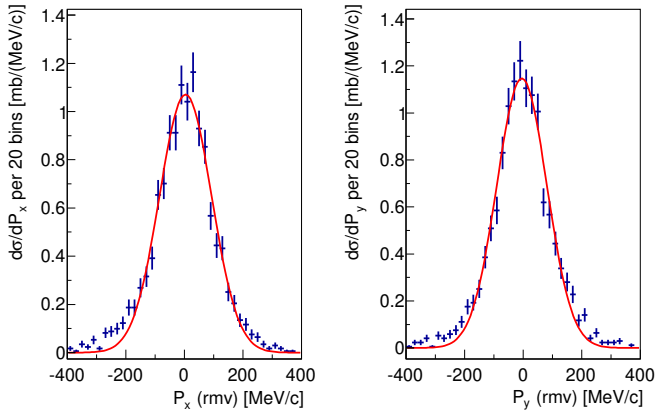

Figure 3.10: Momentum distributions of ^{13}N fragments of both transverse components, i.e. P_x and P_y, normalise to the single-proton cross section. Fragments have been obtained from removal reactions of ^{14}O projectiles on a proton target contribution.

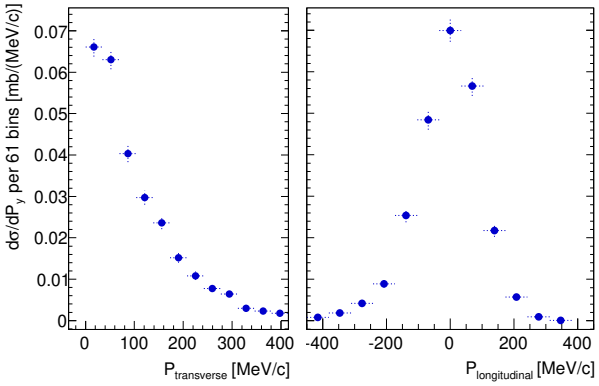

Figure 3.11: Total transverse and longitudinal momentum distributions in the centre-of-mass of ^{13}N fragments after ^{14}O projectiles knocked-out a single-proton on a proton target.

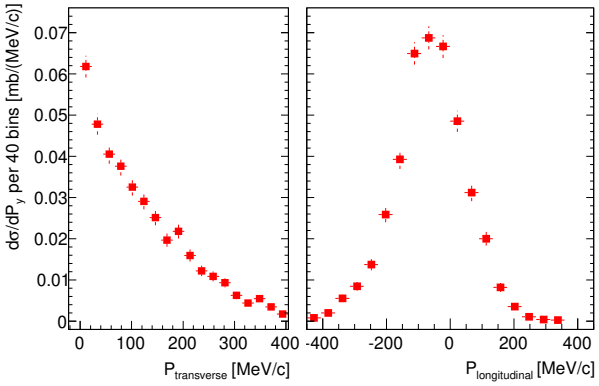

Figure 3.12: Total transverse and longitudinal momentum distributions in the centre-of-mass of ^{13}O fragments after ^{14}O projectiles knocked-out a single-neutron on a proton target.

Even though, we obtained slightly asymmetrical longitudinal momentum distributions, Gaussian fits between (-400,400) MeV/c are performed to extract the σ parameter which is linked with FWHM through the equation $FWHM = 2\sqrt{2ln2}\sigma = 2.355\sigma$. We also include information in our tables of the RMS (Root Mean Square). .

As it was explained in section 2.6 we remind that we use the positions measurements[2] registered by in-beam silicon detectors to calculate the momenta of nuclei.

We should mention that one of the silicon detectors used to register positions measurements[3], DSSSD1, had some operation issues[4]. This fact was also observed in previous works of [27, 32] which reported the same malfunction in the s-side of DSSSD1. This disadvantage affects in some cases to the P_x evaluation.

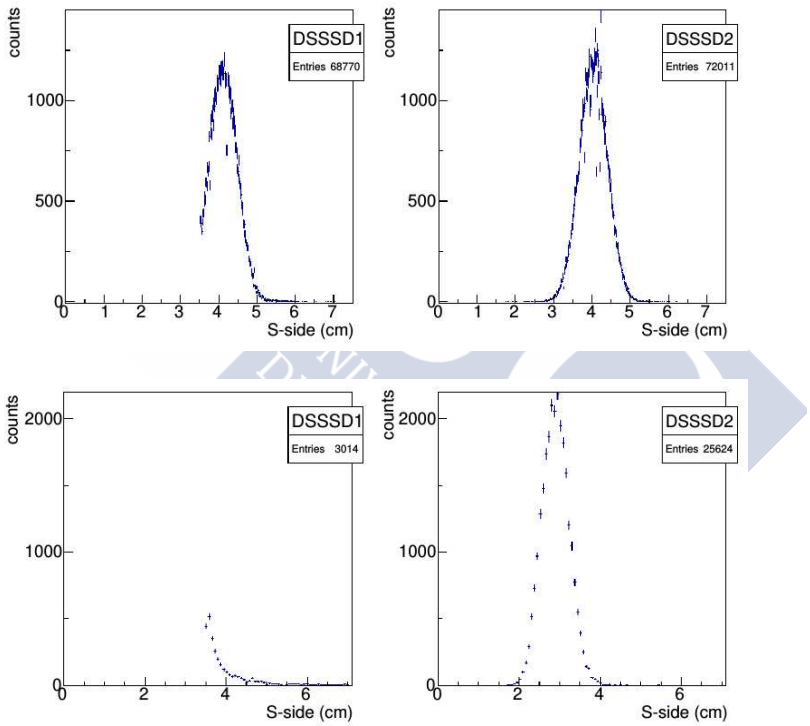

Figure 3.13: Signals form S- sides belong to the two first in-beam silicon detectors (DSSSD1 and DSSSD2). The setting 1 and ^{14}O projectiles have been selected for the top figure, whereas in the bottom we have depicted setting 2 and ^{16}O. A slightly cut is appreciate for the S-side of DSSSD1 for setting 1 and huge event-losses for setting 2; the rest strips in both settings worked perfectly.

[2]these detectors were located in front of the target and allow to calculate the incoming angles of projectiles

[3]these detectors were located in front of the target and allow to calculate the incoming angles of projectiles, and therefore to obtain the momenta of nuclei

[4]several strips in the s-side of DSSSD1 did not registered signals, concretely from 0.0 to 3.4 cm

For neutron-deficient configuration, in particular for an incoming selection of ^{14}O projectiles the top pictures in Figure 3.13 depict, the incomplete signal (bottom left histogram) recorded in the s-side of DSSSD1. The missing ratio of events in this case (for projectiles belonging to setting 1) is not very important, around of 5% of the total incoming events, and allows to reconstruct adequately both components of the transverse momentum. However, we will focus our analysis on P_y solely since for the rest of nuclei studied (stable and neutron-rich projectiles, which are belonged to other settings, as bottom pictures in Figure 3.13 show) statistics registered was not sufficiently to reconstruct P_x, being the missing rate are around of 50%.

3.1.4 Summary of the Results

Cross sections for one proton and one neutron removal reactions induced by oxygen and nitrogen projectiles on a proton targer are summarised in Tables 3.6, and 3.7 respectively. Additionally RMS and FWHM measurements, obtained from P_y component of transverse momentum distribution, are presented[5]. Full tables can be found in Appendix D.

Reaction	E_p [MeV]	σ_{exp} [mb]	RMS [MeV/c]	$FHWM$ [MeV/c]
^{13}O(p,pX)^{12}N	397	7.26 (0.46) ^{e}	92.6 (3.0)	204.4 (7.5) ^{e}
^{14}O(p,pX)^{13}N	349	15.45 (0.32) ^{e}	105.7 (1.5)	236.6 (4.8) ^{e}
^{15}O(p,pX)^{14}N	308	26.91 (0.73) ^{i}	114.9 (1.9)	259.6 (5.6) ^{i}
^{16}O(p,pX)^{15}N	450	31.42 (0.62) ^{i}	117.5 (1.5)	266.4 (4.9) ^{i}
^{17}O(p,pX)^{16}N	406	9.11 (0.61) ^{e}	114.0 (1.3)	257.5 (4.6) ^{e}
^{18}O(p,pX)^{17}N	369	18.68 (0.63) ^{i}	115.5 (2.7)	261.5 (7.0) ^{i}
^{19}O(p,pX)^{18}N	442	6.08 (0.46) ^{i}	116.7 (2.7)	264.6 (7.1) ^{i}
^{20}O(p,pX)^{19}N	415	9.69 (0.45) ^{i}	121.1 (2.2)	275.5 (6.1) ^{i}
^{21}O(p,pX)^{20}N	448	8.09 (0.10) ^{e}	120.0 (1.3)	272.5 (4.7) ^{e}
^{22}O(p,pX)^{21}N	414	9.12 (0.10) ^{i}	120.1 (1.8)	272.8 (5.3) ^{i}

Table 3.5: Results for one proton removal reactions of oxygen projectiles on a proton target. Reaction channel, energy at the middle of the target, corrected x-removal cross section, Root Mean Square values (RMS) and Full Width at Half Maximum (FWHM) (after straggling subtraction) of the P_y component of the transverse momentum are shown. Symbols ^{i} and ^{e} denote exclusive and inclusive measurements respectively. The statistical uncertainties appears between parenthesis at the right side of each value and include the standard deviations.

All cross sections are calculated using the measurements from the stable region and only statistical errors are displayed (in brackets).The relative systematic uncertainties are about $7-8\%$ and $10-12\%$ for one-proton and neutron removal reactions respectively

[5]Only FWHM values include intrinsic resolution and straggling effects see equation 2.17.

Reaction	E_p [MeV]	σ_{exp} [mb]	RMS [MeV/c]	$FHWM$ [MeV/c]
^{13}O(p,pX)^{12}O(*)	397	2.38 (0.24) ^{i}	-	-
^{14}O(p,pX)^{13}O	349	15.16 (0.33) ^{e}	113.4 (2.3)	259.7 (6.9) ^{e}
^{15}O(p,pX)^{14}O	308	7.68 (0.54) ^{e}	102.1 (5.5)	231.9 (13.7) ^{e}
^{16}O(p,pX)^{15}O	450	28.93 (0.59) ^{i}	113.0 (2.0)	257.8 (6.6) ^{i}
^{17}O(p,pX)^{16}O	406	14.33 (0.92) ^{i}	115.0 (1.5)	266.9 (6.5) ^{i}
^{18}O(p,pX)^{17}O	369	15.66 (0.49)^{i}	105.5 (3.1)	239.0 (8.4) ^{i}
^{19}O(p,pX)^{18}O	442	36.73 (0.61) ^{i}	120.5 (1.4)	274.3 (5.4) ^{i}
^{20}O(p,pX)^{19}O	415	37.28 (0.52) ^{i}	112.3 (1.5)	254.8 (5.3) ^{i}
^{21}O(p,pX)^{20}O	448	37.79 (0.47) ^{i}	116.8 (1.0)	266.1 (4.5) ^{i}
^{22}O(p,pX)^{21}O	414	40.64 (0.47) ^{i}	116.4 (1.3)	265.9 (5.1) ^{i}

Table 3.6: Results for one proton removal reactions of oxygen projectiles on a proton target. Reaction channel, energy at the middle of the target, corrected x-removal cross section, Root Mean Square values (RMS) and Full Width at Half Maximum (FWHM) (after straggling subtraction) of the P_y component of the transverse momentum are shown. Symbols ^{i} and ^{e} denote exclusive and inclusive measurements respectively. The statistical uncertainties appears between parenthesis at the right side of each value and include the standard deviations. The cross section of the reaction ^{13}O(p,pX)^{12}O(*) has been calculated via de-excitation of unbound nuclei ^{12}O in ^{10}C fragments in coincidence with the dectection of 2 proton-signals into the proton arm. It is an inclusive measurement since we do not apply any γ conditions to select either the ground state or excited states (which have been observed in [77]).

(see equation 3.3). Uncertainties of FWHM values, include the subtraction of intrinsic resolution and straggling effects.

Reaction	E_p [MeV]	σ_{exp} [mb]	RMS [MeV/c]	$FHWM$ [MeV/c]
^{12}N(p,pX)^{11}C	370	23.11 (0.33) [i]	103.5 (1.0)	229.6 (4.4)
^{13}N(p,pX)^{12}C	323	20.83 (0.45)[i]	112.5 (1.6)	269.1 (5.2)
^{14}N(p,pX)^{13}C	368	7.10 (0.34) [i]	111.4 (3.5)	249.3 (8.6)
^{15}N(p,pX)^{14}C	401	13.23 (0.50)[i]	115.7 (0.8)	260.4 (5.4)
^{16}N(p,pX)^{15}C	471	1.41 (0.17) [i]	*102.0 (9.7)*	*225.9 (21.9)*

Reaction	E_p [MeV]	σ_{exp} [mb]	RMS [MeV/c]	$FHWM$ [MeV/c]
^{12}N(p,pX)^{11}N(*)	370	6.22 (0.16) [i]	108.8 (3.7) *	245.2 (7.8) *
^{13}N(p,pX)^{12}N	323	8.12 (0.32) [e]	118.6 (4.4)	269.0 (11.1)
^{14}N(p,pX)^{13}N	368	4.01 (0.41) [e]	94.3 (5.2)	208.6 (12.0)
^{15}N(p,pX)^{14}N	401	20.53 (0.70) [i]	116.4 (0.7)	263.6 (4.2)
^{16}N(p,pX)^{15}N	471	37.64 (1.29) [i]	112.4 (3.7)	253.6 (9.5)

Table 3.7: Measured cross section of single-proton and neutron removal reactions for nitrogen projectiles on a proton target. RMS and FWHM are obtained from ^{10}C fragments in coincidence with 1-proton signals into the proton arm since ^{11}N is an unbound nucleus and the most probable de-excitation channel is the proton-evaporation.

USC
UNIVERSIDADE
DE SANTIAGO
DE COMPOSTELA

Chapter 4

Quasi-Free Scattering

We present in this chapter cross sections and fragment momentum distributions for reactions induced by exotic projectiles on a proton target under Quasi-Free Scattering (QFS) condition.

In QFS channels, the particle kinematics is close to the free scattering between incoming and outgoing nucleons. These reactions are a valuable tool to extract single particle information of nuclei involved in the reaction. QFS has been extensively applied in direct kinematics using high energy protons (or electron beams) impinging on stable targets [6, 7, 8]. The versatile R^3B-LAND set-up has allowed the extension of this kind of studies to unstable isotopes in inverse kinematics The simultaneous detection of two angle-correlated knocked nucleons (one belonging to the target and another coming from the projectile) in coincidence with incoming projectile and emerging fragment signals can be achieved. The rather strict kinematic correlations between the two light nucleons ensures that we are selecting one step reactions.

In this analysis, we have covered the species previously studied in the single nucleon removal channels, focusing on neutron-deficient region for two nuclear chains with charges Z=8 and Z=7.

The notation followed to identify these channels is ${}^{A}_{Z}X(p,pn)^{A-1}_{Z}X$ for (p,pn) reactions, where the charge of incoming and outgoing nucleus is conserved. Whereas, in (p,2p) channels the nuclear ejectile reduces a unit its charge, i.e. ${}^{A}_{Z}X(p,2p)^{A-1}_{Z-1}Y$.

Incoming projectile and outgoing fragment identifications for each QFS channel follow procedures described in Chapter 3. In order to detect the footprints from the two outgoing nucleons we reconstruct two high energy signals, recorded by CB calorimeter and keeping a relative polar angle minor than 90 deg.

In order to avoid unnecessary repetitions we show an example of the identification of QFS reaction induced by ^{14}O, which is displayed on the right picture of Figure 4.1.

The drawn ellipses correspond to the determination of QFS events; i.e. Out_{τ}^{QFS} for (p,2p) inside the solid red curve, and for (p,pn), into dashed blue ellipse (under *reaction trigger* condition). The left picture in Figure 4.1 displays the number of incoming projectiles recorded under *fragment trigger* which reach the TFW, and allow us to evaluate Inc_{τ}.

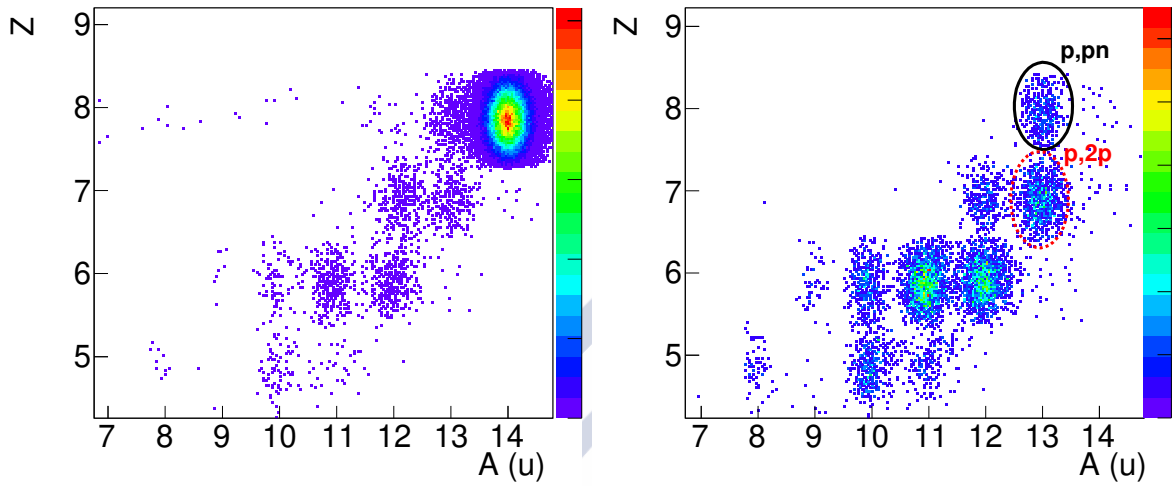

Figure 4.1: Left picture depicts a fragment identification matrix (Z versus A) for ^{14}O projectiles on a CH_2 target under *fragment trigger* - left picture - and under QFS condition together with *reaction trigger* - right one. To emphasise the QFS identification of (p,pn) and (p,2p) channels solid black ellipse and dashed red ellipse have been depicted.

This example is of interest, since fragments coming from $^{14}O(p,2p)^{13}N$ and $(p,pn)^{13}O$ reactions correspond in both cases to final recoil nucleus with small proton separation energies, i.e. $S_p(^{13}O) = 1.5MeV$ and $S_p(^{13}N) = 1.9MeV$. An inspection on the structure of these nuclei shows that they do not have bound excited states below the proton emission threshold[1] and, thus, yield us to exclusive measurements.

4.1 Cross Sections and Fragment Momentum Distributions for QFS

Cross sections and reconstructed momentum distributions for QFS channels are presented in this section. The extra detection of two angle-correlated nucleons limits in some cases statistics producing large uncertainties. Systematical uncertainties for (p,2p) and

[1] We have confirmed this fact since we have not registered footprints of γ-rays in the γ spectra or other products like a nucleus plus light particles.

(p,pn) channels are fixed at 6% and 13% of the (mean) evaluated cross sections (further details can be found in section 2.5.2). The corresponding momentum distributions of the vertical projection "y" of the transverse component, P_y, are settled in the Appendix C, together with distributions extracted for the single-nucleon removal channels. In this section, only the average of RMS and FWHM estimated for the aforementioned P_y distribution, is shown.

Figures 4.2 and 4.3 display the cross sections of (p,2p) - blue circles - and (p,pn) - red squares - QFS channels measured for oxygen (A=13-22) and nitrogen (A=12-16) projectiles. In addition, Tables 4.1, 4.3, 4.2 and 4.4 summarise for each reaction the energy at the middle of the target, the calculated cross sections, RMS and FWHM for P_y momentum distributions[2]. We denote with symbols ^{i} and ^{e} inclusive and exclusive measurements, and we show in parenthesis statistical uncertainties.

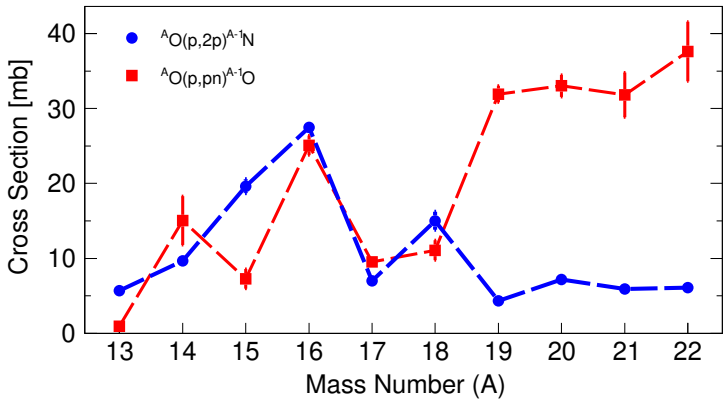

Figure 4.2: Cross sections as a function of the projectile mass number for (p,2p) - blue circles - and (p,pn) - red squares - channels induced by oxygen projectiles on a proton target.

General features observed in the systematic study of QFS cross sections can be explained using "simple" nuclear structure arguments, such as particle separation energies (settled in Table A1 of Appendix A), and the independent-particle model (IPM).

It should be noted that cross sections of ^{13}O(p,pn)^{12}O(*) and ^{12}O(p,pn)^{11}N(*) have not been directly measured due to the fact that both fragments are unbound. ^{12}O breaks up into ^{10}C plus two protons and the ^{11}N ejectile de-excites to one proton plus ^{11}C. Using the spectroscopic information reported in [78, 77] we could infer the inclusive cross section of the ground and some excited states resonances of ^{12}O. Similarly the inclusive measurement of ^{11}N was achieved ground and, at least, one excited states reported in [79, 80]. These measurements needed the use of the proton arm to detect the emitted protons from the unbound fragments, in coincidence with the carbon final fragments recorded in the

[2]FWHM results are corrected by intrinsic momentum resolutions and straggling effects.

fragment arm. These processes must be corrected by the one or two protons detection efficiency, evaluated in the R^{3}BRoot framework using GEANT4 simulations (explained in section 2.5.2), and yield to $EFF_p = 0.62 \pm 0.07$ and $EFF_{2p} = 0.45 \pm 0.15$, respectively.

We analyse in detail the cross section as follow,

- We focus firstly on (p,2p) and (p,pn) reactions induced by oxygen projectiles. We use particle separation energies of the final fragments (taken the smallest value) to compare the relative stability (see Table A1). The cross section of ^{15}O(p,2p)^{14}N is found to be larger than the measured for the (p,pn) channel (i.e. ^{15}O(p,pn)^{14}O). The fragment ^{14}O has a smaller proton separation energy than his mirror nuclei ^{14}N, i.e. $S_p(^{14}O) < S_p(^{14}N)$. Therefore, energetically speaking, ^{14}N is more stable than ^{14}O; being the (p,2p) cross section larger than the calculated for (p,pn) channel. Similar behaviour is observed for reactions induced by ^{18}O projectiles, where the (p,pn) cross section is smaller than the measured for (p,2p) channel, due to $S_n(^{17}O) < S_n(^{17}N)$. Cross sections associated to (p,2p) and (p,pn) channels for the ^{16}O projectile are similar, with the (p,2p) channel slightly higher than the (p,pn). This could also be explained considering that similar structure of protons and neutrons and being ^{15}O a nucleus less bound than ^{15}N, i.e. $S_p(^{15}O) < S_p(^{15}N)$.

- We describe the systematics observed for oxygen isotopes in (p,2p) and (p,pn) channels. For both data-sets, two zones are clearly observed (see Figure 4.2), and allow us to divide the discussion in neutron-deficient and -rich projectiles.

  For (p,2p) channel the proton is always removed-out from the same orbital, i.e. $p_{1/2}$ level [3]. We firstly focus on neutron-rich nuclei (from A=19) where cross sections are rather similar, around 6-7 mb. Moving to the stable zone, a relative maximum in cross sections is observed for ^{16}O projectile. And for the neutron-deficient side we appreciate a inverse proportional reduction in the cross sections with A going towards proton-drip line. It can be explained because the fragment S_p threshold reduces accordingly and the proton evaporation becomes a relevant channel that is opened at low energies. Therefore, nitrogen fragments could transform in a more stable carbon isotope (reducing the measured cross section) if they get enough excitation energy.

  For the (p,pn) channel the removed neutron can stay in different orbitals, i.e. for $^{13-14}$O projectiles valence neutron is in $p_{3/2}$, for $^{15-16}$O it stays in $p_{3/2}$, and for $^{17-22}$O it stays in $d_{5/2}$. (p,pn) cross sections are also show in Figure 4.2 (red squares). For the neutron-rich projectiles, we observe a smooth growth of the cross section with the projectile mass (from 30 mb up to approx. 40 mb), that could be explained with the simply fact that more neutrons can participate in the reactions, enlarging

[3] from an extreme IPM description, this level corresponds to the closest one to the Fermi level and it is utterly filled for oxygen isotopes.

their cross sections. Moreover, the neutron separation energy in neutron-rich oxygen isotopes is rather constant with some small fluctuation due to even-odd changes in the projectile mass number. These see-saw effects are also reproduced in our measurements where higher cross sections are related to even-even projectiles. On the contrary, in neutron-deficient region de-excitation *via* proton emission becomes highly probable related to low separation energies of this channel. The cross section increase with the projectile mass number, and it reaches a maximum at A=16.

- We concentrate on ^{15,14}O projectiles leading to ^{14,13}O fragments. One would expect that the cross section of ^{15}O(p,pn)^{14}O reaction should be a bit larger than, a priori, the less probable channel ^{14}O(p,pn)^{13}O. However, we observe the opposite effect that can be understood as having more nucleons candidates. For ^{14}O projectile we find up to four neutrons settled in $p_{3/2}$ below the Fermi level, while the next orbit, $p_{1/2}$, is empty and above the Fermi level and relatively close in energy to the filled shell. The heavier ^{15}O nucleus has a unique valence neutron at $p_{1/2}$ orbit, the closest to the Fermi level, and the others four stay in a deeper and complete shell,$p_{3/2}$ where it is less probable to knock-out a neutron, and particle-hole excitations are also less common than for the ^{14}O nucleus.

An extension of this analysis was performed to nitrogen neutron-deficient isotopes covering from A=12 to A=16 (see Figure 4.3).

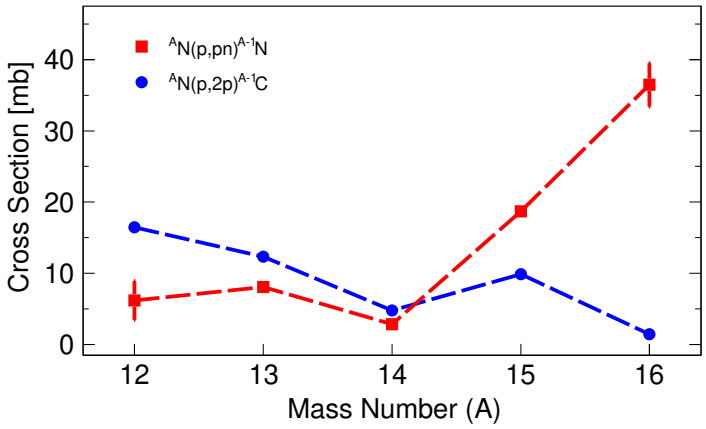

Figure 4.3: Cross sections for (p,2p) - blue circles - and (p,pn) - red squares - channels induced by nitrogen isotopes from covering $A = 12$ to $A = 16$).

- The (p,2p) channel transforms nitrogen projectiles into carbon nuclei which are, in principle, more stables (see blue circles in Figure 4.3). We observe reduction while A increases, a contrary effect to what we had for the same reaction on neutron-deficient oxygen. The cross section increases when the projectile is approaching to

the proton drip line. Additionally, the kink in ^{15}N of the (p,2p) systematic is due to the larger stability of the final ^{14}C fragments respect to his neighbours ^{13}C and ^{15}C.

- For (p,pn) cross sections (red squares in Figure 4.3). From the stable ^{14}N and goind to heavier projectiles, a linear growth in the cross section is observed, since the reaction yields to a nitrogen with one neutron less (reaching a A-1 fragment), which are more stable fragments. The cross sections for neutron deficient nitrogen projectiles (^{12,13}N) are rather constant around 6-7 mb.

Reaction	E_p [AMeV]	σ^{p2p}_{exp} [mb]	RMS [MeV/c]	$FWHM$ [MeV/c]
^{13}O(p,2p)^{12}N	397	5.67 (0.57) ^{e}	103.0 (11.9)	233.9 (28.1) ^{e}
^{14}O(p,2p)^{13}N	349	9.67 (0.48) ^{e}	102.9 (4.8)	231.3 (11.2) ^{e}
^{15}O(p,2p)^{14}N	308	19.63 (0.93) ^{i}	107.6 (4.1)	245.5 (10.5) ^{i}
^{16}O(p,2p)^{15}N	450	27.48 (0.71) ^{i}	113.0 (3.0)	257.9 (7.9) ^{i}
^{17}O(p,2p)^{16}N	406	6.99 (0.39) ^{e}	113.7 (3.4)	259.0 (8.8) ^{e}
^{18}O(p,2p)^{17}N	369	15.02 (1.27) ^{i}	108.3 (5.7)	246.0 (13.9) ^{i}
^{19}O(p,2p)^{18}N	442	4.34 (0.45) ^{i}	126.6 (6.1)	292.1 (15.0) ^{i}
^{20}O(p,2p)^{19}N	415	7.17 (0.47) ^{i}	124.4 (6.0)	286.1 (14.7) ^{i}
^{21}O(p,2p)^{20}N	448	5.91 (0.28) ^{e}	114.7 (5.0)	261.3 (12.6) ^{e}
^{22}O(p,2p)^{21}N	414	6.10 (0.45) ^{i}	128.4 (9.1)	297.1 (21.9) ^{i}

Table 4.1: Measured cross section for (p,2p) reactions of oxygen projectiles. We also show Root-Mean-Square values (RMS) and Full Width at Half Maximum (FWHM) of P_y component of the transverse momentum. Symbols ^{i} and ^{e} denote exclusive and inclusive measurements respectively.

Reaction	E_p [MeV]	σ^{p2p} [mb]	RMS [MeV/c]	$FHWM$ [MeV/c]
^{12}N(p,2p)^{11}C	370	16.44 (0.49) ^{i}	103.5 (2.6)	231.9 (7.2)
^{13}N(p,2p)^{12}C	323	12.34 (0.55) ^{i}	109.6 (4.0)	247.1 (10.1)
^{14}N(p,2p)^{13}C	368	4.76 (0.70) ^{i}	*93.5 (7.8)*	*208.8 (8.5)*
^{15}N(p,2p)^{14}C	401	9.89 (0.51)^{i}	113.4 (1.9)	256.8 (5.8)
^{16}N(p,2p)^{15}C	471	1.45 (0.81) ^{i}	*102.6 (28.5)*	*104.1 (68.5)*

Table 4.2: Measured cross section for (p,2p) induced by nitrogen projectiles. RMS and FWHM values are calculated from transverse momentum distributions (P_y). Same as 4.1.

Reaction	E_p [AMeV]	Removal shell	σ_{exp}^{ppn} [mb]	RMS [MeV/c]	$FWHM$ [MeV/c]
^{13}O(p,pn)^{12}O(*)	397	$0p_{3/2}$	0.92 (0.23) [i]	-	-
^{14}O(p,pn)^{13}O	349	$0p_{3/2}$	15.05 (3.26) [e]	111.7 (6.1)	255.9 (14.8) [e]
^{15}O(p,pn)^{14}O	308	$0p_{1/2}$+$0p_{3/2}$	7.28 (1.32) [e]	111.6 (18.7)	258.3 (45.0) [e]
^{16}O(p,pn)^{15}O	450	$0p_{1/2}$+$0p_{3/2}$	25.07 (1.32) [i]	116.2 (5.2)	266.1 (12.7) [i]
^{17}O(p,pn)^{16}O	406	$0p_{1/2}$+$0d_{5/2}$	9.55 (0.31) [i]	107.3 (3.6)	243.4 (9.2) [i]
^{18}O(p,pn)^{17}O	369	$0p_{1/2}$+$0d_{5/2}$	11.08 (1.34) [i]	113.1 (10.1)	258.3 (24.1) [i]
^{19}O(p,pn)^{18}O	442	$0d_{5/2}$	31.93 (1.12) [i]	116.4 (3.8)	264.3 (9.6) [i]
^{20}O(p,pn)^{19}O	415	$0d_{5/2}$	33.02 (1.48) [i]	110.2 (4.2)	249.9 (10.1) [i]
^{21}O(p,pn)^{20}O	448	$0d_{5/2}$	31.83 (2.98) [i]	111.9 (2.6)	254.2 (7.1) [i]
^{22}O(p,pn)^{21}O	414	$0d_{5/2}$	37.59 (3.98) [i]	118.6 (3.5)	271.5 (8.9) [i]

Table 4.3: Measured cross section, RMS and FWHM of P_y for (p,pn) reactions of oxygen projectiles. Same as 4.1 where it has been included shell (or shells) of the removed neutron.

Reaction	E_p [MeV]	Removal Shell	σ_{ppn} [mb]	RMS[MeV/c]	$FHWM$ [MeV/c]
^{12}N(p,pn)^{11}N(*)	370	$0p_{3/2}$	6.18 (2.71) [e]	-	-
^{13}N(p,pn)^{12}N	323	$0p_{3/2}$+$0p_{1/2}$	7.68 (0.80) [e]	*109.6 (8.4)*	*246.8 (28.2)*
^{14}N(p,pn)^{13}N	368	$0p_{3/2}$+$0p_{1/2}$	2.94 (0.83) [e]	*101.0 (7.9)*	*228.3 (36.2)*
^{15}N(p,pn)^{14}N	401	$0p_{1/2}$	18.94 (02) [i]	114.6 (2.0)	259.2 (6.1)
^{16}N(p,pn)^{15}N	471	$0p_{1/2}$+$0d_{5/2}$	38.03 (3.18) [i]	98.7 (7.9)	219.7 (20.4)

Table 4.4: Measured cross section, RMS and FWHM of P_y for (p,pn) reactions of nitrogen projectiles. Same as 4.1 where it has been included shell (or shells) of the removed neutron.

4.2 Exclusive Measurements

We could go one step forward in our analysis presenting two different reactions that lead to the same final nucleus ^{14}N, where exclusive measurements can be estimated.

State	$P_{^{15}O(p,2p)^{14}N}(\%)$	$P_{^{15}N(p,pn)^{14}N}(\%)$
g.s.	50.83 (7.22)	48.92 (3.56)
^{1st} at 2.32 MeV	15.01 (1.41)	9.43 (0.50)
^{2nd}at 6.20 MeV	17.97 (1.71)	19.71 (1.05)
^{3rd}at 7.02 MeV	16.19 (2.01)	21.95 (1.14)

Table 4.5: Population rates of the three excited and ground states considered of ^{14}N fragments. QFS (p,2p) and (p,pn) channels on a proton has been considered to estimate these rates.

We depict in Figures 4.4 and 4.5 gamma spectra of ^{14}N fragments de-excitation under QFS conditions for ^{15}O(p,2p)^{14}N and ^{15}N(p,pn)^{14}N reactions, respectively. The population rate have estimated following the same procedure described in Chapter 3 considering

(the states and γ-rays) of level scheme of ^{14}N (Figure 3.8). It should be noted that the reconstructed gamma spectra is highly sensitive to the carbon subtraction procedure, some events could appear above 8MeV, the single-particle energy threshold of ^{14}N. Nevertheless, the calculated feeding rates up to this threshold show a fair agreement between both channels (see Table 4.5), and with the obtained rates of nucleon removal cases (see Table 3.4 in the previous Chapter 3).

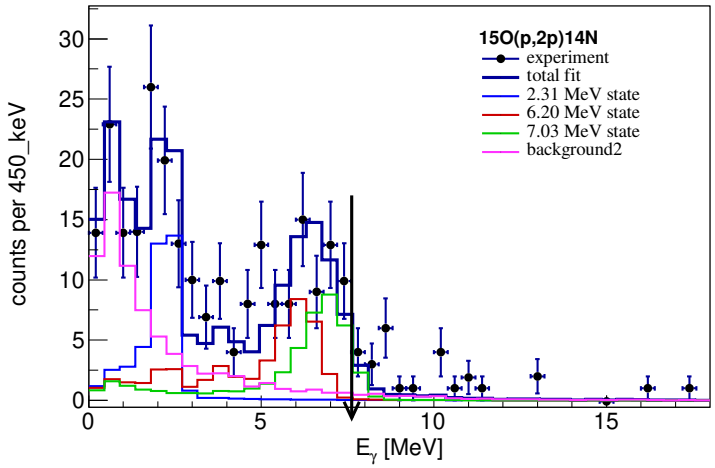

Figure 4.4: Gamma spectrum of ^{14}N fragments from (p,2p) QFS induced by ^{15}O nuclei (black dots). Three excited and the ground state have been considered (see the level scheme in Figure 3.8) into the simulations and are depicted (coloured) separately specifying by its energy. The total fit (obtained *via* Chi-squared method), which includes the atomic background with the three excited states, have been perfomed up to $S_p = 7.6MeV$ (black arrow).

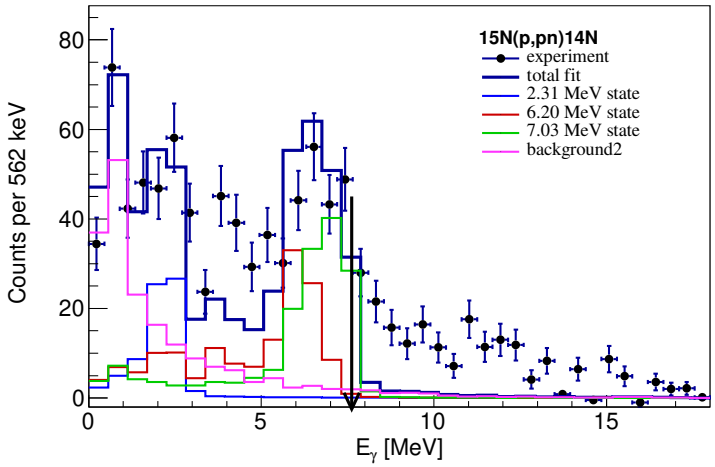

Figure 4.5: Gamma spectrum of ^{14}N fragments from (p,pn) QFS induced by ^{15}N nuclei. The same aforementioned excited states and procedure have been followed.

These population rates allowed us to extract exclusive cross section measurements for (p,2p) and (p,pn) reactions shown in Table 4.6.

	$\sigma^{(p,2p)}$ [mb]	$\sigma^{(p,pn)}$ [mb]
Inclusive	19.63 (0.93) [1.18]	18.71 (0.50) [2.81]
g.s.	7.85 (1.18) [0.56]	9.15 (0.71) [1.53]
0+ ^{1st} at 2.32 MeV	2.32 (0.25) [0.22]	1.76 (0.11) [0.30]
1+ ^{2nd}at 6.20 MeV	2.78 (0.30) [0.27]	3.69 (0.22) [0.62]
2+ ^{3rd}at 7.02 MeV	2.50 (0.33) [0.24]	4.11 (0.24) [0.69]

Table 4.6: Exclusive cross sections for QFS channels, (p,2p) and (p,pn), for the three excited and ground states considered of ^{14}N fragments. Uncertainties in parenthesis are purely statistical whereas systematic are present brackets. Inclusive results for both channels are showed to easy comparison.

4.3 Comparison with Previous Results

Our experiment addressed the systematic study of QFS induced by light exotic projectiles (Z=7-8). Some of the results analysed have been already published by different collaborators ([15, 16, 27, 28, 30]) and we will made use of them for comparison.

We start with ^{16}O (stable isotope), previously analysed by L.Atar [16], and presented in this context (in Table 4.7) to show the robustness of our analysis.

Reaction channel	σ^{1}_{QFS} [mb]	σ^{work}_{QFS} [mb]
^{13}O (p,2p) ^{12}N	5.78 (0.91)	5.67 (0.57)
^{14}O (p,2p) ^{13}N	10.23 (0.80)	9.67 (0.46)
^{15}O (p,2p) ^{14}N	18.92 (1.82)	19.63 (0.88)
^{16}O (p,2p) ^{15}N	26.84 (0.90)	27.48 (0.71)
^{17}O (p,2p) ^{16}N	7.90 (0.26)	6.99 (0.39)
^{18}O (p,2p) ^{17}N	17.80 (1.04)	15.02 (1.27)
^{21}O (p,2p) ^{20}N	5.31 (0.23)	5.91 (0.28)

Table 4.7: Cross sections for QFS channels evaluated in this work. Data of σ^{1}_{QFS} are taken from [16].

The comparison has been extended to other oxygen isotopes analysed by L.Atar [16] and P.Díaz [15]. We observed very good agreement for all comparisons (see Tables 4.7 and 4.8)). Some small differences between evaluated values are probably due to slightly different selection criteria used in the data sorting and QFS efficiencies evaluation (see Table 2.4).

The comparison with [15] deserves a special attention (see Table 4.8). The known angular anisotropy of the neutron-proton cross section demanded a deeper research to reproduce properly CB neutron detection efficiency, and thus, to obtain correct cross sections of (p,pn) channels. In the publication [15], the neutron detection efficiency was simulated using a realistic proton-neutron angular distribution evaluated by means of a full Fadevv/AGS calculation, whereas in this work we imposed an asymmetric distribution parametrised from DWIA calculations for proton-neutron interactions collected in [66]. Even these different approaches, the results obtained overlap within the errors assigned.

Reaction channel	σ^2_{QFS} [mb]	σ^{work}_{QFS} [mb]
^{22}O (p,pn) ^{21}N	39.24 (2.34)	37.59 (3.98)
^{22}O (p,2p) ^{21}N	6.01 (0.41)	6.10 (0.45)

Table 4.8: Cross sections for QFS reactions evaluated in this work. Data of σ^2_{QFS} are taken from [15].

4.3.1 Single-Particle Strength from QFS Cross Sections

Inclusive cross sections showed in [16] were interpreted into the framework of DWIA calculations combined with an eikonal reaction theory [53]. DWIA calculations for the QFS reactions are based on elastic scattering between the incident and knock-out nucleons and they include the effect of final state interactions through the use of complex optical potential (distorting the nucleon wave functions). This theoretical study allowed to evaluate reduction factors (R_s) for the single-particle strength evaluated with the shell model and showed a sizeable quenching compared with pure shell-model strengths. This quenching of 20-30 % was of the order of the one obtained in the past for stable isotopes in (e,e'p) reactions [81].

A tinny dependence with the proton-neutron asymmetry, defined as $\Delta S = S_p(n) - S_n(p)$ for a proton (or a neutron) removal channel was found (see Figure 4.6) which is compatible with state-of-art ab-initio predictions as shown in [82].

The puzzling point came from the conclusions of the systematic analysis of heavy-ion removal reactions induced on light targets at intermediate energies around 100 AMeV. These experiments [11], were interpreted in the framework of an eikonal reaction theory. The R_s data obtained in this case also exhibit for proton-neutron symmetric nuclei a similar quenching to the one found in stable nuclei but this effect was accompanied by a very pronounced dependence of R_s with the proton-neutron asymmetry (i.e. R_s is close to unit for removal of very weakly bound nucleons whereas the value goes significantly down for removal of very bound nucleons). This dependence corresponds to the shadow zone plotted in Figure 4.6.

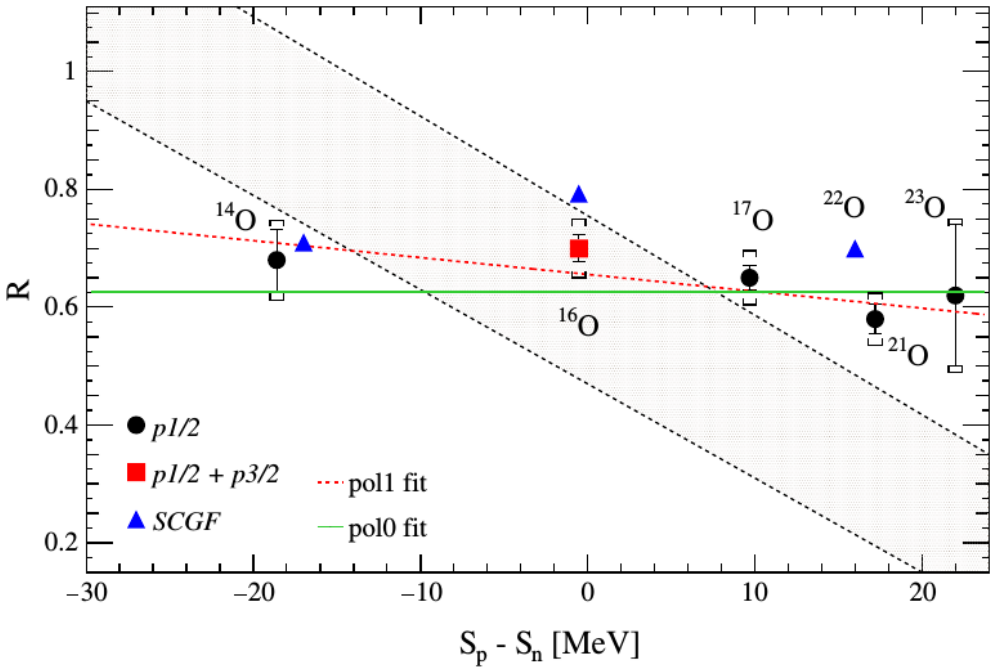

Figure 4.6: Reduction factor R_s derived from (p,2p) measurements as a function ΔS compared with theoretical predictions for Spectroscopic Factors [11]. Shaded region corresponds to the trend extracted of intermediate-energy single nucleon removal cross section. Picture are taken from [16].

In order to complete the picture we will mention other results [83], based on the study of nucleon transfer (pick-up) reaction at much lower energy and ^{14}O beam (18 AMeV) on a deuterium target, that are also in line with the aforementioned conclusions [16].

The study of ^{14}O(p,2p) reaction was also addressed at 250 AMeV by [84]. This work measured the triple differential cross-section for the (p,2p) reaction and reconstructed the proton separation energy spectra going to ^{13}N and also to ^{12}C with fragment excitation energies spanning from 9 up to 15 MeV. Again, the interpretation of this experiment based on DWIA calculations pointed out to the independence of R_s with the difference between the proton-neutron separation energy in agreement with publications [12, 16].

On the other hand, other theoretical description developed for the interpretation of (p,2p) and (p,pn) reactions in the energy range of 300-500 AMeV, based on the sophisticated Faddev/AGS method [85] and the successful adaptation of Continuum Discretised Coupled Channel formalism (CDCC) to derive single-particle cross sections [34] agree as well with a general reduction (quenching) of 20-30% compared with pure IPM calculations and a very small dependence of R_s with the proton-neutron asymmetry.

We have compared our experimental measurements of QFS channels induced by ^{14}O nuclei. Both (p,2p) and (p,pn) reactions are particularly interesting since the final fragments, ^{13}O and ^{13}N, do not have bound excited states below the particle emission threshold, and the measured cross sections are directly exclusive ones.

Theoretical calculations performed by Sevilla's group within the CDCC formalism [33, 34, 86]. Two different potentials, Dirac [87] and Paris-Hamburg (PH) G-matrix effective interaction [88, 89], have been used which results are in close agreement.

In order to compare with our experimental results, these values have been weighted by spectroscopic factors (SF), obtaining theoretical cross sections:

$$\sigma_{th} = \sigma_{sp} \cdot SF \tag{3.1}$$

The spectroscopic factors (SF) can be extracted either using a shell model calculation using WBT interaction for valence shells computed by OXBASH code [90][4], or more sophisticated description such as self-consistent Green's function (SCGF) theory [83, 91].

Table 4.9 summarises the evaluated cross sections, including the sum spectroscopic factors, $\sum C^2S$, for $1p_{1/2}$; and the reduction factors, $R_s = \sigma_{exp}/\sigma_{th}$. We should note that C^2S values were not directly evaluated in this work, but taken from shell model estimations within WBT interaction in [34, 86] and SCGF reported in [83].

Channel	σ_{sp}^{D} [mb]	σ_{sp}^{PH} [mb]	$\sum C^2S$	σ_{th}^{D} [mb] [mb]	σ_{th}^{PH} [mb] [mb]	σ_{exp} [mb] [mb]	R_s^D	R_s^{PH}
(p,pn)	9.02[1]	8.55[1]	3.17[2]	28.59	27.10	15.1 (33) [23]	0.53 (11) [8]	0.56 (11) [8]
(p,2p)	8.51[1]	8.06[1]	1.58[2]	13.45	12.73	9.67 (48) [58]	0.72 (4) [4]	0.76 (4) [4]
(p,pn)	9.02[1]	8.55[1]	3.73[1]	36.23	34.34	15.1 (33) [23]	0.42 (9) [6]	0.44 (9) [6]
(p,2p)	8.51[1]	8.06[1]	1.83[1]	16.77	15.88	9.67 (48) [58]	0.58 (3) [3]	0.61 (3) [3]

Table 4.9: Cross sections summary for (p,2p) and (p,pn) QFS induced by ^{14}O on a proton target. Single-particle, σ_{sp}, and total theoretical calculations were performed using two different potentials, i.e. Dirac (D) and Paris-Hamburg (PH). Spectroscopic factors design with [1] were evaluated by [34, 86, 89] using WBT interaction, whereas [2] are taken from ab-initio microscopic SCGF calculations published in [83].

Figure 4.7 shows the R_s evaluated according to Table 4.9 and are completed with inclusive cross sections of ^{16}O (p,2p), ^{22}O (p,2p) and ^{22}O (p,pn) reaction channels reported in this dissertation and CDCC calculations from [34, 86, 89].

[4] *These calculations were performed including n-particle, n-hole excitations have been chosen to minimum values that reproduce non-zero SF, since the WBT interaction was designed for "pure" np-nh configurations, without mixing different n values*, as it is described in [89]).

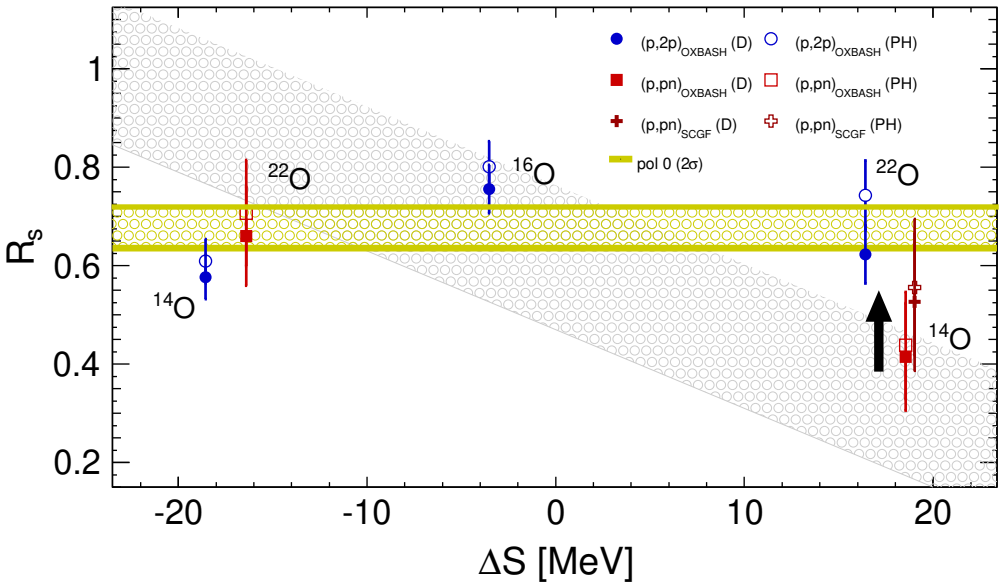

Figure 4.7: Reduction factor R_s inferred from (p,2p) and (p,pn) measurements as a function ΔS. Similar to Figure 4.6, the shaded region depicts the trend extracted of intermediate-energy single nucleon removal cross section [11], and the yellowish shaded area corresponds to a lineal fit for our data (taken R_s^{PH} and SCGF prediction for ^{14}O(p,pn) channel) within a signification of 2σ (to guide the eye). Spectroscopic factors calculated by shell model using WBT interaction (OXBASH) come from [34, 86, 89] and, for the ^{14}O case as well with ab-initio SCGF formalism taken from [12, 91].

Almost no isospin dependence is observed in this picture, and R_s values confirm the trend already shown in [81] and recently in [16, 34].

The high sensitive in R_s to spectroscopic factor used suggests that a careful structure evaluation will be important to ensure robust conclusions and will be object of our interest. In any case the strong dependence of R_s with ΔS obtained at intermediate energy nucleon knock-out [11], is not detected in our data.

4.3.2 Momentum Distributions of QFS Reactions

We concentrate nw to understand the momentum distribution of QFS channels induced by ^{14}O. Figure 4.8 shows normalised distributions of the P_y component of the tri-momenta of ^{13}N (left) and ^{13}O (right) fragments after (p,2p) and (p,pn) reactions, respectively. The experimental results are compared with theoretical calculations by Sevilla's Group [86], where two different potentials (Dirac and Paris-Hamburg) were considered, even though yielding very close results.

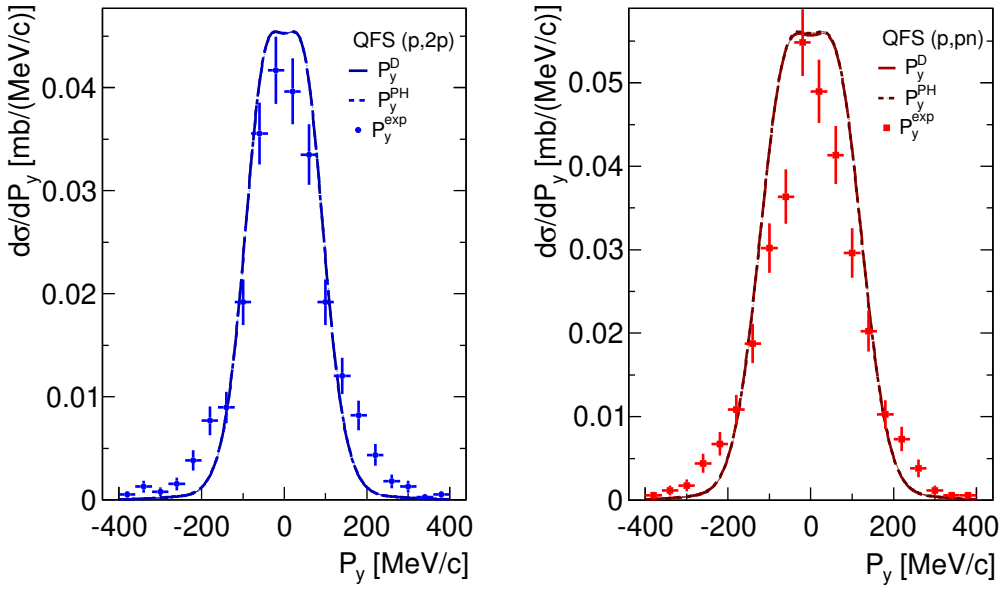

Figure 4.8: Momentum distributions of P_y components of ^{13}N (blue circles) and ^{13}O (red squares) fragments after (p,2p) and (p,pn) reactions of ^{14}O projectiles on a proton target, respectively. Theoretical calculations performed by Sevilla's Group [86] are shown with dashed for two different potentials Dirac potential and dash-dotted lines for Paris-Hamburg, being imperceptible the discrepancies between both distributions.

To minimise misinterpretations due to reduced statistics we have relaxed the QFS conditions and considered the detection of two signals in CB, which are compatible with QFS, but where angle correlations are not entailed. This is a reliable approximation when absorption channel, particularly inelastic ones, are close to zero (see section 4.4).

The (p,2p) channel implies that a proton settled in a $p_{1/2}$ shell is removed, whereas in the (p,pn) reaction, the knocked out neutron comes from a deeper shell as $p_{3/2}$. Thus, we expect wider distributions in the latter case, as, in principle, Figure 4.8 shows. However, the (p,pn) data are narrower than the theoretical description. This wuld be an indicates that one needs to consider mixing configurations, including holes excitations in $p_{3/2}$ to reproduce the experimental shape. For the (p,2p) channel, we obtain a rather good agreement in the central part of the distribution.

In addition, we could calculate the transverse and longitudinal components obtaining distributions displayed in Figure 4.9. ^{13}N fragments come from (p,2p) channel and are depicted with blue circles on the top side, whereas ^{13}O nuclei, obtained from (p,pn) reactions, are represented with red squares.

These distributions present a visible asymmetry, similar to the effect studied in [92]. We follow the definition of asymmetry factor as $A_\Gamma = \Gamma_L/\Gamma_R$ (introduced in [92]). This factor is calculated evaluating the FWHM values from a double Gaussian fit performed

for momentum distributions.

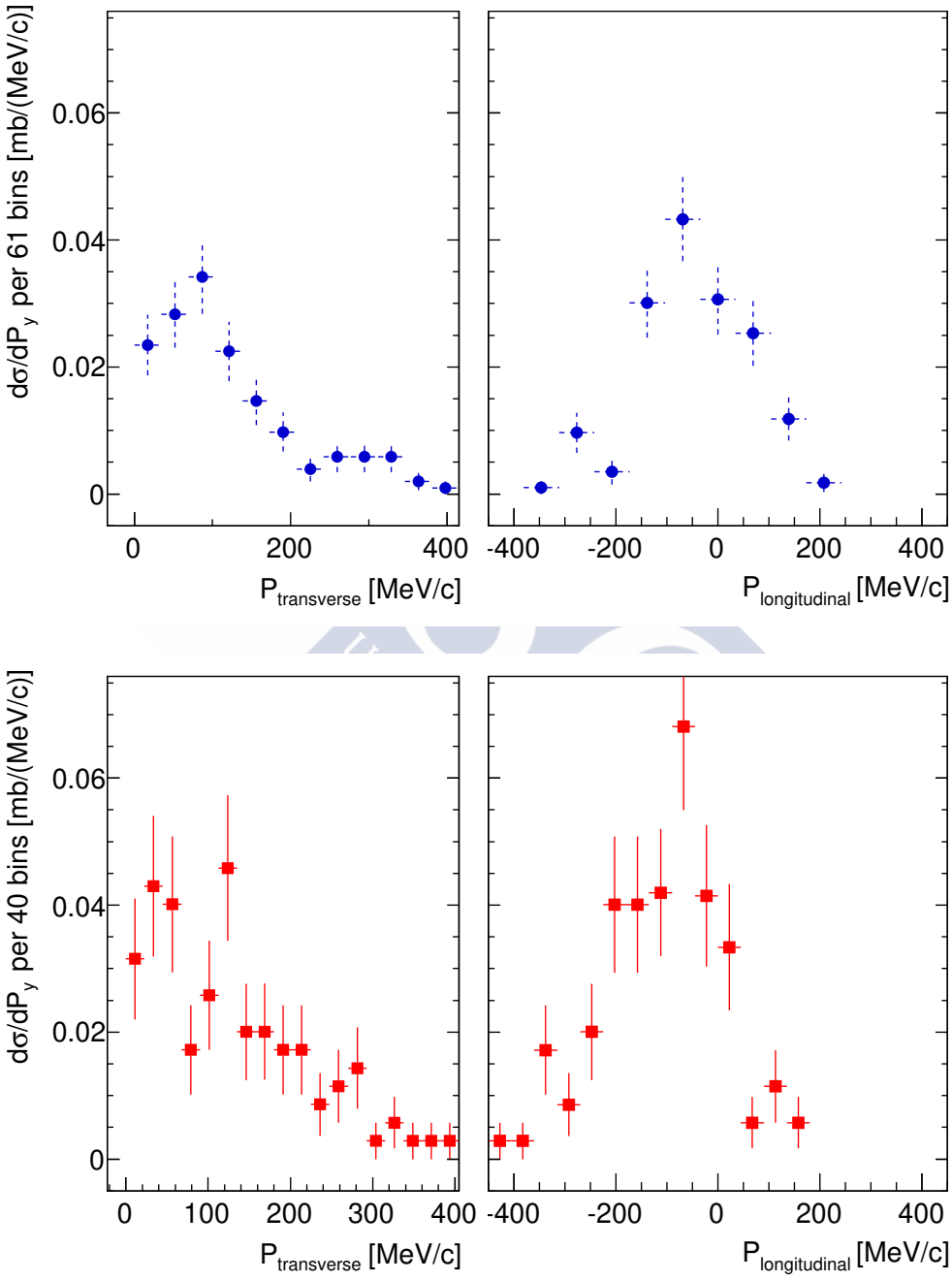

Figure 4.9: Total transverse (left) and longitudinal (right) momentum distributions in the centre-of-mass of ^{13}N (on top with blue circles) and ^{13}O (bottom pictures with red squares) fragments after (p,2p) and (p,pn) reactions of ^{14}O projectiles on a proton target.

The theoretical approach of [92] makes use of DWIA at energies $\sim 250A$ MeV. The authors predict an asymmetry pattern on the momentum distribution which is typified by a steep fall in the high momentum side and "long-ranged" tail in low region. Additionally, this asymmetry is expected to depend on the reaction energy, being more pronounced at intermediate energies as the ones considered in [92]. Even though the higher energy used in this work, this asymmetry is still present in our longitudinal distributions for both (p,2p) and (p,pn) channels (see P_{long} in Figure 4.9). We could estimate the associated asymmetry factors, A_Γ, for longitudinal distributions of (p,2p) and (p,pn) induced by ^{14}O and they are 1.39 and 1.43 (see Figure 4.9). These observations are in rather agreement with previously data [92] A_Γ (see Table

Fragment	E (MeV)	P_{cen}	Γ[MeV/c]	Γ_L[MeV/c]	Γ_R[MeV/c]	A_Γ
^{13}O	100	-92	266	182	84	2.17
^{13}O	200	-53	278	168	110	1.53
^{13}O	349	-7.9(10)	255.9(14.8)	118	87.3	1.39
^{13}N	100	-31	178	104	74	1.41
^{13}N	200	-20	191	113	78	1.45
^{13}N	349	-14.7(8.8)	236.6(4.8)	113	81	1.43

Table 4.10: Asymmetry studied where centre; global, left and right FWHMs of longitudinal momentum distributions are presented for ^{13}O and ^{13}N fragments.

The asymmetry remains constant with energy for (p,2p) channel, whereas in (p,pn) channel it decreases with the rising energy.

4.4 Nucleon-Removal versus Quasi-Free Scattering. Reaction Mechanism Description

A plausible explanation of the differences observed between the isospin dependence on the spectroscopic strength calculated with removal and QFS channels could be the strong surface location of the first ones.

This would mean that absorption effects in the nuclear media could be important and if they are not accurately taken into account could mask the conclusions. With the idea of quantifying the presence of the absorption channels in the removal channel we undertook a deep analysis of the reaction mechanisms, comparing the systematics of nucleon-removal and QFS cross-sections evaluated in this work.

We design a detailed investigation to provide information about the physical processes underline and infer properties of the reaction mechanism occurred.

Measurements from QFS channels provide a clear signature of the nuclear processes involved in the reaction. The strong angular condition applied to the two light outgoing

nucleon guarantees the one step character of this reaction channels. On the other hand, single nucleon-removal reactions induced by ${}^{A}_{Z}$X projectiles take into account all possible nuclear reactions that reach the same final products, i.e. ${}^{A-1}_{Z}$X for neutron and for ${}^{A-1}_{Z-1}$Y proton removal.

Therefore, QFS cross sections are smaller or - in some cases - equal than analogous single removal nucleon measurements. We analyse those processes that could contribute to the single nucleon-removal reaction and lead to identical final fragment.

1. The main contribution to the nucleon-removal channels derives from QFS channels.

2. Inelastic processes, (INE), where the projectile after colliding with the target could de-excite emitting a light particle, should be presented. We have simplified the analysis considering that the emitted particle is either a proton, in the case of neutron-deficient isotopes or a neutron, in proton-rich region. Since we work with high energy beams, this proton (neutron) is, approximately, emitted forward [5] and it follows the same direction and energy that the fragment. Additionally, kinematic simulations were necessary to estimate the detection probability of an evaporated proton by CB, it was found to be $< 1\%$ [6], thus we neglect this contribution.

   At this point, we have estimated the contribution of these processes recorded into the proton arm in coincidence with the A-1 fragments. The evaluated one proton efficiency was evaluated at $EFF_{1p} \sim 62\%$.

   For the evaporated neutron detection with LAND we used an efficiency for one neutron multiplicity at $EFF_{1n} \sim 77\%$, taken from [27].

   In several cases, we could quantify the existence of inelastic channels which can contribute up to 9% and 13% of the single-proton and neutron removal channels, respectively (see Table D4 in Appendix D).

3. We have also considered other nuclear reactions that lead to the same fragment and which imply final states interactions between the knock-out light nucleon and the ejectile. To account these processes, we free in our analysis the QFS condition, leaving only the detection of two high energy signal condition active (not kinematic correction). We name all these contributions under a generic label of absorption, (ABS).

With all these ingredients in mind, the removal cross section can be split as a sum of several individual contributions previously explained.

$$\sigma_{removal} = \sigma_{QFS} + \sigma_{INE} + \sigma_{ABS} \tag{3.2}$$

[5] It is isotropically emitted in the rest of mass.
[6] The polar angles acceptable in CB for protons cover from 9^o to 81^o deg [27].

The results of this analysis for oxygen and nitrogen projectiles are summarised in Table D4 and in Figures D1 and D2, settled in Appendix D. Figures 4.10 and 4.11 exhibit both single-nucleon removal and QFS cross sections where we add inelastic (green diamonds) and absorption (red crosses) contributions.

In order to estimate the strength of the suggested mechanism, we have computed the differences,(residues, $\Delta\sigma_p$), using the removal results as the reference ones.

$$\Delta\sigma = (\sigma_{QFS} + \sigma_{INE} + \sigma_{ABS}) - \sigma_{removal} \tag{3.3}$$

This detailed analysis brings to a complete and coherent experimental overview that could serve a guide to improve the accuracy of the reaction mechanism.

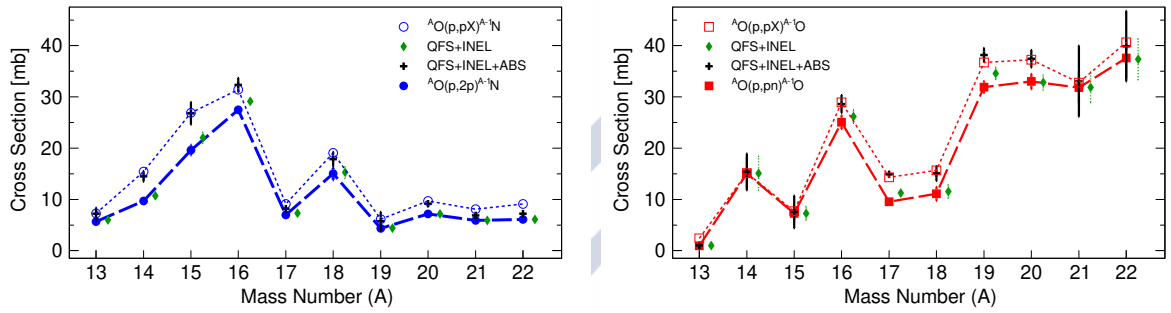

Figure 4.10: Cross section measurements for single-proton/neutron removal and (p,2p)/(p,pn) QFS reactions induced by oxygen projectiles (top and bottom histograms). Inelastic (green diamonds) and absorption channels (black crosses) are added to reproduce together with QFS cross sections the removal channel results.

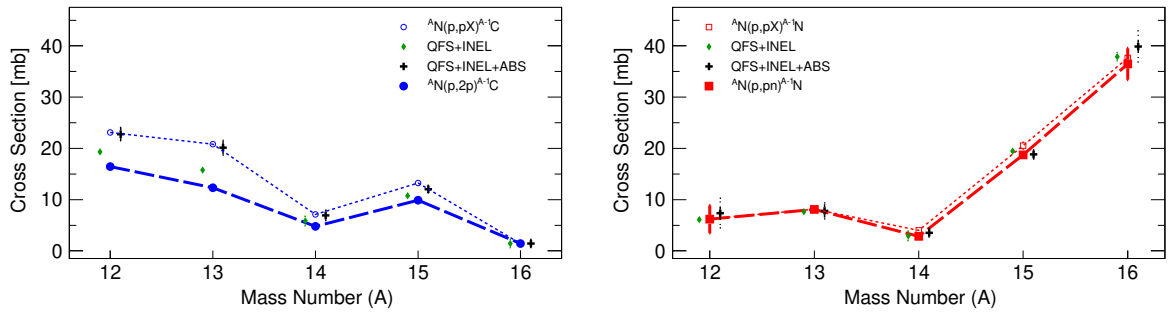

Figure 4.11: Cross sections measurements for single-proton/neutron removal and (p,2p)/(p,pn) QFS reactions induced by oxygen and nitrogen projectiles. Inelastic (green diamonds) and absorption channels (black crosses) are added to reproduce together with QFS cross sections the removal channel results.

Chapter 5

Fragmentation Cross Sections for Light Nuclei

This chapter presents a collection of fragmentation cross-section data induced by stable beams of ^{12}C, ^{14}N, and almost all the oxygen isotopic chain, covering from neutron deficient to neutron-rich nuclei with typical energies of 400 A.MeV on a carbon target. They amount a total of 132 cross-sections, 95 of them up to our knowledge never reported previously. Total reaction cross sections have been also measured for stable nuclei.

These measurements are of interest to validate reaction models and/or descriptions of the different fragmentation stages such as Liège intra-nuclear cascade (INCL code [93]) and abrasion-ablation (ABRABLA07 [94]). Additionally, due to the fact that these reactions involve species (C,O,N) present in the human body composition, their cross sections are relevant in the field of different applications, particularly hadrontherapy treatment and space shielding radio-protection.

5.1 Physical Relevancy

The interaction of charged particles with the human body is described in the framework of electromagnetic and nuclear interactions.

In medicine, particle radiation therapy (RT) has gained popularity becoming a solution to treat various types of tumours. Very often it is used in combination with surgery and chemotherapy[1] to increase effectiveness. Radiotherapy investigations in conjunction with immunotherapy[2], which are not able to block the tumour growth, are also part of the many interesting works in progress [95].

[1] Chemotherapy is the use of any drug to treat any disease.

[2] Immunotherapy also known as biologic therapy, is a type of cancer treatment that consists to boost the natural immune system to help fight cancer.

Ground-breaking works achieved by several reference institutions (such as HIMAC in Japan, GSI in Germany, or PSI in Switzerland) have brought the use of protons and ^{12}C to the present day as a realistic approach to treat and control tumours. These beams exhibit clear advantages over conventional radiotherapy since the energy deposited by protons and heavy ions is more selective (the Bragg peak is better defined) than in the case of X- or γ-rays [96].

Nuclear interactions between beam projectiles and patient tissues might end with the fragmentation of either projectile or target. These effects should be also considered in treatments since they can dramatically degrade the dose localisation widening the Bragg Peak [36]. The exploitation of dedicated experiments designed to use inverse kinematics such as FOOT (FragmentatiOn Of Target [35]), or data acquire in "multi-purpose" set-ups allow to fulfil the existing "gaps" in databases and are important to better compute and estimate doses.

It is observed that a variation of $\pm 10\%$ on the cross sections values induces a variation of $\pm 3\%$ on the LET (Liner Energy Transmission) value in the tumour. This implies that fragmentation and reaction cross sections have to be known within 10% to achieve a 97% of accuracy on the dose computation. Such uncertainties on experimental cross sections measurements are difficult to reach. In this work we could evaluate reactions cross sections within an uncertainties minor than 5.2%, whereas for several fragmentation cross sections statistical uncertainties stay underneath of this confidence interval being the final errors $< 10\%$.

In addition, nuclear fragmentation has also an interest in the context of space radiation exposure, particularly for long-duration missions. The highest radiation health risk comes from Galactic Cosmic Rays that have enough energy to go though the spacecraft shielding [37]. Protons and heavy nuclei undergo nuclear interactions with the space crafts and equipments, and may produce a large number of secondary particles. Contrary to the therapy case, fragmentation processes help in these cases, since these lighter particles have a reduced biological effectiveness [58]. It is thus important to choose those shielding materials that maximise nuclear fragmentation in order to minimise the radiation exposure [37, 55, 56, 58, 59].

5.2 Total Reaction Cross Section

We present here total reaction cross sections for stable nuclei, ^{12}C, ^{14}N and ^{16}O on a carbon target at approximately $450A \cdot MeV$.The total reaction cross section,σ_R, is defined as the sum the total interaction cross section, σ_I, and the inelastic cross section which takes into account the contributions of electromagnetic and nuclear interactions leading to the excitation of collective nuclear modes;

$$\sigma_R = \sigma_I + \sigma_{inelastics} \tag{3.1}$$

As it shows in the previous Chapter 4, the inelastic contribution amounts for a particular channel $\sim 1-2$ mb, whereas interaction cross sections are around a few hundreds of mb. Under these circumstances $\sigma_R \backsimeq \sigma_I$ what introduces relative errors of $\sim 0.15-0.35\%$, smaller than the statistical uncertainties of the measurements. The total interaction cross section is defined as:

$$\sigma_I = \frac{1}{N_t} ln \frac{\gamma_E}{\gamma} \tag{3.2}$$

where $\gamma = N_{out}/N_{int}$ and $\gamma_E = N^E_{out}/N^E_{int}$ are the ratio between the recoil of un-reacted and the incoming nuclei for a carbon and none targets, respectively; N_t are the scattering centres in area units.

The evaluation of interaction cross section is extremely sensitive to the selection used for counting incoming and outgoing events. The secondary reaction probabilities of nuclei with the in-beam detectors have been evaluated following the method described in the section 2.5.2 and are in the order of ($\sim 2\%$). Even tiny neighbouring contamination can yield significant changes in the evaluation of γ. The estimation of the events is carried out with the silicon detectors located in front and behind the target area. To determine incoming events (with and without target) we used the second in-beam silicon detector (DSSSD2), which was the closest detector to the target. Whereas, the third in-beam silicon (DSSSD3, behind the target) was used to estimate the outgoing events (with and without target).

Systematic studies were performed for our three projectiles (^{12}C, ^{14}N and ^{16}O) on a carbon target to determine the stability of the σ_R and yield accurately measurements. We have considered a simultaneous variation in both gates size (DSSSD2 and DSSSD3) to find a stable region of in total reaction cross sections, where the neighbouring contributions can be negligible. Figure 5.1 displays an example for ^{12}C projectiles where σ_R is plotted as a function of the gates size applied in our incoming and outgoing selection. The numbers displayed in the horizontal axes (a.u.) the multiplication factor of the σ values (obtained from Gaussian fits) for projectile and fragment events.

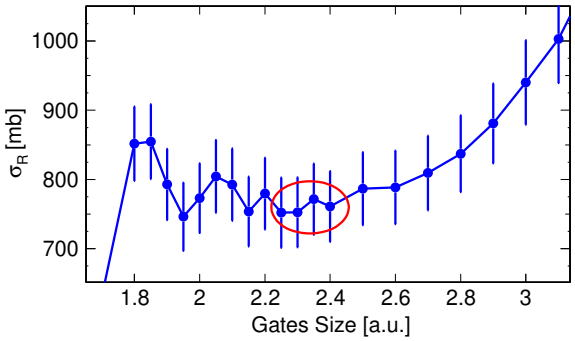

Figure 5.1: Total reaction cross sections as a function of the software gates size applied in the second and third silicon detectors for ^{12}C projectiles on a carbon target (see text for details).

We calculated an average of σ_R in that region obtaining $\overline{\sigma_R} = 763[mb]$ We include the standard deviation and a systematic uncertainty as Table 5.1 summarises together with measurements for ^{14}N and ^{16}O projectiles.

Reaction channel	σ_R [mb]	$\Delta\sigma_R^{stat}$ [mb]	$\Delta\sigma_R^{sys}$ [mb]	$\Delta\sigma_R^T/\sigma_R(\%)$
$^{12}C(C,C)^{12}C$	762.9	27.4	19.1	4.4
$^{14}N(C,C)^{14}N$	794.5	23.2	19.9	3.8
$^{16}O(C,C)^{16}O$	813.4	36.4	20.2	5.1

Table 5.1: Reaction cross section for ^{12}C, ^{14}N and ^{16}O on a carbon target at $450AMeV$. Statistical, where it is considered a standard deviation around the mean, and systematic uncertainties are shown together with the relative error for each case.

These results event with modest precision could be useful to cross-check the predictive power of transport codes [97]. In Figure 5.2, we compare our $\overline{\sigma_R}$ for ^{12}C projectile (black square) with the systematic of published data of σ_R (blue circles, [98, 99, 100]) as a function of the projectile energy.

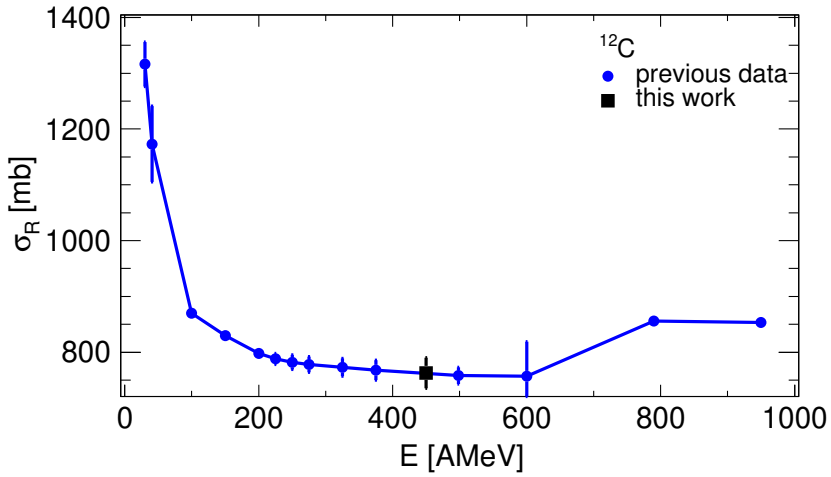

Figure 5.2: Reaction cross sections as a function of the projectile energy for ^{12}C on a carbon target (black square) with available measurements taken from [98, 99, 100] (blue circles).

This measurement fills the gap at high-mid energy range and follows the trend of σ_R with the projectile energy; The total reaction cross section falls steadily around 100 AMeV to reach a minimum (low stable values) around 300-500 AMeV and, then, it increases smoothly up to rise a "constant" value at high energies ($> 1AGeV$).

5.3 Fragmentation Cross Sections of Stable Light Nuclei

We present cross sections measurements for fragmentation reactions using techniques and the corresponding correction factors [3] in chapter 2 . The notation used to identify the reaction channels is: **Ap Bn** where A and B are numbers from 0 to 6 related to the amount of protons (p) and/or neutrons (n) lost in the reaction.

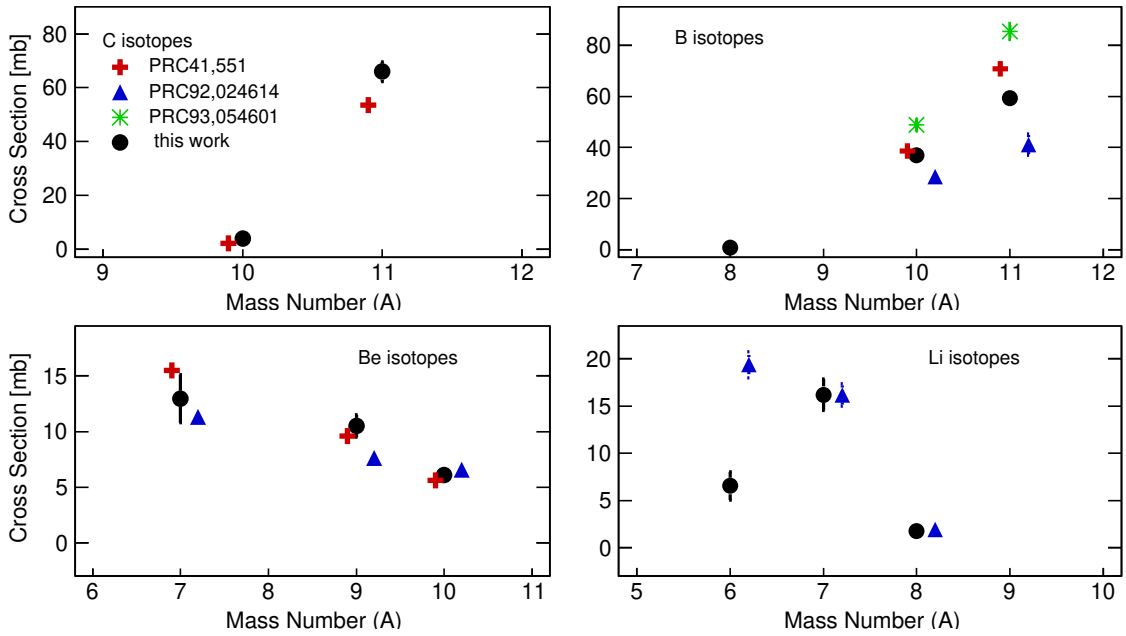

Figure 5.3: Fragmentation cross sections of ^{12}C projectiles on a carbon target at 450 $A \cdot MeV$. Current measurements are depicted with black circles and compared with with previous results red crosses [101], blue triangles [102] and green stars [61].

The left three columns in Table 5.2 summarise the fragmentation cross sections obtained in this analysis for reactions induced by ^{12}C projectiles on a carbon target at 450 $AMeV$. These data which are displayed in Figure 5.3 with black circles and are also compared with previous published data available measured at similar high-mid energies, i.e. red crosses from [101], blue triangles form [102] and green stars from [61].

Depending on the amount of removed protons we group together the reaction channels to ease the discussion.

[3] That include the geometrical acceptance, survival probabilities and the relative trigger efficiency for both projectiles and fragments

$(Z,A)_p$ @ 450 $A \cdot MeV$	$(Z,A)_f$	σ_{frag} [mb]
6,12	6,11	65.95 (3.67)
	6,10	3.93 (0.58)
	5,11	59.36 (2.05)
	5,10	36.99 (2.16)
	5,8	0.82 (0.21)
	4,10	6.07 (0.48)
	4,9	10.51 (0.99)
	4,7	12.95 (2.14)
	3,8	1.76 (0.34)
	3,7	16.20 (4.24)

$(Z,A)_p$ @ 450 $A \cdot MeV$	$(Z,A)_f$	σ_{frag} [mb]
7,14	7,13	16.22 (1.04)
	7,12	1.61 (0.32)
	6,14	0.79 (0.23)
	6,13	18.12 (1.06)
	6,12	104.11 (2.79)
	6,11	23.66 (1.20)
	6,10	1.02 (0.28)
	5,12	3.20 (0.44)
	5,11	32.18 (1.50)
	5,10	27.72 (1.60)
	5,8	0.78 (0.43)
	4,11	0.15 (0.09)
	4,10	1.82 (0.34)
	4,9	5.37 (0.81)
	4,7	2.19 (0.55)

$(Z,A)_p$ @ 450 $A \cdot MeV$	$(Z,A)_f$	σ_{frag} [mb]
8,16	8,15	71.01 (1.70)
	8,14	3.28 (0.40)
	7,15	67.10 (1.73)
	7,14	56.92 (1.62)
	7,13	11.93 (0.80)
	7,12	0.82 (0.25)
	6,14	5.70 (0.48)
	6,13	31.10 (1.14)
	6,12	51.93 (1.57)
	6,11	17.50 (1.00)
	6,10	0.82 (0.33)
	5,13	0.20 (0.07)
	5,12	1.93 (0.25)
	5,11	18.17 (0.85)
	5,10	15.78 (0.94)
	4,10	1.06 (0.20)
	4,9	3.80 (0.45)

Table 5.2: Cross sections for fragmentation reactions with stable light nuclei on a carbon target (0.935 $g \cdot cm^{-2}$) at 450 $AMeV$. For unbound nuclei, ^{9}B and ^{8}Be, their associated cross sections have been measured given a value closer to zero (< 0.10 mb).

The first branch, the measured cross sections for carbon isotopes, i.e 0p1n- and 0p2n-removal channels, are in fair agreement with [101]. Even considering the differences in projectile energy since in [101] where it was used slightly higher energy beams, $\sim 600 AMeV$.

In one proton removal channels, we compare the 1p0n and 1p1n- removal channels (leading to ^{11}B and ^{10}B) with available measurements. Our cross sections fall between results from [101] and [102]. That can be explained since our cross sections were measured at energies settled between the used in [101] (at 600 AMeV) and in [102] (at 397 AMeV).

We went to discuss the comparison with data already reported in [61] (green stars), where the energy beam was the same. The experimental method perform to calculate these measurements was also identical. The unique difference relies on the calculation of *relative trigger efficiency factor*, RTE. In [61] they estimate an RTE around of 85% calculated *via* a minimisation procedure for all 1pxn channels. In this work, we have split the evaluation of this correction factor depending on the target characteristic and as well as the reaction channels (see section 2.3 in Chapter 2). Table 5.3 shows a comparison with R.Thies results taken from [61] for 1p0n- and 1p1n-removal channels. Additionally, we have included for 1p0n removal channel a recent value coming from V.Panin [14] (to be published), performed at 398 AMeV.

On the other hand, the most exotic channel that implies up to three removed neutrons, 1p3n, obtaining ^{8}B fragment is reported for the first time. The associated statistical uncertainty increase up to 20% due to limitations in the geometrical acceptance. We should note that the 1p2n channels is not shown since ^{9}B is unbound nucleus. Although we could detect some footprints belonging to "this" mass and charge, the associated cross section for this channel is low than 0.10 mb.

	$\sigma_{1p0n}[mb]$	$\sigma_{1p1n}[mb]$
R.Thies [61]	85.4± 3.1	48.8 ± 2.2
V.Panin [14]	60.9± 2.7	-
This work	59.4 ± 2.1	37.0 ± 2.2

Table 5.3: Cross section comparison for 1p0n- and 1p1n- removal channels of ^{12}C projectiles impinging on a carbon target at 450 $AMeV$. The uncertainties showed are purely statistical. Results are taken from [61] measured at the same energy (450 AMeV) and [14] at 398 AMeV.

For the rest of removal channels going to lighter fragments, Z=4 and Z=3 (2pxn- and 3pxn- channels), fragmentation cross sections are in acceptable good agreement with [101] and [102] data. Both trend and as individual measurements are reproduced. The exception is to the most exotic channel, i.e 3p3n-removal channel (^{6}Li) which implies up to six knocked-out nucleons. This corresponds to our detection limit, where the geometrical acceptance of experimental set-up was very low ($< 10\%$ [4]). Moreover, the calibration of the silicon detectors is guarantee to remain stable up to changes in two charge units, and, in this case, it was performed for Z=6 [5]. For this reason, those fragmentation cross sections yielding to lithium isotopes are given with large systematic uncertainties. The final measured cross section (systematic uncertainty included) is $6.5 \pm 2.1 \pm 13.8$ mb, being roughly compatible with 19.4 ± 1.4mb [101].

Figures 5.4 and 5.5 complete this section showing the corresponding fragmentation cross sections induced by ^{14}N and ^{16}O projectiles on a carbon target at 450AMeV with statistical uncertainties. Again, data from [101] are displayed for comparison. We observe similar results for fragmentations of ^{16}O projectiles, emphasising the 0pXn and 1pXn channels where we reproduce completely the previous measurements. However, the ^{14}N only the global trend is achieved, and our measurements are systemically smaller that the data presented in [101]. That could come from the geometrical acceptance factor applied for this projectile.

[4] That implies only 1 of 10 fragments produced in the nuclear fragmentation reaches the final TFW detector

[5] For oxygen and nitrogen projectiles the silicon calibrations were for Z=8 and Z=7, respectively

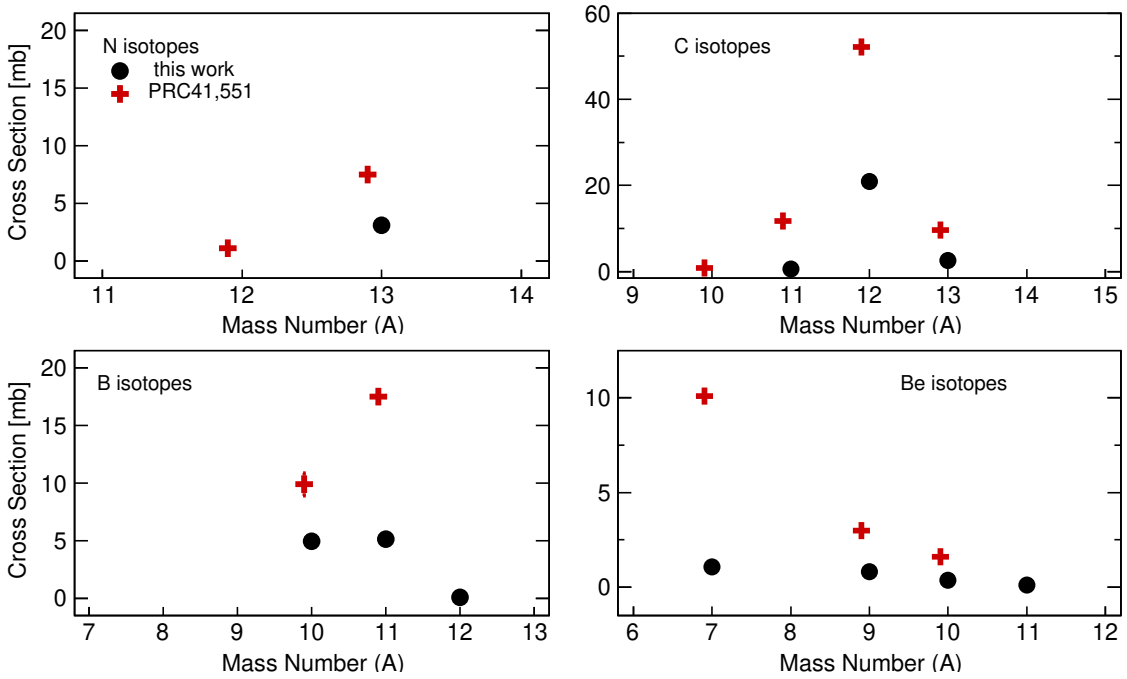

Figure 5.4: Fragmentation cross sections of ^{14}N projectiles on a carbon target at 450 $A \cdot MeV$. Current measurements are depicted with black circles and data from [101] with red crosses.

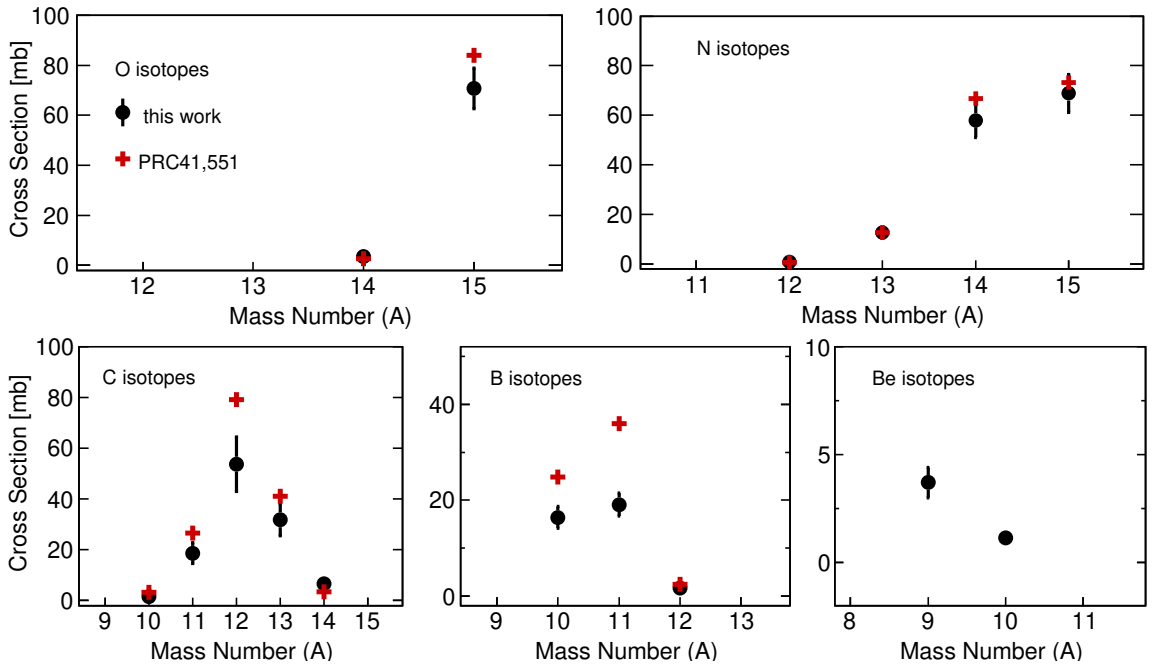

Figure 5.5: Fragmentation cross sections of ^{16}O projectiles on a carbon target at 450 $A \cdot MeV$. Same as 5.4.

5.4 Oxygen Induced Fragmentation Reactions

5.4.1 Theoretical Framework

In the case of light projectiles, even a relatively small excitation energy gained may be comparable with their total binding energy, resulting in the explosive decay or breakup of the excited nuclei. This phenomenon is usually described by means of breakup or multi-fragmentation models coupled to other codes that describe the nuclear collision.

In order to describe the collision between the projectile nucleus (i.e. ^{12} C, ^{14} N, ^{16} O) with carbon target, two different codes have been used: the abrasion model [94] and the Liège intranuclear-cascade model INCL [72]. Both models are utilised to describe nucleus-nucleus (NN) collisions, but they contain different approaches as explained below.

The abrasion model can only be used to describe nucleus-nucleus collisions.

Assuming the Fermi-gas model, nucleons occupying the overlap volume of the colliding nuclei are distributed randomly in momentum space inside the Fermi spheres of projectile and target nuclei. These nucleons, when removed during the collision, leave holes in the Fermi sea. Each hole is associated with a certain energy obtained according to the single particle-hole picture, considering an isospin-independent potential depth. Using the Fermi-gas distribution of the single-particle levels, the gained excitation energy is described by a linear distribution between 0 and 40 MeV, providing an average excitation energy of 13.5 MeV per removed nucleon. In this approximation, shell effects are neglected and the nucleon-separation energies are isospin independent, assuming a constant value for all nuclei. The internal energy of the single holes is then redistributed among all the degrees of freedom of the remaining nucleus, which thermalises and forms a compound nucleus. The total excitation energy gained by the remnant is given by the sum of the single particle-hole excitations, being proportional to the number of removed nucleons and the depth of the hole created inside the potential [94].

In this particular approach, the collision can be described in terms of Glauber's picture [103], assuming that at relativistic energies the bombarding energy is well above the Fermi energy. Under this assumption, Karol's approximation [104] is used to determine the total interaction cross sections and only the nucleons in the overlap region between projectile and target nuclei (participants) interact strongly, while the nucleons outside this zone (spectators) remain undisturbed. It is assumed that the trajectories of the interacting nucleons are straight lines and the nucleons participating to the interactions are those which belong to that part of the projectile nucleus which geometrically overlap with the target nucleus [103]. The masses of the remaining nuclei (projectile and target spectators) are thus determined by the geometrical overlap as a function of the impact parameter. The neutron-to-proton (N/Z) ratio of the remaining nucleus is determined just by statistical considerations, where the distribution of the N/Z ratio after the collision is calculated by

using the hyper-geometrical approach [105]. Thus, the average N/Z ratio of the remaining nucleus corresponds to the one of the initial nucleus, although with large statistical fluctuations, which lead to large variations in the N/Z ratio of the reaction products [106].

In order to reproduce cross section for light projectiles, a multiplication factor, which modifies the excitation energy, has been introduced, F_{EE}. Figures 5.8 and 5.6 depict the ABRABLA07 predictions using different factors ($F_{EE} = 2.0, 1.0, 0.75$) for reactions induced by ^{13,16} O projectiles for the first Figure and ^{22} O nuclei for the second one. The first factor, $F_{EE} = 2.00$, was originally performed for peripheral collision studies with much heavier nuclei, like ^{197}Au [107, 108, 109]. Since we are dealing with light nuclei, we have studied the effect of two factors, 1.0 and 0.75, that correspond to smaller gain of excitation energy than the standard value. Additionally, other R^{3}B collaborators in [61] performed a similar analysis to extend the application of the ABRABLA07 code. In this mass region, we have calculated *via* minimization the cross section differences (predicted and measured) for oxygen, nitrogen, carbon, and boron fragments and fixed excitation energies correction factor, i.e. $F_{EE} = 0.75$ for $A = 13-16$, and $F_{EE} = 1.00$ for $A = 20, 22$.

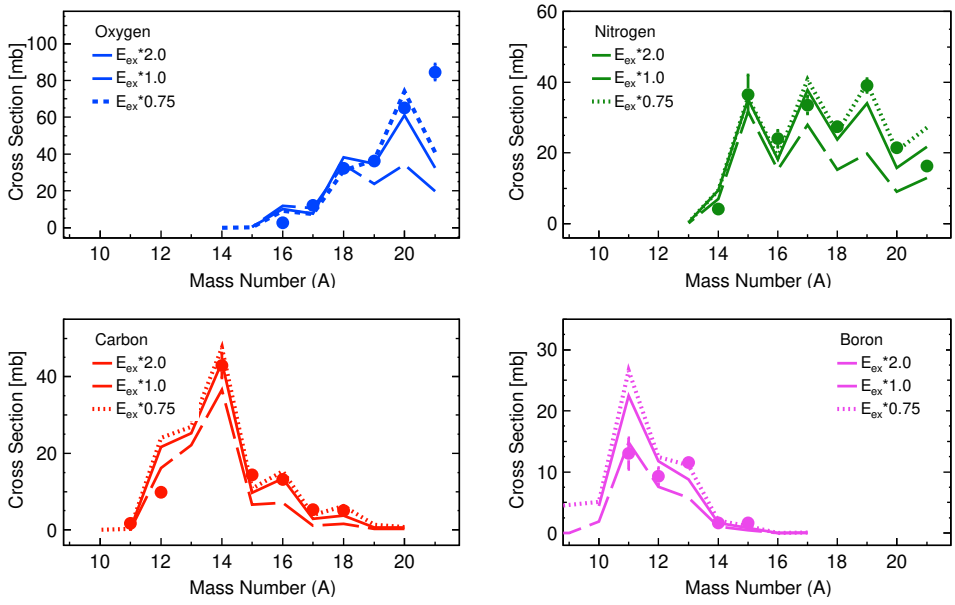

Figure 5.6: Experimental cross sections with ABRABLA07 predictions for reactions induced by ^{22}O projectiles performed for 0.75,1.0 and 2.0 factors in the excitation energy..

The second model that we propose to describe nucleon-nucleon collisions is the dynamic code INCL, which can be considered as a Monte Carlo method to solve numerically the dynamic transport equations describing particle-nucleus and NN collisions. The nature of INCL is essentially classical, being assumed that hadrons are perfectly localised in phase space and that they are bound by a potential. In this approach, the nuclear

collision is treated as successive relativistic binary hadron-hadron collisions separated in time, where the positions and momenta of hadrons are followed as time evolves.

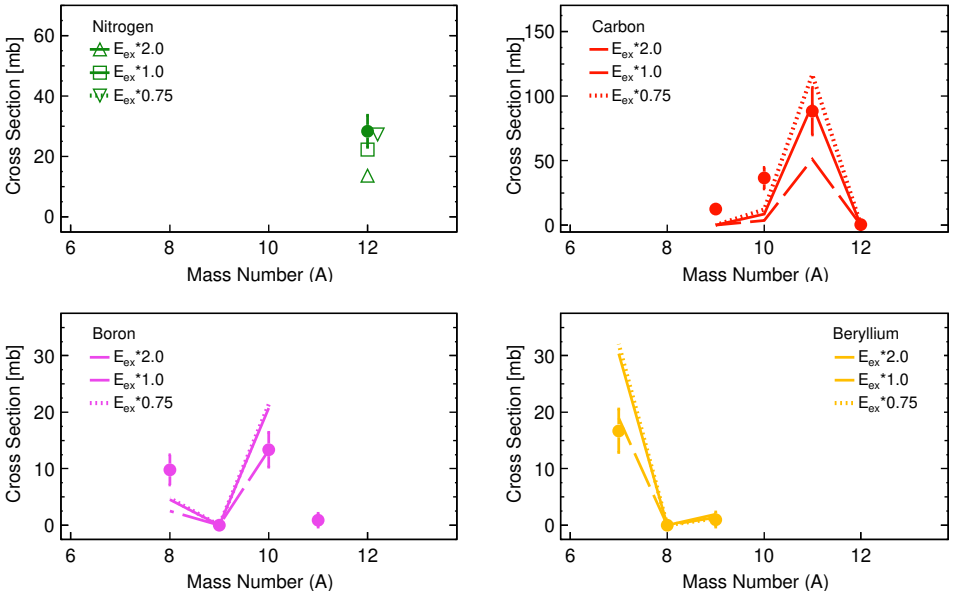

Figure 5.7: Experimental cross sections with ABRABLA07 predictions for reactions induced by ^{13}O projectiles performed for 0.75,1.0 and 2.0 factors in the excitation energy.

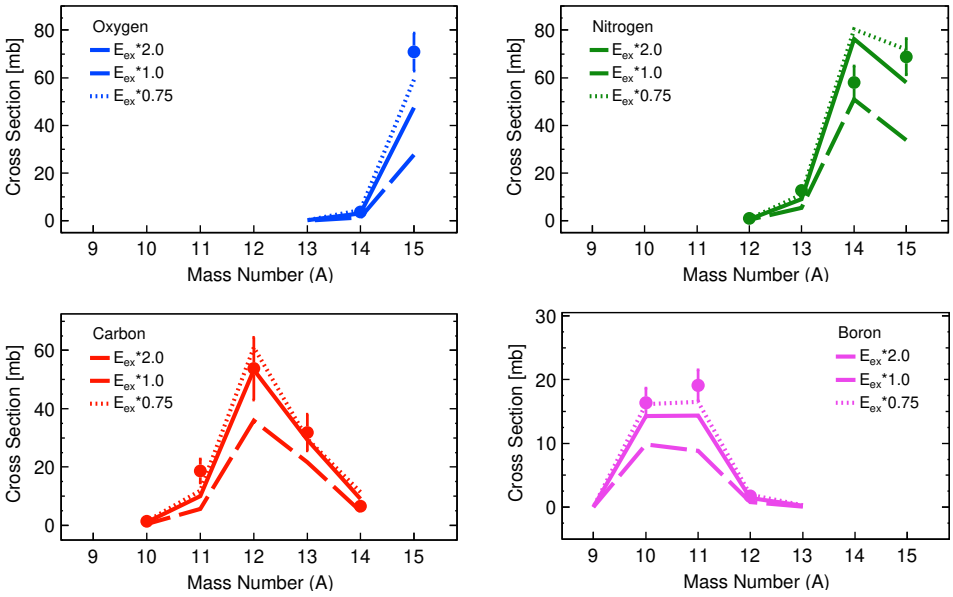

Figure 5.8: Experimental cross sections with ABRABLA07 predictions for reactions induced by ^{16}O projectiles performed for 0.75,1.0 and 2.0 factors in the excitation energy.

It is also assumed that hadrons move along straight trajectories until they undergo a collision with another hadron or until they reach the surface, where they could eventually escape. Cross sections are determined from a set of collision events taken at different impact parameters and for which nucleon positions and momenta are initially sampled for each participant nucleus.

In INCL, NN reactions are modelled as a sequence of binary collisions between the hadrons present in the system. Here, one must note that projectile and target nuclei are treated in different ways. Assuming reactions in inverse kinematics, projectile nucleus is represented by a potential well according to the Woods-Saxon distribution, whose radius depends on the nucleon momentum [110]. The potential well depth for nucleons is calculated according to optical models, including isospin dependences [111], while radii and diffuseness parameters of the neutron and proton density profiles are taken from Hartree-Fock-Bogoliubov calculations since they provide a good description of single-nucleon removal processes in spallation reactions [93]. For target nucleus, those treated by INCL ($A \leq 18$), the nucleon momenta are described with a Gaussian distribution considering the same RMS momentum (3/5 p_F) for protons and neutrons, with $p_F = 270$ MeV/c.

For the dynamical description of the collision between projectile and target nuclei, each event is fired at a given impact parameter b, ranging from 0 to a distance b_{max} given by the sum of the maximum radius of projectile and target nuclei. If two hadrons approach each other at a distance lower than a minimum distance, they interact. The minimum distance is calculated from energy-dependent parametrizations of the hadron-hadron interaction cross sections for all possible collisions according to [112]. During the cascade process, the particles inside the projectile volume are divided into participants and spectators. Participants are defined as particles that have collided with at least one other participant, while spectators are the rest of particles. Collisions between spectators are forbidden in order to eliminate the spontaneous boiling of the Fermi sea. For projectile nucleons, a strict Pauli blocking is also applied to the first collision to account for surface effects and for effects of the depletion of the Fermi sea [113], while it is neglected for target nucleons [72]. For the subsequent collisions, INCL applies the Pauli principle according to the usual procedures by means of statistical blocking factors. In addition, a consistent dynamical Pauli blocking is applied to all particles at the end of the cascade process to reject non-physical results, see [110] for more details.

Usually INCL can calculate reaction in inverse kinematics. However, if the target is heavier than A=18, the collision will be performed in direct kinematics since INCL code cannot estimate collision with projectile masses $A > 18$.

Both models, Abrasion and INCL, provide hot excited remnants which are characterised in atomic and mass numbers, excitation energy, and angular momenta. An extra approach is performed to describe the production of the final nuclear residues. In this work, an explosive decay (ABLA07) of these remnant nuclei is considered since they have

small masses and relatively high energies.

The ABLA07 code describes the explosive decay as a fragmentation processes based on two phases: a break-up of hot remnants breaks into residues and, de-excitation of these residues *via* sequential evaporations.

The first stage is utilised only if the temperature of the remnant exceeds a mass-dependent freeze-out temperature threshold calculated according to the prescription given by Natowitz and collaborators [114]:

$$T_{freeze-out} = max[5.5, 9.337e^{(-2.82\times10^{-3}A^{Rem})}]\text{MeV} \tag{3.3}$$

where A^{Rem} is the mass number of the remnant. If this temperature threshold is overcome, the system breaks up into fragments and nucleons whose mass is sampled according to an exponential distribution with a slope parameter τ, providing that the sampled mass is rejected when exceeding the maximum available mass given as $A^{Max} = A^{Rem}$ - $A_{freeze-out}$. The $A_{freeze-out}$ corresponds to the freeze-out mass that is determined from the freeze-out temperature and the average energy removed per nucleon in the breakup process according to [115]. The value of τ is calculated assuming a linear dependence on the excitation energy per nucleon in the temperature regime of interest, as explained in [116, 117]. The sampling is performed until the maximum available mass A^{Max} is consumed. The atomic number of the corresponding fragment is also sampled at the same time from a Gaussian distribution centred at a value Z_{mean}, which is determined by imposing that the ratio A/Z is the same of the hot remnant. The width of the distribution is given by:

$$\sigma_Z^2 = \frac{T_{freeze-out}}{C_{sym}} \tag{3.4}$$

where C_{sym} is the symmetry term of the nuclear equation of state [118]. The excitation energies of the resulting hot residues are determined by assuming thermal equilibrium at the freeze-out temperature [115]. Finally, each of the breakup residues with a mass number greater than $A = 4$ will then enter the de-excitation stage.

The de-excitation process of the hot excited residues is performed according to Weisskopf's formalism [119], taking into account the emission of γ-rays, neutrons, light-charged particles, and intermediate-mass fragments (*IMFs*).

For a more realistic description of the de-excitation process, the separation energies and the emission barriers for charged particles are also considered according to the atomic mass evaluation from 2012 [49] and the Bass potential [120], respectively.

In addition, de-excitation by fission is also included according to a dynamical picture described in [121], although this mechanism is no important for the reactions studied in this work.

5.4.2 Oxygen Chain Measurements

We have extended the fragmentation reaction analysis to different oxygen isotopes covering totally the neutron-deficient region ($^{13-15}$O) and partially neutron-rich area

(^{20,22}O). Tables 5.4, and 5.5 present the calculated fragmentation cross sections whereas the measurements of ^{16}O projectiles have been already shown in Table 5.2. In addition, all these results all displayed in Figures 5.9, 5.10 5.11 and compared with the ABRABLA07 and INCL + ABLA07 model predictions.

$(Z,A)_p$ @ 397 $A \cdot MeV$	$(Z,A)_f$	σ_{frag} [mb]
8,13	7,12	23.16 (2.80)
	6,12	4.73 (1.15)
	6,11	75.56 (4.78)
	6,10	37.68 (3.44)
	6,9	9.86 (1.81)
	5,11	1.30 (0.49)
	5,10	12.74 (1.79)
	5,8	7.77 (1.50)
	4,9	1.06 (0.43)

$(Z,A)_p$ @ 349 $A \cdot MeV$	$(Z,A)_f$	σ_{frag} [mb]
8,14	8,13	36.91 (2.31
	7,13	39.32 (2.30)
	7,12	14.29 (1.50)
	7,11	0.24 (0.24)
	6,12	60.41 (3.00)
	6,11	66.35 (3.25)
	6,10	16.88 (1.76)
	6,9	2.85 (0.90)
	5,11	7.45 (0.98)
	5,10	12.20 (1.40)
	5,8	4.82 (0.99)
	4,10	0.25 (0.16)
	4,9	2.93 (0.67)

$(Z,A)_p$ @ 308 $A \cdot MeV$	$(Z,A)_f$	σ_{frag} [mb]
8,15	8,14	11.08 (1.93)
	8,13	3.33 (1.57)
	7,14	64.32 (5.06)
	7,13	32.25 (3.77)
	7,12	5.84 (1.95)
	6,13	24.50 (3.34)
	6,12	60.28 (4.93)
	6,11	41.51 (4.14)
	6,10	3.91 (1.38)
	6,9	1.00 (1.00)
	5,11	9.97 (1.83)
	5,10	12.12 (2.09)
	4,10	1.62 (0.81)
	4,9	10.21 (2.64)

Table 5.4: Cross sections for fragmentation reactions of ^{13}O, ^{14}O and ^{15}O on a carbon target (0.561 $gcm{-}2$). The final fragment is refereed with its Z and A numbers. The cross section is showed with statistical uncertainties in brackets.

For the neutron-deficient projectiles, previous measurements of single-nucleon knock-out reactions induced by ^{14}O at intermediate energies have been reported in [122][6]. The authors presented several cross sections, for 0p1n and 2p1n channels. Although, the former reaction was indirectly measured (see [122] for further details); they could report a cross section of 2p1n channel leading of 60(9) mb, which is consistent with current value of 66.4(3.3) mb (see Figure 5.9).

At first glance, analysing it seems likely that reactions leading to light fragments are more sensitive to shell effects than those induced by stable and neutron-rich isotopes. In these cases (^{14,13} O projectiles), the description provided by INCL+ABLA07 is not very satisfactory, despite it includes shell effects *via* nuclear radius evaluation from Hartree-Fock Bogoliubov approaches and uses the latests single particle energies from [49, 50]. This disagreement could be found in 2pxn channels, which lead to carbon fragments, induced by ^{13}O and ^{14}O isotopes as we can see in Figure 5.9. While, ABRABLA07 predictions reproduce reasonably well the trend of cross sections, even for carbon fragments.

Measurements of heavier projectiles, such as ^{15}O and ^{16}O (depicted in Figure 5.10), provide similar behaviour for both model calculations.

For the neutron-rich projectile , we focused on reactions induced by ^{20,22}O on a carbon target (0.561 $g \cdot cm^{-2}$), displayed in Figure 5.11 (left and right). The two theoretical approaches reproduce acceptably well the majority of the fragmentation channels. The

[6]Performed in the Research Centre for Nuclear Physics (RCNP at Osaka University)[123].

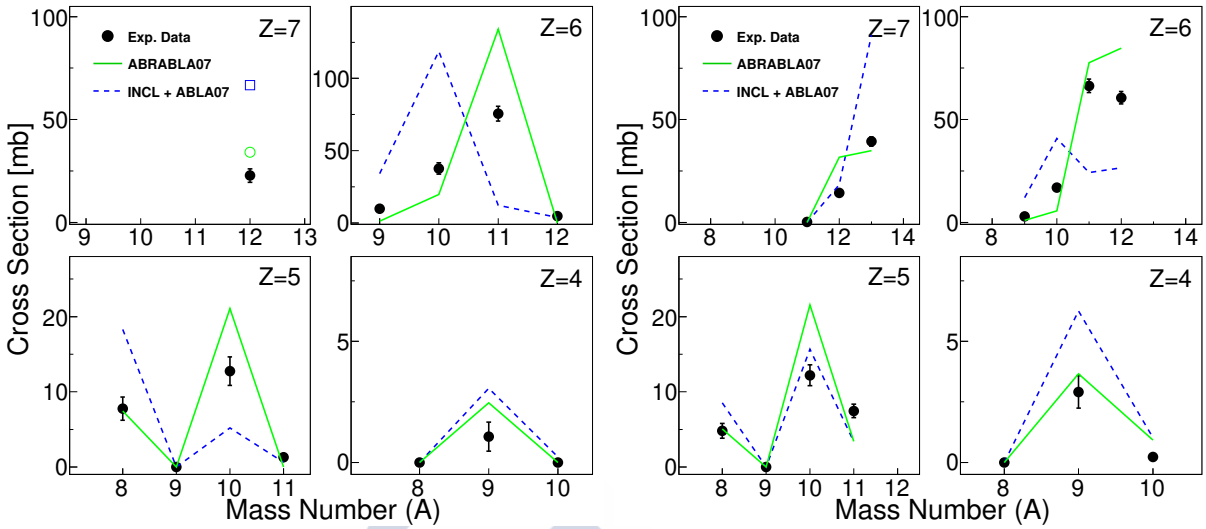

Figure 5.9: Fragment cross sections for ^{13,14} O (left and right) projectiles on a carbon targets (0.561 and 0.935 $g \cdot cm^{-2}$) at 397A MeV, 349A MeV, respectively. Model calculations are included as green solid line for ABRABLA07 and blue dashed line for INCL + ABLA07 codes.

global trend is, also described reflecting the same ups and downs due to changes in the fragments shells. For INCL+ABLA07 calculations only some discrepancies related to one nucleon-removal channels and, in particular to 0p1n channel, are observed and it will be discussed in detail in the next section.

ABRABLA07 calculations[7] value achieve slightly better prediction performances for the 1pxn and 2pxn channels (nitrogen and carbon fragments, Z=7,6); INCL + ABLA07 predictions are closer to measured values for the 3pxn and 4pxn channels (boron and beryllium isotopes, Z=5,4). In general, the fragmentation cross sections evaluated within this work is reproduced accurately with a rough abrasion-ablation model.

5.4.3 Single Neutron-Removal Channels

One-nucleon cross sections deserve special mention. We start analysing in detail the 1p0n, and later, we will focus on the 0p1n channel.

For neutron-deficient projectiles , such as $^{13-14}$O, INCL+ABLA07 calculations over-estimate the 1p0n cross sections by a factor close to two. A plausible explanation for this over-prediction was already introduced in terms of final state interactions (see dissertation [124] and references therein). The high energy beams could be responsible of several interactions of the outcome particle interacts several times before leaving the weakly bound

[7]Using a $f_{EE} = 1.00$

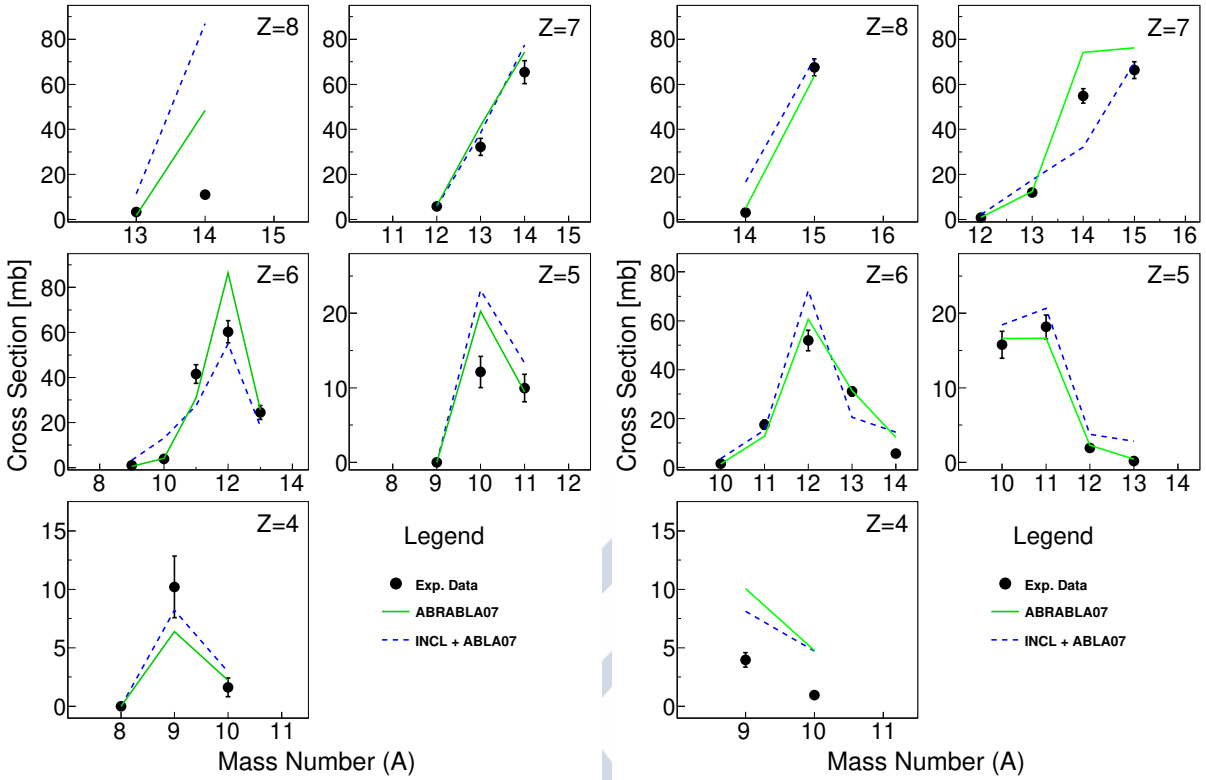

Figure 5.10: Fragment cross sections for ^{15,16} O (left and right) projectiles on carbon target at 308A MeV and 450A MeV. Model calculations are included as green solid line for ABRABLA07 and blue dashed line for INCL + ABLA07 codes.

ejectile and in consequence excite it. As a result, other channels will be populated *via* de-excitation of this ejectile, reducing the measured cross section for the 1p0n channel. This effect will be not taken into account in the theoretical model.

This effect becomes less relevant for stable nuclei, as shown in measurements with ^{16}O shows. Similar behaviour is also observed for ^{15}O projectiles, where the final fragment is a stable nucleus, ^{14}N.

On the contrary, in neutron-rich region we observe a fair reproduction of the cross section, being theoretical measurements quite below than experimental. In this case, other structural effects could come into play and compete with final state interactions reducing these effects.

Turning to the 0p1n channel, over-estimations in the neutron-deficient region and underestimations for neutron-rich projectiles are observed.

For ^{15}O projectiles, since ^{14}O is less stable than ^{14}N, INCL+ABLA07 calculation fails estimation does not reproduce well this cross section.

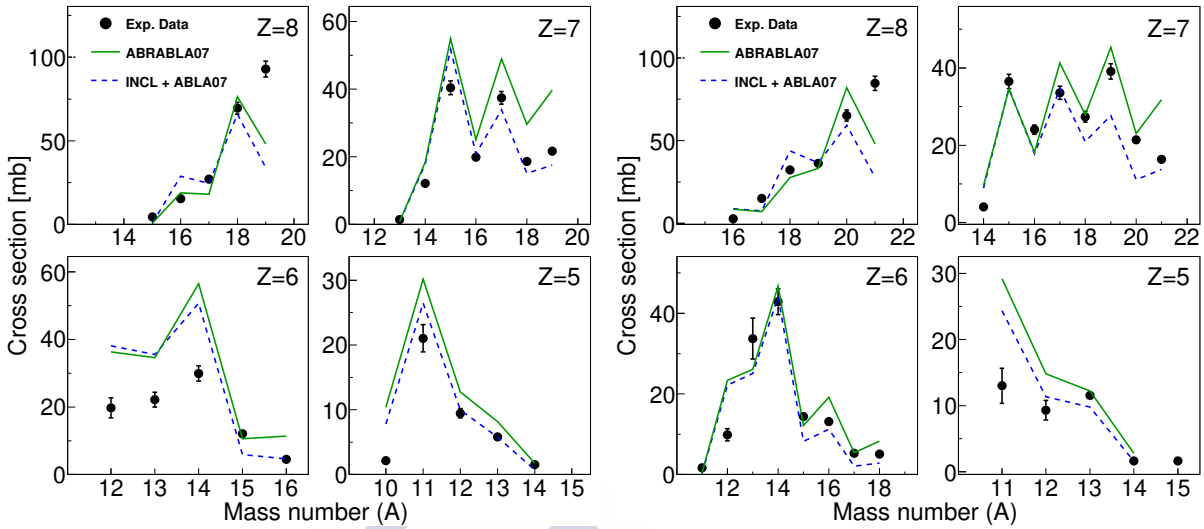

Figure 5.11: Fragment cross section for ^{20} O and ^{22} O projectiles on a carbon target at $\sim$ 400A MeV). Black circles include total uncertainties.

For neutron-rich (^{20} ^{22}O) projectiles, theoretical predictions are, approximately a half of the measured cross sections. Contributions of paring effects, due to the breakup a neutron-pair, which is needed to reach the final even-odd fragment, should be estimated in future works.

To conclude, we have realised that the INCL+ABLA07 code cannot estimate correctly one-nucleon cross sections for exotic projectiles. In these predictions, we observe two different behaviours, depending on the level structure of projectiles. For those nuclei located nearby to proton drip-line (neutron-deficient nuclei), final state interactions become important and must be reckoned; whereas, for neutron-rich projectiles paring effects take precedence over final state interaction.

As addendum, we display in Figure 5.13 QFS a single-nucleon removal cross sections for oxygen and nitrogen compared with INCL + ABLA07. These calculations which reproduce acceptably well the global tendency of these nuclear processes this reaction mechanism but fail predicting some cross sections.

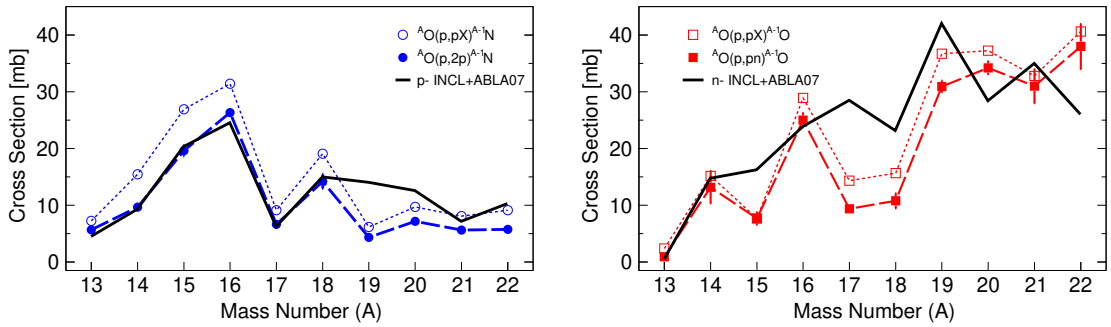

Figure 5.12: QFS (filled) and single-nucleon removal (empty) cross sections for oxygen projectiles (points coloured) and INCL+ABLA07 model predictions (black line).

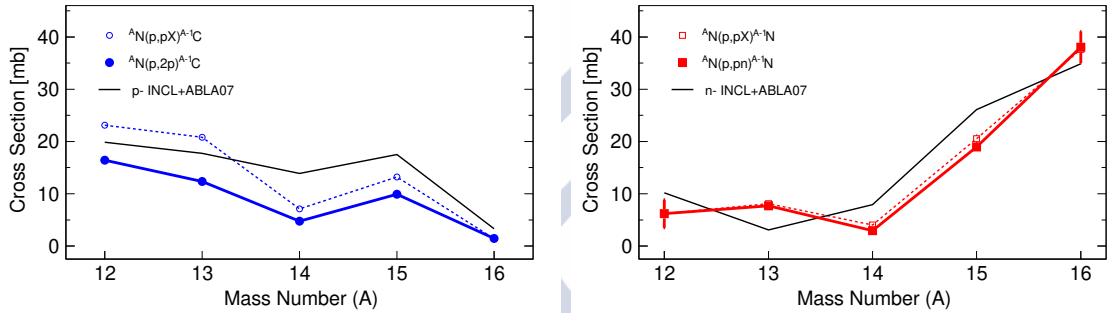

Figure 5.13: QFS (filled) and single-nucleon removal (empty) cross sections for nitrogen projectiles (points coloured) and INCL+ABLA07 model predictions (black line).

$(Z,A)_p$ @ 406 $A \cdot MeV$	$(Z,A)_f$	σ_{frag} $[mb]$
8,20	8,19	92.94 (4.68)
	8,18	69.49 (3.50)
	8,17	27.02 (1.36)
	8,16	15.31 (0.78)
	8,15	4.48 (0.35)
	7,19	21.68 (1.09)
	7,18	18.63 (0.94)
	7,17	37.46 (1.89)
	7,16	19.85 (1.00)
	7,15	40.40 (2.04)
	7,14	12.14 (0.92)
	7,13	1.40 (0.14)
	6,16	4.52 (0.25)
	6,15	12.06 (0.91)
	6,14	29.91 (2.25)
	6,13	22.15 (2.22)
	6,12	19.74 (2.97)
	5,14	1.54 (0.12)
	5,13	5.82 (0.31)
	5,12	9.28 (0.72)
	5,11	21.03 (2.11)
	5,10	2.03 (0.34)
	4,12	1.41 (0.14)
	4,11	3.13 (0.48)
	4,10	6.93 (1.39)

$(Z,A)_p$ @ 414 $A \cdot MeV$	$(Z,A)_f$	σ_{frag} $[mb]$
8,22	8,21	84.60 (4.29)
	8,20	65.18 (3.31)
	8,19	36.28 (1.84)
	8,18	33.22 (1.63)
	8,17	12.05 (0.91)
	8,16	2.73 (0.42)
	7,21	16.33 (0.83)
	7,20	21.43 (1.09)
	7,19	39.07 (1.98)
	7,18	27.37 (1.39
	7,17	33.56 (1.70)
	7,16	24.04 (1.22)
	7,15	36.52 (1.84)
	7,14	3.84 (0.22)
	6,19	0.33 (0.10)
	6,18	5.06 (0.27)
	6,17	5.26 (0.28)
	6,16	13.16 (0.67)
	6,15	14.36 (0.74)
	6,14	42.88 (3.22)
	6,13	33.74 (5.06
	6,12	9.86 (1.48)
	5,15	1.63 (0.59)
	5,14	1.65 (0.13)
	5,13	11.56 (0.59)
	5,12	9.31 (1.41)
	5,11	13.01 (2.60)
	4,11	0.27 (0.11)
	4, 9	1.66 (0.13)

Table 5.5: Cross section measurements for fragmentation reaction of ^{20}O, and ^{22} O on a carbon target (0.561 and 0.935 $g \cdot cm^{-2}$ respectively). The final fragment is described with its Z and A numbers. The cross section is showed with total uncertainties in brackets.

USC
UNIVERSIDADE
DE SANTIAGO
DE COMPOSTELA

Conclusions

This dissertation studies Quasi-Free Reactions in asymmetric isospin nuclei [53] focusing on neutron-deficient nuclei, and in particular, on reactions induced by oxygen (A=13-22) and nitrogen (A=12-16) isotopes. Measurements have been carried out in the R^3B-LAND set-up (Reactions with Relativistic Radioactive Beams [18]) located at GSI, in Darmsdadt.

The experimental procedures have been described in Chapter 1 and 2. Each analysis step has been deeply investigated and compared with simulations in the R^3BRoot framework and previous analysis from other R^3B collaborators [14, 15, 16, 61, 67]. Once the analysis was fulfilled, two main physical observables were calculated, cross section and momentum distributions (P_y and P_{long}), associated to the studied reaction.

Single-nucleon removal reactions of neutron-deficient oxygen and nitrogen on a proton target have been investigated. The study of the corresponding cross sections detecting solely the outgoing fragment provides uniquely inclusive information. The identification of fragment final states configuration has been possible *via* γ-rays detection in coincidence using CB signals. This evaluation has been only possible for some selected cases (lack of statistics).

The experimental method to obtain of exclusive observables has been validated comparing with published data [30] and cross-checking the population of ^{14}N nucleus coming from (p,pX) and (p,nX) reactions. This analysis has been extended to Quasi-Free Scattering (QFS) channels. We have not observed large discrepancies in the excited states identification, neither population rates. In addition, these measurements have an associated smaller uncertainties since QFS channels require the simultaneously detection of two signals compatible with high energy light particles (two nucleons) in CB, and exhibiting a strong polar angular correlation defined by the reaction kinematics.

We have carried out a comparative study of the reaction mechanism included in the single-removal channels achieved with our experimental set-up, and contrasted with QFS. The identification of all channels included in our experimental evaluation of nucleon removal reactions is rather laborious and not always possible. The removal channels present the advantage of having significantly higher statistics than QFS. This point is important since lack of statistics could sometimes induced to erroneous conclusions.

Since we work with exotic nuclei, where some nucleons fall nearby Fermi surface, their levels can be mixed decreasing the occupation values. This could favour absorption effects in the nuclear media which could be significant in some cases. These contributions have been estimated to be around 10% (going up to 25% for $^{16,17}O$ projectiles) and 15% (reaching maximums in $^{14,19}O$ projectiles) for neutron and proton channels, respectively.

The "weight" of these absorption effects has been calculated *via* differences between QFS cross sections and measurements under less restricted conditions where the angular condition of the two scattered light particles has been released. The origin of these reactions is not fully determined; even though it has been already investigated in previous works in medium mass neutron-rich nuclei [124].

Another channel contributing to the neutron removal comes from inelastic processes between projectile and target, which lead to the same final fragment *via* nucleon-evaporation after the collision. Measured cross sections using the proton arm afford us to quantify these effects, being up to 9% and 13% of the single proton and neutron removal channels.

At this point, we have identified the majority of nuclear processes that can contribute to the removal cross sections; i.e. $\sigma_{removal} = \sigma_{QFS} + \sigma_{ABS} + \sigma_{INE}$. The data description achieved is good and has been quantified with the residues that fall nearby to zero in all studied channels, that underscores the soundness of the analysis.

Another goal of this work was to gain information on the structure of the exotic nuclei under study. This was possible by means of comparing with theoretical models. Reduction factor, R_s, takes into account how well the model reproduce the expectations of the extreme independent-particle model (IPM). Prior experiments, beginning with electro-induced proton knocked-out reactions (e,e'p) [81] observed for many stable species analysed a quenching of 20-30 % between experimental and theoretically evaluated cross sections. The advent of radioactive beams afford a rather complete study of nucleon removal of exotic projectiles on light targets at the intermediate energies, leaded by MSU [11]. They used these reactions to determine the quenching factor making use of eikonal theory. They yield to similar conclusions to electron QFS, but introduce a new discussion element: the existence of strong dependence of R_s with the neutron-proton asymmetry ($\Delta S = S_p - S_n$ for a proton removal channel). Later, transfer [83] and QFS reactions interpreted into the framework of DWIA [16] confirmed the existence of general quenching factor, but infer a small dependence ΔS.

We have again addressed this kind of analysis in this Ph.D. focusing on QFS induced by ^{14}O projectiles on a proton target (i.e. ^{14}O(p,2p)^{13}N and ^{14}O(p,pn)^{13}O). Since both reactions they lead to final fragments without any bound excited state below particle emission thresholds ($S_{n/p}$), exclusive measurements are directly provided. Theoretical calculations, performed by Sevilla's group ([34, 86]) within the Continuum Discretised Coupled Channels formalism (CDCC), and using two different potentials (Dirac and Paris-Hamburg) have been used to estimate single-particle cross sections (σ_{sp}) for these channels.

To obtain theoretical cross sections, we have considered shell model calculations (WBT interaction) for those channels were np-nh do not have mixing configurations, whereas in the case of ^{14}O(p,pn) channel, where four neutrons can be strong candidates to be removed, we have utilised a more sophisticated description, such as self-consistent Green's function (SCGF) theory [83, 91].

The obtained R_s values reflect a slight dependence on the asymmetry in concordance with [16, 83], confirming an overall quenching factor of about 0.64-0.72 (within 2 sigma). This value extracted from current data is a preliminary estimation.

The comparison of momentum distributions for (p,2p) and (p,pn) reactions induced by ^{14}O with theoretical evaluations [86], is also performed. The shape observed for (p,2p) distribution matches with the CCDC model using a simplify IPM description of the nuclear levels (FWHM compatible), where the footprints of removed proton could be found in a "pure" $p_{1/2}$ shell. For the sibling channel, i.e. (p,pn), experimental distributions are narrower than expected. In these case, the knocked-out neutron comes, in principle, from $p_{3/2}$. This disagreement would maybe indicate that mixing configurations, including holes excitations in $p_{3/2}$ (above the Fermi level), should be taken into account to reproduce the experimental shape.

For both channels, we also notice an asymmetry in the shape of longitudinal momentum distributions. Similar effects have already reported in [92], for lower energies (at 100-200 AMeV) are were identify with large differences between proton and neutron separation energies.

In the last Chapter, we have presented a systematic analysis of fragmentation reactions, leading to lighter fragments; and total interaction cross sections for ^{12}C, ^{14}N, and ^{16}O. These measurements are relevant in particle radiation therapy since fragmentation reactions degrade the dose localisation widening the Bragg Peak [36] and could fill some of the existing "data gaps" in the computational codes used to estimate doses. Contrary to the therapy case, the correct decisions of shielding materials are based on materials that produce reactions going to lighter particles due to their reduced biological effectiveness [58].

Two theoretical approaches, based on abrasion-ablation (ABRABLA07) and intranuclear cascade (INCL+ABLA07), have been used to describe these reaction channels. They allow us to understand the behaviour of these model calculations in the neutron-deficient region.

For ABRABLA07 code, the excitation energy factor has been analysed spanning from 0 to 2. The purpose was to determine the correct contribution of the excitation energies involved in the reaction and to enhance the prediction capabilities for light nuclei, since the code was originally used for the study of heavy isotopes, like ^{197}Au [107]. Finally, the

use of two different E_{ex} values is needed to be considered (0.75 for very light projectiles,- $^{13-16}$O, ^{12}C, ^{14}N - and 1.00 for heavier ones - $^{20-22}$O).

The INCL+ABLA07 predictions describe almost all channels except one-proton zero-neutron and zero-proton one-neutron reactions (1p0n and 0p1n). In these cases, other processes such as final states interactions or neutron-breakup have been proposed in order to explain the discrepancies. For the neutron removal channel case, two different behaviours depending on the level structure of projectiles (i.e. their mass) have been observed; over-estimations for neutron-deficient and underestimations for neutron-rich projectiles. In these nuclei located nearby the proton drip-line (neutron-deficient nuclei), final state interactions become important and must be reckoned. On the other hand, for neutron rich projectiles paring effects seem to play a major role.

The R^{3}B collaboration at the international FAIR Accelerator Facility, would afford in close future to conduct accurate experiments on the topics addressed in this work. FAIR Accelerator Facility would provide higher intensity, and higher beam energies; additionally R^{3}B would achieve significantly larger detector geometrical acceptance and intrinsic resolution and detection efficiencies.

In parallel, new theoretical approaches, in the structure and reaction fields, would be also necessary to improve the understanding of collisions between exotic projectiles and light targets.

Resumen

Uno de los objetivos de esta tesis es la exploración de núcleos exóticos ligeros para ampliar nuestra compresión de las correlaciones nucleónicas en materia asimétrica y estudiar la evolución de la estructure nuclear con la asimétria N-Z. Se ha estudiado haciendo uso de reacciones nucleares de dispersión casi libre de hadrones, QFS[8], (p,2p) y (p,pn) en cinemática inversa en R^{3}B[9]. Este tipo de reacciones es una alternativa experimental muy interesante a las de (e,e'p) [81] o de arranque [11] ("knock-out"). Su fortaleza radica en sensibilidad al estudio de orbitales (tanto de valencia como internas) de protones y de neutrones. El sistema de detección está dotado de una gran acceptancia geométrica y provee al investigador de una completa información sobre el proceso de dispersión . Proporciona además conocimiento sobre la estructura individual de los estados de partícula independiente del núcleo objeto de estudio.

El análisis se ha centrado en la cadena isotópica del oxígeno y en varios isótopos de nitrógeno cubriendo la zona de núcleos deficitarios en neutrones de la carta de núcleos. Este trabajo complementa a los anterioes de la colaboración R^3B [23, 27, 28, 30, 31]. Además, para estos núcleos, se ha extendido el análisis cubriendo los canales de fragmentación para un blanco de carbono, obteniendo medidas de las secciones eficaces asociadas. Se ha usado como referencia las medidas obtenidas para haces de núcleos estables ^{12}C, ^{14}N, y el propio ^{16}O. Estas medidas pueden ser relevantes en los campos de radioterapia, en particular en el tratamiento con hadrones, [36] y en la protección espacial pasiva [37] donde se requiere de medidas experimentales de gran precisión. Las secciones eficaces de fragmentación y de reacción aquí presentadas permiten completar las carencias existentes en las bases de datos.

[8]Del acrónimo inglés Quasi-Free Scattering.
[9]Reactions with Relativistic Radiactive Beams.

Descripción experimental

En los últimos años se está implementado con gran éxito un dispositivo experimental, instalado en la "Cave C" en el centro de haces pesados GSI (Darmsdadt, Alemania, Figura 1.1.) el cual detallaremos a continuación. Este dispotivo es el precursor del experimento R^3B que se locarizará en la futura instalación internacacional FAIR[10].

Un haz primario de iones de $^{40}Ar^{+11}$, producido en la fuente de iones, se aceleró en el UNILAC (UNIversal Linar ACelerator) y, posteriormente, se inyectó en el acelerador circular SIS-18 acalzando energías de hasta 500 AMeV (ver Figura 1.1). A continuación el haz viajó hasta el separador de fragmentos, FRS, que se compone de cuatro etapas cada una de ellas conformada por un dipolo magnético, que dobla el haz; cinco quadropolos, que lo focalizan; y dos sexpolos, que corrigen de aberraciones. En la entrada del FRS se situó un blanco de berilio (4.011 g/cm^2) para producir a través de reacciones de fragmentación un cokctail de haces secundarios. La función del FRS es identificar y separar estos núcleos dependiendo de su cociente massa-carga dado por la siguiente ecuación:

$$B\rho = \frac{p}{Q} \propto \frac{A}{Z} \cdot \beta\gamma \tag{3.5}$$

donde $B\rho$ es la rigidez magnética característica de la configuración del FRS; p, Q, Z son el momento, carga y número atómico de la partícula consideranda Durante el presente trabajo se usa unidades naturales (c=1, propias de la física nuclear) y además $\beta = v$ y l factor de Lorentz queda, $\gamma = 1/\sqrt{1-\beta^2}$.

En nuestro experimento, S393, se han utilizado 6 diferentes valores de rigidez magnética permitiendo a los investigadores analizar un amplio rango de A/Z desde 1.5-3.0. El FRS contó con dos plásticos centelleadores que se encargaron de medir tiempos de vuelos, con los que se determinan las velocidades de los iones. Estos centelleadores están localizados en los planos focales S2 y S8 de la Figura 1.2.

La selección de los núcleos pertenecientes al haz secundarios que se muestra en la Figura 1.2 se logró en dos etapas y permitió identificar en vuelo isotópicamente los fragmentos, es decir, determinar su masa y número atómico, y así como también su velocidad.

El dispositvo experimental empleado se denomina R^3B-LAND (ver Figura). Está alojado en la cueva C del GSI y fue diseñado a principios de los años 90 siendo regularmente actualizado. R^3B-LAND es la semilla para el futuro experimento R^3B en el centro FAIR [18].

Se divide en tres grandes areas que permiten identificar la velocidad, carga y posición de todos los fragmentos implicados en la reacción.

En la primera zona denominada "área del proyectil" (Projectil Area) se registraron medidas de tiempo de vuelo de los iones de nuestro haz secundario a través de los tiempos registrados por varios centelleadores plásticos (los dos anteriores, S2 y S8 del FRS, y

[10]Facility Antiproton Ion Research

POS[11]). Además se contó con un colimador activo que servía para centrar el haz, y un detector de silicio PSP[12] con el que obtener medidas de la posición y pérdidas de energía.

A continuación, en el "área del blanco" (Target Area), el haz atravesó dos dobles detectores altamente segmentados de silicio, impactó con el blanco y a su salida, volvió a atravesar otros dos idénticos detectores de silicio (DSSSDs[13]). Los blancos se alojaron en una rueda mecánica permitiendo cambiar remotamente entre diferentes materiales. Alrededor de esta, se acopló una caja en cuyas caras laterals se situaron más detectores de silicio para medir energía y posiciones de los fragmentos ligeros de las reacciones QFS. Por último, rodeando a todos estos detectores, se situó el calorímetro Crystal Ball [22], compuesto por 159 cristales de (NaI(Tl)) en configuración esférica cubriendo casi 4-pi en ángulo sólido. El propósitio de CB es la identificación de rayos γ, provenientes de los núcleos excitados, asćomo de partículas ligeras (nucleones) producidos en la reacción nuclear.

Los fragmentos salientes atraviesan el electroimán ALADIN para ser seleccionados según su masa y carga. Nos encontramos en el "área de los fragmentos" (Fragment Area) donde los fragmentos producidos en la reacción y seleccionados por ALADIN recorren distintas trayectorias atravesando diversos detectores. Cada una de las tres ramas se encargó de la detección de un tipo de partícula. Los neutrones, con carga neta cero, no se deflectan, siguen trayectorias rectilíneas y son detectados por LAND situado al final y perpendicularmente a la línea de haz. Los fragmentos cargados y protones son dirigidos hacia la rama de fragmentos y protones respectivamente. Varios detectores de fibra (GFIs) y cámaras de deriva (PDCs) así como paredes de tiempo de vuelo (TFW y PTW), nos permiten obtener medidas de las posiciones, pérdida de energía y tiempo de vuelo.

Todo ello permite al investigador obtener e identificar tanto los projectiles como los fragmentos producidos en la reacción y obtener medidas e información en cinemática completa.

Cabe mencionar que durante este trabajo se han utilizado varios tipos de disparadores - triggers - que perminten a los investigadores seleccionar, mediante software, aquellos eventos que fueron guardados bajo una serie de requisitos. Los más usados han sido el disparador de fragmento (fragment trigger), que conlleva registro en el TFW, el disparador de reacción (reaction trigger) asociado con eventos que han depositado un energía superior a la umbral en CB y a su vez impactan en TFW y diversas condiciones para seleccionar protones y neutrones en sus respectivas ramas.

[11] POsition-sensitive Scintillator
[12] Position-sensitive SiPin diodes
[13] Double-side Silicon Strip Detectors.

Reaciones de arranque de nucleones.

Las reacciones de aranque de un nucleón se han estudiado en cinemática inversa. En ellas, un protón o un neutrón es extraído fuera del proyectil cuando éste impacta sobre el blanco. En particular, reacciones inducidades por oxígneos y nitrógenos deficitarios en neutrones sobre un blanco de protón. La notación seguida es: ${}^{A}_{Z}X(p,pX)^{A-1}Y$.

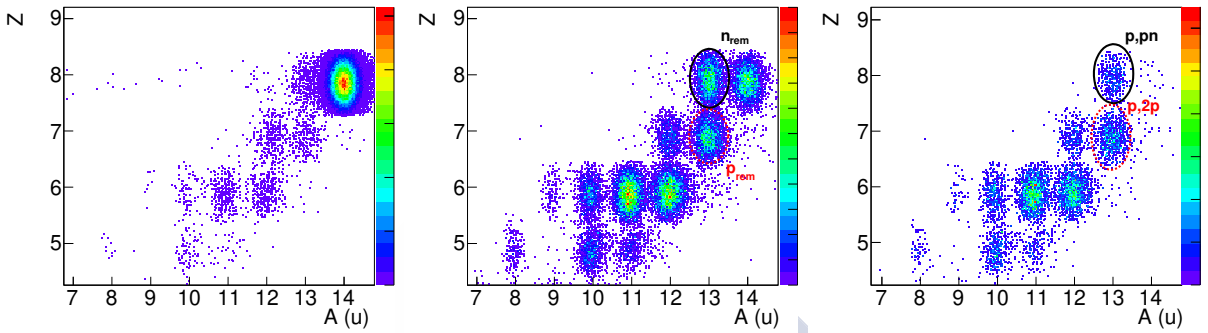

Figure R1: Identifación, carga frente a la masa (Z frente A), para los fragmentos reconstruidos a partir de proyectiles de ^{14}O sobre un blanco de CH_2. Izquierda bajo la condición *fragment trigger*, centro *reaction trigger* y derecha, condicions de QFS.

Identificamos, a partir de las señales resitrados en los detectores y mediante programas informáticos, tanto el proyectil, como el fragmento, e imponemos las condiciones para seleccionar ambos núcleos con la mejor resolución y la menor contaminación isotópica posible. Las gráficos de la Figura R1 son un ejemplo de diagramas en dos dimensiones que representan la carga frente a la masa para los fragmentos que han llegado al detector TFW. Se aplican diferentes condiciones (lógicas de registro de datos o "triggers") con las que medimos o bien la contribución residual del proyectil, a la izquierda de la anterior Figura; o los fragmentos que han reaccionado, en el histograma de la derecha de la misma.

Seleccionando cada fragmento de manera unívoca, es decir en carga y masa, isotópicamente se han podido reconstruir las distribuciones de momento[14] y, evaluar las secciones eficaces de estas reacciones.

A continuación se muestran en la Figura R2 las secciones eficaces de arranque de un protón/neutrón para proyectiles de oxígeno y nitrógeno, acompañadas únicamente de sus correspondientes incertidumbres estadísticas.

[14]También fue necesario medidas de velocidades y posiciones para lo que se usó los de detectores de silicio

Los espectros de de-excitación por emisión de rayos gamma se han podido reconstruir a partir de las señales registrados en el calorímetro CB usando para ello un programa de reconstrucción de sucesos "addback" que incluyendo la correciń Doppler[15].

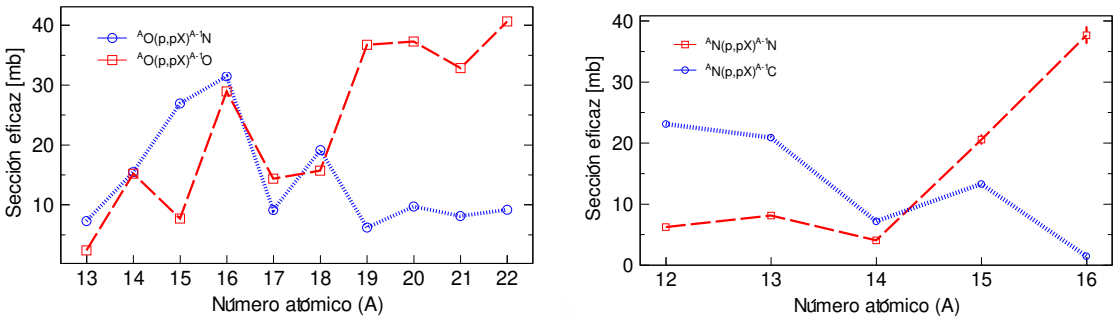

Figure R2: Secciones eficaces de arranque de un protrón/neutrón para proyectiles de oxígeno y nitrógeno.

Validamos nuestro método experimental de dos maneras complementarias. Los espectro gamma de fragmentos de ^{15}N se han obtenido a patir de los canales de arranque de protón (neutrón) para proyectiles de ^{16}O (^{15}N). Además se han comparado con los resultados previamente analizados en la tesis[30] alcanzándose similares poblaciones relativas para los mismos estados excitados considerados.

Posteriormente, se comparó otros dos espectros gamma para el mismo núcleo, ^{14} N (ver Figura 3.7), que fueron producidos por dos reacciones diferentes, una de arranque de neutrón con proyectiles de ^{15}N y otra de arranque de un protón para núcleos ^{15}O, llegando a la misma conclusión anterior.

Reaciones dispersión casi libre de hadrones.

El procedimiento experimental seguido es similar al explicado en las reacciones de arranque de nucleones. Se identifica isotópicamente el proyectil y el fragmento; con la salvedad de que ahora ha de imponerse la condición de "QFS" o de dos eventos (dos protones o protón-neutrón) de alta energía correlacionados angularmente en el detector CB (ver el gráfico de la derecha en la Figura R1).

Secciones eficaces, distribuciones de momento y espectros gamma se han obtenido para una serie de reacciones de QFS con los mismos núcleos anteriormente mencionados.

[15]Los rayos-γ emitidos desde núcleos moviendose a velocidades cercanas a la de la luz deben ser corregidos por este efecto

En la siguiente Figura (R3) se muestran las secciones eficaces para los canales (p,2p) y (p,pn) con proyectiles de oxígeno y nitrógeno.

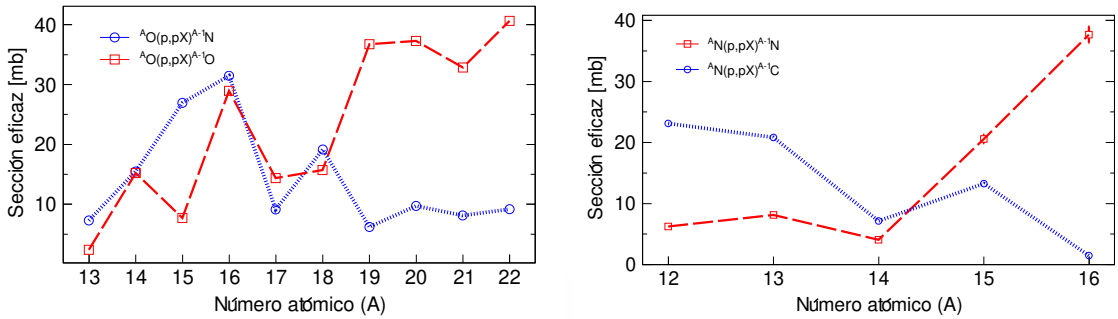

Figure R3: Secciones eficaces (mb) en función del número másico del proyectil para los canales de (p,2p) - círculos azules - y (p,pn) - cuadrados rojos - producidos por núcleos de oxígeno y nitrógeno sobre un blanco de protón.

Por ejemplo, se han obtenido espectros de desexcitación similares a los anteriores para los fragmentos ^{14} N pero ahora bajo al condición de QFS tal y como muestra la tabla resumen R1. Por tanto, se observan los mismos estados excitados bajo la condición de arranque y de QFS, con parecidas poblaciones, que concuerdan entre súna vez considerados los errores en las medidas. Tambień, se obtuvieron similares espectros gamma para núcleos de ^{14} N procedentes de reacciones con distintos proyectiles, es decir, ^{15}O(p,2p)^{14} N y ^{15}N(p,pn)^{14}N. La detección simultánea del fragmento y su desexcitación gamma permite seleccionar differentes configuraciónes finales en el ejectriles y, por lo tranto proporciona medidas exclusivas.

	σ^{p-rmv} (mb)	$\sigma^{(p,2p)}$ (mb)	σ^{n-rmv} (mb)	$\sigma^{(p,pn)}$ (mb)
Inclusiva	26.91 (0.73)[2.42]	19.63 (0.93)[1.18]	20.53 (0.70)[2.62]	18.94 (0.51)[2.81]
g.s.	6.53 (0.52)[0.76]	7.85 (1.18)[0.56]	9.94 (0.40)[1.49]	9.15 (0.71)[1.53]
0+ ^{1st} at 2.32 MeV	3.20 (0.17)[0.37]	2.32 (0.25)[0.22]	3.05 (0.16)[0.46]	1.79 (0.10)[0.30]
1+ ^{2nd}at 6.20 MeV	3.11 (0.17)[0.36]	2.78 (0.30)[0.27]	4.10 (0.22)[0.61]	3.69 (0.22)[0.62]
2+ ^{3rd}at 7.02 MeV	2.62 (0.15)[0.31]	2.50 (0.33)[0.24]	3.44 (0.18)[0.52]	4.11 (0.24)[0.69]

Table R1: Secciones eficaces exclusivas (mb) para fragmentos de ^{14}N producidos con reacciones de arranque de un protón ($p-rmv$), (p,2p), arranque de un neutrón ($n-rmv$) y (p,pn), respectivamente para tres estados excitados además del fundamental. Se muestra la sección inclusia para todos los canales mencionados. Los errores estadísticos van entre paréntesis, mientras que los sistemáticos se representan entre corchetes.

Mecanismo de reacción. Interpretación de los resultados.

Gracias a la gran versatilidad del dispositivo experimental, se han podido analizar en profundidad y comparar entre sí las medidas para los dos canales anteriores.

En el presente trabajo se han cuantificado las diversos canales de reacción que contribuyen a la sección eficaz de arranque de un nucleón: $\sigma_{arranque} = \sigma_{QFS} + \sigma_{ABS} + \sigma_{INE}$ donde σ_{QFS} son las anteriores medidas para dispersión casi libre, σ_{ABS} está relacionado con procesos absortivos cuyo origen está aún en investigación; y σ_{INE} es debido a procesos inelásticos durante la colisión y la posterior emisión de un nucleón.

Los fenómenos absortivos se han cuantificado aplicando una condición "relajada" de QFS, donde se ha exigido la detección de dos señales en CB compatibles con dos nucleons de alta energía, pero no se ha tenido en cuenta la correlación angular de los dos nucleons salientes. Los valores típicos de esta contribución son 10% (maíxmo en torno a 25% para los proyectiles de $^{16,17}O$) para arranque de neutrones y de 15% (máximo en 24% para $^{14,19}O$) para los canales con protón.

Los procesos inelásticos han sido estimados usando la rama de protones y LAND e imponiendo la condición de un evento asociado a un protón o un neutrón (emitido en la misma direacción del haz, con una velocidad similar) a los canales de arranque de nucleón. Estas contribuciones son, como máximo, del 9% y 13% para los canales de un protón y un neutrón arrancados respecitivamente.

Otro objetivo del presente trabajo fue estudiar las propiedades de la estructura nuclear de los núcleos exóticos bajo análisis. Para ello, se hizo uso del factor de reducción o "quenching" (R_s el cuál estima lo bien que se reproduce el modelo extremo de partícula independiente, o cualquier otro modelo de estructura nuclear, para una descripción teórica en particular del mecanismo de reacción

Estudios previos de electro difusión fueron capaces de estimar el "quenching" en torno a 20-30% ([81]). Posteriormente y usando haces radiactivos a energías intermedias en MSU [11] se obtuvieron conclusiones similares a las anteriores mediante la comparación de los resultados obtenidos con las prediciones teóricas del modelo "eikonal". Estos trabajos introducieron una nueva variable, la fuerte dependencia de R_s con la asimetría neutrón-protón dado por $\Delta S = S_p - S_n$ para el canal de arranque de protones. Años después, reacciones de transferencia [83] y reacciones de dispersión en el marco de la aproximación de impulso-ondas deformadas, DWIA[16] [16] corroboraron el orden de magnitud del factor R_s, pero observaron una muy pequeña dependencia de R_s con ΔS, menos acuciada que la observada por los científicos de MSU.

[16]acrónimo del inglés Distorted Wave Impulse Approximation, DWIA

En este trabajo, se ha podido extraer factores de reducción para diversas reacciones de QFS usando predicciones teóricas del grupo teórico de Sevilla, [34] bajo la aproximación de canales acoplados discreticamente al contínuo, CDCC [17] y usando dos potenciales diferentes, (Dirac and Paris-Hamburg) para la descripción de la reacción y con un modelo de estructura con interacción WBT que permite obtener la ocupación de los nucleones. La associación de ambos modelos permite calcular las secciones eficaces teóricas. Los resultados de R_s obtenidos son muy parecidos a los anteriores y, muestran una nula o muy ligera dependencia de R_s en la asimetría, tal y como se representa en la Figura R4. Destacar que para el canal ^{14}O(p,pn) se ha considerado un factor espectroscópico calculado mediante ab-initio SCGF según [12, 91].

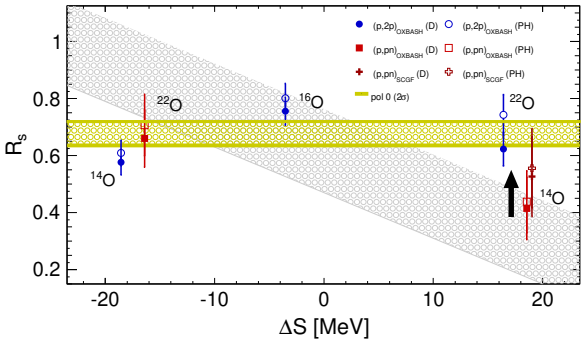

Figure R4: R_s calculado para canales (p,2p) and (p,pn) representado en función de ΔS. La región grisácea representa la tendencia predicha por [11], mientras que la zona amarillenta corresponde a un ajuste de nuestros datos (con el potencial Paris-Hamburg) para el caso con una significanción de 2 σ.

Nos hemos centrado en unos canales en concreto, ^{14}O(p,2p)^{13}N y ^{14}O(p,pn)^{13}O, ya que ambas reacciones producen fragmentos sin estados excitados ligados por debajo del umbral de emisión de partículas a energía ($S_{n/p}$) dando lugar a directamente a medidas exclusivas. Por ello, se ha comparado las distrubiciones de momento de estos canales con las predicciones del grupo de Sevilla [86].

Si bien para el canal (p,2p) la forma experimental de la distribución de momento de la componente "y", y por tanto también la anchura de esta, es compatible con las predicciones teóricas calculadas según el modelo CDCC antes descrito y para aún model simple de estructura nuclear (IPM) considerado sólo una subcapa pura de $p_{1/2}$; para su homólogo (p,pn) la distribución experimental es más estrecha de lo esperado. En este caso, el neutrón "arrancado" pertenece a una única subcapa $p_{3/2}$. Una plausible explicación radica en que las excitaciones partícula hueco puedan poblar capas por encima del nivel de Fermi y la consideración de todas estas configuraciones aumentaría la anchura de la distribución.

Evaluando distribuciones del momento longitudinal se ha encontrado una ligera asimetría para estos dos canales. Estos efectos habían sido predichos [92] para energías intermedias (100-200AMeV) y se han interpretado como una consecuencia de las grandes diferencias entre la energía de separacón de protón y de neutrón, (ΔS).

[17] Acrónico de Continuum Discretised Coupled Channels, CDCC

Reacciones de fragmentación

El último capítulo nos hemos centrado en el estudio de los canales de fragmentación que producen elementos más ligeros. Además se ha calculado las sección de reacción para los principales núcleos estables que constituyen el cuerpo humano, ^{12}C, ^{14}N, y ^{16}O.

Paralelamente, hemos utilizado dos códigos computacionales basados en el modelo de abrasión-ablación (ABRABLA07) y en la cascada intranuclear junto con ablación del remante excitado INCL+ABLA07 para reproducir la tendencia de las secciones efiaces. Ambos códigos reproducen casi todos los canales, pero cabe mencionar ciertos aspectos relevantes.

En el caso de ABRABLA07, el factor multiplicativo de la energía de excitación ha sido modificado (mediante un análisis sistemático de residuos) para que reproduzca reacciones con projectiles ligeros ya que originalmente fue desarrollado para estudiar isótopos pesados como el oro.

Para el caso de los canales de arranque de un único nucleón la INCL+ABLA07 no es capaz predecir el orden de magnitud de las secciones experimentales. Ya sea para el canal cero-protón un-neutrón (0p1n), donde se subestima; o para su análogo un-protón cero-neutrón (1p0n), arrancados donde se sobreestimata los valores esperimentales; la discusión del porqué ocurre este fenómeno sigue abierta. Por una parte esperamos para los núcleos cercanos a la línea de goteo de protones las interacciones de estados finales sean más importantes mientras que para los núcleos ricos en neutrones el efecto de ruptura de pares de neutrones tendría un peso relativo mayor.

Como trabajo futuro mecionar que nuevas y sofisticadas aproximaciones teóricas podrán permitir un mejor conocimiento de ciertos canales de reacciones, sobre todo en núcleos exóticos sobre blancos ligeros.

El experimento R^{3}B, en el accelerador FAIR, podrá afrontar medidas más precisas gracias a haces más energéticos e intensos, así como una mayor acceptancia geométrica y una eficiencia de detección mayor que la actual.

USC
UNIVERSIDADE
DE SANTIAGO
DE COMPOSTELA

Appendix A

A	Isotope	S_n[MeV]	S_p[MeV]	Isotope	S_n[MeV]	S_p[MeV]	Isotope	S_n[MeV]	S_p[MeV]
8	^{8}C	-	-0.1						
9	^{9}C	14.3	1.3						
10	^{10}C	21.3	4.0	^{10}N	-	-2.6	-	-	-
11	^{11}C	13.1	8.7	^{11}N	22.6	-1.3	-	-	-
12	^{12}C	18.7	16.0	^{12}N	15.0	0.6	^{12}O	-	-0.3
13	^{13}C	4.5	17.6	^{13}N	20.1	1.9	^{13}O	16.9	1.5
14	^{14}C	8.2	20.8	^{14}N	10.6	7.6	^{14}O	23.2	4.6
15	^{15}C	1.2	21.1	^{15}N	10.8	10.2	^{15}O	13.2	7.3
16	^{16}C	4.3	22.6	^{16}N	2.5	11.5	^{16}O	15.7	12.1
17	^{17}C	0.7	23.4	^{17}N	5.9	13.1	^{17}O	4.1	13.8
18	^{18}C	4.2	26.14	^{18}N	2.8	15.2	^{18}O	8.0	15.9
19	^{19}C	-	-	^{19}N	5.3	16.4	^{19}O	4.0	17.1
20	^{20}C	2.9	28.5	^{20}N	2.2	17.9	^{20}O	7.6	19.3
21	-	-	-	^{21}N	4.6	19.6	^{21}O	3.8	21.0
22				^{22}N	1.3	20.9	^{22}O	6.9	23.3
23				^{23}N	1.8	22.6	^{23}O	2.7	24.7

Table A1: Neutron and proton separation energies for C, N and O nuclei taken from [50].

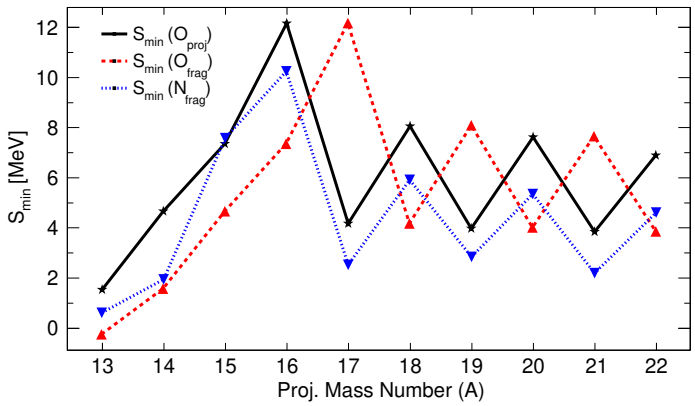

Figure A1: Minimum separation energies for O projectiles and fragments and N fragments.

Appendix B: Correction Factors

Secondary Reactions Probability

Detector	Material	Length (cm)	Thickness (mgcm^{-2})
S8	plastic	0.30	0.00
POS	plastic	0.20	206.46
PSP	Si	0.02	74.56
DSSSD1	Si	0.03	69.90
DSSSD2	Si	0.03	69.90
Target Set1&4	C (5mm)	0.25	935.00
CH2 9.81	0.49	922.14	69.9
Target Set2&3	CH2 5mm	0.25	460.60
C(3mm)	C	561.00	467.5
Vacuum	-	10.90	0.00
DSSSD3	Si	0.03	69.90
DSSSD4	Si	0.03	69.90
Vacuum	Si	97.30	0.00
ALADIN	He	144.20	25.81
Air	N,O,He	146.86	188.86
GFI-1	plastic	0.10	103.20
Air	N,O,He	72.00	92.59
GFI-2	plastic	0.10	103.20
Air	N,O,He	600.00	771.60
TFW	plastic	1.00	1032.30

Table B1: S393 characteristics used for Secondary Reactions Probability estimated by ATIMA and Amadeus codes.

Geometrical Acceptance

O fragments		
A	# removed neutrons	Acceptance (%)
22	0	95.10
21	1	98.90
20	2	99.93
19	3	98.94
18	4	94.12
17	5	80.88
16	6	70.85
15	7	59.00

N fragments		
A	# removed neutrons	Acceptance (%)
21	0	97.40
20	1	99.74
19	2	99.71
18	3	98.29
17	4	92.45
16	5	85.10
15	6	77.20
14	7	37.90

C fragments		
A	# removed neutrons	Acceptance (%)
20	0	96.4
19	1	99.4
18	2	99.99
17	3	99.95
16	4	96.41
15	5	87.17
14	6	68.04
13	7	42.70
12	8	20.69
11	9	5.50

B fragments		
A	# removed neutrons	Acceptance (%)
16	3	89.75
15	4	99.99
14	5	99.21
13	6	91.83
12	7	67.51
11	8	25.68

Be fragments		
A	# removed neutrons	Acceptance (%)
13	5	99.04
12	6	94.53
11	7	81.26
10	8	56.59
9	9	28.76
8	10	9.41

Table B2: Acceptance rates for several fragments belonging to setting 4 and with physical parameters evaluated from ^{22}O projectiles.

O fragments			N fragments		
A	# removed neutrons	Acceptance (%)	A	# removed neutrons	Acceptance (%)
21	0	98.91	20	0	99.71
20	1	99.99			

Table B3: Acceptance rates for several fragments belonging to setting 4 and with physical parameters evaluated from ^{21}O projectiles.

O fragments			N fragments		
A	# removed neutrons	Acceptance (%)	A	# removed neutrons	Acceptance (%)
20	0	97.90	19	0	96.08
19	1	98.85	18	1	97.23
18	2	98.15	17	2	96.72
17	3	97.13	16	3	95.37
16	4	91.98	15	4	94.52
15	5	90.25	14	5	91.37
14	6	83.88	13	6	88.13
13	7	63.14	12	7	78.48
C fragments			B fragments		
A	# removed neutrons	Acceptance (%)	A	# removed neutrons	Acceptance (%)
18	0	91.40	15	2	66.53
17	1	99.70	14	3	78.91
16	2	96.70	13	4	95.89
15	3	89.21	12	5	89.87
14	4	82.33	11	6	73.58
13	5	71.57	10	7	51.72
12	6	61.79			
11	7	43.62			

Be fragments		
A	# removed neutrons	Acceptance (%)
15	1	83.33
14	2	95.00
13	3	97.36
12	4	86.57
11	5	50.92
10	6	23.05

Table B4: Acceptance rates for several fragments belonging to setting 4 and with physical parameters evaluated from ^{20}O projectiles.

O fragments			N fragments		
A	# removed neutrons	Acceptance (%)	A	# removed neutrons	Acceptance (%)
19	0	98.85	18	0	97.34
18	1	98.15			

Table B5: Acceptance rates for several fragments belonging to setting 3 and with physical parameters evaluated from ^{19}O projectiles.

O fragments			N fragments		
A	# removed neutrons	Acceptance (%)	A	# removed neutrons	Acceptance (%)
18	0	96.51	17	0	92.54
17	1	94.87			

Table B6: Acceptance rates for several fragments belonging to setting 2 and with physical parameters evaluated from ^{18}O projectiles.

O fragments			N fragments		
A	# removed neutrons	Acceptance (%)	A	# removed neutrons	Acceptance (%)
17	0	99.85	16	0	97.41
16	1	98.15			

Table B7: Acceptance rates for several fragments belonging to setting 2 and with physical parameters evaluated from ^{17}O projectiles.

O fragments			N fragments		
A	# removed neutrons	Acceptance (%)	A	# removed neutrons	Acceptance (%)
16	0	96.51	15	0	98.47
15	1	94.79	14	1	92.59
14	2	86.78	13	2	80.97
13	3	71.81	12	7	62.8
C fragments			B fragments		
A	# removed neutrons	Acceptance (%)	A	# removed neutrons	Acceptance (%)
14	0	99.87	13	0	99.71
13	1	97.42	12	1	96.67
12	2	89.21	11	2	84.86
11	3	73.83	10	3	60.87
10	4	53.51			

Be fragments		
A	# removed neutrons	Acceptance (%)
10	2	83.04
9	3	63.59

Table B8: Acceptance rates for several fragments belonging to setting 2 and with physical parameters evaluated from ^{16}O projectiles.

O fragments			N fragments		
A	# removed neutrons	Acceptance (%)	A	# removed neutrons	Acceptance (%)
15	0	98.57	14	0	98.87
14	1	92.28	13	1	96.43
13	2	58.55	12	2	61.10
C fragments			B fragments		
A	# removed neutrons	Acceptance (%)	A	# removed neutrons	Acceptance (%)
13	0	97.94	12	0	97.07
12	1	98.36	11	1	96.33
11	2	95.31	10	2	90.16
10	3	78.32	9	3	88.51
9	4	38.92	8	4	83.22
Be fragments			Li fragments		
A	# removed neutrons	Acceptance (%)	A	# removed neutrons	Acceptance (%)
11	0	83.69	10	0	82.47
10	1	79.25	9	1	61.78
9	2	47.53			
8	3	15.98			
7	4	8.78			

Table B9: Acceptance rates for several fragments belonging to setting 1 and with physical parameters evaluated from ^{15}O projectiles.

O fragments		
A	# removed neutrons	Acceptance (%)
14	1	99.03
13	2	92.64

N fragments		
A	# removed neutrons	Acceptance (%)
13	0	99.67
12	1	82.64
11	2	61.11

C fragments		
A	# removed neutrons	Acceptance (%)
12	0	99.97
11	1	98.56
10	2	87.91
9	3	50.18

B fragments		
A	# removed neutrons	Acceptance (%)
12	0	99.99
11	1	93.45
10	2	85.48
9	3	71.80
8	4	58.58

Be fragments		
A	# removed neutrons	Acceptance (%)
10	0	97.30
9	1	78.17
8	2	55.12
7	3	29.96

Table B10: Acceptance rates for several fragments belonging to setting 1 and with physical parameters evaluated from ^{14}O projectiles.

O fragments		
A	# removed neutrons	Acceptance (%)
13	0	83.80

N fragments		
A	# removed neutrons	Acceptance (%)
12	0	85.25

C fragments		
A	# removed neutrons	Acceptance (%)
11	0	99.89
10	1	91.00
9	2	82.04

B fragments		
A	# removed neutrons	Acceptance (%)
10	0	91.78
9	1	88.65
8	2	84.98

Be fragments		
A	# removed neutrons	Acceptance (%)
9	0	89.73
8	1	86.14
7	2	78.40

Li fragments		
A	# removed neutrons	Acceptance (%)
8	0	41.30
7	1	31.30
6	2	15.30

Table B11: Acceptance rates for several fragments belonging to setting 1 and with physical parameters evaluated from ^{13}O projectiles.

Nitrogen Projectiles (A=12-16)

N fragments			C fragments		
A	# removed neutrons	Acceptance (%)	A	# removed neutrons	Acceptance (%)
12	0	98.78	14	0	99.99
11—	1	91.50			

Table B12: Acceptance rates for several fragments belonging to setting 1 and with physical parameters evaluated from ^{12}N projectiles.

N fragments			C fragments		
A	# removed neutrons	Acceptance (%)	A	# removed neutrons	Acceptance (%)
13	0	93.61	14	0	99.41
12	1	98.80			

Table B13: Acceptance rates for several fragments belonging to setting 1 and with physical parameters evaluated from ^{13}N projectiles.

N fragments			C fragments		
A	# removed neutrons	Acceptance (%)	A	# removed neutrons	Acceptance (%)
14	0	99.47	13	0	99.41
13	1	99.94	12	1	96.00
12	2	99.51	11	2	86.50
			10	3	69.21
B fragments			Be fragments		
A	# removed neutrons	Acceptance (%)	A	# removed neutrons	Acceptance (%)
12	0	99.21	11	0	98.92
11	1	91.90	10	1	92.68
10	2	69.61	9	2	73.33
9	3	51.76	8	3	64.15
8	4	39.38	7	4	41.70

Li fragments		
A	# removed neutrons	Acceptance (%)
8	2	28.21
7	3	23.27
6	4	17.50

Table B14: Acceptance rates for several fragments belonging to setting 2 and with physical parameters evaluated from ^{14}N projectiles.

N fragments			C fragments		
A	# removed neutrons	Acceptance (%)	A	# removed neutrons	Acceptance (%)
15	0	99.99	14	0	99.41
14	1	99.57			

Table B15: Acceptance rates for several fragments belonging to setting 2 and with physical parameters evaluated from ^{15}N projectiles.

N fragments			C fragments		
A	# removed neutrons	Acceptance (%)	A	# removed neutrons	Acceptance (%)
16	0	98.51	15	0	99.99
15	1	95.40			

Table B16: Acceptance rates for several fragments belonging to setting 3 and with physical parameters evaluated from ^{16}N projectiles.

^{12}C Projectiles

C fragments			B fragments		
A	# removed neutrons	Acceptance (%)	A	# removed neutrons	Acceptance (%)
12	0	99.99	11	0	99.21
11	1	92.02	10	1	91.90
10	2	72.14	9	2	69.61
			8	3	51.76

Be fragments			Li fragments		
A	# removed neutrons	Acceptance (%)	A	# removed neutrons	Acceptance (%)
11	0	99.52	8	2	61.05
10	1	96.02	7	3	29.33
9	2	91.50	6	4	9.45
8	3	75.00			
7	4	51.00			

Table B17: Acceptance rates for several fragments belonging to setting 2 and with physical parameters evaluated from ^{12}C projectiles.

USC
UNIVERSIDADE
DE SANTIAGO
DE COMPOSTELA

Appendix C: Momentum Distributions

Momentum distributions for single nucleon removal channel ("knock-out") and its corresponding QFS reaction induced by oxygen and nitrogen respectively.

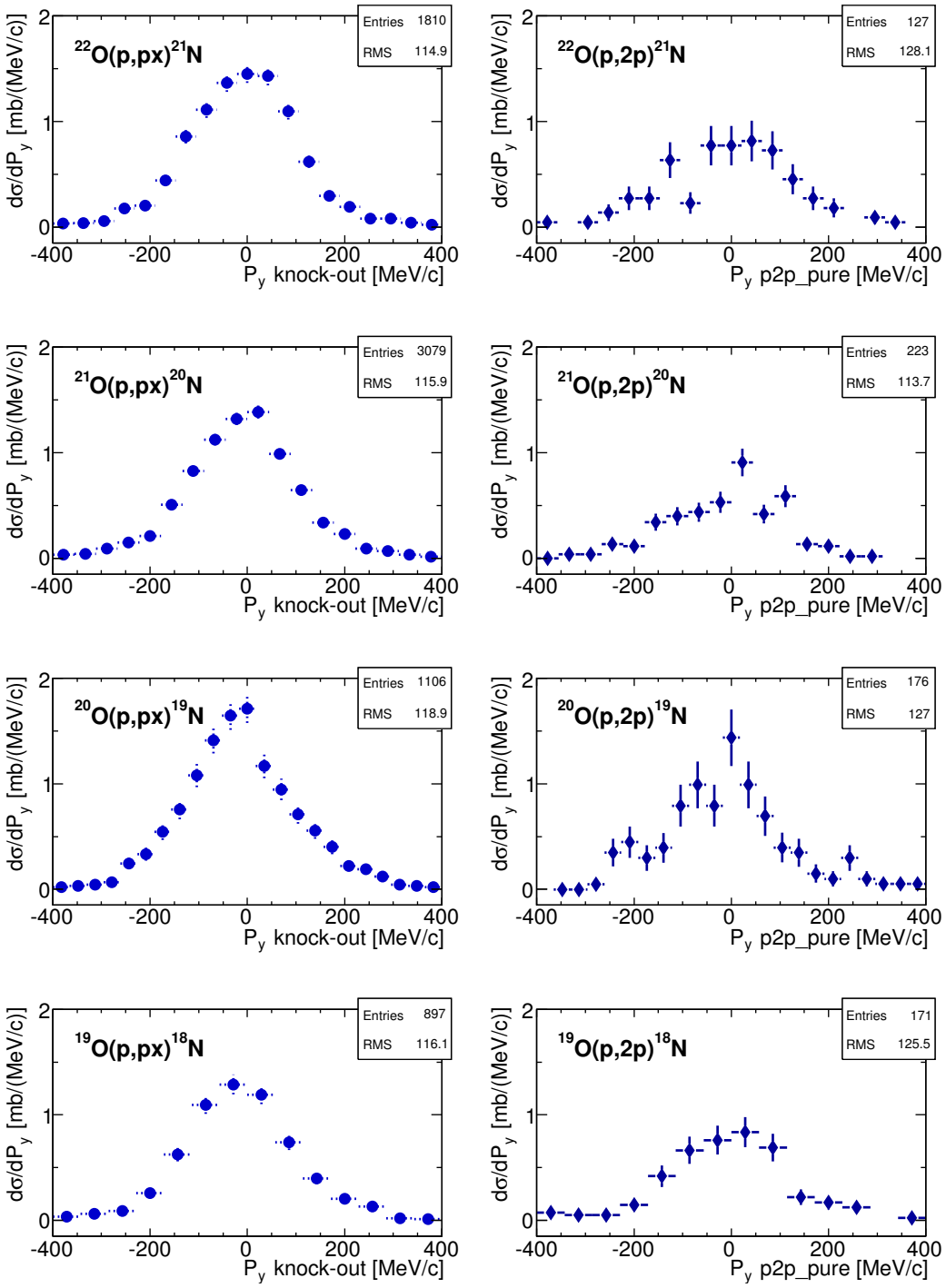

Figure C1: Distributions of P_y component for nitrogen nuclei obtained from single-proton removal (left) and (p,2p) reactions (right histograms) induced by ^{22,21,20,19}O projectiles on a proton target.

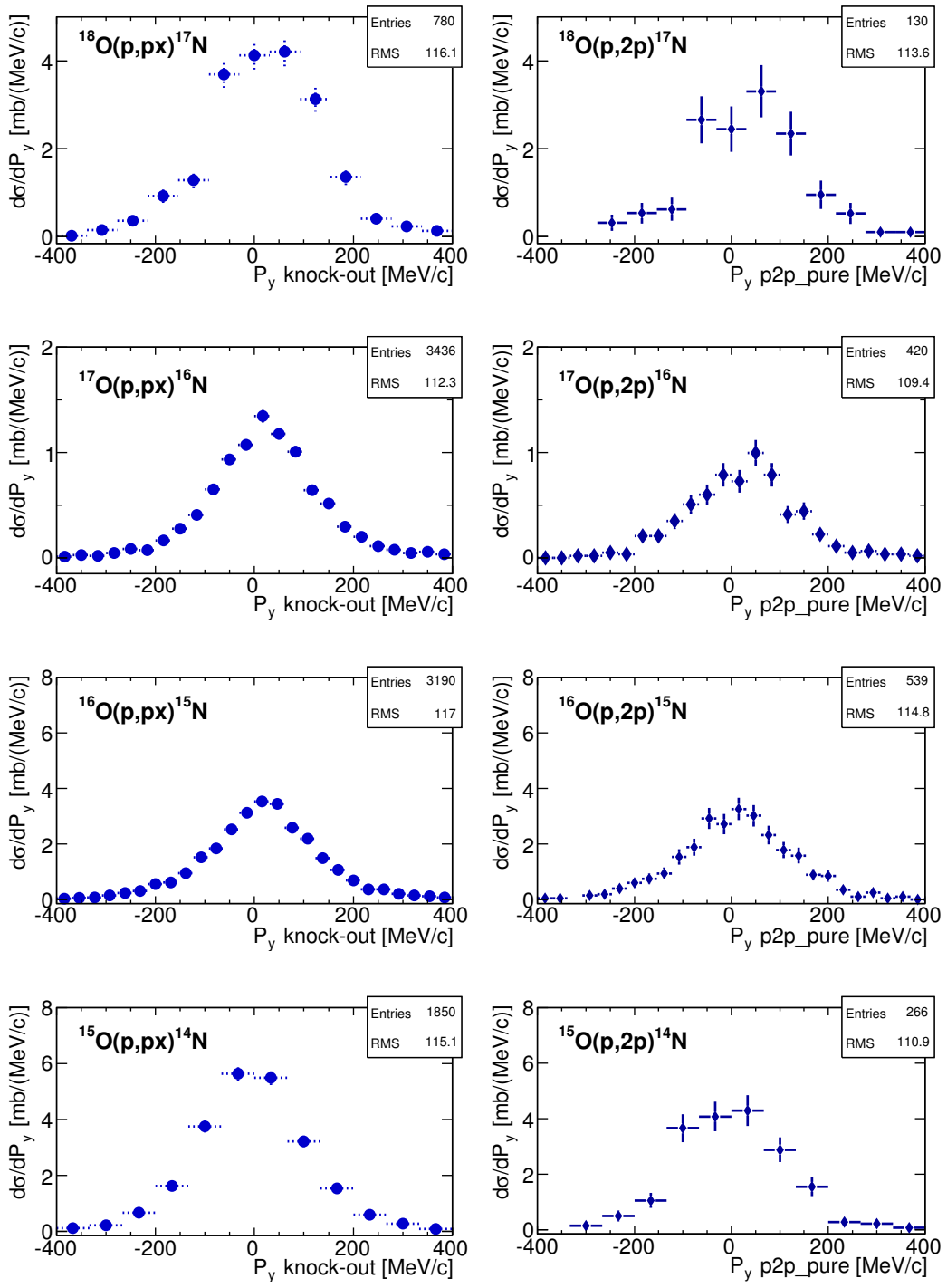

Figure C2: Distributions of P_y component for nitrogen nuclei obtained from single-proton removal (left) and (p,2p) reactions (right histograms) induced by ^{18,17,16,15}O projectiles on a proton target.

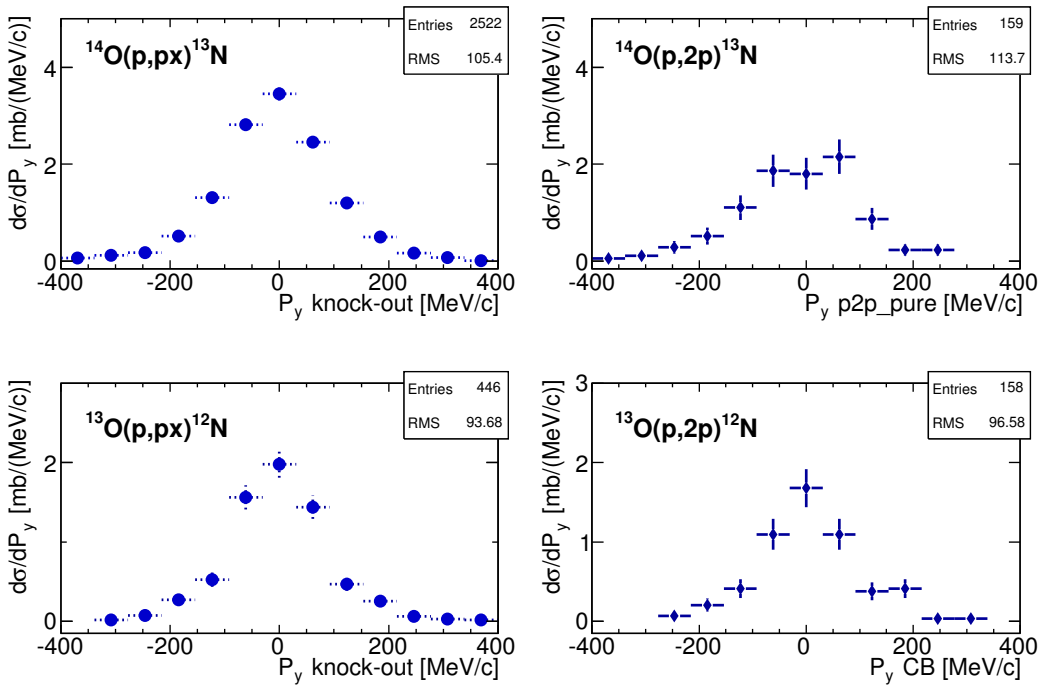

Figure C3: Distributions of P_y component for nitrogen nuclei obtained from single-proton removal (left) and (p,2p) reactions (right histograms) induced by ^{14,13}O projectiles on a proton target.

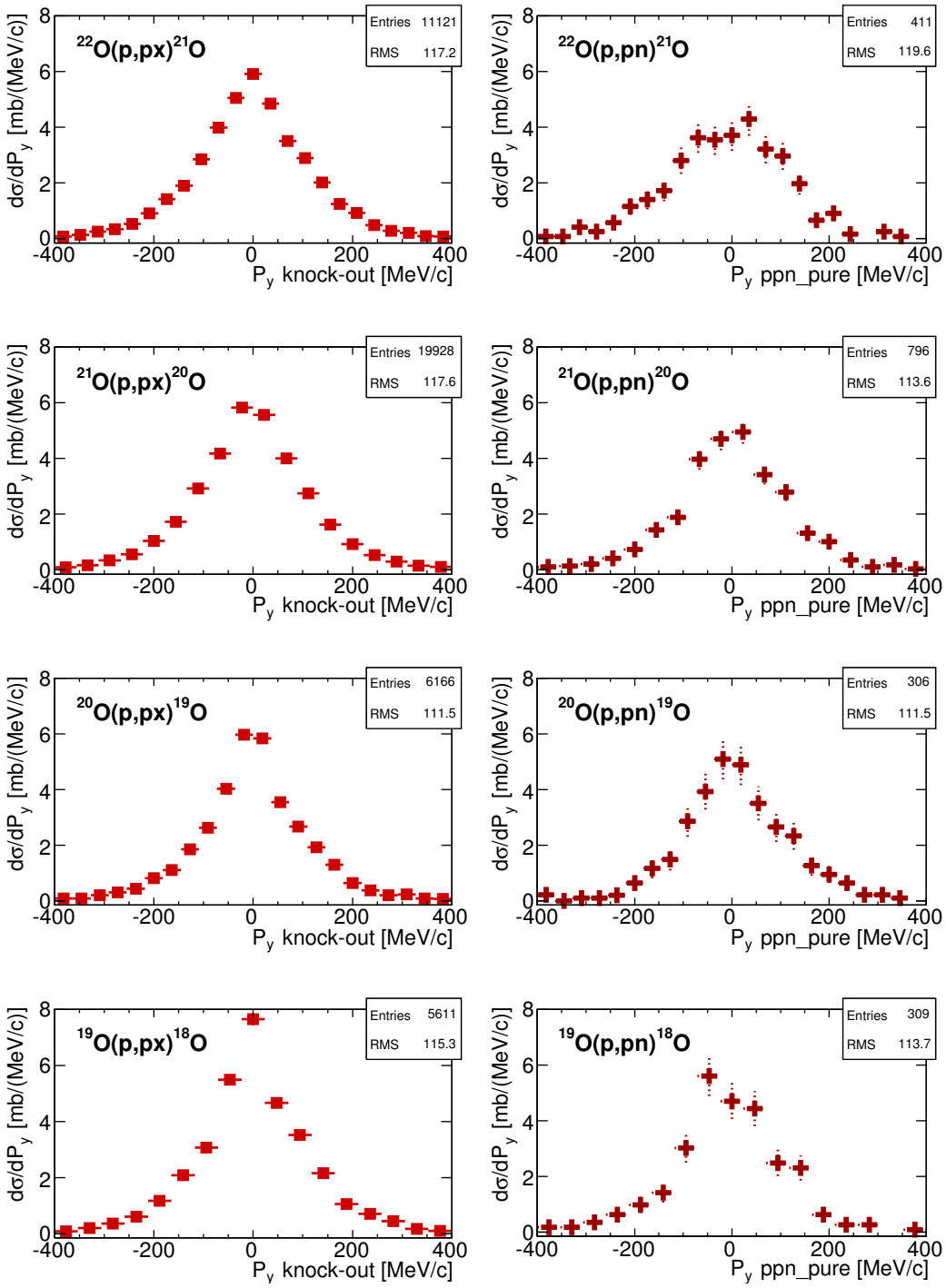

Figure C4: Distributions of P_y component for oxygen nuclei obtained from single-neutron removal (left) and (p,pn) reactions (right histograms) induced by ^{22,21,20,19}O projectiles on a proton target.

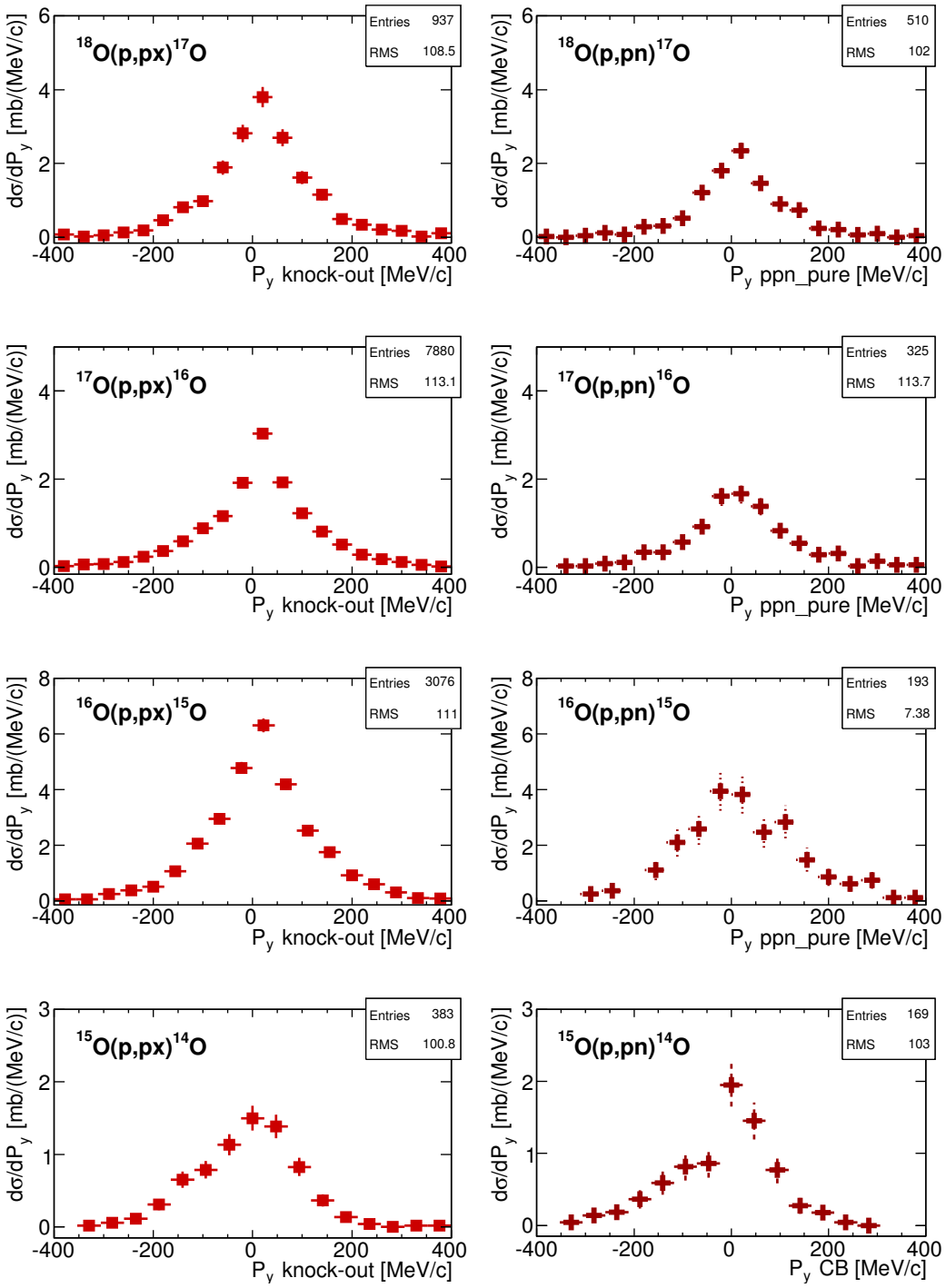

Figure C5: Distributions of P_y component for oxygen nuclei obtained from single-neutron removal (left) and (p,pn) reactions (right histograms) induced by ^{18,17,16,15}O projectiles on a proton target.

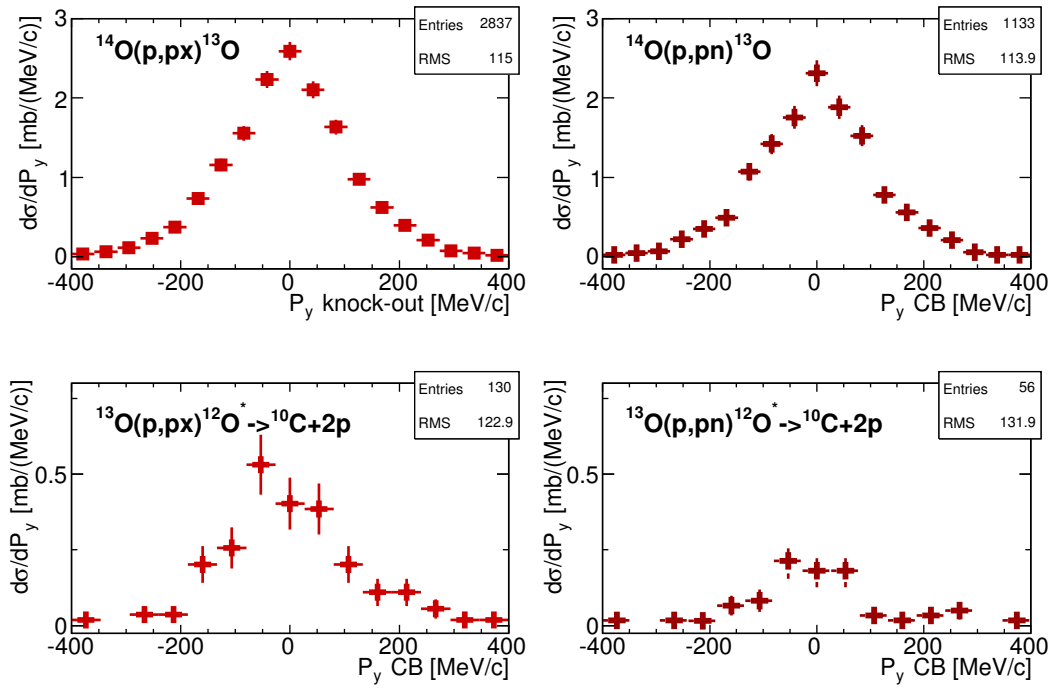

Figure C6: Distributions of P_y component for oxygen nuclei obtained from single-neutron removal (left) and (p,pn) reactions (right histograms) induced by ^{14,13}O projectiles on a proton target.

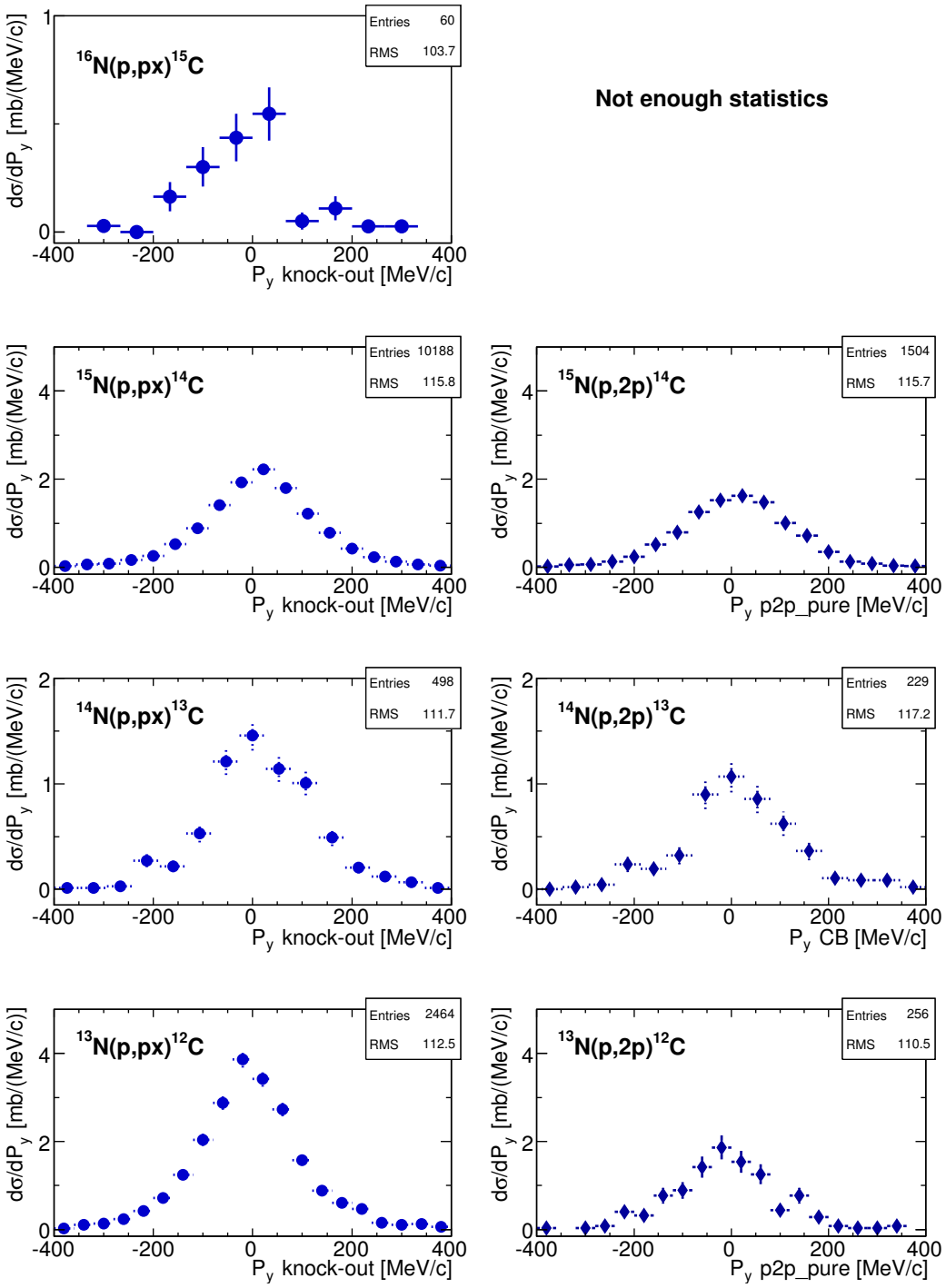

Figure C7: Distributions of P_y component for carbon nuclei obtained from single-proton removal (left) and (p,2p) reactions (right histograms) induced by ^{16,15,14,13}N projectiles on a proton target.

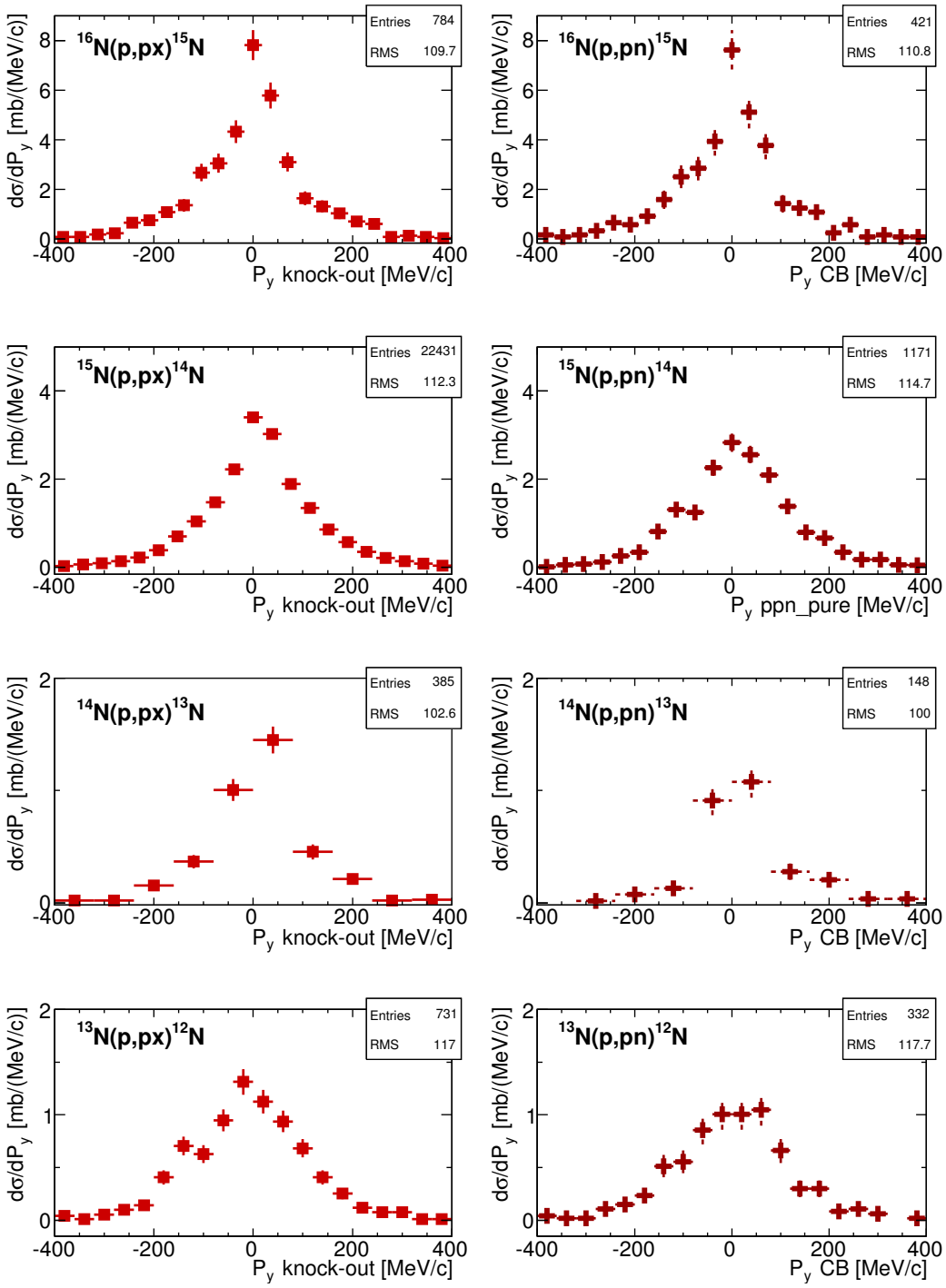

Figure C8: Distributions of P_y component for nitrogen nuclei obtained from single-neutron removal (left) and (p,pn) reactions (right histograms) induced by ^{16,15,14,13}N projectiles on a proton target.

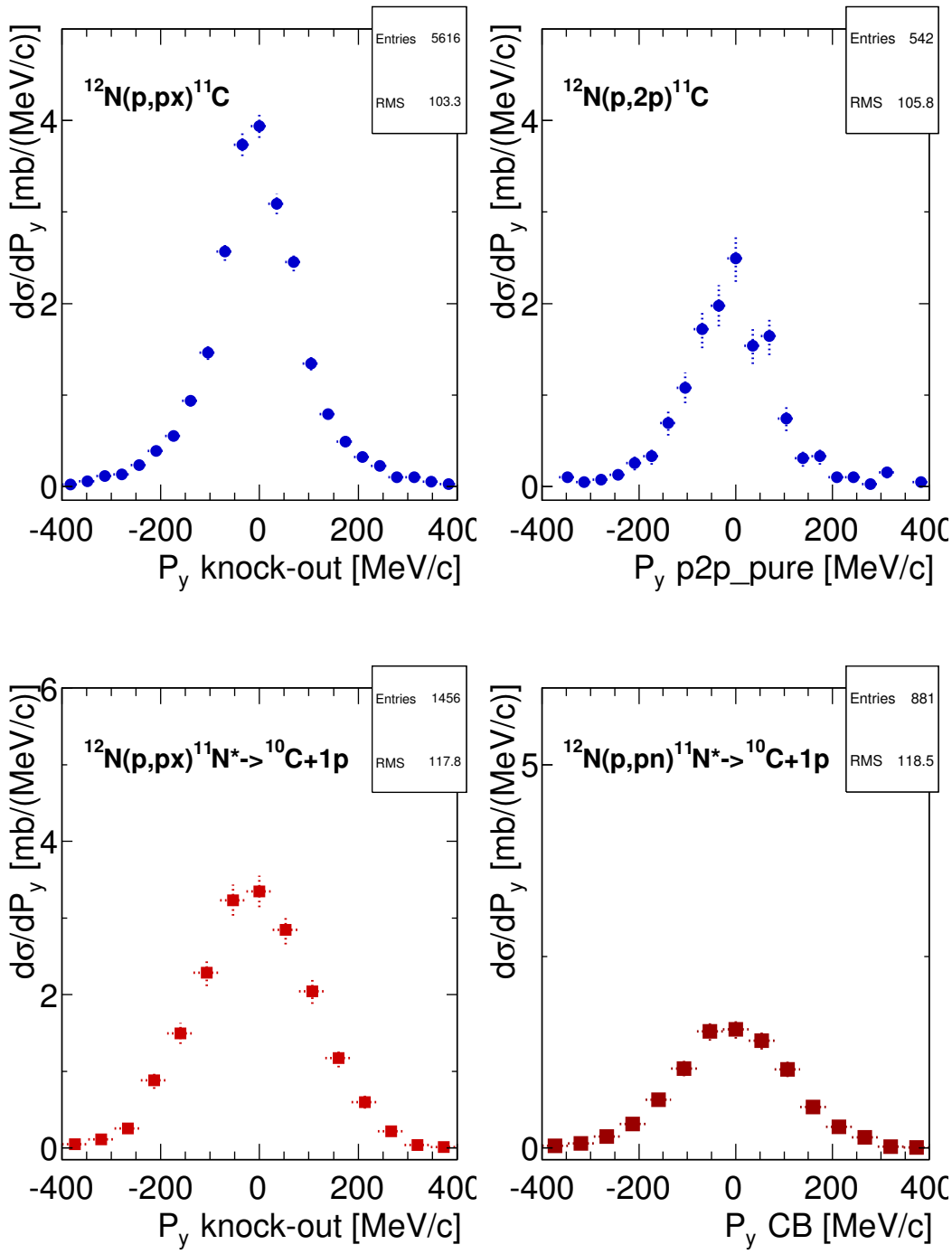

Figure C9: Distributions of P_y component for carbon/nitrogen nuclei obtained from single-proton/neutron removal (left) and (p,2p)/(p,pn) reactions (right histograms) induced by ^{12}N projectiles on a proton target.

Appendix D: Cross Sections

Following, Tables D1, D2 and D3 summarise cross sections measurements of single-nucleon removal reactions together with the corresponding QFS channel. These values were calculated on polyethylene, carbon and proton targets. Additionally, the projectile energy at middle of the corresponded polyethylene target (the thickness of targets, even for the same were different for each setting).

Projectile	E(AMeV)	$\sigma^{CH_2}_{n-rmv}$[mb]	σ^{C}_{n-rmv}[mb]	σ^{H}_{n-rmv}[mb]	$\sigma_{(p,pn)}$[mb]
^{13}O	397	9.89 (0.58)*	5.16 (1.04)*	2.38 (0.24) [0.38]*	0.92 (0.23) [0.18]*
^{14}O	349	67.23 (1.39)	36.91 (2.31)	15.16 (0.33) [1.82]	15.05 (3.26) [2.26]
^{15}O	308	27.34 (1.15)	10.81 (1.96)	7.68 (0.52) [0.92]	7.28 (1.32) [1.09]
^{16}O	450	123.48 (2.64)	69.60 (1.79)	28.93 (0.59) [3.47]	25.07 (1.26) [3.76]
^{17}O	406	75.57 (4.04)	49.05 (2.55)	12.86 (0.92) [1.64]	9.55 (0.31) [1.43]
^{18}O	369	89.66 (2.84)	58.49 82.85)	15.66 (0.49) [1.88]	11.08 (1.27) [1.66]
^{19}O	442	157.34 (2.00)	81.19 (1.36)	36.73 (0.61) [4.41]	31.93 (1.12) [4.79]
^{20}O	406	167.49 (0.91)	92.94 (0.54)	37.27 (0.52) [4.47]	33.02 (1.48) [4.95]
^{21}O	448	183.16 (0.76)	115.45 (0.82)	32.79 (0.63) [3.93]	31.83 (2.98) [4.78]
^{22}O	414	160.56 (0.64)	84.60 (0.69)	40.64(0.47)[4.88]	37.59 (3.87) [5.64]

Table D1: Summary of cross section measurements of single neutron-removal and (p,pn) reactions induced by oxygen projectiles on polyethylene, carbon and proton targets. Statistical and systematic uncertainties are shown in parenthesis and square brackets respectively.

Projectile	E(AMeV)	$\sigma^{CH_2}_{p-rmv}$[mb]	σ^{C}_{p-rmv}[mb]	σ^{H}_{p-rmv}[mb]	$\sigma_{(p,2p)}$[mb]
^{13}O	397	38.03 (1.59)	22.76 (2.80)	6.69 (0.46) [0.60]	5.67 (0.57) [0.32]
^{14}O	349	70.21(1.40)	39.58 (2.28)	15.45 (0.28) [1.16]	9.67 (0.48) [0.58]
^{15}O	308	117.47 (2.72)	64.65 (5.06)	26.91 (0.74) [2.82]	19.63 (0.93) [1.18]
^{16}O	450	118.63 (2.59)	60.11 (1.55)	31.42 (0.54) [3.39]	27.48 (0.71) [1.62]
^{17}O	406	36.17 (2.03)	17.95 (1.10)	9.11(0.49) [1.11]	6.99 (0.39) [0.42]
^{18}O	369	74.00 (2.66)	36.24 (1.82)	18.68 (0.63) [2.32]	15.02 (1.27) [0.86]
^{19}O	442	27.97 (0.90)	15.67 (0.79)	6.08 (0.45) [0.73]	4.34 (0.42) [0.26]
^{20}O	406	41.06 (0.91)	21.68 (0.12)	9.69 (0.45) [0.87]	7.17 (0.47) [0.43]
^{21}O	448	23.82 (0.07)	7.64 (0.08)	8.09 (0.11) [0.73]	5.91 (0.29) [0.35]
^{22}O	414	34.57 (0.15)	15.91 (0.14)	9.12 (0.10) [0.82]	6.10 (0.45) [0.37]

Table D2: Summary of cross section measurements of single proton-removal and (p,2p) reactions induced by oxygen projectiles on polyethylene, carbon and proton targets Statistical and systematic uncertainties are shown in parenthesis and square brackets respectively.

Proj	E(MeV)	$\sigma^{CH_2}_{n-rmv}$[mb]	σ^{C}_{n-rmv}[mb]	σ^{H}_{n-rmv}[mb]	$\sigma_{(p,pn)}$[mb]
^{12}N	370	38.67 (2.17)*	26.22 (1.52)*	6.22 (0.16) [1.01]*	6.18 (2.71) [0.99]*
^{13}N	323	27.28 (0.39)	11.04 (1.29)	8.12 (0.32) [1.06]	8.08 (0.85) [1.21]
^{14}N	450	24.19 (1.24)	16.16 (1.04)	4.01 (0.70) [0.52]	2.94 (0.83) [0.43]
^{15}N	401	108.75 (0.74)	68.03 (0.61)	20.53 (0.70) [2.67]	18.71 (0.51) [2.81]
^{16}N	471	176.86 (6.69)	101.58 (4.45)	37.64 (1.29) [4.89]	36.47 (3.05) [5.47]

Proj	E(MeV)	$\sigma^{CH_2}_{p-rmv}$[mb]	σ^{C}_{p-rmv}[mb]	σ^{H}_{p-rmv}[mb]	$\sigma_{(p,2p)}$[mb]
^{12}N	370	121.07 (1.76)	74.86 (2.50)	23.11(0.33) [2.08]	16.44 (0.49) [0.99]
^{13}N	323	94.08 (0.25)	52.42 (2.86)	20.83(0.45) [1.87]	12.34 (0.55) [0.74]
^{14}N	450	33.31 (1.42)	17.39 (1.02)	7.10(0.34) [0.64]	4.76 (0.70) [0.29]
^{15}N	401	49.47 (0.52)	25.08 (0.33)	13.23(0.50) [1.19]	9.89 (0.50) [0.59]
^{16}N	471	14.66 (1.72)	11.84 (1.32)	1.41(0.17) [0.13]	1.45 (0.81) [0.09]

Table D3: Corrected cross sections for neutron- and proton-removal channels and (p,pn) and (p,2p) QFS reactions for nitrogen projectiles (from A=12-16). Statistical and systematic uncertainties are shown in parenthesis and square brackets respectively.

Channel	σ_{p-rmv} [mb]	σ_{p2p} [mb]	σ_{INE} [mb]	σ_{ABS} [mb]	$\Delta\sigma_p$ [mb]
$^{13}O->^{12}N$	7.26 (0.46)	5.67 (0.57)	0.37 (0.39)	1.21(0.94)	0.01 (1.25)
$^{14}O->^{13}N$	15.45 (0.32)	9.67 (0.48)	1.04 (0.46)	3.79(0.78)	0.94 (1.08)
$^{15}O->^{14}N$	26.91 (0.73)	19.63 (0.93)	2.40 (0.65)	4.77(1.85)	0.11 (2.29)
$^{16}O->^{15}N$	31.42 (0.62)	27.48 (0.71)	1.68 (0.23)	3.17 (1.16)	-0.91 (1.51)
$^{17}O->^{16}N$	9.11 (0.61)	6.99 (0.39)	0.30 (0.02)	0.91 (0.25)	0.91 (0.77)
$^{18}O->^{17}N$	18.68 (0.63)	15.02 (1.27)	0.24 (0.14)	2.60 (1.35)	0.82 (1.96)
$^{19}O->^{18}N$	6.15 (0.45)	4.34 (0.42)	0	1.34 (0.28)	0.34 (0.68)
$^{20}O->^{19}N$	9.69 (0.45)	7.17 (0.47)	0	2.01 (0.50)	0.51 (0.82)
$^{21}O->^{20}N$	8.09 (0.13)	5.91 (0.29)	0	0.98 (0.51)	1.20 (0.62)
$^{22}O->^{21}N$	9.12 (0.10)	6.10 (0.42)	0	1.13 (0.38)	1.89 (0.59)

Channel	σ_{n-rmv} [mb]	σ_{ppn} [mb]	σ_{INE} [mb]	σ_{ABS} [mb]	$\Delta\sigma_n$ [mb]
$^{13}O->^{10}C+2p$	2.38 (0.24)	0.92 (0.23)	0.07 (0.07)	0.04 (0.07)	1.34 (0.25)
$^{14}O->^{13}O$	15.16 (0.33)	15.05 (3.26)	0.06 (0.09)	0.29 (1.37)	-0.24 (3.54)
$^{15}O->^{14}O$	7.68 (0.54)	7.28 (1.32)	0.00 (0.00)	0.27 (2.86)	0.13 (3.15)
$^{16}O->^{15}O$	28.93 (0.59)	25.07 (1.32)	1.12 (0.16)	2.44 (1.09)	0.31 (1.72)
$^{17}O->^{16}O$	14.33 (0.92)	9.55 (0.33)	1.72 (0.08)	3.63 (0.27)	-0.58 (0.40)
$^{18}O->^{17}O$	15.66 (0.49)	11.08 (1.34)	0.46 (0.08)	3.54 (0.57)	0.58 (1.43)
$^{19}O->^{18}O$	36.73 (0.61)	31.93 (1.16)	2.64 (0.32)	3.62 (0.69)	-1.47 (1.35)
$^{20}O->^{19}O$	37.27 (0.52)	33.02 (1.48)	-0.21 (0.03)	4.62 (0.83)	-0.17 (1.70)
$^{21}O->^{20}O$	32.79 (0.63)	31.83 (2.98)	0.04 (0.00)	1.19 (0.27)	-0.27 (3.98)
$^{22}O->^{21}O$	40.64 (0.47)	37.59 (3.98)	-0.25 (0.08)	2.56 (0.18)	0.74 (3.98)

Channel	σ_{p-rmv} [mb]	σ_{p2p} [mb]	σ_{INE} [mb]	σ_{ABS} [mb]	$\Delta\sigma_p$ [mb]
$^{12}N->^{11}C$	23.11 (0.33)	16.44 (0.49)	2.86 (0.54)	3.48 (1.01)	0.33 (1.28)
$^{13}N->^{12}C$	20.83 (0.45)	12.34 (0.55)	3.18 (0.45)	4.60 (1.14)	0.48 (1.44)
$^{14}N->^{13}C$	7.10 (0.34)	4.76 (0.70)	1.08 (0.39)	1.08 (0.49)	0.18 (1.00)
$^{15}N->^{14}C$	13.23 (0.50)	9.89 (0.50)	0.85 (0.11)	1.31 (0.26)	1.2 (0.76)
$^{16}N->^{15}C$	1.41 (0.17)	1.45 (0.81)	0.0 (0.00)	0.003 (0.0001)	-0.04 (0.82)

Channel	σ_{n-rmv} [mb]	σ_{ppn} [mb]	σ_{INE} [mb]	σ_{ABS} [mb]	$\Delta\sigma_n$ [mb]
$^{12}N->^{10}C$	6.22 (0.16)	6.18 (2.71)	-0.06 (0.01)	1.26 (1.03)	-1.16(2.90)
$^{13}N->^{12}N$	8.12 (0.32)	8.08 (0.80)	-0.04 (0.03)	0.17 (1.27)	-0.09(1.56)
$^{14}N->^{13}N$	4.01 (0.70)	2.85 (0.83)	0.01 (0.04)	0.58(0.24)	0.57(0.86)
$^{15}N->^{14}N$	20.53 (0.70)	18.71 (0.51)	0.50 (0.28)	0.62(1.19)	0.70(0.91)
$^{16}N->^{15}N$	37.64 (1.29)	36.47 (3.18)	-0.13 (0.05)	2.00(1.96)	-0.70(3.01)

Table D4: Corrected cross section for single-proton and neutron removal; (p,2p) and (p,pn); proton and neutron evaporation; and absorptive channels induced by oxygen (A=13-22) and nitrogen (A=12-16) projectiles on a proton target. $\Delta\sigma_n = \sigma_{tot} - \sigma_{n-rmv}$.

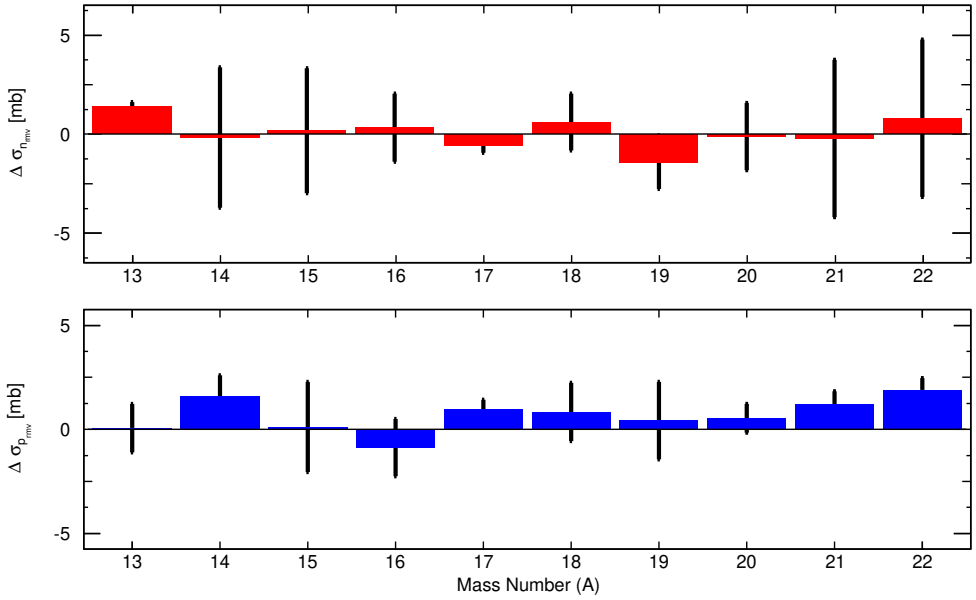

Figure D1: Residues for oxygen projectiles depicted as filled coloured bar with total uncertainties (vertical black lines).

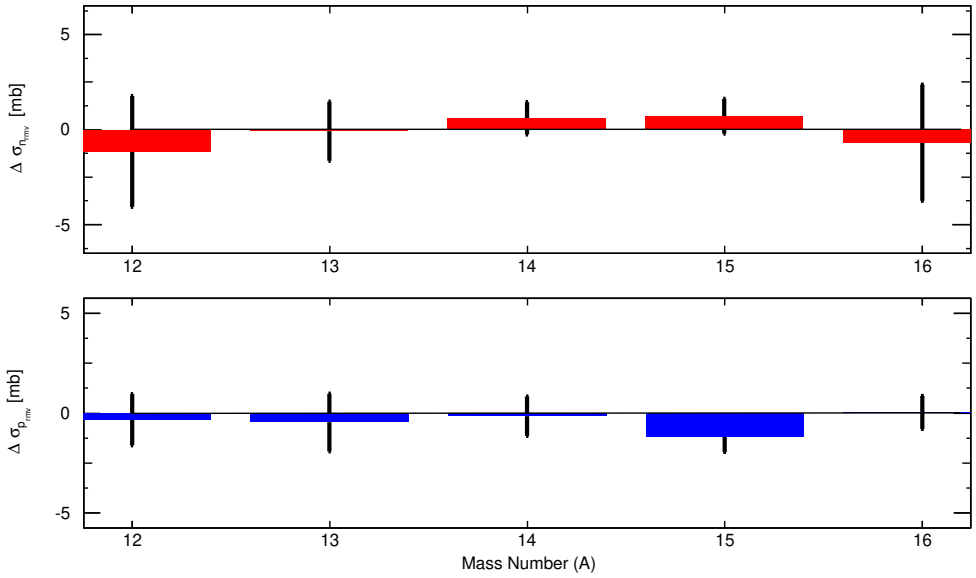

Figure D2: Residues for nitrogen projectiles depicted as filled coloured bar with total uncertainties (vertical black lines).

Bibliography

[1] Maria G. Mayer. On closed shells in nuclei. *Phys. Rev.*, 74:235–239, Aug 1948.

[2] Otto Haxel, J. Hans D. Jensen, and Hans E. Suess. On the "magic numbers" in nuclear structure. *Phys. Rev.*, 75:1766–1766, Jun 1949.

[3] Timothy Symons, Yogendra Viyogi, G D. Westfall, P Doll, D E. Greiner, H Faraggi, P J. Lindstrom, David Scott, H Crawford, and C McParland. Observation of new neutron-rich isotopes by fragmentation of 205-mev/nucleon ar 40 ions. *Phys. Rev. Lett.*, 42:40–43, 01 1979.

[4] G. D. Westfall, T. J. M. Symons, D. E. Greiner, H. H. Heckman, P. J. Lindstrom, J. Mahoney, A. C. Shotter, D. K. Scott, H. J. Crawford, C. McParland, T. C. Awes, C. K. Gelbke, and J. M. Kidd. Production of neutron-rich nuclides by fragmentation of 212-mev/amu ^{48}Ca. *Phys. Rev. Lett.*, 43:1859–1862, Dec 1979.

[5] R. Subedi, R. Shneor, P. Monaghan, B. D. Anderson, K. Aniol, J. Annand, J. Arrington, H. Benaoum, F. Benmokhtar, W. Boeglin, J.-P. Chen, Seonho Choi, E. Cisbani, B. Craver, S. Frullani, F. Garibaldi, S. Gilad, R. Gilman, O. Glamazdin, J.-O. Hansen, D. W. Higinbotham, T. Holmstrom, H. Ibrahim, R. Igarashi, C. W. de Jager, E. Jans, X. Jiang, L. J. Kaufman, A. Kelleher, A. Kolarkar, G. Kumbartzki, J. J. LeRose, R. Lindgren, N. Liyanage, D. J. Margaziotis, P. Markowitz, S. Marrone, M. Mazouz, D. Meekins, R. Michaels, B. Moffit, C. F. Perdrisat, E. Piasetzky, M. Potokar, V. Punjabi, Y. Qiang, J. Reinhold, G. Ron, G. Rosner, A. Saha, B. Sawatzky, A. Shahinyan, S. Širca, K. Slifer, P. Solvignon, V. Sulkosky, G. M. Urciuoli, E. Voutier, J. W. Watson, L. B. Weinstein, B. Wojtsekhowski, S. Wood, X.-C. Zheng, and L. Zhu. Probing cold dense nuclear matter. *Science*, 320(5882):1476–1478, 2008.

[6] J. Mougey, M. Bernheim, A. Bussirè, A. Gillebert, Phan Xuan Hô, M. Priou, D. Royer, I. Sick, and G.J. Wagner. Quasi-free (e, e'p) scattering on 12c, 28si, 40ca and 58ni. *Nuclear Physics A*, 262(3):461 – 492, 1976.

[7] G. Van Der Steenhoven, H.P. Blok, E. Jans, M. De Jong, L. Lapikás, E.N.M. Quint, and P.K.A. De Witt Huberts. Knockout of 1p protons from 12c induced by the (e, e'p) reaction. *Nuclear Physics A*, 480(3):547 – 572, 1988.

[8] Gerhard Jacob and TH. A. J. Maris. Quasi-free scattering and nuclear structure. ii. *Rev. Mod. Phys.*, 45:6–21, Jan 1973.

[9] L. Lapikás. Quasi-elastic electron scattering off nuclei. *Nuclear Physics A*, 553:297–308, March 1993.

[10] P.G. Hansen and J.A. Tostevin. Direct reactions with exotic nuclei. *Annual Review of Nuclear and Particle Science*, 53(1):219–261, 2003.

[11] A. Gade, P. Adrich, D. Bazin, M. D. Bowen, B. A. Brown, C. M. Campbell, J. M. Cook, T. Glasmacher, P. G. Hansen, K. Hosier, S. McDaniel, D. McGlinchery, A. Obertelli, K. Siwek, L. A. Riley, J. A. Tostevin, and D. Weisshaar. Reduction of spectroscopic strength: Weakly-bound and strongly-bound single-particle states studied using one-nucleon knockout reactions. *Phys. Rev. C*, 77:044306, Apr 2008.

[12] F. Flavigny, A. Obertelli, A. Bonaccorso, G. F. Grinyer, C. Louchart, L. Nalpas, and A. Signoracci. Nonsudden limits of heavy-ion induced knockout reactions. *Phys. Rev. Lett.*

[13] Thomas Aumann. Prospects of nuclear structure at the future gsi accelerators. *Progress in Particle and Nuclear Physics*, 59(1):3 – 21, 2007. International Workshop on Nuclear Physics 28th Course.

[14] Panin V. personal communication.

[15] Quasifree (p, pn) scattering of light neutron-rich nuclei near $n = 14$.

[16] L. Atar, S. Paschalis, C. Barbieri, C. A. Bertulani, P. Díaz Fernández, M. Holl, M. A. Najafi, V. Panin, H. Alvarez-Pol, T. Aumann, V. Avdeichikov, S. Beceiro-Novo, D. Bemmerer, J. Benlliure, J. M. Boillos, K. Boretzky, M. J. G. Borge, M. Caamaño, C. Caesar, E. Casarejos, W. Catford, J. Cederkall, M. Chartier, L. Chulkov, D. Cortina-Gil, E. Cravo, R. Crespo, I. Dillmann, Z. Elekes, J. Enders, O. Ershova, A. Estrade, F. Farinon, L. M. Fraile, M. Freer, D. Galaviz Redondo, H. Geissel, R. Gernhäuser, P. Golubev, K. Göbel, J. Hagdahl, T. Heftrich, M. Heil, M. Heine, A. Heinz, A. Henriques, A. Hufnagel, A. Ignatov, H. T. Johansson, B. Jonson, J. Kahlbow, N. Kalantar-Nayestanaki, R. Kanungo, A. Kelic-Heil, A. Knyazev, T. Kröll, N. Kurz, M. Labiche, C. Langer, T. Le Bleis, R. Lemmon, S. Lindberg, J. Machado, J. Marganiec-Gałkazka, A. Movsesyan, E. Nacher, E. Y. Nikolskii, T. Nilsson, C. Nociforo, A. Perea, M. Petri, S. Pietri, R. Plag, R. Reifarth, G. Ribeiro, C. Rigollet, D. M. Rossi, M. Röder, D. Savran, H. Scheit, H. Simon, O. Sorlin, I. Syndikus, J. T. Taylor, O. Tengblad, R. Thies, Y. Togano, M. Vandebrouck, P. Velho, V. Volkov, A. Wagner, F. Wamers, H. Weick, C. Wheldon, G. L. Wilson, J. S. Winfield, P. Woods, D. Yakorev, M. Zhukov, A. Zilges, and K. Zuber. Quasifree $(p, 2p)$ reactions on oxygen isotopes: Observation of isospin independence of the reduced single-particle strength. *Phys. Rev. Lett.*, 120:052501, Jan 2018.

[17] Or Hen, Gerald A. Miller, Eli Piasetzky, and Lawrence B. Weinstein. Nucleon-nucleon correlations, short-lived excitations, and the quarks within. *Rev. Mod. Phys.*, 89:045002, Nov 2017.

[18] The R3B collaboration. Neutron-rich nuclei at and beyond the dripline in the range z=4 to z=10 studied in kinematically complete measurement of direct reaction at relativistc energy. In *S393 proposal*. 2010.

[19] Håkan T. Johansson. *Huting Tools Beyond the Driplines*. Dissertation, Chalmers Universty of Technology, Göteborg, Sweden, 2010.

[20] Dominic Rossi. *Investigation of the Dipole Response of Nickel Isotopes in the Presence of a High-Frequency Electromagnetic Field*. Dissertation, Johann Wolfgang Goethe-Universität, 2010.

[21] Saúl Beciero Novo. *Coulomn Dissoation of ^{17}P at 498 A MeV: an indirect a measurement of the astrophysical $^{26}Si(p,\gamma)$ reaction*. Dissertation, Universidade de Santiago de Compostela, España, 2011.

[22] Felix Wamers. *Quasi-Free-Scaterring and One-Proton-Removal Reactions with the Proton-Dripline Nucleus ^{17}Ne at Relativistic Beam Energies*. Dissertation, Technische Universität Darmstadt, Germany, 2011.

[23] Valerii Panin. *Fully Exclusive Measurements of Quasi-Free single-Nucleon Knockout Reations in Inverse Kinematics*. Dissertation, Technische Universität Darmstadt, Germany, 2012.

[24] Christoph Caesar. *Beyond the Neutron Drip-Line:Superheavy Oxygen Isotopes*. Dissertation, Technische Universität Darmstadt, Germany, 2012.

[25] Christoph Langer. *Coulomb Dissociation of ^{31}Cl and ^{32}Ar constraining the rp process*. Dissertation, Technische Universität Darmstadt, Germany, 2012.

[26] Alina Movsesyan. *Quasi-free one-proton and one-neutron knockout reactions on ^{57}Ni*. Dissertation, Technische Universität Darmstadt, Germany, 2013.

[27] Paloma Díaz Fernández. *An investigation into quasi-free scattering of light neutron-rich nuclei around N=14*. Dissertation, Universidade de Santiago de Compostela, España, 2013.

[28] Matthias Holl. *Quase-Free Scatering from Relativistic Neutron-Deficient Carbon Isotopes*. Dissertation, Technische Universitüt Darmstadt, Germany, 2014.

[29] Marcel Heine. *Measurement of (n,γ)-Rates of Light Neutron-Rich Nuclei for the r-Process Nucleosynthesis*. PhD thesis, Technische Universität, Darmstadt, January 2015.

[30] Leyla Atar. *Investigaction of the single-Particle Structure of Oxygen Isotopes in Quasi-free Knockout Reactions at the R^3B/LAND Setup.* Dissertation, Technische Universität Darmstadt, Germany, 2015.

[31] Ronja M. A. Thies. *Bits and Pieces for the Nuclear Puzzle.* Dissertation, Chalmers Universty of Technology, Göteborg, Sweden, 2016.

[32] Ana Isabel Martinho Henriques. *Nucleon knockout of 11Be from the collision with a proton target at high energies.* Dissertation, Ciencias ULibsoa, 2017.

[33] M. Gómez-Ramos and A. M. Moro. Interplay of projectile breakup and target excitation in reactions induced by weakly bound nuclei. *Phys. Rev. C*, 95:034609, Mar 2017.

[34] M. Gómez-Ramos and A.M. Moro. Binding-energy independence of reduced spectroscopic strengths derived from $(p, 2p)$ and (p, pn) reactions with nitrogen and oxygen isotopes. *Physics Letters B*, 785:511 – 516, 2018.

[35] Andrey Alexandrov, S Argirò, Giuseppe Battistoni, Nicola Belcari, Silvia Biondi, Maria Giuseppina, Graziano Bruni, S Brambilla, Niccolò Camarlinghi, Piergiorgio Cerello, Esther Ciarrocchi, Alberto Clozza, G De Lellis, Antonia Di Crescenzo, Marco Durante, R Faccini, Veronica Ferrero, F Ferroni, Christian Finck, and Bormio . The foot (fragmentation of target) experiment pos(bormio2017)023 the foot (fragmentation of target) experiment. 01 2017.

[36] Marta Rovituso and Chiara La Tessa. Nuclear interactions of new ions in cancer therapy: impact on dosimetry. *Translational Cancer Research*, 6(S5), 2017.

[37] Chiara La Tessa, Michael Sivertz, I-Hung Chiang, Derek Lowenstein, and Adam Rusek. Overview of the nasa space radiation laboratory. *Life Sciences in Space Research*, 11:18–23, 2016. Exported from https://app.dimensions.ai on 2019/02/24.

[38] Hans Geissel and Yuri A. Litvinov. Experiments with the frs facility at gsi. *Nuclear Instruments and Methods in Physics Research Section B: Beam Interactions with Materials and Atoms*, 266(19):4176 – 4182, 2008. Proceedings of the XVth International Conference on Electromagnetic Isotope Separators and Techniques Related to their Applications.

[39] Fair, facility for antiproton and ion research in europe gmbh, 2019.

[40] H.G: Essel and N. Kurz. *Multi-Branch System Reference Manual*, 2010.

[41] Håkan T. Johansson. The daq always runs, 2006.

[42] R. Plag. land02: featurin the unoffical guide to the unofficial version of land02, 2018.

[43] B. Alpat, G. Ambrosi, Ph. Azzarello, R. Battiston, P. Bene, B. Bertucci, S. Bizzaglia, M. Bizzarri, S. Blasko, M. Bourquin, Ph. Bouvier, W.J. Burger, M. Capell, C. Cecchi, Y.H. Chang, E. Cortina, N. Dinu, G. Esposito, E. Fiandrini, D. Haas, H. Hakobyan, M. Ionica, R. Ionica, A. Kounine, V. Koutsenko, A. Lebedev, C. Lechanoine-Leluc, C.H. Lin, F. Masciocchi, M. Menichelli, S. Natale, M. Paniccia, A. Papi, M. Pauluzzi, E. Perrin, M. Pohl, D. Rapin, J.P. Richeux, W. Wallraff, M. Willenbrock, and P. Zuccon. Charge determination of nuclei with the ams-02 silicon tracker. *Nuclear Instruments and Methods in Physics Research Section A: Accelerators, Spectrometers, Detectors and Associated Equipment*, 540(1):121 – 130, 2005.

[44] V. Metag, D Habs, , and K. Helmer. The darmstadt-heidelberg-crystal-ball. *Lecture notes in Physics*, 178:163–178, 1983.

[45] T. Blaich, T. W. Elze, H. Emling, H. Freiesleben, K. Grimm, W. Henning, R. Holzmann, G. Ickert, J. G. Keller, H. Klingler, W. Kneissl, R. König, R. Kulessa, J. V. Kratz, D. Lambrecht, J. S. Lange, Y. Leifels, E. Lubkiewicz, M. Proft, W. Prokopowicz, C. Schütter, R. Schmidt, H. Spies, K. Stelzer, J. Stroth, W. Walus, E. Wajda, H. J. Wollersheim, M. Zinser, E. Zude, and LAND Collaboration. A large area detector for high-energy neutrons. *Nuclear Instruments and Methods in Physics Research A*, 314:136–154, April 1992.

[46] J Cub, G Stengel, A GrÃ¼nschloÃŸ, K Boretzky, T Aumann, W Dostal, B Eberlein, Th.W Elze, H Emling, G Ickert, J Holeczek, R Holzmann, J.V Kratz, R Kulessa, Y Leifels, H Simon, K Stelzer, J Stroth, A Surowiec, and E Wajda. A large-area scintillating fibre detector for relativistic heavy ions. *Nuclear Instruments and Methods in Physics Research Section A: Accelerators, Spectrometers, Detectors and Associated Equipment*, 402(1):67 – 74, 1998.

[47] K. Mahata, H.T. Johansson, S. Paschalis, H. Simon, and T. Aumann. Position reconstruction in large-area scintillating fibre detectors. *Nuclear Instruments and Methods in Physics Research Section A: Accelerators, Spectrometers, Detectors and Associated Equipment*, 608(2):331 – 335, 2009.

[48] H. Geissel et al. The GSI projectile fragment separator (FRS): A Versatile magnetic system for relativistic heavy ions. *Nucl. Instrum. Meth.*, B70:286–297, 1992.

[49] A. H. Wapstra F. G. Kondev M. MacCormick X. Xu G. Audi, M. Wang and B. Pfeiffer. Nuclear masses 2012. *Chin. Phys. C*, 36.

[50] Brookhaven National Laboratory. National nuclear data center, 2018.

[51] S.M. Lukyanov, A.G. Artukh, B.A. Gvozdev, V.B. Kutner, Yu.E. Penionzhkevich, L. Bex, M.P. Bourgarel, and J. Ferme. Production and acceleration of 48ca-beams with the ecr source in the jinr-ganil experiment. *Nuclear Instruments and Methods in*

Physics Research Section B: Beam Interactions with Materials and Atoms, 47(1):102 – 105, 1990.

[52] A. Navin, D. W. Anthony, T. Aumann, T. Baumann, D. Bazin, Y. Blumenfeld, B. A. Brown, T. Glasmacher, P. G. Hansen, R. W. Ibbotson, P. A. Lofy, V. Maddalena, K. Miller, T. Nakamura, B. V. Pritychenko, B. M. Sherrill, E. Spears, M. Steiner, J. A. Tostevin, J. Yurkon, and A. Wagner. Direct evidence for the breakdown of the $N = 8$ shell closure in ^{12}be. *Phys. Rev. Lett.*, 85:266–269, Jul 2000.

[53] T. Aumann, C. A. Bertulani, and J. Ryckebusch. Quasifree (p,2p) and (p,pn) reactions with unstable nuclei. *Phys. Rev. C*, 88:064610, Dec 2013.

[54] J. A. Tostevin and A. Gade. Systematics of intermediate-energy single-nucleon removal cross sections. *Phys. Rev. C*, 90:057602, Nov 2014.

[55] Marco Durante and Francis A. Cucinotta. Physical basis of radiation protection in space travel. *Rev. Mod. Phys.*, 83:1245–1281, Nov 2011.

[56] John W. Norbury, Jack Miller, Anne M. Adamczyk, L.H. Heilbronn, Lawrence W. Townsend, Steve Blattnig, Ryan Norman, Stephen Guetersloh, and Cary Zeitlin. Nuclear data for space radiation. *Radiation Measurements*, 47:315â€“363, 05 2012.

[57] Francesco Tommasino, Emanuele Scifoni, and Marco Durante. New ions for therapy. *International Journal of Particle Therapy*, 2(3):428–438, 2015.

[58] John W. Norbury, Walter Schimmerling, Tony Slaba, Edouard I. Azzam, Francis F. Badavi, Giorgio Baiocco, Eric Benton, Veronica Bindi, Eleanor Blakely, Steve Blattnig, David Boothman, Thomas B. Borak, Richard Britten, Stan Curtis, Michael Dingfelder, Marco Durante, William Dynan, Amelia Eisch, S Robin Elgart, and Cary Zeitlin. Opinion/position paper galactic cosmic ray simulation at the nasa space radiation laboratory. *Life Sciences in Space Research*, 8, 02 2016.

[59] Cary Zeitlin and Chiara La Tessa. The role of nuclear fragmentation in particle therapy and space radiation protection. *Frontiers in Oncology*, 6:65, 2016.

[60] Benjamin Braunn, Alain Boudard, J.-C David, Arjan Koning, Anne Leprince, Sylvie Leray, and Davide Mancusi. Assessment of nuclear-reaction codes for proton-induced reactions on light nuclei below 250 mev. *European Physical Journal Plus*, 130, 07 2015.

[61] R. Thies, A. Heinz, T. Adachi, Y. Aksyutina, J. Alcantara-Núñes, S. Altstadt, H. Alvarez-Pol, N. Ashwood, T. Aumann, V. Avdeichikov, M. Barr, S. Beceiro-Novo, D. Bemmerer, J. Benlliure, C. A. Bertulani, K. Boretzky, M. J. G. Borge, G. Burgunder, M. Camaño, C. Caesar, E. Casarejos, W. Catford, J. Cederkäll, S. Chakraborty, M. Chartier, L. V. Chulkov, D. Cortina-Gil, R. Crespo, U. Datta,

P. Díaz Fernández, I. Dillmann, Z. Elekes, J. Enders, O. Ershova, A. Estradé, F. Farinon, L. M. Fraile, M. Freer, M. Freudenberger, H. O. U. Fynbo, D. Galaviz, H. Geissel, R. Gernhäuser, K. Göbel, P. Golubev, D. Gonzalez Diaz, J. Hagdahl, T. Heftrich, M. Heil, M. Heine, A. Henriques, M. Holl, G. Ickert, A. Ignatov, B. Jakobsson, H. T. Johansson, B. Jonson, N. Kalantar-Nayestanaki, R. Kanungo, R. Knöbel, T. Kröll, R. Krücken, J. Kurcewicz, N. Kurz, M. Labiche, C. Langer, T. Le Bleis, R. Lemmon, O. Lepyoshkina, S. Lindberg, J. Machado, J. Marganiec, V. Maroussov, M. Mostazo, A. Movsesyan, A. Najafi, T. Nilsson, C. Nociforo, V. Panin, S. Paschalis, A. Perea, M. Petri, S. Pietri, R. Plag, A. Prochazka, A. Rahaman, G. Rastrepina, R. Reifarth, G. Ribeiro, M. V. Ricciardi, C. Rigollet, K. Riisager, M. Röder, D. Rossi, J. Sanchez del Rio, D. Savran, H. Scheit, H. Simon, O. Sorlin, V. Stoica, B. Streicher, J. T. Taylor, O. Tengblad, S. Terashima, Y. Togano, E. Uberseder, J. Van de Walle, P. Velho, V. Volkov, A. Wagner, F. Wamers, H. Weick, M. Weigand, C. Wheldon, G. Wilson, C. Wimmer, J. S. Winfield, P. Woods, D. Yakorev, M. V. Zhukov, A. Zilges, and K. Zuber. Systematic investigation of projectile fragmentation using beams of unstable b and c isotopes. *Phys. Rev. C*, 93:054601, May 2016.

[62] F. Wamers, J. Marganiec, F. Aksouh, Yu. Aksyutina, H. Álvarez-Pol, T. Aumann, S. Beceiro-Novo, K. Boretzky, M. J. G. Borge, M. Chartier, A. Chatillon, L. V. Chulkov, D. Cortina-Gil, H. Emling, O. Ershova, L. M. Fraile, H. O. U. Fynbo, D. Galaviz, H. Geissel, M. Heil, D. H. H. Hoffmann, H. T. Johansson, B. Jonson, C. Karagiannis, O. A. Kiselev, J. V. Kratz, R. Kulessa, N. Kurz, C. Langer, M. Lantz, T. Le Bleis, R. Lemmon, Yu. A. Litvinov, K. Mahata, C. Müntz, T. Nilsson, C. Nociforo, G. Nyman, W. Ott, V. Panin, S. Paschalis, A. Perea, R. Plag, R. Reifarth, A. Richter, C. Rodriguez-Tajes, D. Rossi, K. Riisager, D. Savran, G. Schrieder, H. Simon, J. Stroth, K. Sümmerer, O. Tengblad, H. Weick, C. Wimmer, and M. V. Zhukov. First observation of the unbound nucleus ^{15}Ne. *Phys. Rev. Lett.*, 112:132502, Apr 2014.

[63] M. Vandebrouck, A. Lepailleur, O. Sorlin, T. Aumann, C. Caesar, M. Holl, V. Panin, F. Wamers, S. R. Stroberg, J. D. Holt, F. de Oliveira Santos, H. Alvarez-Pol, L. Atar, V. Avdeichikov, S. Beceiro-Novo, D. Bemmerer, J. Benlliure, C. A. Bertulani, S. K. Bogner, J. M. Boillos, K. Boretzky, M. J. G. Borge, M. Caamaño, E. Casarejos, W. Catford, J. Cederkäll, M. Chartier, L. Chulkov, D. Cortina-Gil, E. Cravo, R. Crespo, U. Datta Pramanik, P. Díaz Fernández, I. Dillmann, Z. Elekes, J. Enders, O. Ershova, A. Estradé, F. Farinon, L. M. Fraile, M. Freer, D. Galaviz, H. Geissel, R. Gernhäuser, J. Gibelin, P. Golubev, K. Göbel, J. Hagdahl, T. Heftrich, M. Heil, M. Heine, A. Heinz, A. Henriques, H. Hergert, A. Hufnagel, A. Ignatov, H. T. Johansson, B. Jonson, J. Kahlbow, N. Kalantar-Nayestanaki, R. Kanungo, A. Kelic-Heil, A. Knyazev, T. Kröll, N. Kurz, M. Labiche, C. Langer, T. Le Bleis, R. Lemmon, S. Lindberg, J. Machado, J. Marganiec, F. M. Marqués, A. Movsesyan, E. Nacher, M. Najafi, E. Nikolskii, T. Nilsson, C. Nociforo, S. Paschalis, A. Perea,

M. Petri, S. Pietri, R. Plag, R. Reifarth, G. Ribeiro, C. Rigollet, M. Röder, D. Rossi, D. Savran, H. Scheit, A. Schwenk, H. Simon, I. Syndikus, J. T. Taylor, O. Tengblad, R. Thies, Y. Togano, P. Velho, V. Volkov, A. Wagner, H. Weick, C. Wheldon, G. Wilson, J. S. Winfield, P. Woods, D. Yakorev, M. Zhukov, A. Zilges, and K. Zuber. Effective proton-neutron interaction near the drip line from unbound states in ^{25,26}F. *Phys. Rev. C*, 96:054305, Nov 2017.

[64] G. Ribeiro, E. Nácher, O. Tengblad, P. Díaz Fernández, Y. Aksyutina, H. Alvarez-Pol, L. Atar, T. Aumann, V. Avdeichikov, S. Beceiro-Novo, D. Bemmerer, J. Benlliure, C. A. Bertulani, J. M. Boillos, K. Boretzky, M. J. G. Borge, M. Caamano, C. Caesar, E. Casarejos, W. Catford, J. Cederkäll, M. Chartier, L. Chulkov, D. Cortina-Gil, E. Cravo, R. Crespo, U. Datta Pramanik, I. Dillmann, Z. Elekes, J. Enders, O. Ershova, A. Estrade, F. Farinon, L. M. Fraile, M. Freer, H. O. U. Fynbo, D. Galaviz, H. Geissel, R. Gernhäuser, P. Golubev, K. Göbel, J. Hagdahl, T. Heftrich, M. Heil, M. Heine, A. Heinz, A. Henriques, M. Holl, A. Hufnagel, A. Ignatov, H. T. Johansson, B. Jonson, N. Kalantar-Nayestanaki, R. Kanungo, A. Kelic-Heil, N. Kurz, T. Kröll, M. Labiche, C. Langer, T. Le Bleis, R. Lemmon, S. Lindberg, J. Machado, J. Marganiec, A. Movsesyan, T. Nilsson, C. Nociforo, V. Panin, S. Paschalis, A. Perea, M. Petri, S. Pietri, R. Plag, R. Reifarth, C. Rigollet, K. Riisager, D. Rossi, M. Röder, D. Savran, H. Scheit, H. Simon, O. Sorlin, I. Syndikus, J. T. Taylor, R. Thies, P. Velho, A. Wagner, F. Wamers, M. Vandebrouck, H. Weick, C. Wheldon, G. Wilson, C. Wimmer, J. S. Winfield, P. Woods, M. V. Zhukov, A. Zilges, and K. Zuber. Structure of ^{13}Be studied in proton knockout from ^{14}B. *Phys. Rev. C*, 98:024603, Aug 2018.

[65] L. V. Chulkov, B. Jonson, and M. V. Zhukov. Light nuclei in the vicinity of the dripline and beyond. *The European Physical Journal A*, 51(8):97, Aug 2015.

[66] NN-OnLine, 2019.

[67] Panin V. personal communication.

[68] N. Iwasa H. Geissel and H. Weick. Mocadi code, 2016.

[69] K. Sümmerer. Improved empirical parametrization of fragmentation cross sections. *Phys. Rev. C*, 86:014601, Jul 2012.

[70] Fairroot, 2019.

[71] R3brootsimulations and data analysis for r3b, 2019.

[72] Davide Mancusi, Alain Boudard, Joseph Cugnon, Jean-Christophe David, Pekka Kaitaniemi, and Sylvie Leray. Extension of the liège intranuclear-cascade model to reactions induced by light nuclei. *Phys. Rev. C*, 90:054602, Nov 2014.

[73] P. Malzacher J. Kunzendorf H. Geissel, C. Scheidenberger and H. WeickH. Atima code, 2016.

[74] A. J. Hartzler and R. T. Siegel. 400-mev neutron-proton scattering. *Phys. Rev.*, 95:185–192, Jul 1954.

[75] V. Panin, J.T. Taylor, S. Paschalis, F. Wamers, Y. Aksyutina, H. Alvarez-Pol, T. Aumann, C.A. Bertulani, K. Boretzky, C. Caesar, M. Chartier, L.V. Chulkov, D. Cortina-Gil, J. Enders, O. Ershova, H. Geissel, R. GernhÃ¤user, M. Heil, H.T. Johansson, B. Jonson, A. KeliÄ‡-Heil, C. Langer, T. Le Bleis, R. Lemmon, T. Nilsson, M. Petri, R. Plag, R. Reifarth, D. Rossi, H. Scheit, H. Simon, H. Weick, and C. Wimmer. Exclusive measurements of quasi-free proton scattering reactions in inverse and complete kinematics. *Physics Letters B*, 753:204 – 210, 2016.

[76] Gerhard Jacob and TH. A. J. Maris. Quasi-free scattering and nuclear structure. *Rev. Mod. Phys.*, 38:121–142, Jan 1966.

[77] D. Suzuki, H. Iwasaki, D. Beaumel, M. Assié, H. Baba, Y. Blumenfeld, F. de Oliveira Santos, N. de Séréville, A. Drouart, S. Franchoo, J. Gibelin, A. Gillibert, S. Giron, S. Grévy, J. Guillot, M. Hackstein, F. Hammache, N. Keeley, V. Lapoux, F. Maréchal, A. Matta, S. Michimasa, L. Nalpas, F. Naqvi, H. Okamura, H. Otsu, J. Pancin, D. Y. Pang, L. Perrot, C. M. Petrache, E. Pollacco, A. Ramus, W. Rother, P. Roussel-Chomaz, H. Sakurai, J.-A. Scarpaci, O. Sorlin, P. C. Srivastava, I. Stefan, C. Stodel, Y. Tanimura, and S. Terashima. Second 0^+ state of unbound ^{12}O: Scaling of mirror asymmetry. *Phys. Rev. C*, 93:024316, Feb 2016.

[78] H T Fortune and R Sherr. Update on 12o(g.s.) width for simultaneous 2p decay. *Journal of Physics G: Nuclear and Particle Physics*, 40(5):055102, mar 2013.

[79] H.T. Fortune. Narrow resonances in 11n and 15f. *Nuclear Physics A*, 968:342 – 349, 2017.

[80] H. T. Fortune. Energies and widths in ^{11}N. *Phys. Rev. C*, 98:014307, Jul 2018.

[81] G.J. Kramer, H.P. Blok, and L. Lapikás. A consistent analysis of (e,ep) and (d,3he) experiments. *Nuclear Physics A*, 679(3):267 – 286, 2001.

[82] C. Barbieri. Role of long-range correlations in the quenching of spectroscopic factors. *Phys. Rev. Lett.*, 103:202502, Nov 2009.

[83] F. Flavigny, A. Gillibert, L. Nalpas, A. Obertelli, N. Keeley, C. Barbieri, D. Beaumel, S. Boissinot, G. Burgunder, A. Cipollone, A. Corsi, J. Gibelin, S. Giron, J. Guillot, F. Hammache, V. Lapoux, A. Matta, E. C. Pollacco, R. Raabe, M. Rejmund, N. de Séréville, A. Shrivastava, A. Signoracci, and Y. Utsuno. Limited

asymmetry dependence of correlations from single nucleon transfer. *Phys. Rev. Lett.*, 110:122503, Mar 2013.

[84] S. Kawase, T. Uesaka, T. L. Tang, D. Beaumel, M. Dozono, T. Fukunaga, T. Fujii, N. Fukuda, A. Galindo-Uribarri, S. Hwang, N. Inabe, T. Kawabata, T. Kawahara, W. Kim, K. Kisamori, M. Kobayashi, T. Kubo, Y. Kubota, K. Kusaka, C. Lee, Y. Maeda, H. Matsubara, S. Michimasa, H. Miya, T. Noro, Y. Nozawa, A. Obertelli, K. Ogata, S. Ota, E. Padilla-Rodal, S. Sakaguchi, H. Sakai, M. Sasano, S. Shimoura, S. Stepanyan, H. Suzuki, T. Suzuki, M. Takaki, H. Takeda, A. Tamii, H. Tokieda, T. Wakasa, T. Wakui, K. Yako, J. Yasuda, Y. Yanagisawa, R. Yokoyama, K. Yoshida, K. Yoshida, and J. Zenihiro. Exclusive quasi-free proton knockout from oxygen isotopes at intermediate energies. *Progress of Theoretical and Experimental Physics*, 2018(2):021D01, February 2018.

[85] E. Cravo, R. Crespo, and A. Deltuva. Distortion effects on the neutron knockout from exotic nuclei in the collision with a proton target. *Phys. Rev. C*, 93:054612, May 2016.

[86] A. Moro M. Gómez-Ramos. personal communication.

[87] Sirwan Hama, B C. Clark, E Cooper, H S. Sherif, and Robert Mercer. Global dirac optical potentials for elastic proton scattering from heavy nuclei. *Phys. Rev. C*, 41:2737–2755, 07 1990.

[88] M. S. Onegin. Constructing effective nucleonâ€“nucleon interaction on the basis of the idaho potentiali. *Physics of Atomic Nuclei*, 71(4):771â€“780, 2008.

[89] M. Gómez-Ramos. *A Transfer to the Continuum formalism for the study of* (p, pn) *and* $(p, 2p)$ *reactions on unstable nuclei.* Dissertation, Universidade de de Sevilla, España.

[90] Mihai Horoi and Alex Brown. Downloading the nuclear structure shell model code oxbash from internet. *https://arxiv.org/abs/nucl-th/9406020*, 07 1994.

[91] V. Somà, C. Barbieri, and T. Duguet. Ab initio self-consistent gorkov-green's function calculations of semi-magic nuclei: Numerical implementation at second order with a two-nucleon interaction. *Phys. Rev. C*, 89:024323, Feb 2014.

[92] Kazuyuki Ogata, Kazuki Yoshida, and Kosho Minomo. Asymmetry of the parallel momentum distribution of (p, pn) reaction residues. *Phys. Rev. C*, 92:034616, Sep 2015.

[93] Jose Luis Rodríguez-Sánchez, Jean-Christophe David, Davide Mancusi, Alain Boudard, Joseph Cugnon, and Sylvie Leray. Improvement of one-nucleon removal and total reaction cross sections in the liège intranuclear-cascade model using hartree-fock-bogoliubov calculations. *Phys. Rev. C*, 96:054602, Nov 2017.

[94] J.-J. Gaimard and K.-H. Schmidt. A reexamination of the abrasion-ablation model for the description of the nuclear fragmentation reaction. *Nuclear Physics A*, 531(3):709 – 745, 1991.

[95] Takashi Shimokawa, Liqiu Ma, Ken Ando, Katsutoshi Sato, and Takashi Imai. The future of combining carbon-ion radiotherapy with immunotherapy: Evidence and progress in mouse models. *International Journal of Particle Therapy*, 3(1):61–70, 2016.

[96] Herman D. Suit, Thomas Delaney, Saveli Goldberg, Harald Paganetti, Ben Clasie, Leo Gerweck, Andrzej Niemierko, E. V. van Hall, Jacob Flanz, Josh Hallman, and Alexei Trofimov. Proton vs carbon ion beams in the definitive radiation treatment of cancer patients. *Radiotherapy and oncology : journal of the European Society for Therapeutic Radiology and Oncology*, 95 1:3–22, 2010.

[97] Felix Horst, Giulia Aricò, Kai-Thomas Brinkmann, Stephan Brons, Alfredo Ferrari, Thomas Haberer, Andrea Mairani, Katia Parodi, Claire-Anne Reidel, Uli Weber, Klemens Zink, and Christoph Schuy. Measurement of ^{4}He charge- and mass-changing cross sections on h, c, o, and si targets in the energy range 70–220 mev/u for radiation transport calculations in ion-beam therapy. *Phys. Rev. C*, 99:014603, Jan 2019.

[98] D. Q. Fang, W. Q. Shen, J. Feng, X. Z. Cai, J. S. Wang, Q. M. Su, H. Y. Zhang, P. Y. Hu, Y. G. Ma, Y. T. Zhu, S. L. Li, H. Y. Wu, Q. B. Gou, G. M. Jin, W. L. Zhan, Z. Y. Guo, and G. Q. Xiao. Measurements of total reaction cross sections for some light nuclei at intermediate energies. *Phys. Rev. C*, 61:064311, May 2000.

[99] A. Ozawa, T. Suzuki, and I. Tanihata. Nuclear size and related topics. *Nuclear Physics A*, 693(1):32 – 62, 2001. Radioactive Nuclear Beams.

[100] M. Takechi, M. Fukuda, M. Mihara, K. Tanaka, T. Chinda, T. Matsumasa, M. Nishimoto, R. Matsumiya, Y. Nakashima, H. Matsubara, K. Matsuta, T. Minamisono, T. Ohtsubo, T. Izumikawa, S. Momota, T. Suzuki, T. Yamaguchi, R. Koyama, W. Shinozaki, M. Takahashi, A. Takizawa, T. Matsuyama, S. Nakajima, K. Kobayashi, M. Hosoi, T. Suda, M. Sasaki, S. Sato, M. Kanazawa, and A. Kitagawa. Reaction cross sections at intermediate energies and fermi-motion effect. *Phys. Rev. C*, 79:061601, Jun 2009.

[101] W. R. Webber, J. C. Kish, and D. A. Schrier. Individual isotopic fragmentation cross sections of relativistic nuclei in hydrogen, helium, and carbon targets. *Phys. Rev. C*, 41:547–565, Feb 1990.

[102] T. Ogawa, T. Sato, S. Hashimoto, D. Satoh, S. Tsuda, and K. Niita. Energy-dependent fragmentation cross sections of relativistic ^{12}C. *Phys. Rev. C*, 92:024614, Aug 2015.

[103] R. J. Glauber and G. Matthiae. High-energy scattering of protons by nuclei. *Nucl. Phys.*, B21:135–157, 1970.

[104] Paul J. Karol. Nucleus-nucleus reaction cross sections at high energies: Soft-spheres model. *Phys. Rev. C*, 11:1203–1209, Apr 1975.

[105] Luiz F. Oliveira, Raul Donangelo, and John O. Rasmussen. Abrasion-ablation calculations of large fragment yields from relativistic heavy ion reactions. *Phys. Rev. C*, 19:826–833, Mar 1979.

[106] J. Benlliure, K.-H. Schmidt, D. Cortina-Gil, T. Enqvist, F. Farget, A. Heinz, A.R. Junghans, J. Pereira, and J. Taieb. Production of neutron-rich isotopes by cold fragmentation in the reaction 197au + be at 950 a mev. *Nuclear Physics A*, 660(1):87 – 100, 1999.

[107] K.-H. Schmidt, T. Brohm, H.-G. Clerc, M. Dornik, M. Fauerbach, H. Geissel, A. Grewe, E. Hanelt, A. Junghans, A. Magel, W. Morawek, G. MÃ¼nzenberg, F. Nickel, M. PfÃ¼tzner, C. Scheidenberger, K. SÃ¼mmerer, D. Vieira, B. Voss, and C. Ziegler. Distribution of ir and pt isotopes produced as fragments of 1 a gev 197au projectiles: a thermometer for peripheral nuclear collisions. *Physics Letters B*, 300(4):313 – 316, 1993.

[108] A.R. Junghans, M. de Jong, H.-G. Clerc, A.V. Ignatyuk, G.A. Kudyaev, and K.-H. Schmidt. Projectile-fragment yields as a probe for the collective enhancement in the nuclear level density. *Nuclear Physics A*, 629(3):635 – 655, 1998.

[109] M. de Jong, K.-H. Schmidt, B. Blank, C. BÃ¶ckstiegel, T. Brohm, H.-G. Clerc, S. Czajkowski, M. Dornik, H. Geissel, A. Grewe, E. Hanelt, A. Heinz, H. Irnich, A.R. Junghans, A. Magel, G. MÃ¼nzenberg, F. Nickel, M. PfÃ¼tzner, A. Piechaczek, C. Scheidenberger, W. Schwab, S. SteinhÃ¤user, K. SÃ¼mmerer, W. Trinder, B. Voss, and C. Ziegler. Fragmentation cross sections of relativistic 208pb projectiles. *Nuclear Physics A*, 628(3):479 – 492, 1998.

[110] A. Boudard, J. Cugnon, S. Leray, and C. Volant. Intranuclear cascade model for a comprehensive description of spallation reaction data. *Phys. Rev. C*, 66:044615, Oct 2002.

[111] A. Boudard, J. Cugnon, J.-C. David, S. Leray, and D. Mancusi. New potentialities of the liège intranuclear cascade model for reactions induced by nucleons and light charged particles. *Phys. Rev. C*, 87:014606, Jan 2013.

[112] J. Cugnon, D. L'Hôte, and J. Vandermeulen. Simple parametrization of cross-sections for nuclear transport studies up to the gev range. *Nuclear Instruments and Methods in Physics Research Section B: Beam Interactions with Materials and Atoms*, 111(3):215 – 220, 1996.

[113] J. Cugnon and P. Henrotte. The low-energy limit of validity of the intranuclear cascade model. *Eur. Phys. J. A*, 16(3):393–407, 2003.

[114] J. B. Natowitz, R. Wada, K. Hagel, T. Keutgen, M. Murray, A. Makeev, L. Qin, P. Smith, and C. Hamilton. Caloric curves and critical behavior in nuclei. *Phys. Rev. C*, 65:034618, Mar 2002.

[115] K.-H. Schmidt, M.V. Ricciardi, A.S. Botvina, and T. Enqvist. Production of neutron-rich heavy residues and the freeze-out temperature in the fragmentation of relativistic 238u projectiles determined by the isospin thermometer. *Nuclear Physics A*, 710(1):157 – 179, 2002.

[116] C. Sfienti, M. De Napoli, P. Adrich, T. Aumann, C.O. Bacri, T. Barczyk, R. Bassini, S. Bianchin, C. Boiano, A.S. Botvina, A. Boudard, J. Brzychczyk, A. Chbihi, J. Cibor, B. Czech, J.-E. Ducret, H. Emling, J. Frankland, and M. Hellstr˙ Gross properties and isotopic phenomena in spectator fragmentation. *Nuclear Physics A*, 787(1):627 – 632, 2007. Proceedings of the Ninth International Conference on Nucleus-Nucleus Collisions.

[117] A. S. Botvina, N. Buyukcizmeci, M. Erdogan, J. Łukasik, I. N. Mishustin, R. Ogul, and W. Trautmann. Modification of surface energy in nuclear multifragmentation. *Phys. Rev. C*, 74:044609, Oct 2006.

[118] A.S. Botvina, A.S. Iljinov, I.N. Mishustin, J.P. Bondorf, R. Donangelo, and K. Sneppen. Statistical simulation of the break-up of highly excited nuclei. *Nuclear Physics A*, 475(4):663 – 686, 1987.

[119] V. F. Weisskopf and D. H. Ewing. On the yield of nuclear reactions with heavy elements. *Phys. Rev.*, 57:472–485, Mar 1940.

[120] R.Bass. Proceedings of the symposium on deep inelastic and fusion reactions with heavy ions. *Lecture Note in Physics*, 117.

[121] B. Jurado, K.-H. Schmidt, and J. Benlliure. Time evolution of the fission-decay width under the influence of dissipation. *Physics Letters B*, 553(3):186 – 190, 2003.

[122] Y. L. Sun, J. Lee, Y. L. Ye, A. Obertelli, Z. H. Li, N. Aoi, H. J. Ong, Y. Ayyad, C. A. Bertulani, J. Chen, A. Corsi, F. Cappuzzello, M. Cavallaro, T. Furono, Y. C. Ge, T. Hashimoto, E. Ideguchi, T. Kawabata, J. L. Lou, Q. T. Li, G. Lorusso, F. Lu, H. N. Liu, S. Nishimura, H. Suzuki, J. Tanaka, M. Tanaka, D. T. Tran, M. B. Tsang, J. Wu, Z. Y. Xu, and T. Yamamoto. Experimental study of the knockout reaction mechanism using ^{14}O at 60 mev/nucleon. *Phys. Rev. C*, 93:044607, Apr 2016.

[123] T. Shimoda, H. Miyatake, and S. Morinobu. Design study of the secondary-beam line at rcnp. *Nuclear Instruments and Methods in Physics Research Section B: Beam Interactions with Materials and Atoms*, 70(1):320 – 330, 1992.

[124] Javier Díaz Cortés. *Single-Nucleon Knockout and Total Reactions Cross Sections in Medium-Mass Neutron-Rich Nuclei.* Dissertation, Universidade de Santiago de Compostela, España.

"It was quite the most incredible event that has ever happened to me in my life. It was almost as incredible as if you fired a 15-inch shell at a piece of tissue paper and it came back and hit you."

Ernest Rutherford